

# **Structural health monitoring of non-linear hysteretic structures**

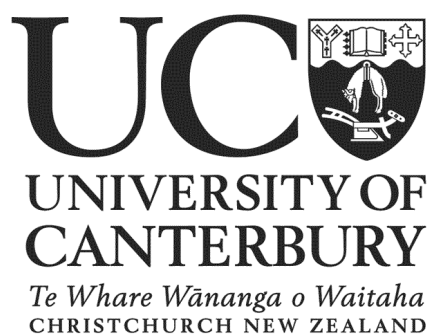
**Eimantas Poškus**

A thesis presented in partial fulfillment of the requirements for the degree of

Doctor of Philosophy

in Mechanical Engineering

at the



University of Canterbury

Christchurch, New Zealand

December 2017

---

## Abstract

---

Ensuring life safety is the primary design and maintenance requirement for civil structures designed to be serviceable for a specific lifetime. However, structures subjected to a number of factors may experience quicker or more gradual deterioration than anticipated, or even a premature loss of function. Scheduled visual inspection is the oldest and most commonly used damage monitoring technique, but has significant disadvantages when quick damage assessment and certainty are needed, such as after a major seismic event. Quick, accurate and quantitative determination of the damage state is vital following an earthquake, to estimate damage, remaining life-time, and ensure safe re-occupancy, if possible.

Rapid development of sensor technology and increasing computing power has enabled continuous structural monitoring using various sensing techniques. The measured data can be analyzed using structural health monitoring (SHM) methods. SHM refers to all elements of the process of identifying mechanical properties of a structural system, comparing it with previous states, detecting changes/abnormalities, and relating these to damage. A successful SHM method should be able to automatically identify and locate damage after large, non-linear response events.

The majority of existing, primarily vibration based, SHM techniques have serious limitations in situations where a quick, accurate, and quantitative assessment is needed. More specifically, many SHM techniques perform well when structures behave linearly and are subjected to ambient loads, but this does not apply to earthquake events. Moreover, some methods can only work off-line, involve significant computational effort and/or human input, and/or do not provide any indication of damage location and/or severity.

To address these limitations, this thesis explores the application of a novel SHM implementation strategy composed of a novel modal parameter identification and its subsequent application to a proven hysteresis loop analysis (HLA) method. The study demonstrates the proposed strategy can be readily used to track the performance of non-linear degrading structures subjected to strong ground motion, essentially in real-time and without human input. Thus, the proposed tools can be used to support/replace visual inspection results, reduce downtime, minimize business disruptions and, most importantly, maximize life safety.

More specifically, this thesis proposes and analyses the application of a novel modal parameter identification technique, which performs in near real-time and, most importantly, is efficient when approximating non-linear structures subjected to relatively short duration ground motion inputs. The technique operates in modal space and is based on a pre-defined optimization process, which decouples frequency response spectra of interfering, generally higher frequency, modes. Optimization can be realized over relatively short time windows to provide continuous monitoring of highly non-linear, degrading structures.

In particular, identified modal parameters can be readily used to identify damage. However, modal parameters can have very poor sensitivity to damage and are often difficult to interpret. Thus, it is challenging to infer the location and severity of damage based on detected changes/variation in modal parameters alone. In this research, the identified time-varying modal parameters are used to decompose the structural response and reconstruct single mode dominant restoring force-deformation hysteresis loops, which can be readily analyzed using recently developed hysteresis loops analysis (HLA). The versatility and robustness of HLA has been explored in a number of studies. However, the analyzed case structures employed in these validation cases exhibited very small contribution from the higher modes, which typically can cause significant irregularities, and make effective implementation of HLA more problematic. Hence, this thesis aims to improve the robustness of HLA, using mode segregation and reconstruction of single mode dominant, regular shape hysteresis loops from non-linear structural response.

First, this research develops a modal parameter output-only identification technique, which is validated for a simple time-invariant linear structure. Second, the output-only method is extended to an input-output method enabling operators to carry out near-real time identification of non-linear structures, which is validated for a simple time-varying non-linear structure. Third, the input-output method is validated using the simulation results of a more complex non-linear multi-degree-of-freedom structure, formulated using fiber elements. Finally, the proposed SHM strategy, consisting of continuous modal parameter identification and subsequent application of HLA is validated for two experimental non-linear structures.

Overall, this thesis proposes a novel system identification technique, which performs output-only identification of linear structures and, more importantly, provides input-output real-time modal parameter tracking of highly non-linear structures. Thus, the method extends the application of modal SHM methods to non-linear cases. The proposed technique performs successfully without operator input and can be easily automated to provide continuous modal tracking and damage detection. The technique performs both as stand-alone for damage detection and in combination with HLA for damage quantification as demonstrated for highly non-linear cases.



---

## Acknowledgments

---

I would like to thank my supervisors Associate Professor Geoffrey Rodgers and Distinguished Professor J. Geoffrey Chase for providing guidance mentoring, and being supportive. Thanks for giving me freedom to make my own mistakes and allowing me to explore different opportunities.

I would also like to express my appreciation to EQC for providing funding this research.

Thesis reviewers are greatly appreciated for their critical, constructive and supportive feedback.

Many thanks to Cong and Reza for insightful discussions about structural health monitoring. Big thanks to Arsalan for demonstrating me how shear walls fail during earthquake motion in slow motion - 1 week. My office mates, flat mates, climbing mates, cycling mates and running mates are thanked for great moments, adventures and for putting milestones during the course of my PhD. And big thanks to New Zealand for slowing down the time and flavoring my PhD experience.

I am also grateful to my parents for being supportive and encouraging me to explore the opportunities that come across my life. And finally, thanks to my partner Monique for endless support, for encouraging me to come to New Zealand and challenge a PhD, for keeping me sane, and providing me a kick or brake when needed.

The work presented in Chapter 5 is in print to be published as:

- Poskus, E, Rodgers, GW, Zhou, C and Chase, JG (2017). “Damage Identification for Hysteretic Structures Using a Mode Decomposition Method,” Computer Aided Civil Infrastructure Engineering (CACIE), accepted Sept 2017 – to appear, ISSN: 1467-8667.

---

# Contents

---

<b>1</b>	<b>Introduction</b>	<b>1</b>
1.1	Background . . . . .	1
1.2	Review of SHM methods . . . . .	4
1.2.1	Parametric methods . . . . .	6
1.2.2	Non-parametric methods . . . . .	9
1.3	Summary outcomes of prior art . . . . .	21
1.4	Thesis objective . . . . .	22
1.5	Preface . . . . .	23
<b>2</b>	<b>Output-only modal parameter identification</b>	<b>25</b>
2.1	Introduction . . . . .	25
2.2	Method . . . . .	26
2.2.1	Mode decoupling . . . . .	26
2.2.2	Mode shape approximation using output-only data . . . . .	30
2.2.3	Methodology details . . . . .	34
2.2.4	Mode identification summary . . . . .	38
2.3	Method validation and analyses . . . . .	42
2.3.1	Test structure . . . . .	42
2.3.2	Initial modal parameter identification . . . . .	43
2.4	Results and Discussion . . . . .	44
2.4.1	Initial modal parameter identification . . . . .	44
2.4.2	Limitations . . . . .	47
2.5	Summary . . . . .	48

<b>3</b>	<b>Input-output modal parameter identification</b>	<b>49</b>
3.1	Introduction . . . . .	49
3.2	Method . . . . .	50
3.2.1	Mode decoupling . . . . .	50
3.2.2	Input-output identification . . . . .	51
3.2.3	Initial mode identification and mode evolution . . . . .	56
3.3	Method validation and analyses . . . . .	59
3.3.1	Test structure . . . . .	59
3.3.2	Input ground motions and input parameters . . . . .	59
3.4	Results . . . . .	61
3.4.1	Modal parameter evolution . . . . .	61
3.4.2	Output-only identification . . . . .	64
3.4.3	Parameter sensitivity analysis . . . . .	67
3.4.4	Overall discussion and limitations . . . . .	69
3.5	Summary . . . . .	71
<b>4</b>	<b>Non-linear analysis using fiber formulation and modal parameter identification</b>	<b>73</b>
4.1	Introduction . . . . .	73
4.2	Methodology . . . . .	74
4.2.1	FE modeling using fiber formulation . . . . .	74
4.2.2	Modal parameter identification . . . . .	75
4.3	Validation study using simulated non-linear response . . . . .	77
4.3.1	FE model . . . . .	77
4.3.2	Non-linear simulation . . . . .	81
4.3.3	Modal parameter identification . . . . .	83
4.4	Results and Discussion . . . . .	84
4.4.1	Initial modal parameter identification . . . . .	84
4.4.2	Modal parameter identification for a suite of EQ inputs . . . . .	86
4.5	Summary . . . . .	93

<b>5</b>	<b>Damage Identification for Hysteretic Structures Using a Novel Mode Filtering Method</b>	<b>95</b>
5.1	Introduction . . . . .	95
5.2	Methodology . . . . .	96
5.2.1	Reconstruction of hysteresis loops for selected modes . . . . .	96
5.2.2	Mode shape identification . . . . .	98
5.3	Method validation using experimental structure . . . . .	101
5.3.1	Analyses . . . . .	103
5.4	Results and discussion . . . . .	105
5.4.1	Reconstructed hysteresis loops for Tests 1 to 9 . . . . .	105
5.4.2	Hysteresis loop analysis . . . . .	106
5.4.3	Modal parameter identification . . . . .	109
5.4.4	Overall damage identification . . . . .	110
5.4.5	Limitation and other aspects . . . . .	111
5.5	Summary . . . . .	113
<b>6</b>	<b>Modal parameter identification for a 5-story full scale test structure</b>	<b>115</b>
6.1	Introduction . . . . .	115
6.2	Method . . . . .	116
6.3	Method validation and analyses . . . . .	116
6.3.1	Test structure . . . . .	116
6.3.2	Analyses . . . . .	118
6.4	Results and Discussion . . . . .	121
6.4.1	Base isolated structure . . . . .	121
6.4.2	Fixed base structure . . . . .	130
6.5	Summary . . . . .	139
<b>7</b>	<b>Application of mode decomposition and HLA</b>	<b>141</b>
7.1	Introduction . . . . .	141
7.2	Method . . . . .	142
7.2.1	Modal parameter identification and mode decoupling . . . . .	142

7.2.2	Hysteresis loop analysis (HLA)	143
7.3	Method validation	150
7.3.1	Test structure	150
7.3.2	Analyses	150
7.4	Results and Discussion	153
7.4.1	Base isolated structure	153
7.4.2	Fixed base structure	161
7.5	Summary	173
<b>8</b>	<b>Conclusions</b>	<b>175</b>
<b>9</b>	<b>Future research</b>	<b>180</b>
9.1	Improving time resolution and accuracy of modal parameter tracking	180
9.2	Identification using limited number of DOFs	181
9.3	Formulation of objective functions using raw FRS	181
9.4	Identification of non-classically damped systems	182
9.5	Incorporation of EMD	182
9.6	Comparison to other identification methods	182
9.7	Further validation with HLA	183

---

## List of Figures

---

1.1	Maintenance plan and structural performance under unexpected failures. . . . .	3
1.2	Classification of different SHM methods . . . . .	5
2.1	(a) FRF fitting, frequency bandwidth and shape function estimation (b) Shape function, $N_i$ , overlapped with receptance, $\bar{y}_i^{abs}(\omega)$ to obtain isolated FRS, $\bar{y}_i^{iso}$ .	32
2.2	Mode-by-mode optimization example for a 3 DOF system. The term <i>abs</i> in the subscript of $corr_j^{iso,abs,i}$ and $\bar{y}_i^{abs}$ refers to the calculations based on the absolute measurements. . . . .	33
2.3	Example structure with double modes: a) Cantilever structure b) Two orthogonal modes aligned with the principal axes x and y c) Multiple sets of orthogonal vectors . . . . .	35
2.4	Flow chart for initial mode-by-mode optimization for any given time window .	41
2.5	Bridge pier test structure and a simplified 4 DOF model used for simulation . .	43
2.6	Input ground motion time histories and frequency spectra for (a) white noise 2.5%g RMS and (b) selected earthquake ground motions . . . . .	44
3.1	Receptance (left) and inertance (right) FRS and FRF for a 3DOF system . . . .	53
3.2	Mode-by-mode optimization example for a 3 DOF system for input excitations with non-uniform frequency content . . . . .	54
3.3	Flow chart for initial mode-by-mode optimization for any given time window .	57
3.4	Flow chart for identification of modal parameter evolution . . . . .	58
3.5	Input ground motion time history in x direction and frequency spectra for white noise 2.5%g RMS and selected earthquake ground motions . . . . .	60

3.6	Absolute acceleration response time history of the selected DOFs ( $\phi_1$ and $\phi_3$ ) of time-variant structure subjected to white noise (0-120s) and earthquake (120-200s) excitations, with the damage occurring at $t = 135s$ . . . . .	62
3.7	Modal frequency evolution identified based on 5% RMS signal to noise ratio using $L = 5T_1$ window length, effective peak width $W = 5$ and assumed mass matrix with 30% error . . . . .	63
3.8	Mode shape evolution identified based on 5% RMS signal to noise ratio using $L = 5T_1$ window length, effective peak width $W = 5$ and assumed mass matrix with 30% error . . . . .	63
3.9	Modal frequency evolution identified based on 5% RMS signal to noise ratio using $L = 20T_1$ window length, effective peak width $W = 5$ and assumed mass matrix with 30% error . . . . .	65
3.10	Mode shape evolution identified based on 5% RMS signal to noise ratio using $L = 20T_1$ window length, effective peak width $W = 5$ and assumed mass matrix with 30% error . . . . .	65
3.11	Modal frequency evolution identified based on 20% RMS signal to noise ratio using $L = 20T_1$ window length, effective peak width $W = 5$ and assumed mass matrix with 30% error . . . . .	66
3.12	Mode shape evolution identified based on 20% RMS signal to noise ratio using $L = 20T_1$ window length, effective peak width $W = 5$ and assumed mass matrix with 30% error . . . . .	66
3.13	Modal frequency evolution identified based on 20% RMS signal to noise ratio using $L = 20T_1$ window length, effective peak width $W = 10$ and assumed mass matrix with 30% error . . . . .	68
3.14	Mode shape evolution identified using output-only measurements based on 5% RMS signal to noise ratio using $L = 20T_1$ window length, effective peak width $W = 5$ and assumed mass matrix with 30% error . . . . .	68



3.15	(a) Total mean absolute error (MAE) of identified frequencies estimated for different RMS noise levels, window lengths (L) and peak widths (W) a) assuming the mass matrix, $M$ , is known and b) assuming 30% error in mass matrix estimation	69
3.16	(a) Mean absolute error (MAE) estimated for different RMS noise levels, window lengths (L) and peak widths (W) a) assuming the mass matrix, $M$ , is known and b) assuming 30% error in mass matrix estimation	70
4.1	Flow chart for fiber element state determination loop implemented inside Newton-Raphson structure's integration loop [173]	76
4.2	Flow chart for identification of modal parameter evolution	77
4.3	Elevation and plan views of modelled full-scale test structure [179]	79
4.4	Simplified 2D fiber model constructed using beam and column fiber elements	79
4.5	Input ground motion time histories for EQ3 and EQ6 events	82
4.6	Mode shapes identified from 30 seconds white noise excitation response	84
4.7	A comparison between identified and simulated mode shape evolutions of 5 modes for earthquake input EQ3. Vertical dashed line marks the effective duration of earthquake event	87
4.8	A comparison between identified and simulated mode shape evolutions of 5 modes for earthquake input EQ6. Vertical dashed line marks the effective duration of earthquake event	88
4.9	Estimated mean absolute error (MAE) of identified mode shape coefficients for different earthquake inputs using data polluted with 10% RMS noise sorted in ascending MAE order	90
4.10	Unit normalized smoothed frequency spectra of selected input ground motions, for which the identification produced the best and poorest accuracy of higher modes	91
4.11	A comparison between identified and simulated modal frequency evolutions of 5 modes for earthquake input EQ3. Vertical dashed line marks the effective duration of earthquake event	92

4.12	A comparison between identified and simulated modal frequency evolutions of 5 modes for earthquake input EQ6. Vertical dashed line marks the effective duration of earthquake event . . . . .	92
4.13	A comparison between identified and simulated modal frequency evolutions of 5 modes for earthquake input EQ6. Vertical dashed line marks the effective duration of earthquake event . . . . .	92
5.1	Mode-by-mode mode shape identification for a MDOF system . . . . .	99
5.2	a) Bridge pier on the shake table [165]; and b) sensor location with basic dimensions . . . . .	102
5.3	Base moment versus displacement loops reconstructed from white noise (WN) and earthquake (EQ) excitation tests 1-9 using a) raw acceleration data; and b) mode decomposed data . . . . .	107
5.4	The overall evolution of the elastic stiffness from Test 1 to Test 9 (WN – white noise, EQ- earthquake excitation) . . . . .	108
5.5	The overall mode shape evolution from Test 1 to Test 9 for $\hat{\Phi}(2, 1)$ and $\hat{\Phi}(1, 2)$ , where $\hat{\Phi}(1, 1) = \hat{\Phi}(2, 2) = 1$ due to normalization . . . . .	109
5.6	Identified modal damping ratios and frequencies for two dominant modes . . .	110
6.1	a) Bare structural frame before installation of non-structural components b) Building equipped with the facade c) Base isolator detail. Pictures taken from [191] . . . . .	117
6.2	Front and plan views of the 5 storey concrete structure and accelerometer spatial arrangement . . . . .	117
6.3	Receptance FRF of BI structure for the first lowest 10 identified modes . . . .	122
6.4	Identified first ten mode shapes . . . . .	123
6.5	Modal frequency evolution . . . . .	124
6.6	Modal frequency versus RMS ground excitation estimated for two selected test groups . . . . .	125

6.7	Modal frequency evolution identified in Astroza et al. [116] study using only ambient vibration data. Figure modified from [116] . . . . .	126
6.8	Equivalent modal damping ratio evolution for the selected modes identified from the ambient vibrations and white noise excitation . . . . .	127
6.9	Modal damping versus RMS ground excitation identified from the ambient and white noise ground excitation . . . . .	129
6.10	Mode shape $\Phi(:,i) = [\phi_1 \dots \phi_{24}]$ , evolution for white noise (WN) and earthquake (EQ) excitations . . . . .	131
6.11	FRFs for the first ten identified modes . . . . .	132
6.12	Identified first ten mode shapes for the FB building . . . . .	133
6.13	Modal frequency evolution of the first seven modes for white noise (WN) and earthquake (EQ) excitations . . . . .	134
6.14	Modal frequency relation to RMS ground excitation at different stages of the test protocol for modes 1-L, 5-L and 7-L . . . . .	135
6.15	Modal damping, $\xi$ , evolution of the first seven modes for white noise (WN) and earthquake (EQ) excitations . . . . .	135
6.16	Modal damping, $\xi$ , of the first seven modes identified for different RMS input ground excitation levels . . . . .	136
6.17	Mode shape 1-L, $\Phi(:,i) = [\phi_1 \dots \phi_{24}]^T$ , evolution for white noise (WN) and earthquake (EQ) excitations. . . . .	137
6.18	Mode shape 5-L, $\Phi(:,i) = [\phi_1 \dots \phi_{24}]^T$ , evolution for white noise (WN) and earthquake (EQ) excitations. . . . .	138
6.19	Mode shape 7-L, $\Phi(:,i) = [\phi_1 \dots \phi_{24}]^T$ , evolution for white noise (WN) and earthquake (EQ) excitations. . . . .	138
7.1	Piecewise linear hysteretic models ( $r = 1, 2, 3, 4$ ) for an arbitrary sub-half cycle	144
7.2	Flow chart for optimal number of segments identification for selected sub-half cycle . . . . .	149
7.3	a) Structure with monitored 24 DOFs b) Assumed hysteretic model for the BI structure c) Assumed hysteretic model for the FB structure . . . . .	152

7.4	a) Typical hysteretic behavior of base isolators and HLA approximation and b) typical hysteretic pinching behavior of RC structure and HLA approximation using $r = 4$ segment model . . . . .	153
7.5	Base isolator hysteresis loops reconstructed for white noise(WN) and earthquake excitations (EQ). The grey lines represent restoring force history from the previous cycles . . . . .	155
7.6	Base isolator hysteresis loops reconstructed for white noise (WN) and earthquake excitations (EQ). The grey lines represent restoring force history from the previous cycles . . . . .	156
7.7	Post-elastic stiffness evolution of rubber bearings for earthquake (EQ) and white noise (WN) tests . . . . .	157
7.8	Elastic stiffness evolution of the superstructure for earthquake (EQ) tests for the BI structure . . . . .	158
7.9	A comparison of hysteresis loops reconstructed for tests EQ3, EQ4 and EQ6 using raw (left) and decoupled (red) acceleration data . . . . .	160
7.10	Hysteresis loops reconstructed for each inter-story of FB building for tests WN1 to WN3 . . . . .	162
7.11	Hysteresis loops reconstructed for each inter-story of FB building for tests EQ3 to WN4 . . . . .	163
7.12	Hysteresis loops reconstructed for each inter-story of FB building for tests WN5 to EQ6 . . . . .	164
7.13	Interstory stiffness evolution for white noise (WN) and earthquake (EQ) excitations . . . . .	166
7.14	Overall superstructure shear stiffness evolution for white noise (WN) and earthquake tests (EQ), where the dashed blue line represents the shear stiffness identified at the end of BI testing, as shown in Figure 7.8 . . . . .	167
7.15	Comparison of inter-story shear force versus displacement loops reconstructed for test EQ4 using raw (left) and decoupled (right) acceleration data . . . . .	170

7.16	Comparison of inter-story shear force versus displacement loops reconstructed for test EQ5 using raw (left) and decoupled (right) acceleration data . . . . .	171
7.17	A comparison of inter-story pinching stiffness evolution profiles obtained using decoupled (black) and raw (red) hysteresis loops for white noise (WN) and earthquake (EQ) excitations . . . . .	172

---

## List of Tables

---

2.1	Calculated modal parameters of a 4 DOF system . . . . .	42
2.2	Identified modal frequencies for different signal noise levels . . . . .	45
2.3	Identified equivalent modal damping for different signal noise levels . . . . .	45
2.4	Identified mode shape coefficients for different levels of signal noise . . . . .	45
2.5	Identified modal frequencies for different signal noise levels based on earth- quake response data . . . . .	46
2.6	Equivalent modal damping for different signal noise levels identified from re- sponse to earthquake excitation . . . . .	46
2.7	Identified mode shape coefficients for different levels of signal noise based on the response to earthquake excitation . . . . .	47
3.1	A list of parameters used for modal parameter identification . . . . .	61
4.1	Member properties used for 2D FE model . . . . .	80
4.2	Estimated first 5 modal parameters . . . . .	81
4.3	A suite of 20 input ground motions [184] . . . . .	82
4.4	Comparison of simulated and identified modal parameters using 30 seconds white noise excitation response, with and without noise added to the response data before identification. . . . .	85
4.5	Identified modal frequencies for different signal noise levels based on white noise excitation response . . . . .	85
4.6	Equivalent modal damping for different signal noise levels identified from re- sponse to white noise excitation . . . . .	85

5.1	Input ground motions to test structure . . . . .	102
5.2	Summary of elastic stiffness evolution before and after the tests . . . . .	108
6.1	Input ground motions for the base isolated test structure . . . . .	118
6.2	Input ground motions for the fixed base test structure . . . . .	118
6.3	Data segmentation summary . . . . .	121
7.1	Constrains imposed on HLA . . . . .	146
7.2	Identified total shear stiffness of the superstructure at the start and the end of the earthquake (EQ) and white noise (WN) tests . . . . .	158
7.3	Identified inter-story shear stiffness at the start and the end of the earthquake (EQ) and white noise (WN) tests for the FB configuration . . . . .	168
7.4	Identified inter-story shear stiffness at the start and the end of the earthquake (EQ) and white noise (WN) tests for the FB configuration . . . . .	169

# CHAPTER 1

---

## Introduction

---

### 1.1 Background

Earthquakes are one of the most costly natural disasters worldwide. Strong ground motions damage infrastructure and buildings, and, most importantly, can lead to loss of life, all of which have an enormous economic and impact cost. The Canterbury earthquakes resulted in significant damage across Christchurch, where the rebuild is estimated to cost the equivalent of approximately 20 percent of New Zealand's gross domestic product (GDP). In March 2011, Japan was hit by a devastating earthquake and tsunami, which caused damage equivalent to 4 percent of Japan's GDP [1]. Even more devastating consequences were seen in Haiti (2010), Guatemala (1976), Nicaragua (1972), and El Salvador (1986), where the economic losses of approximately 120, 98, 82, and 40% of GDP were estimated for each country, respectively [2, 3].

Ensuring life safety is the primary requirement for structural engineers when designing structures. Most structures are designed to last a specific lifetime, meaning they are expected to resist the effects caused by various hazards without losing integrity. However, unpredictable and infrequent natural disasters, increasing load demands, poor design and maintenance, overuse, fatigue, harsh environments, and ageing effects can shorten the anticipated structural life-time. In addition, for economic reasons, structures in seismically active areas are designed to sustain a certain amount of sacrificial damage, which typically appears in the form of concrete member cracking or spalling, and/or yielding of steel reinforcement. A number of studies demonstrated



sudden loss of a structure's functionality can have a significant economic, social and environmental impacts [4–6]. Thus, timely maintenance and retrofit/upgrade of structures is essential in ensuring long-term safety and functionality.

Life-cycle management (LCM) provides tools for efficient maintenance strategies, which allows owners to maximize the lifetime, safety, and functionality of structures. Typically, the maintenance strategy consists of periodic damage identification, maintenance and retrofit. Damage identification, to date, is most often carried out based on visual inspection. However, this type of assessment is very much dependent on the qualifications and experience of the engineer. This visual inspection method is also relatively slow and time consuming, and it is sometimes impossible or impractical to inspect all potential damage areas due to non-structural components and building services. Thus, damage associated to low-cycle fatigue effects [7, 8] or yielding of reinforcement can easily be underestimated.

To achieve better insight into structural system performance, structural health monitoring (SHM) can be employed. SHM is a non-destructive process of capturing the mechanical properties of a structural system, comparing it with previous states, detecting changes/abnormalities, which in turn can be related to damage. Hence, reliable SHM can be used to support/validate or replace visual inspection results, and could be implemented into LCM to improve decision making processes.

Continuous SHM opens possibilities to provide up-to-date structural status and predictions of future performance, which would allow scheduling of inspection, maintenance and repair works as needed [9]. Such smart management would ensure cost effective LCM and, most importantly, maximize structural safety. A typical example of maintenance plan implemented using smart management is illustrated in Figure 1.1. The benefits of an integrated framework of LCM coupled with SHM have been demonstrated for wind turbines [10, 11], which allowed operators to optimize the operational performance of the wind turbines and to precisely schedule maintenance work at minimum associated life-cycle costs. SHM and optimization of mainte-

nance strategies has also been analyzed for bridge structures [12–14], ship structures [15], and aerospace systems [16].

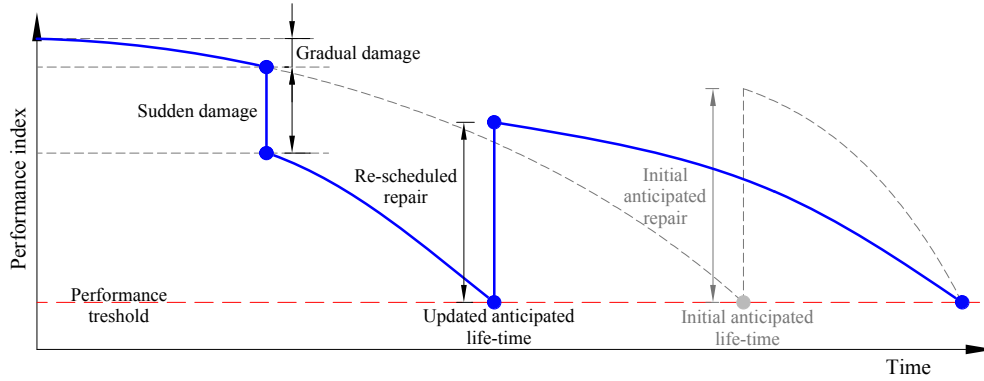


Figure 1.1: Maintenance plan and structural performance under unexpected failures. Figure reproduced from [4]

The need for reliable SHM and LCM tools was emphasized after the series of Canterbury earthquakes. Structures subjected to a series of strong ground motion events might potentially suffer from low-cycle fatigue, which is described as a failure mode of steel members. It is caused by a small number of high level tension and compression strains [7], which are well beyond the elastic strain limit. Christchurch city was subjected to a large number of strong ground motions, potentially imposing such cumulative cyclic damage to RC structures [8, 17], which might have contributed to the complete loss of integrity in some cases.

The majority of well-established vibration based SHM techniques have been developed for linear systems, meaning these methods can be used to track the performance of slowly degrading structures, where degradation is seen in modal frequencies. However, strong ground motion is often destructive in the short term, triggering a non-linear response. Thus these methods will fail to provide the true state of structure.

A reliable and quick damage identification allows responsible authorities to prioritize repairs, ensure safe re-occupancy, and minimize business disruptions, all of which are crucial when re-establishing the normal operation of communities. However, as noted, many current

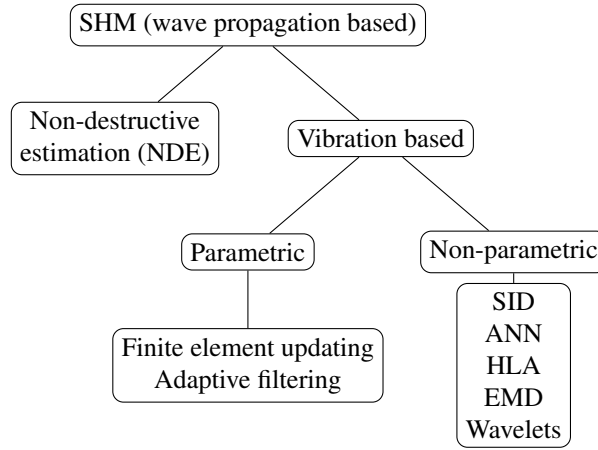
SHM methods do not easily or accurately offer this potential, especially not without human intervention. In response, a new vibration based, non-parametric SHM strategy is proposed in this thesis. The proposed strategy consists of a novel modal parameter identification technique and its application to reconstruction of single mode dominant hysteresis loops, which can be readily analysed using hysteresis loops analysis [18–20]. The proposed modal parameter identification technique is simple, intuitive, can be implemented nearly-real time. Most importantly, it is effective when identifying non-linear structures and could be automated for use without human input.

## 1.2 Review of SHM methods

Structural health monitoring covers a broad range of techniques and methods, tailored to monitor different structural systems and provide different levels or types of damage identification [21]. These levels of damage identification are:

- Level 1: Identifying the presence of damage
- Level 2: Localizing the damage
- Level 3: Quantifying the damage
- Level 4: Predicting the remaining life-time

SHM techniques can also be distinguished into two major categories, as shown in Figure 1.2, based on the underlying approaches used and outcomes achieved. The first group, non-destructive evaluation (NDE), covers a large number of different techniques, including ultrasonic guided waves [22, 23], lamb waves [24, 25], X-ray [26, 27], acoustic emission [28, 29], and electromagnetic testing [30]. They are used to detect the presence of discontinuities, which would affect the service-life of a structural element [31]. NDE has found applications in many fields [32] and all NDE methods offer a good sensitivity to damage at the element level, but are onerous and highly complex at the global, full structure scale. For these reasons, NDE is often used as an additional tool to quantify the severity of damage (Level 3 identification), when the location of the damage has been localized [33].



*Figure 1.2: Classification of different SHM methods*

The second group, vibration based SHM, relies on data collected from an array of sensors, typically accelerometer, strain gages or GPS, and different computational algorithms. Together, the goal is to detect abnormalities or changes in monitored linear response parameters, such as frequency, damping, stiffness and damage index. One of the main features of vibration based SHM is the ability to perform structural screening on-line or nearly on-line, thus enabling operators to make quick decisions, maximize life-safety, and potentially minimize downtime costs. The availability of data immediately following a large earthquake can be extremely valuable to first responders and regulatory bodies such as civil defence.

Vibration based SHM methods are typically regarded as global methods due to limited number of sensors used to monitor the structure and the level of information extracted using these methods [33]. Hence, in some cases, determination of damage location and severity is still a challenging task. Vibration based SHM can thus be further divided into two groups, based on the underlying concepts and outcomes of the algorithms adopted: 1) non-parametric and 2) parametric.

Non-parametric methods, also known as data-driven or model free methods, are not restrained by any of assumptions in terms of the geometry, materials and overall behaviour of the structure. They thus have very versatile applications. In contrast, parametric methods are typically more complex, require more operator input and expertise since they are bound to un-

derlying model assumptions. However, their typical use of underlying models enables damage localization if the assumptions are correct [18].

### **1.2.1 Parametric methods**

#### **Finite element updating**

A typical dynamic system can be represented by a set of modal parameters, which are expected to vary with damage. However, often the identified changes in modal parameters are difficult to interpret and a spatial distribution of the structural damage is hard to extract [34]. To circumvent this problem, SHM using finite element (FE) updating was introduced, which is based on replicating the dynamic properties of the structure by modification or identification of the mass, stiffness and/or damping matrices of a structural model [35]. System parameters are updated based on the discrepancies captured between the mathematical model and the physical structure itself. Once a reliable FE model is established, which is available to represent the monitored structure, it can be used to predict the response to future earthquakes and the remaining life time.

However, obtaining a reliable reference model is a challenging task as there is number of factors that influence the effective FE model [34, 36]. For example, systematic errors can be observed due to simplified assumptions adopted in the FE model. Uncertainty in boundary conditions, measurement errors, incomplete and/or imprecise modal data, sensor noise, and uncertainty of damage, all add further potential errors. Finally, these methods require significant human input and judgement, as a result. FE updating methods can be further distinguished into two categories [37]: direct and indirect methods.

Direct methods are based on altering the stiffness and/or mass matrices directly using simple and fast non-iterative calculations [37]. The main drawback of these methods is they may provide results with no physical meaning and often require a complete set of mode shape vectors [38], which is difficult to obtain for a real structure. Indirect FE updating methods offer more physically meaningful results at the expense of higher computational efforts as they often adopt highly sophisticated iterative computations. However, indirect FE updating methods are

more widely used for SHM implementation due to easier interpretation when inferring damage [38].

Frequency response functions (FRFs) obtained directly from the acceleration measurements were used to update the FE model in [39], which minimized the errors associated with modal parameter identification. However, this method requires incorporating a reliable damping model, which complicates the optimization process [38]. To reduce the number of variables and to obtain more physically meaningful damage patterns, [40, 41] used a set of damage functions for determination of the bending stiffness of an experimental beam structure. Modal frequencies can be used to formulate multiple objective functions, which were weighted based on modal participation factors to determine the most likely damage pattern for an experimental beam structure [42]. FE updating methods were used to identify the damage for a full-scale composite beam structure based on the identified modal parameters [43]. The modal parameters (frequency, damping, mode shapes and macro-strain mode shapes) were extracted from low intensity impulse response data after each sequence of increasingly destructive pseudo-static testing. Moaveni et al. [44] identified progressive damage for a full-scale 3-story infilled reinforced concrete (RC) frame induced by a number of different intensity ground motions. The modal parameters used for the objective function were determined using deterministic-stochastic subspace identification method based on white noise excitation response data. The identified damage factors demonstrated good consistency with the secant stiffness calculated from the hysteresis loops and indicated that the damage was concentrated in the infill walls.

### **Adaptive filtering techniques**

A large number of various real-time or near real-time adaptive filtering techniques have been proposed for damage identification of non-linear structures. For example, adaptive least mean squares (LMS) filtering provides an efficient algorithm for real time or near real time monitoring of structures subjected to dynamic loads. As opposed to the least squares optimization technique, the LMS filtering is an adaptive filtering that uses the approximation of gradient op-

timization and convergence from sample to sample. Chase et al. [45,46] used LMS methods for a benchmark problem and non-linear rocking structure to detect changes in structural stiffness. In another example, a modified LMS-based SHM was used to identify the parameters of hysteretic SDOF structure by [47]. Overall, the main drawback of this method was found to be that it requires a full response measurement, which is hard to obtain. The velocity and displacement responses obtained through the single and double integration of measured acceleration response might contain a significant drift, which is difficult to eliminate in real time without additional data. LMS methods are also susceptible to error when the assumed model does not match observed response [18].

The performance of an on-line recursive least-squares (RLS) identification technique with constant forgetting factor using input and output accelerations was assessed on a three-floor shake table benchmark model at NCREC in Taiwan by [48]. The proposed method was capable of identifying time-varying modal properties. RLS was also used for non-linear structures in [49]. However, again, it requires an underlying assumed model.

An adaptive tracking technique, based on least-square estimation (LSE) has been proposed for identification of non-linear hysteretic structures [50]. For a general linear or non-linear system identification, full response measurements are needed, which is highly impractical. An improved non-linear structural identification approach, known as a sequential non-linear least-square estimation (SNLSE) [51], was proposed, which is capable of tracking structural changes on-line using only the measurements of acceleration responses. It had significant advantages compared to the extended Kalman filter (EKF) technique in terms of the stability and convergence of the model, and computational effort.

To reduce the number of sensors required in the SHM, the SNLSE method was extended to cover the general case with unknown inputs and unknown outputs, known as SNLSE-UI-UO [52]. However, the numerical damage identification example presented relied on horizontal inter-story drifts, which is not practical in real life situations based on currently available sensor

technology. A more simple method requiring less computational effort was proposed using an adaptive quadratic sum-squares error approach (QSSE) [53].

A comparative study was carried out between different methods [54]. Three SHM techniques, referred to as the adaptive extended Kalman filter (AEKF), adaptive sequential non-linear least-square estimation (ASNLSE) and adaptive quadratic sum-squares error (AQSSE), were compared using experimental data. The authors concluded AQSSE technique was the most accurate, efficient and practical method for structural damage identification for the assessed study. An adaptive quadratic sum-square error with unknown inputs (AQSSE-UI) has been proposed and tested on experimental data [55]. The method proved capable of tracking time-varying parameters, such as stiffness and strength degradation and the identified hysteresis loops exhibited a good correlation with the experimental ones.

A Kalman filter [56], known as a state estimator, used in many scientific fields has also been employed in SHM to overcome limitations in sensor availability [57–60]. The original Kalman filtering tool is limited to linear dynamic systems, but its variations in the form of extended Kalman filter (ExKF), unscented Kalman filter (UKF), and ensemble Kalman filter (EnKF) make it applicable to the analysis of non-linear dynamic systems. A number of studies demonstrated the efficiency of these filters for damage identification of non-linear systems [61–66]. These studies found the significant advantage of UKF is the ability to identify non-Gaussian and highly non-linear systems. It is worth noting that the UKF was successfully implemented for identification of hysteresis parameters and recovery of residual displacement [67]. However, again, it requires the response to match an assumed underlying model, which may not be practical or accurate.

## **1.2.2 Non-parametric methods**

### **Empirical mode decomposition**

Empirical mode decomposition (EMD) is a time domain method, involving the extraction of a finite number of underlying basis functions, also called intrinsic mode functions, representing



the response of a system [68]. The extracted basis functions are transformed into frequency domain using Hilbert transformation (HT), which allows for estimation of instantaneous frequencies. The special feature of this method is that it can handle non-linear and non-stationary systems. The performance of EMD has been demonstrated for an experimental 3 DOF system [69]. The authors used the extracted IMFs to estimate the time-frequency distributions and the relative phase angle between the successive DOFs, which enabled inference the damage location.

EMD has been adopted as a pre-processing tool to decompose the response into several modal response functions. These function are then processed by stochastic subspace identification (SSI) to identify the modal parameters [70]. The combination of EMD and SSI allowed extraction of stable poles, eliminating the contribution from noise and other interfering modes when identifying the modal parameters for a bridge structure.

Rezaei et al. [71] used an EMD damage index, based on the energy of the first IMF extracted from free response data, to detect the presence and location of the damage for a cantilever steel pipe. A similar SHM implementation strategy has been implemented by [72], who utilized two damage sensitive parameters to detect the damage occurrence in the pipeline girth welds. EMD has also been used to determine the frequency and location of the damage for a simulated bridge structure subjected to moving load [73].

For buildings, Xu et al. [74] used EMD to detect the damage for an experimental three-story shear-type structure caused by a sudden change of structural stiffness. The damage was located by analysing the first IMF component of each floor and detecting the spatial distribution of the spikes. Lin et al. [75] applied EMD and HT to extract the modal frequencies, damping ratios and mode shapes from noise free response data for a simulated IASC-ASCE four-story benchmark problem. The estimated modal parameters allowed reconstruction of the stiffness and damping matrices, which identified the damage with a high accuracy.

The main issue with EMD, is the need for operator input and interpretation. Each mode must be evaluated for its structural relevance. Changes in modes may be due to damage or small non-linearities or sensor failure. Hence, it is not operator independent or able to be fully automated.

### **Application of Wavelets**

Wavelet transformation (WT) has attracted significant attention in many diverse research areas, such as speech recognition [76], meteorology [77], biomedicine [78] and many other fields. The method is a generalized form of Fourier transformation (FT) and windowed Fourier transformation (WFT) [79]. The main difference between the WT and FT lies in the basis functions used to represent other functions. The WT technique is superior to the FT in the analysis of non-stationary signals due to its ability to transform the signal from time series into time-frequency space, which enables tracking of dominant modes in time [80]. In addition, WT allows for decomposing the signal into a set of basis function of various resolutions [81]. The functionality of the WT technique for SHM has been demonstrated in a number of studies.

For example, [82] used the WT to detect discontinuities in decomposed signal components, which indicated the structural damage. Jiang et al. [83] used wavelet packets together with Bayesian hypothesis testing to denoise the measured response and improve accuracy when using other SHM methods. Kim et al. [84] utilized a wavelet low-pass filter to find the optimal control parameters for a tuned liquid column damper. [85] used a discretized synchrosqueezed wavelet and Hilbert transformations to identify the modal frequencies and equivalent damping ratios based on ambient vibration measurements obtained from a super-high rise building.

Sun et al. [81] proposed the wavelet packet transformation (WPT) in conjunction with neural network (NN) to determine the level of structural damage. In particular, they used trained NN model to detect the abnormalities based on wavelet component energies. The study was conducted for a simulated structure demonstrated promising results. However, as the authors emphasized, the NN model needs training and the excitation must be repeatable to enable the

comparison of damage states.

Sun et al. [86] used statistical analysis to analyse the extracted wavelet energies and infer the damage of an experimental test structure. Further, Amezquita et al. [87] proposed a methodology based synchrosqueezed wavelet transform (SWT) combined with the chaos theory, namely fractality dimension, to detect, locate and quantify the damage. The method was validated using experimental data of a scaled model.

Curadelli et al. [88] used WT to determine the instantaneous damping coefficients to infer the damage for the experimental concrete beam and experimental scaled six-story frame structure. The authors concluded that the identified damping is more sensitive to structural damage compared to the modal frequency. This difference makes it a more suitable measure for SHM implementations.

### **Artificial neural networks**

Artificial neural network (ANN), inspired by biological nervous systems, are a mathematical model, which can learn and solve problems through pattern recognition. This model can be seen as a non-linear adaptive function, which can transform a set of inputs into a set of outputs [89]. A typical neural network consists of a large number of nodes, which, depending on the type of ANN, can be arranged and interconnected in a number of different ways by forming so called layers. The nodes are interconnected using links, which represent adaptive weighting coefficients. Thus, depending on the architecture of the ANN, the outputs of one node are weighted and passed as an input to another node [35]. The weighting coefficients are determined through the process of learning and training, by minimizing the error between the predicted and measured outputs. Hence, once the optimal ANN model is set up to represent the healthy, undamaged structure, it can be used for SHM purposes to detect abnormalities occurring due to damage.

Mangal et al. [90] studied two ANN structures, namely back-propagation and adaptive res-

onance theory (ART), for application of on-line SHM for offshore platforms . The trained ANN models were tested for detecting different patterns of structural damage. The study concluded that both methods combined provided a good results for damage detection.

Masri et al. [91] used the ANN to identify structural changes for a 5 DOF experimental structure. The authors used two ANN setups with different inputs and outputs to replicate the dynamics of the analysed model. A reference ANN was established through the process of learning to approximate the healthy structure, which was then used to predict the response. The presence of damage was detected by estimating the error between the measured and predicted outputs.

Gonzalez et al. [92] used a multi-layer feed-forward ANN to detect damage in a simply supported bridge structure. The ANN model was trained for a large number of damage scenarios based on the inputs of the first mode modal strain energy difference and the outputs of element flexural stiffness. The method demonstrated very good potential in locating and quantifying damage. However, the authors used rather dramatic damage scenarios, with large reductions in member stiffness, which may not be realistic.

Finally, Osornio et al. [93] used a multiple signal classification method in conjunction with ANN. The goal was to automate the damage identification, location and quantification for a truss-type structure. The presented method was able to locate and quantify even low levels of damage caused by corrosion.

Overall, the ANN method is suitable for situations where a significant database is available. However it is difficult to specify an explicit algorithm due to structural complexity and non-linear behaviour [94]. Therefore, the effectiveness of ANN is highly reliant on the scale of training, where poorly trained models can lead to failure to generalize and inaccurate results [95]. However, ANN methods are easy to set-up as they require no a-priori knowledge, thus are highly practical for complex structures with complex behaviour.

## **System identification methods**

The majority of SHM techniques implemented to date are based on system identification (SID) methods. These methods aim to construct mathematical models using measured structural responses and inputs. They typically describe the structure in terms of the modal properties. These properties can be re-evaluated at selected time intervals to track/detect the damage and account for non-linear behaviour using one of well established techniques [96–98]. Since all SID methods presented herein suffer from the same or similar weaknesses, concluding statements are provided at the end of this section and not separately for each method.

### *ERA based methods*

The eigensystem realization algorithm (ERA) proposed by [99] is one of the most commonly used output only modal parameter identification methods based on the impulse response of a system. The algorithm utilizes a Hankel matrix decomposition and identification of control and output matrices. The modal frequencies and mode shape vectors are determined by solving the eigenvalue problem [100].

This method, combined with the natural excitation technique (NExT), became a powerful tool in analysing modal characteristics based on ambient vibrations [43,101,102]. However, the method is based on assuming the structure behaves within a linear range. It also requires a full response measurement under white noise or ambient data, which is not available immediately after infrequent and unpredictable seismic events.

Observer-Kalman Filter Identification (OKID) is an extension of ERA and was developed for the cases where the impulse response is not measured directly. The method is based on construction of state-space models for linear time-invariant systems from observation data. Fraccio et al. [103] applied ERA/OKID to identify the damage in an experimental steel frame. Two damage scenarios were considered by altering the steel member sizes. Although the method yielded an accurate identification of modal frequencies, as the authors stated, the frequency changes were not sensitive to damage, thus making it impractical to detect the damage. How-

ever, the method was able to identify the stiffness matrix representing the damaged structure, which indicated the damage precisely.

Lus et al. [104] investigated the application of OKID for identification of state space models. These identified models can subsequently be used for reconstruction of second-order (finite element) models to obtain physical parameters and detect any damage occurring in the structure by analyzing the changes in these parameters. The method was tested for a simulated ASCE benchmark problem for reconstruction of stiffness matrices, which identified the damage accurately.

Moaveni et al. [105] used OKID-ERA among other methods to identify the modal frequencies and equivalent damping ratios of a 7-story full-scale building slice based on white noise excitation data. Similarly, [106] employed ERA/DC complemented by the OKID method to determine the system parameters of a 2 story building structure. To circumvent the limitations of OKID, when identifying the system parameters based on earthquake response, the authors refined the identified state-space models using the non-linear optimization algorithms proposed by [107]. The reconstructed models allowed for the analysis of the soil-structure interaction effects and prediction of the system's response to future earthquakes.

Benedetti et al. [108] applied a two step algorithm to identify the modal parameters of real and simulated structures using only two response measurements retrieved from earthquake events. Similarly, Siringoringo et al. [109] performed a continuous SHM of an asymmetric base-isolated building, which was subjected to strong ground motion events. The authors employed two system identification methods to quantify the modal parameters of time-variant systems. The first method, based on multi-input-multi-output, assumed time-invariant system for selected time windows. The authors used relatively long time windows (50s) to identify the modal parameters, which were assumed to be constant for the analysed time segment. For the second method, the authors used the time-variant recursive least-square (RLS) method and an autoregressive with exogenous inputs model to identify time varying modal frequencies and

equivalent damping ratios.

### *Stochastic subspace identification*

Stochastic subspace identification (SSI) proposed by [110] is a widely used output-only state-space model identification technique used for linear structures excited by long duration broadband white noise excitation. SSI can be implemented based on two different approaches. In the first variation, covariance driven stochastic subspace identification (SSI-cov) assumes the covariances can be decomposed [111]. Thus, the estimated covariances are assembled into a Toeplitz matrix, which is then processed using singular value decomposition to obtain the system state matrices.

The second variation, a data-driven stochastic subspace identification (SSI-DATA), is known as a more robust, but slower method, based on constructing a block Hankel matrix consisting of past and future output data blocks. Data reduction is performed for the projected Hankel matrix using QR-factorization, which simplifies to the product of observability matrix and the Kalman states [112]. The system state matrices obtained are then used to calculate the modal parameters.

Both methods result in a comparable accuracy in terms of modal parameter identification [111]. However, SSI-DATA appeared to be more robust and allowed for predicting the response of separate modes. In situations where a large amount of sensors are needed to monitor the structure, [112] proposed to use reference based SSI, where only the selected past output are used to construct forward innovation forms. Reynders et al. [113] applied a combined deterministic-stochastic subspace identification to account for artificial excitation used for experimental test structures.

In contrast, Peeters et al. [114] identified the modal properties of a stadium structure during a game using SSI-COV and concluded that the modal frequencies are decreasing and the damping is increasing with increasing number of people present. Mevel et al. [115] identified two-floor steel structure using SSI-COV based on vibrations recorded during impact testing.

Similarly, Astroza et al. [116] used SSI-Data to identify the modal parameters of a 5-storey concrete structure using ambient vibrations. Yu et al. [70] used SSI in conjunction with EMD to identify the modal parameters of a real-scale bridge structure subjected to operational conditions. In a similar study, Wu et al. [117, 118] used a hierarchical sifting process to extract stable poles, and consequently improve the reliability of modal parameter identification. SSI has also been successfully implemented for other bridge structures [119, 120].

#### *Enhanced frequency domain decomposition*

Enhanced frequency domain decomposition (EFDD) [121–125] decomposes the response into a set of single-degree-of-freedom (SDOF) spectral density functions using singular value decomposition (SVD). The technique extracts the approximate mode shapes, modal frequencies and damping ratios. It assumes the input excitation is a broadband white noise and the spectral contribution from the adjacent modes is small.

The performance of EFDD was compared with other techniques when identifying the modal parameters for a seven-story full-scale building [105]. The authors reported EFDD provided consistently lower modal damping ratios for the modes with low spectral energy. Similar findings were reported in [126, 127], where different SID methods were employed for modal parameter identification of a five-story test structure. Yang et al. [128, 129] used EFDD to investigate the influence of soil frosts effects on the modal properties of a 20-story building and bridge structure.

#### *Autoregressive models*

Autoregressive models (AR) and their different variations of it (ARMA, ARX, ARMAX) are used to obtain a data-based mathematical representation of a healthy undamaged system, which can predict the response under different types of inputs. In the case of damage or a change in structural properties, the established autoregressive functions will not be capable of predicting the response accurately. Hence, it will result in an increase in the residual error, which can be captured using different statistical analysis tools.



Silva et al. [130] proposed to track the probability density function of the ARMA residual, defined as the difference between the predicted and the actual response. Fuzzy clustering is adopted to define the threshold values that characterize the presence of damage. Similarly, Loh et al. [131] used ARX and ARMAX models to identify modal frequencies and damping ratios for linear time-invariant systems. To identify time-varying modal parameters, the authors used recursive identification methods with adaptive forgetting factors.

In a different approach, Beskhyroun et al. [132] proposed to divide the structure into a number of substructures and use ARX and ARMAX methods to obtain a modal information for each substructure. A similar approach was adopted by [133], where the approximated parameters of ARX models were directly used to locate the damage. ARMA models were also used by [134] to model the response of the ASCE benchmark structure. To detect and localize the damage, the authors introduced a new damage-sensitive feature, based on the first three auto regressive components. Finally, Yao et al. [135] used two different statistical pattern recognition methods to infer the damage for experimental test structures based on estimated autoregressive models.

### *PolyMAX*

PolyMAX or p-LSCF, known as poly-reference least-squares complex frequency domain method, is a non-iterative output-only modal parameter identification technique, which uses frequency response functions (FRF) as the main input data [136]. The method is based on weighted least-squares approach and estimates frequency transfer functions, assuming they can be approximated using the common-denominator approach. PolyMAX has been proven to result in significantly more robust system identification (stable poles) [137, 138] compared to other well known methods, which allows for establishing an automated SHM. However, the method demonstrates systematic errors when identifying modal parameters [139].

Brownjohn et al. [120] compared the performance of PolyMAX with NExT/ERA and SSI-COV when identifying the modal parameters of a suspension bridge. The authors concluded

that SSI-COV performed the best, thus decided to use it for continuous implementation of SHM. Magalhaes et al. [140] implemented on-line automatic modal parameter identification for a bridge structure using PolyMAX. The identification results were compared with SSI-COV. The authors concluded both methods provided very comparable overall results. However, the detailed analysis revealed that PolyMAX can provide clearer variation of the modal damping ratios. Finally, Hu et al. [141] used PolyMAX for automated modal parameter identification of a wind turbine.

#### *Time domain methods*

Kim et al. [142] proposed a novel modal parameter identification technique operating in the time domain. The method can extract high resolution mode shapes and modal frequencies using output-only measurements and is based on single-degree-of-freedom analogy. The method assumes that the modes are not closely spaced and can be isolated using regular filtering techniques. The mode shapes are estimated using singular value decomposition of the output energy correlation matrix. In another study, Kim et al. [143] used FE model updating method to obtain a baseline FE model of damaged structure. The baseline model was then utilized to estimate modal parameters and subsequently to detect damage in offshore jacket structures.

#### *Overview of SID methods*

A number of system identification studies have been carried out for real or test structures, where the performance of several different SID methods was compared. For example, Astroza et al. [116, 126, 127] used three SID methods, namely SSI, NExT and DSI to characterise five-story test structure subjected to ambient and white noise excitations. Babek et al. [105] used six different SID methods to identify the modal properties of a seven-story full-scale building. The employed methods were: 1) multiple-reference natural excitation technique combined with eigensystem realization algorithm (MNExT-ERA); 2) SSI-Data; 3) EFDD; 4) deterministic-stochastic subspace identification (DSI); 5) OKID-ERA; and 6) general realization algorithm (GRA). In both studies the authors concluded that modal frequencies identified using different SID methods were consistent. In contrast, the identified equivalent damping ratios demonstrated significantly larger variability across different SID methods.

However, most of SID methods discussed herein suffer from similar limitations which were discussed by Reynders [144]. The majority of stochastic SID methods perform well when the structure is excited purely by broadband white noise excitation, which is rarely available in real life situations. In addition, SID methods often require long duration response data for which a time-invariant system behaviour is assumed. This means that for especially long duration measurements changes in environmental conditions, such as temperature and humidity might not be accounted for. Moreover, some methods require tuning and careful selection of system order, which requires a considerable operator input and expertise. Finally, SID methods assume a linear system throughout the analysed time window. Hence, the methods are not capable of taking into account the non-linear behaviour.

### **Hysteresis loop analysis**

Path dependent hysteresis loops represent the structure's restoring force at different deformation levels and are reconstructed using a dense array of accelerometers installed in the structure. Strong ground motions often causes structural damage, resulting in yielding, pinching, stiffness and strength degradation, which can typically be well captured by reconstruction of hysteresis loops. One of the first attempts to utilize hysteresis loops for real-time SHM purposes was carried out by Iwan et al. [145]. The authors used real vibration data from a 9-story library to reconstruct hysteresis loops and demonstrate the potential benefits of the proposed SHM technique. In a different approach, Xu et al. [146] used non-linear regression analysis to identify the hysteresis loops reconstructed using acceleration data and infrequently measured displacements. However, the proposed method was limited to simple bilinear hysteresis loops. Thus, more complex hysteretic models could not be identified.

Zhou et al. [147] proposed a more robust hysteresis loop analysis (HLA), capable of identifying complex hysteretic models exhibiting yielding, pinching and stiffness degradation to address this issue. The reconstructed loops are subdivided into loading and unloading sub-half cycles, which are then approximated by a series of piecewise linear segments using regression

analysis and F-type hypothesis testing. The performance of the method has been demonstrated in a number of studies [18–20].

### **1.3 Summary outcomes of prior art**

The vast majority of SID techniques are limited to linear time-invariant systems and they perform best when the long duration response data is available and the input loads meet specific characteristics. For example, ERA/OKID has been shown to be limited to ambient vibration data [61, 105–107]. The authors in the former studies concluded that OKID performs well in situations when the measured response data is long, polluted with white and zero-mean noise, and the input excitation is rich in frequency content. Most of the methods can only identify modes, excited at a high energy. Thus, the methods perform well when the input excitation is broad band white noise with a constant frequency distribution across the frequency spectrum. However, earthquake excitations are usually relatively short and have much more specific and limited frequency content, which can be localized in specific frequency ranges. In addition, structures subjected to strong ground motion events often respond in a non-linear manner, thus making successful SID even more difficult.

In contrast, adaptive filtering methods provide real-time tracking of non-linear systems. However, all these methods rely on some inherent model assumptions, which sometimes do not represent the reality accurately enough [148]. Thus, they can encounter serious limitations when identifying real-life structures and data when the assumed model does not match observed response [18].

SHM based on hysteresis loop analysis (HLA) [147] offers a simple, effective and intuitive SHM tool for damage identification of non-linear hysteretic structures. The method performs well when the structural response is single mode dominant, thus producing regular shape hysteresis loops. However, strong ground motion can trigger higher modes in taller structures which can have a significant contribution to the total response. The presence of higher modes typically

results in irregular hysteresis loops, which are hard to identify as accurately when using HLA. Alternatively, the influence of higher modes can be alleviated by applying  $n^{th}$  order Butterworth low-pass filters. However, it requires a careful selection of cut-off frequencies, which might be a challenging task in case of highly non-linear response and/or close proximity of modes.

## 1.4 Thesis objective

The primary objective of this study is to develop a method to enable nearly real-time tracking of modal parameters (mode shape, frequency and damping) over relatively short time windows. The identified time-varying modal parameters can directly be used to infer the presence of damage and/or non-linearities occurring during the response of unpredictable strong ground motion events. Moreover, the approximated mode shape coefficients can be used to decompose the response into separate modes. Mode decomposed responses allow reconstruction of single mode dominant, "smooth" hysteresis loops for the governing modes, free of the interfering modes. Subsequently, the reconstructed regular shaped hysteresis loops can be easily analysed using HLA to identify the location and severity of damage.

To address these objectives, this thesis aims to develop a novel modal parameter identification technique, which can provide continuous tracking of modes participating in the response with significant contribution. As mentioned in the literature review, the majority of SID methods developed to date can operate under free response data or long duration linear response, which is excited by white noise broadband ambient loads. Consequently, the main goal of this study is to develop a technique, which can track the relevant modes of linear and non-linear systems excited by relatively short duration strong ground motion. The study develops the methods, which account for different response data acquisition situations: a) when no input excitation force measurements are available; and b) when input excitation is known.

The proposed modal parameter identification tools are developed on simulated data of MDOF time-variant systems. To analyse its robustness, the method is tested for different levels of added noise. Finally, the proposed SHM strategy, consisting of modal parameter identification and ap-

plication of HLA, is implemented to analyse data from full-scale test structures.

## 1.5 Preface

**Chapter 2** presents a novel output-only modal parameter identification technique, which allows identification of linear time-invariant systems using long duration response data. The major feature of this method is the ability to perform identification of structures excited by both, broadband white noise and non-stationary earthquake inputs. The performance of the proposed tool is validated on a simulated 4 DOF RC structure where all the true values of modal parameters are known. It is thus a true numerical validation. A parameter study is carried out to demonstrate the robustness of the proposed technique when identifying the structure superimposed with different levels of noise.

**Chapter 3** presents an extended version of modal parameter identification technique, which enables tracking of relevant modes over relatively short time windows. The method takes advantage of measured input excitation, and is thus considered an input-output identification technique. The proposed tool can perform real-time monitoring of structures subjected to any type of relatively long input excitation. The performance of the proposed input-output modal parameter identification technique is validated on a simulated 4 DOF structure for different ground motion inputs. A parameter study is carried out to investigate the influence of different parameters on the identification accuracy.

**Chapter 4** explores the application of novel input-output modal parameter identification technique simulated structure, assembled using fiber elements.

**Chapter 5** explores the application of novel input-output modal parameter identification technique in conjunction to hysteresis loop analysis (HLA) on a full-scale experimental bridge pier structure. Real-time tracking of the mode shapes is achieved, allowing for mode decomposition and reconstruction of "smooth" single mode dominant hysteresis loops. Damage severity

is subsequently quantified using HLA.

**Chapter 6** presents the results of real-time modal parameter identification carried out for a full-scale 5-story reinforced concrete test structure. The identification algorithm was applied to experimental data from both base isolated and fixed base structural configurations. The identified modal parameters are then used to detect the presence of damage and to provide a basis for modal decomposition.

**Chapter 7** presents the results from a further SHM implemented for a 5-story test structure. The identified evolution of the modal parameters from **Chapter 6** is used to decompose the response into separate modes and reconstruct single mode dominant hysteresis loops, which are analysed using a constrained HLA. A brief introduction to constrained HLA method is also provided.

**Chapter 8** concludes the presented research and **Chapter 9** discusses future work.

## CHAPTER 2

---

### Output-only modal parameter identification

---

#### 2.1 Introduction

A number of different structural health monitoring (SHM) methods have been developed to identify damage. Many are vibration-based SHM methods developed to capture changes in modal parameters [105, 120, 126, 127, 149–151]. These changes can be represented as a damage index [35, 87, 152, 153] or used for reconstruction of second order models [104, 106, 107]. They are popular because of their use with measured, small ambient vibrations to identify linear responses and systems.

The eigensystem realization algorithm (ERA) [99] and its combination with natural excitation techniques (NExT/ERA) [43, 100, 101, 154] or the Observer/Kalman Filter Identification (OKID) [103, 155, 156] are two of the most commonly used modal parameter identification techniques for linear time-invariant systems subjected to white noise excitations. A number of studies [105, 120, 126] used a stochastic subspace identification (SSI) [156] technique to identify the modal parameters of simulated and real life structures. Successful SHM in these conditions has also been implemented using different variations of autoregressive moving average (ARMA) [130, 157–159] and enhanced frequency domain decomposition (EFDD) methods [105, 123, 126, 160].

All these techniques are limited to linear time-invariant systems. Moreover, most perform



best when the input loads meet specific characteristics, such as broad band white noise, which is not a natural or typical condition. The ability to easily use ambient vibrations without constraint would be more ideal for regular monitoring using an output-only SHM method.

This chapter presents a new modal parameter identification technique based on mode decomposition to perform as an output only identification technique for linear time-invariant systems using relatively long duration response measurements extracted from ambient load or even larger, shorter duration earthquake induced vibrations. The method presented is not limited to any characteristics of the input load and is capable of identifying modal parameters with a good accuracy even for high signal noise levels. For longer, non-linear seismic responses these parameters can be identified over short windows over the event. Finally, the approximated constant mode shapes can be used to decompose the modes, which can be used for reconstruction of single mode dominant hysteresis loops that can be readily analyzed using hysteresis loop analysis (HLA) [18, 147].

## 2.2 Method

### 2.2.1 Mode decoupling

The equation of motion of a linear multi-degree-of-freedom (MDOF) system is described:

$$\mathbf{M}\{\ddot{\mathbf{X}}\} + \mathbf{C}\{\dot{\mathbf{X}}\} + \mathbf{K}\{\mathbf{X}\} = \mathbf{M}\mathbf{r}\{\ddot{\mathbf{X}}_g\} \quad (2.1)$$

where  $\mathbf{M}$ ,  $\mathbf{C}$ ,  $\mathbf{K}$  are the mass, damping and stiffness matrices,  $\mathbf{r}$  is the excitation influence vector,  $\{\ddot{\mathbf{X}}\}$ ,  $\{\dot{\mathbf{X}}\}$  and  $\{\mathbf{X}\}$  are the acceleration, velocity and displacement vectors of MDOF system, respectively, and  $\{\ddot{\mathbf{X}}_g\}$  is the ground motion acceleration.

The linear MDOF system response can be represented as the weighted, linear sum of indi-

vidual vibration modes:

$$X(t) = \sum_{i=1}^n \phi_i \cdot \bar{x}_i(t) = \Phi \bar{X}(t) = \begin{bmatrix} \phi_{1,1} \cdot \bar{x}_1(t) + \cdots + \phi_{1,n} \cdot \bar{x}_n(t) \\ \vdots \\ \phi_{i,1} \cdot \bar{x}_1(t) + \cdots + \phi_{i,n} \cdot \bar{x}_n(t) \\ \vdots \\ \phi_{n,1} \cdot \bar{x}_1(t) + \cdots + \phi_{n,n} \cdot \bar{x}_n(t) \end{bmatrix} \quad (2.2)$$

where  $n$  is the number of modes,  $\bar{X}(t) = \begin{bmatrix} \bar{x}_1(t) & \bar{x}_2(t) & \cdots & \bar{x}_i(t) & \cdots & \bar{x}_n(t) \end{bmatrix}^T$  is modal response vector of  $n$  modes at time instant  $t$ , where each row of  $\bar{X}(t)$  represents each mode,  $\bar{x}_i(t)$ ,  $\Phi = \begin{bmatrix} \phi_1 & \phi_2 & \cdots & \phi_i & \cdots & \phi_n \end{bmatrix}$  is the  $n \times n$  mode shape matrix calculated by solving an eigenvalue problem, where  $\phi_i = \begin{bmatrix} \phi_{1,i} & \phi_{2,i} & \cdots & \phi_{i,i} & \cdots & \phi_{n,i} \end{bmatrix}^T$  is  $n \times 1$  mode shape vector of the  $i^{th}$  mode.

$\Phi$ , can be identified using one of many existing SHM methods [35, 43, 87, 99–101, 103–107, 120, 123, 126, 127, 130, 149–160]. In this study, a relatively simple tool is proposed to approximate  $\hat{\Phi}$  using the principle of mode superposition. The modal response of a linear structure can be described, per Equation (2.2), from which:

$$\bar{X} = \hat{\Phi}^{-1} \cdot X = \begin{bmatrix} \hat{\phi}_{1,1} & \cdots & \hat{\phi}_{1,n} \\ \vdots & \ddots & \vdots \\ \hat{\phi}_{n,1} & \cdots & \hat{\phi}_{n,n} \end{bmatrix}^{-1} \cdot \begin{bmatrix} \phi_{1,1} \cdot \bar{x}_1 + \cdots + \phi_{1,n} \cdot \bar{x}_n \\ \vdots \\ \phi_{n,1} \cdot \bar{x}_1 + \cdots + \phi_{n,n} \cdot \bar{x}_n \end{bmatrix} \quad (2.3)$$

where  $n$  is the number of DOFs, and  $\hat{\Phi}$  is an approximate mode shape matrix, where ideally  $\hat{\Phi} = \Phi$ . The hat symbol here is used to denote the identified/approximated parameters in this study.

In real structures, the exact number of modes contributing to the structure's response is often unknown and can be very large, as with suspension bridges [161]. For practical reasons only a limited number of DOFs are monitored, making full mode decomposition infeasible. However,

partial decomposition can be carried out using limited DOFs, which is still practical for real structures, because higher modes often have negligible response energy. In addition, most civil structure design codes neglect the influence of higher modes, as they contribute less than 10% to the total effective modal mass [162].

For a structure modeled with  $m = 2$  DOFs of  $n$  total DOFs using Equation (2.2) for  $X$ , the estimated modal response  $\bar{X}_{p,m}$ , where  $p$  in the subscript refers to partial decoupling, can be written:

$$\begin{aligned}\bar{X}_{p,2} &= \hat{\Phi}^{-1} \cdot X = \begin{bmatrix} \hat{\phi}_{1,1} & \hat{\phi}_{1,2} \\ \hat{\phi}_{2,1} & \hat{\phi}_{2,2} \end{bmatrix}^{-1} \cdot \begin{bmatrix} \phi_{1,1} \cdot \bar{x}_1 + \phi_{1,2} \cdot \bar{x}_2 + \dots + \phi_{1,n} \cdot \bar{x}_n \\ \phi_{2,1} \cdot \bar{x}_1 + \phi_{2,2} \cdot \bar{x}_2 + \dots + \phi_{2,n} \cdot \bar{x}_n \end{bmatrix} = \\ &= \frac{1}{\det(\hat{\Phi})} \begin{bmatrix} (\hat{\phi}_{2,2} \cdot \phi_{1,1} - \hat{\phi}_{1,2} \cdot \phi_{2,1}) \bar{x}_1 + (\hat{\phi}_{2,2} \cdot \phi_{1,2} - \hat{\phi}_{1,2} \cdot \phi_{2,2}) \bar{x}_2 \\ (-\hat{\phi}_{2,1} \cdot \phi_{1,1} + \hat{\phi}_{1,1} \cdot \phi_{2,1}) \bar{x}_1 + (-\hat{\phi}_{2,1} \cdot \phi_{1,2} + \hat{\phi}_{1,1} \cdot \phi_{2,2}) \bar{x}_2 \\ + \dots + (\hat{\phi}_{2,2} \cdot \phi_{1,n} - \hat{\phi}_{1,2} \cdot \phi_{2,n}) \bar{x}_n \\ + \dots + (-\hat{\phi}_{2,1} \cdot \phi_{1,n} + \hat{\phi}_{1,1} \cdot \phi_{2,n}) \bar{x}_n \end{bmatrix} \quad (2.4)\end{aligned}$$

where  $\phi_{j,i}$  and  $\hat{\phi}_{j,i}$  represent the true and identified mode shape coefficients, respectively. If  $\hat{\phi}_{j,i}$  can be identified exactly, then  $\hat{\phi}_{1,1} = \phi_{1,1}$ ,  $\hat{\phi}_{2,1} = \phi_{2,1}$ ,  $\hat{\phi}_{1,2} = \phi_{1,2}$  and  $\hat{\phi}_{2,2} = \phi_{2,2}$ . From the assumed perfect identification, the result of the decomposition is defined:

$$\begin{aligned}\bar{X}_{p,2} &= \begin{bmatrix} 1 \cdot \bar{x}_1 + 0 \cdot \bar{x}_2 + \dots + \frac{(\hat{\phi}_{2,2} \cdot \phi_{1,i} - \hat{\phi}_{1,2} \cdot \phi_{2,i})}{\det(\hat{\Phi})} \bar{x}_i + \dots + \frac{(\hat{\phi}_{2,2} \cdot \phi_{1,n} - \hat{\phi}_{1,2} \cdot \phi_{2,n})}{\det(\hat{\Phi})} \bar{x}_n \\ 0 \cdot \bar{x}_1 + 1 \cdot \bar{x}_2 + \dots + \frac{(-\hat{\phi}_{2,1} \cdot \phi_{1,i} + \hat{\phi}_{1,1} \cdot \phi_{2,i})}{\det(\hat{\Phi})} \bar{x}_i + \dots + \frac{(-\hat{\phi}_{2,1} \cdot \phi_{1,n} + \hat{\phi}_{1,1} \cdot \phi_{2,n})}{\det(\hat{\Phi})} \bar{x}_n \end{bmatrix} = \\ &= \begin{bmatrix} 1 \cdot \bar{x}_1 + 0 \cdot \bar{x}_2 + \dots + \alpha_{1,i} \cdot \bar{x}_i + \dots + \alpha_{1,n} \cdot \bar{x}_n \\ 0 \cdot \bar{x}_1 + 1 \cdot \bar{x}_2 + \dots + \alpha_{2,i} \cdot \bar{x}_i + \dots + \alpha_{2,n} \cdot \bar{x}_n \end{bmatrix} \quad (2.5)\end{aligned}$$

where  $\alpha_{1,i}$  and  $\alpha_{2,i}$  are scaling factors that result for each mode,  $i$ .

More generally, for a system with  $m$  modeled DOFs of  $n$  total DOFs, the estimated modal

response  $\bar{X}_p$  can be written:

$$\begin{aligned} \bar{X}_{p,m} &= \begin{bmatrix} 1 \cdot \bar{x}_1 + 0 \cdot \bar{x}_2 + \cdots + 0 \cdot \bar{x}_m + \alpha_{1,m+1} \bar{x}_{m+1} + \cdots + \alpha_{1,n} \bar{x}_n \\ 0 \cdot \bar{x}_1 + 1 \cdot \bar{x}_2 + \cdots + 0 \cdot \bar{x}_m + \alpha_{2,m+1} \bar{x}_{m+1} + \cdots + \alpha_{2,n} \bar{x}_n \\ \vdots \\ 0 \cdot \bar{x}_1 + 0 \cdot \bar{x}_2 + \cdots + 1 \cdot \bar{x}_m + \alpha_{m,m+1} \bar{x}_{m+1} + \cdots + \alpha_{m,n} \bar{x}_n \end{bmatrix} = \\ &= \begin{bmatrix} 1 & 0 & \cdots & 0 & \alpha_{1,m+1} & \cdots & \alpha_{1,n} \\ 0 & 1 & \cdots & 0 & \alpha_{2,m+1} & \cdots & \alpha_{2,n} \\ \vdots & \vdots & \ddots & \vdots & \vdots & \ddots & \vdots \\ 0 & 0 & \cdots & 1 & \alpha_{m,m+1} & \cdots & \alpha_{m,n} \end{bmatrix} \cdot \bar{X} = A \cdot \bar{X} \end{aligned} \quad (2.6)$$

where  $\alpha_{m,n}$  is the  $n^{th}$  mode scaling factor and  $A$  is a mode scaling matrix defining contribution of omitted modes,  $m+1 \dots n$ . Thus, the  $i^{th}$  modal response will consist of the  $i^{th}$  mode itself and scaled modes that are omitted by a perfectly approximated ( $\hat{\Phi} = \Phi$ ) mode shape matrix ( $\hat{\Phi}$ ). The contribution of other modes is thus, ideally, equal to zero.

It can also be shown for the approximated mode shape matrix,  $\hat{\Phi}$ , where modal coefficients are optimized only for the  $i^{th}$  mode (with a goal  $\hat{\Phi}(:,i) = \Phi(:,i)$ ) using Equation (2.3), the following mode decomposition and mode scaling matrix,  $A$ , is obtained:

$$\bar{X}_{p,m} = \hat{\Phi}^{-1} X = \begin{bmatrix} \alpha_{1,1} & \alpha_{1,2} & \cdots & 0 & \alpha_{1,m+1} & \cdots & \alpha_{1,n} \\ \alpha_{2,1} & \alpha_{2,2} & \cdots & 0 & \alpha_{2,m+1} & \cdots & \alpha_{2,n} \\ \vdots & \vdots & \ddots & \vdots & \vdots & \ddots & \vdots \\ \alpha_{i,1} & \alpha_{i,2} & \cdots & 1 & \alpha_{i,m+1} & \cdots & \alpha_{i,n} \\ \vdots & \vdots & \ddots & \vdots & \vdots & \ddots & \vdots \\ \alpha_{m,1} & \alpha_{m,2} & \cdots & 0 & \alpha_{m,m+1} & \cdots & \alpha_{m,n} \end{bmatrix} \cdot \begin{bmatrix} \bar{x}_1 \\ \bar{x}_2 \\ \vdots \\ \bar{x}_i \\ \vdots \\ \bar{x}_n \end{bmatrix} \quad (2.7)$$

Thus, the modal response of the  $i^{th}$  mode,  $\bar{x}_i$ , is removed from the modal responses of all other modes due to the zeros in the  $i^{th}$  column. This result means the full/partial decomposition per Equation (2.6) can be achieved by approximating each mode shape individually, thus applying mode-by-mode identification.

### 2.2.2 Mode shape approximation using output-only data

Mode contribution/coupling can be quantified by calculating its energy content in the frequency domain. Ideally, the  $i^{th}$  mode would have very small spectral energy in the other modes if  $\hat{\Phi}(:, i)$  is perfectly identified as in Equation (2.7). Assuming the absolute acceleration is monitored, thus  $\ddot{X}^{abs} = \ddot{X} - r\ddot{X}_g$ , the decomposed modal absolute acceleration,  $\bar{\ddot{X}}$ , can be represented in the frequency domain by carrying out an FFT analysis:

$$\bar{Y}(\hat{\Phi}) = |FFT(\bar{\ddot{X}}_{p,m})| = |\bar{\ddot{X}}_{p,m} \cdot W_{FFT}| = |\hat{\Phi}^{-1} \cdot \ddot{X}^{abs} \cdot W_{FFT}| \quad (2.8)$$

where  $W_{FFT}$  is the Fourier transformation matrix defined as  $W_{FFT}(n, k) = W_N^{(n-1)(k-1)}$  where  $W_N = e^{(-2\pi i)/N}$ ,  $(n = 1 \dots N)$ ,  $N$  is the discrete length of the monitored signal  $X$ , and  $k = 1 \dots K$ , where  $K$  is the number of frequency bins in the analysis.

As a result  $\bar{Y}(\hat{\Phi}) = \begin{bmatrix} \bar{y}_1 & \bar{y}_2 & \dots & \bar{y}_m \end{bmatrix}^T$  is  $m \times K$ , where each row of  $\bar{Y}(\hat{\Phi})$  represents the frequency response spectrum (FRS) of each mode. In case of perfect identification,  $\hat{\Phi} = \Phi$ , the FRS of each mode,  $\bar{y}_i$ , will represent a Single-Degree-of-Freedom (SDOF) linear time-invariant (LTI) mechanical system, which for the  $i^{th}$  mode response can be described:

$$\bar{y}_i(\omega) = \bar{F}(\omega) \cdot H_i(\omega) \quad (2.9)$$

where  $\bar{F}(\omega)$  is the Fourier transform of an input and  $H_i(\omega)$  is the frequency response function for the  $i^{th}$  mode.

For perfect identification,  $\hat{\Phi}(:, i) = \Phi(:, i)$  per Equation (2.7), the  $i^{th}$  mode response will have zero contribution from other modes. This contribution can be quantified in the frequency domain by calculating the cross correlation of the  $i^{th}$  mode's frequency response spectrum with respect to the frequency response spectrum of the other modes:

$$corr^i(\hat{\Phi}) = \bar{y}_i^n(\hat{\Phi}) \cdot \bar{Y}^n(\hat{\Phi})^T \quad (2.10)$$

where  $\bar{y}_i^n$  is the normalized FRS of the  $i^{th}$  mode and  $\bar{Y}^n(\hat{\Phi}) = \begin{bmatrix} \bar{y}_1^n & \bar{y}_2^n & \dots & \bar{y}_m^n \end{bmatrix}^T$  where  $\bar{y}_i^n$  is the normalized FRS of  $i^{th}$  mode, defined:

$$\bar{y}_i^n = \frac{\bar{y}_i}{\sqrt{\bar{y}_i^T \bar{y}_i}} \quad (2.11)$$

As a result  $corr^i(\hat{\Phi})$  is  $1 \times m$  correlation matrix, where the  $i^{th}$  column is equal to 1 since it is FRS correlation of the response with itself. Again, ideally,  $i^{th}$  mode's correlation will be equal to zero with respect to other modes ( $j \neq i$ ). However due to noise, residual effects from the other FRS, close proximity of the modal FRS peaks, and high modal damping, the correlation coefficient may result in non-zero values with other modes.

In addition, during the initial modal parameter identification, when no a priori knowledge about the mode shape matrix is known, the FRS of the  $i^{th}$  mode will contain significant contributions from other modes due to mode coupling (non-zero values in Equation (2.6)). To isolate the  $i^{th}$  mode FRS from the other modes ( $j \neq i$ ), the following step is introduced:

$$\bar{y}_i^{iso}(\hat{\Phi}) = \bar{y}_i(\hat{\Phi}) \cdot \text{diag}(N_i) \quad (2.12)$$

where  $N_i$  is a  $K \times 1$  shape vector used to segregate a given mode's FRS to calculate its energy without other modes contributing, where  $K$ , again, is the number of frequency bins used for FFT analysis as defined in Equation (2.8). The term *diag* refers to transformation of a column vector into a diagonal matrix. Shape vector,  $N$ , can be formulated using any windowing function, as shown in Figure 2.1. A more detailed description on shape function selection is provided in Section 2.2.3.

Again, correlation of the  $i^{th}$  mode's isolated FRS with respect to the full FRS can be expressed as a function of optimized mode shape  $\hat{\Phi}(:, i) = \begin{bmatrix} \hat{\phi}_{1,i} & \hat{\phi}_{2,i} & \dots & \hat{\phi}_{m,i} \end{bmatrix}^T$ :

$$corr^{iso,i}(\hat{\Phi}(:, i)) = \bar{y}_i^{n,iso}(\hat{\Phi}(:, i)) \cdot \bar{Y}^n(\hat{\Phi}(:, i))^T \quad (2.13)$$

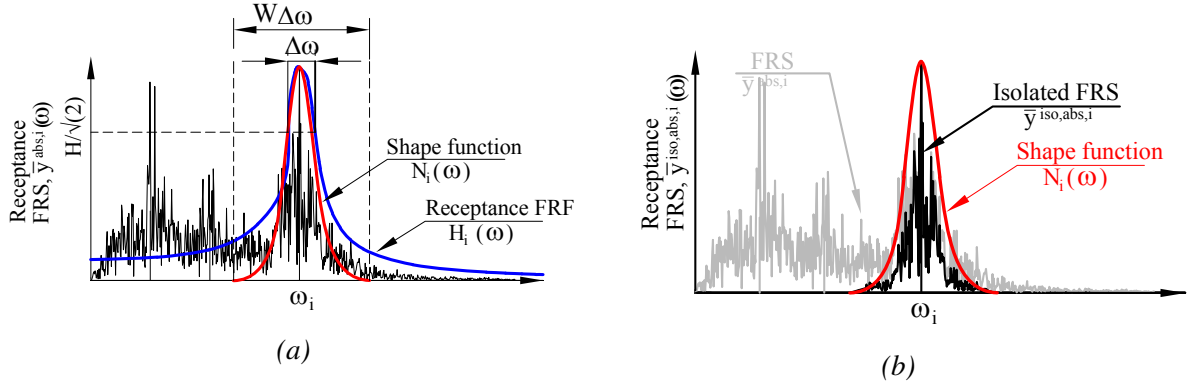


Figure 2.1: (a) FRF fitting, frequency bandwidth and shape function estimation (b) Shape function,  $N_i$ , overlapped with receptance,  $\bar{y}_i^{abs}(\omega)$  to obtain isolated FRS,  $\bar{y}_i^{iso}$

where  $corr^{iso,i}(\hat{\Phi})$  is  $1 \times m$  vector of the  $i^{th}$  mode cross correlation and  $\bar{y}_i^{n,iso}$  is the normalized segregated FRS of the  $i^{th}$  mode normalized using Equation (2.11).

The efficiency of the partial decoupling for mode  $i$  can thus be estimated by summing all the weighted correlation coefficients ( $j = 1..m, j \neq i$ ), excluding correlation of the mode with itself:

$$Corr^{iso,i}(\hat{\Phi}(:,i)) = \sum_{j=1, j \neq i}^m w_j^i \cdot corr_j^{iso,i}(\hat{\Phi}(:,i)) \quad (2.14)$$

where  $w_j^i$  is the weighting coefficient that enforces mode orthogonality or scales the correlation coefficients based on Modal Assurance Criteria (MAC) [163]. As a result, the method enables the identification of modes with very close proximity or even overlapping modes by assigning larger weight coefficients to the modes that demonstrate poorer orthogonality or higher MAC values. A more detailed description of weighting coefficient calculation is provided in Section 2.2.3.

Finally, the solution to the optimal  $i^{th}$  mode shape coefficients can be written as the solution to the following optimization problem:

$$(\hat{\Phi}(:,i)) = \arg \min_{\hat{\Phi}(:,i)} (Corr^{iso,i}(\hat{\Phi}(:,i))) \quad (2.15)$$

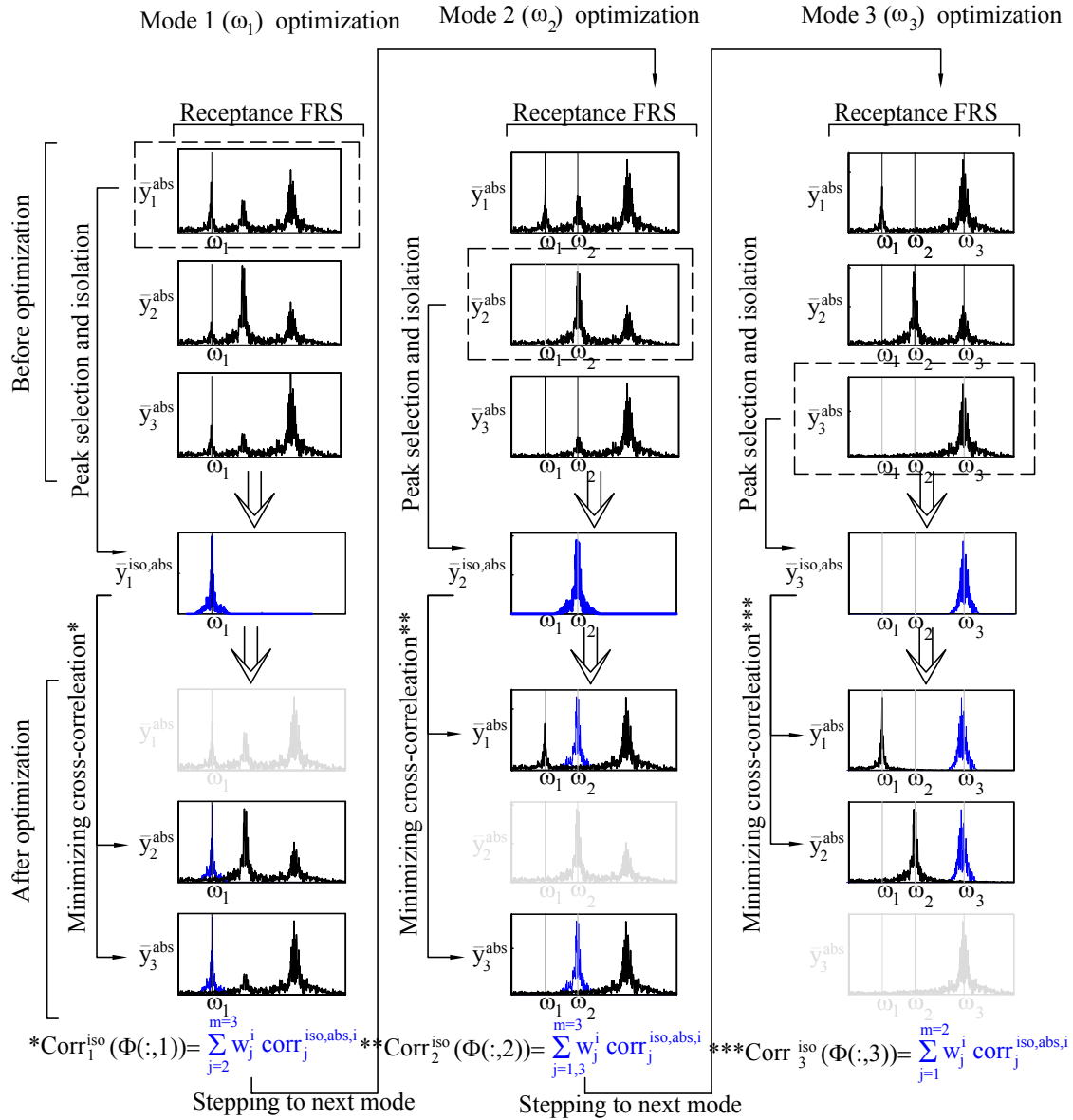


Figure 2.2: Mode-by-mode optimization example for a 3 DOF system. The term  $\text{abs}$  in the subscript of  $\text{corr}_j^{\text{iso,abs},i}$  and  $\bar{y}_i^{\text{abs}}$  refers to the calculations based on the absolute measurements.

Once the optimal approximated mode shape coefficients  $\hat{\Phi}(:,i)$  for mode  $i$  are found, the optimization can proceed for the next mode, as shown in Figure 2.2. When mode-by-mode identification is carried out, detection of new modal frequencies or poles becomes an easy task, because the modes with high spectral energy are already removed from the FRS of unidentified modes due to the zeros in Equation (2.7). The optimization problem can be readily solved using the constrained non-linear multivariable solver available in MATLAB. A more detailed mode identification routine is shown in the flow chart of Figure 2.4.



### 2.2.3 Methodology details

#### Mode proximity and mode orthogonality

When initial modal identification is carried out for structures with overlapping or very closely spaced modes, the first iteration of optimization may not yield very low cross-correlation values, indicating inaccurate mode shape identification. Higher cross-correlation values occur due the presence of another unidentified mode contributing to another mode FRS's with a high energy and thus non zero scaling factors in Equation (2.7). When identifying the second mode, which is adjacent or overlapping with the already identified mode, the optimization might result in coupled modes with poor orthogonality or a high degree of consistency. To enforce mode orthogonality, a weighting factor,  $w_j^i$ , is introduced when calculating the total correlation in Equation (2.14), defined [163]:

$$w_j^i = 1 + (MAC_{i,j})^{0.5}$$

$$MAC_{i,j} = \frac{\left| \hat{\phi}_i^T \cdot \hat{M} \cdot \hat{\phi}_j \right|^2}{\left( \hat{\phi}_i^T \cdot \hat{M} \cdot \hat{\phi}_i \right) \cdot \left( \hat{\phi}_j^T \cdot \hat{M} \cdot \hat{\phi}_j \right)} \quad (2.16)$$

where  $MAC_{i,j}$  is the modal assurance criteria coefficient expressing the degree of consistency or orthogonality between the optimized  $i^{th}$  modal vector,  $\hat{\phi}_i$ , and the  $j^{th}$  modal vector,  $\hat{\phi}_j$ . The term,  $\hat{M}$ , is the assumed/approximated mass matrix of the system, which acts as a scaling matrix. If no priori knowledge is known about the structure to estimate this mass, an identity matrix can be taken.

Equation (2.16) implies greater weights will be applied to the correlation coefficients resulting from the highly consistent modes and, more importantly, the greater total weight,  $w_j^i \cdot corr_j^{iso}$  (from Equation (2.14)), will be put on the modes with high proximity, due to their higher cross-correlation values. The added weighting coefficient will encourage the optimization process to seek an orthogonal mode shape set that results in effective mode decoupling.

Structures having symmetric stiffness around two axes, may posses repeated roots or over-

lapping modes with the same natural frequency. In such cases, multiple linear combinations of orthogonal mode shape sets can exist, which will represent the same motion exhibited by two modes with the same frequency [37]. A simple example is shown in Figure 2.3, where a cantilever bar with symmetric stiffness around both axes is represented as a 2 DOF system. Two modes shapes,  $\phi_1$  and  $\phi_2$  can be represented by an equivalent single mode shape,  $\phi_{sum}$ , as shown in Figure 2.3b. Equally, the same equivalent mode shape,  $\phi_{sum}$ , can also be represented by any set of two orthogonal vectors as shown in Figure 2.3c.

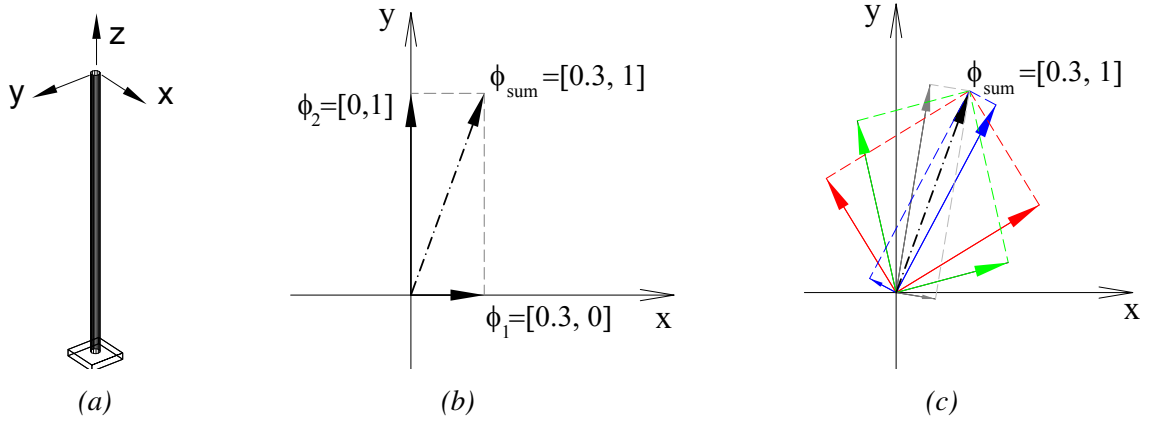


Figure 2.3: Example structure with double modes: a) Cantilever structure b) Two orthogonal modes aligned with the principal axes  $x$  and  $y$  c) Multiple sets of orthogonal vectors

Hence, a linear combination of any set of orthogonal vectors will result in the same equivalent mode shape,  $\phi_{sum}$ , or deformation pattern. However, when the mode shapes are approximated for each time window or even iteration, different mode shape sets may be obtained, which may be misleading when interpreting the modes. To ensure more stable mode shape optimization for cases with double modes, a modified weighting factor is introduced, to enforce mode shape optimization around the principal axes :

$$w_j^i = \left( 1 + \frac{\sqrt{MAC_{i,j}} + \sqrt{MAC_{i,j}^{mirr}}}{2} \right)^2 \quad (2.17)$$

$$MAC_{i,j}^{mirr} = \frac{\left| \left( \hat{\phi}_i^{mirr} \right)^T \cdot \hat{M} \cdot \hat{\phi}_j \right|^2}{\left( \left( \hat{\phi}_i^{mirr} \right)^T \cdot \hat{M} \cdot \hat{\phi}_i^{mirr} \right) \cdot \left( \hat{\phi}_j^T \cdot \hat{M} \cdot \hat{\phi}_j \right)}$$

where  $MAC_{i,j}$  is defined in Equation (2.16) and  $MAC_{i,j}^{mirr}$  is the coefficient expressing the degree

of similarity between optimized mirrored mode shape,  $\hat{\phi}_i^{mirr}$ , and the  $j^{th}$  mode shape,  $\hat{\phi}_j$ . The mirrored mode shape vector,  $\hat{\phi}_i^{mirr}$  is the mode shape vector  $\hat{\phi}_i$  mirrored around either of the principal axes,  $x$  or  $y$ :

$$\hat{\phi}_i^{mirr} = \hat{\phi}_i^{mirr,x} = \begin{bmatrix} \hat{\phi}_{i,x} \\ -\hat{\phi}_{i,y} \end{bmatrix} \quad \text{or} \quad \hat{\phi}_i^{mirr} = \hat{\phi}_i^{mirr,y} = \begin{bmatrix} -\hat{\phi}_{i,x} \\ \hat{\phi}_{i,y} \end{bmatrix} \quad (2.18)$$

where  $\hat{\phi}_{i,x}$  and  $\hat{\phi}_{i,y}$  are the  $i^{th}$  mode shape vector components in  $x$  and  $y$  direction respectively. Thus, the correlation scaling factor provided in Equation (2.17) will enforce mode shape optimization orthogonalized around the principal axes in case of overlapping or very closely spaces modes. It can be noted that the orthogonality criteria can be enforced at different degree by varying the power coefficient values in Equation (2.17). Hence, the orthogonality criteria can be relaxed by assigning greater power coefficients in Equations (2.16) and (2.17).

### Modified Gram-Schmidt orthogonalization

As the mode shape coefficients go through the optimization process of Equation (2.15), it is important to ensure mode orthogonality with respect to the other modes, to allow for the solver to converge optimal values. Mode orthogonality can be obtained using the modified Gram-Schmidt orthogonalization process, which generates a set of mode shape coefficients that is orthogonal to all the subsequent mode shapes. The  $j^{th}$  mode shape can be mass orthogonalized with respect to the  $i^{th}$  mode [164]:

$$\hat{\phi}_j^{orth} = \hat{\phi}_j - \hat{\phi}_i \cdot \frac{\hat{\phi}_j^T \cdot \hat{M} \cdot \hat{\phi}_i}{\hat{\phi}_i^T \cdot \hat{M} \cdot \hat{\phi}_i} \quad (2.19)$$

where  $\hat{M}$  is the assumed/approximated mass matrix. If no a priori knowledge about the structure is known, an identity matrix can be used.

Mode orthogonalization can be implemented as a part of the objective function or as an additional step, which would then require an additional convergence loop. Although the mode shape optimization is carried out for the  $i^{th}$  mode, meaning only the  $\hat{\Phi}(:,i)^{orth}$  terms are being varied, in fact due to the orthogonalization process of Equation (2.19), all the terms of  $\hat{\Phi}^{orth}$  are

being varied in the optimization loop, as shown in flowchart of Figure 2.4. However, after each optimization iteration, only the  $i^{th}$  mode and the rest of unidentified modes will be updated, as defined in Step 8 in Section 2.2.4. This approach ensures that the previously identified modes are not being altered.

### Damping and frequency estimation

A successful mode shape identification allows decomposing the response into separate modes. In the frequency domain this outcome results in a set of single transfer functions, each representing SDOF system without any residuals from adjacent modes, per Equation (2.6). However, in real life situations, structures often have an infinitely large number of modes with very low energy that are difficult to identify. As a result, the modal transfer functions will often contain some contribution from residuals due to unidentified or poorly identified modes [37].

Assuming the contribution from the other modes is negligible, the frequency response spectrum,  $\bar{y}_i(\omega)$ , of  $i^{th}$  mode can be approximated, per Equation (2.9):

$$\bar{y}_i(\omega) = \hat{H}_i(\omega) \cdot \bar{F}(\omega) = \frac{Q_i}{\hat{\omega}_i^2 - \omega^2 + 2i\hat{\xi}_i\omega\hat{\omega}_i} \cdot \bar{F}(\omega) \quad (2.20)$$

where  $\hat{H}_i(\omega)$  is the fitted FRF function for mode  $i$ ,  $\hat{\omega}_i$  is the identified natural frequency and  $\hat{\xi}_i$  is the identified modal damping ratio. Thus, the modal parameters ( $\hat{\omega}_i$  and  $\hat{\xi}_i$ ) can be identified using curve fitting methods [160] given the modal parameters do not vary throughout the analyzed time window and assuming the input excitation,  $\bar{F}(\omega)$ , is known or is constant in case of broadband white noise excitation,  $\bar{F}(\omega) = const$ .

### Peak segregation

Successful mode shape approximation requires careful peak isolation, which is carried out using shape functions,  $N_i$ , per Equation (2.12). A simple example of peak isolation is shown in Figure 2.1. The main idea behind the peak isolation lies in sensitivity of cross-correlation values,  $corr^{iso,i}(\hat{\Phi})$ . Very spiky isolated peaks result in noise sensitive mode cross-correlation values.

In contrast, very flat peaks may cause mode insensitive cross-correlation or, in the case of mode proximity, result in modal energy coupling, as shown in Figure 2.1 .

Peak isolation function,  $N_i$ , can be defined using any data windowing technique. In this study, a peak segregation function,  $N_i$ , is formulated using a Hanning windowing technique. Effective window length is taken as a factor of the estimated frequency bandwidth  $\Delta\omega$  determined from the fitted FRF,  $\hat{H}_i(\omega)$ , (from Equation (2.20)) at the response level of  $|\hat{H}_i|/\sqrt{2}$  as shown in Figure 2.1. Hence, the shape function can be written:

$$\begin{aligned} N_i^{mode}(\omega) &= 0 & \omega < \omega_i - \frac{W}{2} \cdot \Delta\omega \\ &= 0.5 \cdot \left(1 - \cos\left(2\pi \frac{n}{N}\right)\right) & \omega_i - \frac{W}{2} \cdot \Delta\omega \leq \omega \leq \omega_i + \frac{W}{2} \cdot \Delta\omega \\ &= 0 & \omega > \omega_i + \frac{W}{2} \cdot \Delta\omega \end{aligned} \quad (2.21)$$

where  $n = \omega - (\omega_i - \frac{W}{2} \cdot \Delta\omega)$ ,  $N = W \cdot \Delta\omega$  where  $\Delta\omega$  is the frequency bandwidth at the response level of  $|\hat{H}_i|/\sqrt{2}$ , and  $W$  is the assumed effective peak isolation width.

Thus, the mode segregation function,  $N_i^{mode}$ , is re-evaluated for each time window after FRF fitting is performed.

## 2.2.4 Mode identification summary

### Initial modal parameter identification

The initial mode shape identification, when no prior knowledge about the structure is known, can be described as a step process and is shown in the flowchart of Figure 2.4:

**Step 1. Analysis initialization:** Choose the time segment, collect  $m \times s$  data matrix,  $X = \begin{bmatrix} x_1 & x_2 & \cdots & x_m \end{bmatrix}^T$ , where  $m$  is the number of measured DOFs and  $s = (t_1 - t_0) \cdot f_s$  is the number of samples,  $t_0$  is the start and  $t_1$  the end of the time window, and  $f_s$  is the sampling frequency. Assign a random orthogonal mode shape matrix,  $\hat{\Phi}^{init}$ , where *init* refers to initial identification guess. Initialize mode number  $i = 1$ .

**Step 2. Selecting the strongest mode:** Transform the data into the modal space using Equation (2.3), and obtain the FRS of each modal response,  $\bar{Y}(\hat{\Phi}^{init}) = \begin{bmatrix} \bar{y}_1 & \bar{y}_2 & \dots & \bar{y}_m \end{bmatrix}^T$ , by transforming it into the frequency domain using Equation (2.8). Analyse all FRS for unidentified modes, (from  $i$  to  $m$  modes), and find the mode,  $\bar{y}_{e_{max}}$ , with the strongest energy, where  $e_{max}$  is the mode index number. Rearrange the approximated mode shape matrix,  $\hat{\Phi}^{init}(:, [i \ e_{max}]) = \hat{\Phi}^{init}(:, [e_{max} \ i])$  and redo the transformation for  $\bar{Y}(\hat{\Phi}^{init})$  using Equation (2.8).

**Step 3. Mode/ peak identification:** Identify the modal frequency with the strongest energy from the  $i^{th}$  modes's FRS,  $\bar{y}_i^{abs}(\omega)$ , and create shape function,  $N_i^{mode}$ , using Equation (2.21) for the  $i^{th}$  mode, which will segregate the FRS around the selected modal frequency. Calculate the isolated FRS for mode  $i$ ,  $\bar{y}_i^{iso}(\hat{\Phi}^{init})$  using Equation (2.12). Use Equations (2.13) and (2.14) to calculate the initial correlation coefficient  $R_{iter=0} = Corr^{iso,i}(\hat{\Phi}^{init}(:, i))$ .

**Step 4. Setting up an optimization problem / objective function:** Create optimization matrix,  $\hat{\Phi}^{orth} = \hat{\Phi}^k$ . Define the optimization matrix  $i^{th}$  column as a function of  $\hat{\Phi}^{orth}(:, i) = \begin{bmatrix} \hat{\phi}_{1,i}^{orth} & \hat{\phi}_{2,i}^{orth} & \dots & \hat{\phi}_{m,i}^{orth} \end{bmatrix}^T$ . Mode shape coefficients for the other modes will be subjected to Gram-Schmidt orthogonalization. Define the correlation coefficient, calculated per Equation (2.14), as a function of  $\hat{\Phi}^{orth}(:, i) = \begin{bmatrix} \hat{\phi}_{1,i}^{orth} & \hat{\phi}_{2,i}^{orth} & \dots & \hat{\phi}_{m,i}^{orth} \end{bmatrix}^T$ :

$$Corr^{iso,i}(\hat{\Phi}^{orth}(:, i)) = Corr^{iso,i}\left(\begin{bmatrix} \hat{\phi}_{1,i}^{orth} & \hat{\phi}_{2,i}^{orth} & \dots & \hat{\phi}_{m,i}^{orth} \end{bmatrix}^T\right)$$

**Step 5. Solving optimization problem:** Solve linear unconstrained optimization problem using Equation (2.15) and obtain the optimized mode shape coefficients for the  $i^{th}$  mode,  $\hat{\Phi}^{orth}(:, i)$ .

**Step 6. Performing orthogonalization:** Orthogonalize all mode shape coefficients with respect to identified mode shape coefficients,  $\hat{\Phi}^{orth}(:, i)$ , using the modified Gram-Schmidt method, of Equation (2.19). Mode orthogonalization can be implemented inside the objective function or after optimization, by creating an additional convergence loop.

**Step 7. Checking the convergence:** Calculate the total correlation coefficient,  $R_{iter} = Corr^{iso,i}(\hat{\Phi}^{init}(:, i))$

per Equation (2.14), and check the convergence:

$$Conv_{iter} = \frac{R_{iter-1} - R_{iter}}{R_{iter-1}} \quad (2.22)$$

**Step 8. Updating the mode shape matrix:** Update the approximated mode shape matrix's  $i^{th}$  mode shape and the rest of unidentified modes (uidm)  $\hat{\Phi}^{init}(:, [i \text{ uidm}]) = \hat{\Phi}^{orth}(:, [i \text{ uidm}])$ . If the convergence value is greater than  $Conv_{iter} > 1e^{-6}$ , return to **Step 4**.

**Step 9. Mode shape verification:** Verify the newly identified mode by evaluating it's FRS. In case of successful identification, the pole will be clearly visible, whereas the same peak will be removed from other mode's FRS,  $\bar{y}_i(\hat{\Phi}^{init})$ , or in other words the rest of the modes will contain no residuals from the newly identified mode, which acts as a noise. This result means if the whole identification loop process is re-iterated from **Step 3**, by setting  $i = 1$ , thus starting from mode 1, the identification will yield more accurate mode shapes.

**Step 10. Stepping back to look for new modes / poles:** Step to the next mode,  $i = i + 1$ , and return to **Step 2**.

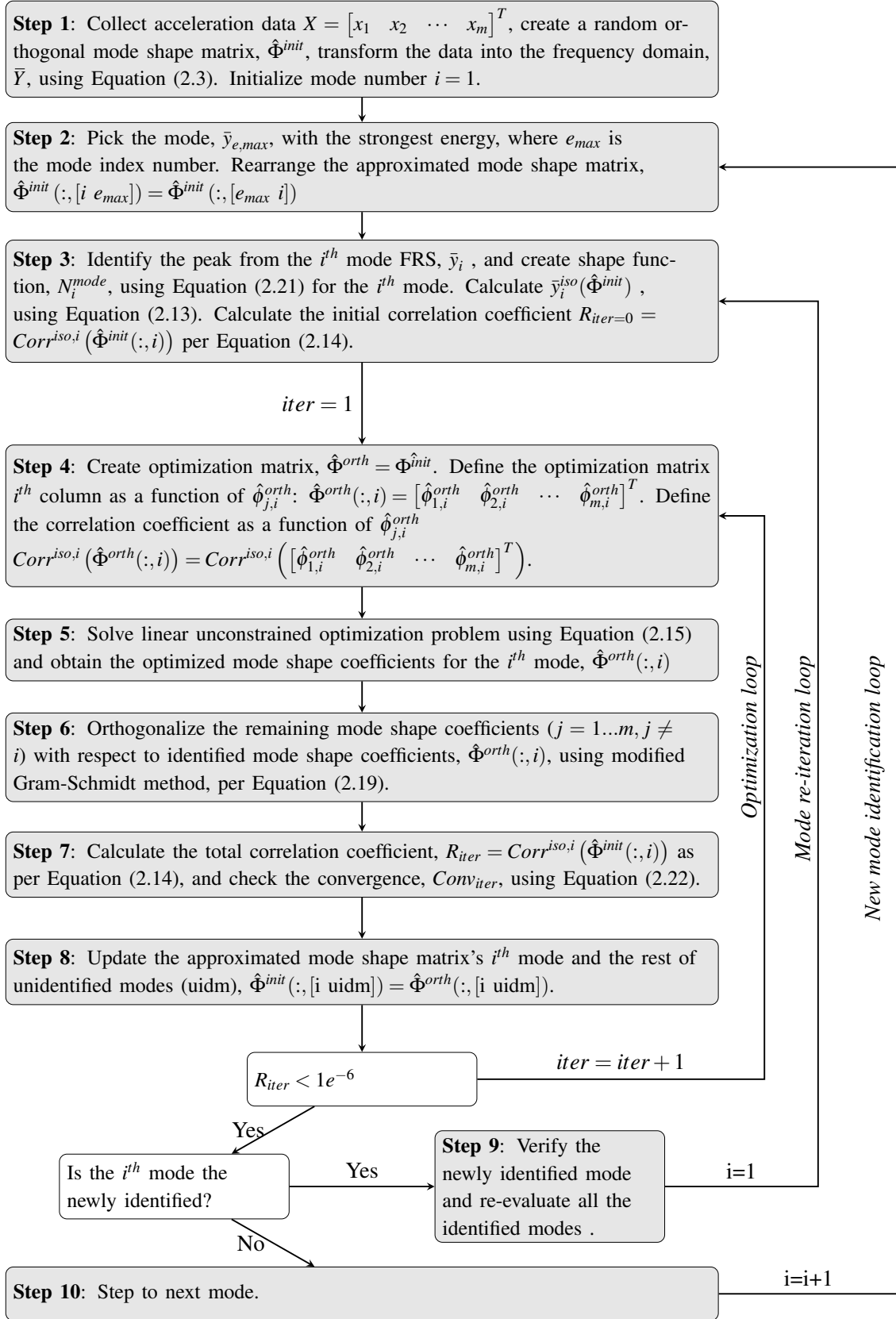


Figure 2.4: Flow chart for initial mode-by-mode optimization for any given time window



## 2.3 Method validation and analyses

### 2.3.1 Test structure

The proposed method is validated analytically using a 3D FE model representing a simplified model of a bridge pier structure, as shown in Figure 2.5. The structure consists of a  $7.3m$  long circular  $1.2m$  diameter reinforced concrete column rigidly connected to the footing. Concrete blocks are attached to the top of the cantilever column, which represents the mass of the bridge deck. The structure is simplified into a 4 degrees-of-freedom (DOF) system, with 2 DOFs in each direction, as shown in Figure 2.5. More details on the test structure are provided in [165]. The estimated effective second moment of area around both axis is  $I_x = I_y = 0.1m^4$ , the modulus of elasticity of the concrete is  $E = 22.9GPa$ . The estimated translational mass in x and y directions is  $M_x = M_y = 2.7 \cdot 10^5 kg$ , whereas the rotational masses around x and y directions are different resulting in  $M_{\phi_x} = 0.68 \cdot 10^6 kg$  and  $M_{\phi_y} = 1.16 \cdot 10^6 kg$ . The following stiffness matrix and diagonal mass matrix are obtained for a linear 4 DOF system:

$$K = \begin{bmatrix} 0.088 & 0.322 & 0 & 0 \\ 0.322 & 1.565 & 0 & 0 \\ 0 & 0 & 0.088 & -0.322 \\ 0 & 0 & -0.322 & 1.565 \end{bmatrix} \cdot 10^9 \quad M = \begin{bmatrix} 0.24 & 0 & 0 & 0 \\ 0 & 1.16 & 0 & 0 \\ 0 & 0 & 0.24 & 0 \\ 0 & 0 & 0 & 0.68 \end{bmatrix} \cdot 10^6 \quad (2.23)$$

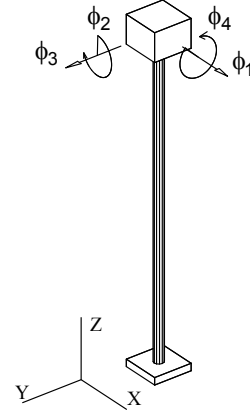
Rayleigh proportional damping  $C = \alpha_0 M + \alpha_1 K$  is assumed acting in the structure with estimated proportionality constants  $\alpha_0 = 0.24$  and  $\alpha_1 = 0.002$ , which provide  $\xi_1 = 3\%$  and  $\xi_3 = 4\%$  critical damping for the first and the third modes, respectively. Calculated modal frequencies and equivalent damping ratios for all modes are shown in Table 2.1

Table 2.1: Calculated modal parameters of a 4 DOF system

Mode	1	2	3	4
Modal frequency, f (Hz)	1.39	1.45	6.46	8.1
Modal damping, $\xi$ (%)	3.00	2.94	4.00	4.80



(a)



(b)

Figure 2.5: a) Bridge pier test structure [165] and b) a simplified 4 DOF model used for simulation

### 2.3.2 Initial modal parameter identification

The initial modal parameter identification is carried out assuming no a priori knowledge about the structure is known. The identification is implemented assuming the input ground excitation is not known (output only). Thus, the objective function is formulated using Equation (2.14). Two different input ground motions are selected to simulate the response of a linear structure: a) 2 minutes long broadband 2.5%g RMS white noise excitation with constant frequency distribution and b) earthquake excitation with peak ground acceleration (PGA) of 0.17g . Time histories of the selected ground input motions are shown in Figure 2.6. The identification is based on the recorded time series of the whole response (120s for WN and 50s for EQ event). The mass matrix is assumed to be calculated with 30% error, thus  $M_{ident} = Z \cdot M$ , where the assumed scaling matrix is  $Z = diag \left( \begin{bmatrix} 1 & 0.7 & 1.3 & 0.7 \end{bmatrix} \right)$ . The effective peak isolation width used in Equation (2.21) is  $W = 5$ .

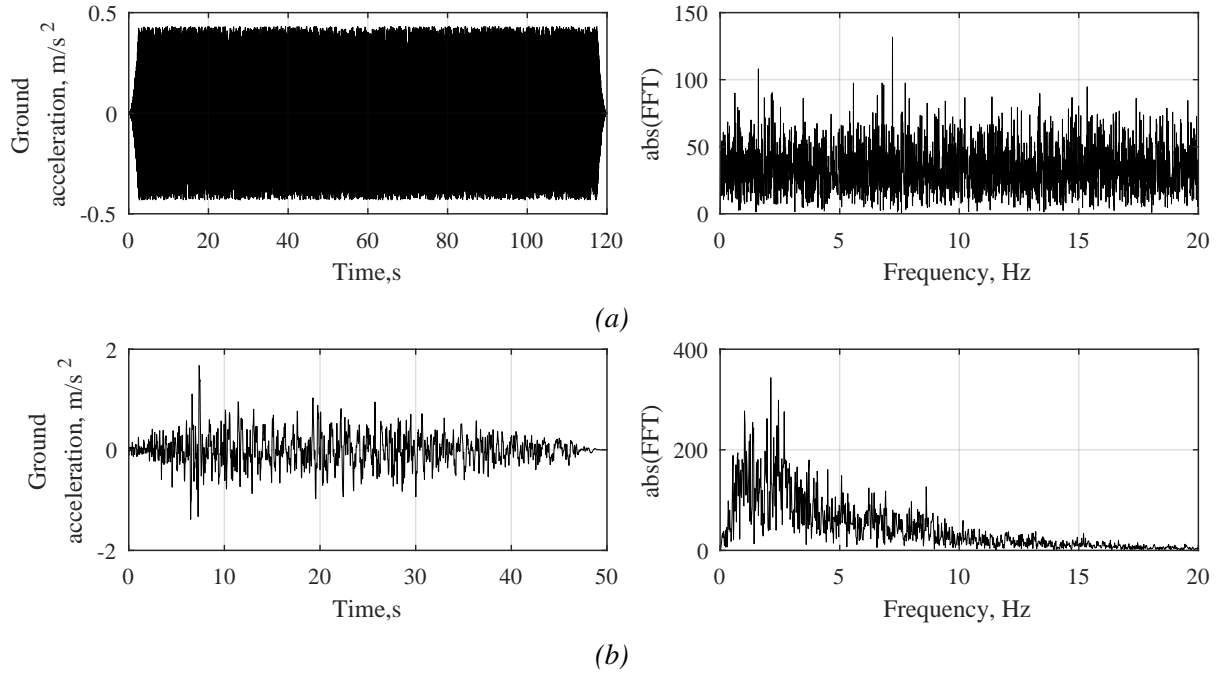


Figure 2.6: Input ground motion time histories and frequency spectra for (a) white noise 2.5%g RMS and (b) selected earthquake ground motions

## 2.4 Results and Discussion

### 2.4.1 Initial modal parameter identification

#### Identification based on white noise excitation

The initial modal parameter identification is carried out using 30 of 120 seconds white noise excitation response data. It is assumed no input ground acceleration is recorded. Thus, identification is based only on the measured acceleration response data. Identification is carried out for 3 different signal noise levels (0%, 5% and 20%) and the results are shown in Tables 2.2 to 2.4.

The identified modal frequencies presented in Table 2.2 demonstrate very good agreement for all the noise levels and the discrepancies,  $\Delta f$ , are lower than 1%. The identified equivalent modal damping ratios, presented Table 2.3 demonstrate poorer consistency compared to identified modal frequencies. The maximum captured error is  $\Delta \xi_1 = 16.3\%$ , for the largest 20% RMS noise. Large discrepancies can be associated to the relatively short 30 seconds window chosen.

Table 2.2: Identified modal frequencies for different signal noise levels

Mode	$f_{model}, Hz$	$\hat{f}_{id,0}, Hz$	$\Delta f, \%$	$\hat{f}_{id,5\%}, Hz$	$\Delta f, \%$	$\hat{f}_{id,20\%}, Hz$	$\Delta f, \%$
Mode 1	1.392	1.396	0.29	1.396	0.27	1.394	0.14
Mode 2	1.449	1.459	0.68	1.459	0.68	1.459	0.67
Mode 3	6.457	6.440	-0.27	6.439	-0.29	6.448	-0.14
Mode 4	8.103	8.074	-0.36	8.074	-0.37	8.061	-0.52

Table 2.3: Identified equivalent modal damping for different signal noise levels

Mode	$\xi_{model}$	$\hat{\xi}_{id,0}$	$\Delta \xi, \%$	$\hat{\xi}_{id,5\%}$	$\Delta \xi, \%$	$\hat{\xi}_{id,20\%}$	$\Delta \xi, \%$
Mode 1	0.030	0.035	15.7	0.034	14.3	0.035	16.33
Mode 2	0.029	0.026	-10.2	0.026	-10.2	0.026	-10.88
Mode 3	0.040	0.042	6.0	0.042	5.7	0.041	3.25
Mode 4	0.048	0.049	1.7	0.049	1.5	0.049	2.08

Table 2.4: Identified mode shape coefficients for different levels of signal noise

Mode		$\phi_{model}$	$\hat{\phi}_{id,0}$	$\Delta \phi, \%$	$\hat{\phi}_{id,5\%}$	$\Delta \phi, \%$	$\hat{\phi}_{id,20\%}$	$\Delta \phi, \%$
Mode 1	$\hat{\phi}_{1,1}$	1.00	1.00	0.00	1.00	0.00	1.00	0.00
	$\hat{\phi}_{2,1}$	-0.22	-0.22	2.62	-0.23	3.31	-0.22	2.02
	$\hat{\phi}_{3,1}$	0.00	0.00	-0.33	0.00	-0.35	0.00	-0.34
	$\hat{\phi}_{4,1}$	0.00	0.01	1.03	0.01	1.06	0.01	1.04
Mode 2	$\hat{\phi}_{1,2}$	0.00	0.01	0.60	0.01	0.61	0.01	0.58
	$\hat{\phi}_{2,2}$	0.00	0.01	0.80	0.01	0.80	0.01	0.77
	$\hat{\phi}_{3,2}$	1.00	1.00	0.00	1.00	0.00	1.00	0.00
	$\hat{\phi}_{4,2}$	0.21	0.21	-0.14	0.21	-0.09	0.21	0.00
Mode 3	$\hat{\phi}_{1,3}$	1.00	1.00	0.00	1.00	0.00	1.00	0.00
	$\hat{\phi}_{2,3}$	0.93	0.93	-0.44	0.93	-0.57	0.92	-1.08
	$\hat{\phi}_{3,3}$	0.00	0.02	2.11	0.02	1.99	0.02	2.42
	$\hat{\phi}_{4,3}$	0.00	-0.04	-4.44	-0.04	-4.45	-0.05	-4.52
Mode 4	$\hat{\phi}_{1,4}$	0.00	0.00	-0.09	0.00	-0.13	0.00	0.02
	$\hat{\phi}_{2,4}$	0.00	0.00	0.03	0.00	0.04	0.00	0.00
	$\hat{\phi}_{3,4}$	-0.61	-0.62	0.23	-0.62	0.41	-0.61	-0.65
	$\hat{\phi}_{4,4}$	1.00	1.00	0.00	1.00	0.00	1.00	0.00

Table 2.4 shows the identified mode shape coefficients,  $\hat{\phi}$ . The method yields accurate mode shape coefficient identification even for high signal noise levels. The maximum captured relative error is  $\Delta \xi = 4.52\%$ , for the 20% added RMS noise case.

## Identification based on earthquake excitation

Initial modal parameter identification based on the earthquake response is carried out using 50 seconds of recorded absolute acceleration response data. It is assumed no input ground acceleration is recorded. Thus, identification is based only on the measured response data. As for the white noise excitation data, the identification is carried out for 3 different added signal noise levels. The identified modal frequencies, shown in Table 2.5, demonstrate very good agreement for all the noise levels and the discrepancies,  $\Delta f$ , are lower than 1%.

The identified equivalent damping ratios,  $\hat{\xi}$ , shown in Table 2.6, demonstrate smaller errors compared to identification results based on WN excitation. More accurate values can be explained by longer analysed response time history used for identification. The maximum recorded error is  $\Delta \xi = 7.0\%$  corresponding to 20% added RMS noise.

Table 2.5: Identified modal frequencies for different signal noise levels based on earthquake response data

Mode	$f_{model}, Hz$	$\hat{f}_{id,0}, Hz$	$\Delta f, \%$	$\hat{f}_{id,5\%}, Hz$	$\Delta f, \%$	$\hat{f}_{id,20\%}, Hz$	$\Delta f, \%$
Mode 1	1.392	1.397	0.32	1.396	0.31	1.397	0.34
Mode 2	1.449	1.451	0.11	1.451	0.11	1.451	0.12
Mode 3	6.457	6.433	-0.37	6.434	-0.37	6.435	-0.35
Mode 4	8.103	8.032	-0.88	8.033	-0.87	8.033	-0.87

Table 2.6: Equivalent modal damping for different signal noise levels identified from response to earthquake excitation

Mode	$\xi_{model}$	$\hat{\xi}_{id,0}$	$\Delta \xi, \%$	$\hat{\xi}_{id,5\%}$	$\Delta \xi, \%$	$\hat{\xi}_{id,20\%}$	$\Delta \xi, \%$
Mode 1	0.030	0.028	-6.7	0.028	-7.0	0.028	-7.00
Mode 2	0.029	0.028	-3.4	0.028	-3.7	0.028	-3.40
Mode 3	0.040	0.039	-1.8	0.039	-1.8	0.039	-1.75
Mode 4	0.048	0.046	-4.6	0.046	-5.0	0.046	-4.79

Table 2.7 shows the identified mode shape coefficients,  $\hat{\phi}$ . The method yields accurate mode shape coefficient identification for all the noise levels. The maximum captured relative error is  $\Delta \phi = 6.85\%$ , for the 5% signal noise levels.

The results show the proposed method is capable of accurate identification of modal parameters. The initial parameter identification for a 4 DOF system is carried out using only

Table 2.7: Identified mode shape coefficients for different levels of signal noise based on the response to earthquake excitation

Mode		$\phi_{model}$	$\hat{\phi}_{id,0}$	$\Delta\phi, \%$	$\hat{\phi}_{id,5\%}$	$\Delta\phi, \%$	$\hat{\phi}_{id,20\%}$	$\Delta\phi, \%$
Mode 1	$\hat{\phi}_{1,1}$	1.00	1.00	0.00	1.00	0.00	1.00	0.00
	$\hat{\phi}_{2,1}$	-0.22	-0.21	-2.07	-0.21	-1.88	-0.21	-2.25
	$\hat{\phi}_{3,1}$	0.00	0.00	-0.04	0.00	-0.03	0.00	-0.03
	$\hat{\phi}_{4,1}$	0.00	0.00	0.13	0.00	0.11	0.00	0.09
Mode 2	$\hat{\phi}_{1,2}$	0.00	0.00	0.05	0.00	0.08	0.00	0.07
	$\hat{\phi}_{2,2}$	0.00	0.00	0.07	0.00	0.11	0.00	0.09
	$\hat{\phi}_{3,2}$	1.00	1.00	0.00	1.00	0.00	1.00	0.00
	$\hat{\phi}_{4,2}$	0.21	0.20	-4.13	0.20	-4.17	0.20	-4.13
Mode 3	$\hat{\phi}_{1,3}$	1.00	1.00	0.00	1.00	0.00	1.00	0.00
	$\hat{\phi}_{2,3}$	0.93	0.93	-0.10	0.93	0.04	0.94	0.58
	$\hat{\phi}_{3,3}$	0.00	0.05	4.50	0.05	4.53	0.04	3.89
	$\hat{\phi}_{4,3}$	0.00	-0.07	-6.79	-0.07	-6.85	-0.07	-6.83
Mode 4	$\hat{\phi}_{1,4}$	0.00	0.00	-0.15	0.00	-0.17	0.00	-0.01
	$\hat{\phi}_{2,4}$	0.00	0.00	0.05	0.00	0.06	0.00	0.00
	$\hat{\phi}_{3,4}$	-0.61	-0.62	0.39	-0.61	-0.21	-0.61	0.10
	$\hat{\phi}_{4,4}$	1.00	1.00	0.00	1.00	0.00	1.00	0.00

the measured response assuming the system is time-invariant. The identified modal frequencies and mode shape coefficients demonstrate very good consistency with the simulated model for all the noise levels. In contrast, identification of the equivalent modal damping ratios tend to yield lower accuracy. Similar findings have been obtained in a number of studies [105–107], where the identified damping ratios demonstrated larger deviations than the frequencies. The method yields equally accurate identification for both white noise and earthquake induced ground motion.

## 2.4.2 Limitations

The proposed method operates in the modal space and is based on mode decomposition, thus a linear time-invariant system (LTI) is assumed throughout the analyzed time window. However, strong ground motion will often trigger inelastic behavior, meaning the principle of mode superposition will no longer be valid. However, most of structures exhibit a non-linear behavior only for a very short time period and the non-linear part comprises a relatively small part of the whole hysteresis loop. In such cases, the method can be applied to shorter time windows, meaning the time windows containing inelastic structure's response will be approximated by an

average mode shape coefficient values that provide the best mode decoupling. Tracking their evolution over time can provide a measure of non-linear monitoring. However, the results presented here provide excellent robustness to noise and accuracy for ambient or more common smaller seismic input.

## **2.5 Summary**

This study presents a novel modal parameter estimation technique, which is capable of identification of modal parameters. The method is based on the principle of mode superposition and assumes that the system is linear time-invariant. The method performs as output-only modal parameter identification technique and is not limited to any type of input loading. This is an important feature, since most of the other system identification methods rely on assumption that the input loading is a broad band white noise. Thus, the presented approach can provide a better insight into structures subjected to strong ground motion events, assuming the structure does not exhibit strong non-linearities.

The method is validated using a simulated data for a 4 DOF time-invariant system, which represents a simplified version of a bridge pier. The results show that the method is capable of identifying modal parameters within reasonable accuracy. The identified constant modal parameters can be readily used for reconstruction of second-order models (FE models) or mode decomposition and reconstruction of single-mode dominant hysteresis loops.

Finally, the presented general mode identification procedure can be easily implemented into more complex MDOF systems as it does not need to rely on any of physical parameters.

## CHAPTER 3

---

### Input-output modal parameter identification

---

#### 3.1 Introduction

Structural health monitoring (SHM) based on modal parameter identification is a well established and commonly used technique used for monitoring of civil structures [105, 106, 120, 149, 161, 166]. Structural stiffness variations occurring due to material degradation, crack formation or change in boundary conditions is represented by the change in modal properties, which can be identified using one of several well developed methods. The eigensystem realization algorithm (ERA) [99] and its combination with natural excitation technique (NExT/ERA) [43, 100, 101, 154], the Observer/Kalman Filter Identification (OKID) [103, 155, 156], and autoregressive functions [130, 157–159] are some of the more commonly used modal parameter identification techniques for linear time-invariant systems.

Most modal parameter identification techniques are developed for stationary, broadband white noise excitations. However, earthquake excitations are relatively short, non-stationary and have a specific frequency content, and large events lead to non-linear response, limiting successful implementation of these approaches. However, only a few studies have been carried out to identify modal parameters of non-linear time-variant systems [106, 108, 109, 167–170].

This chapter presents a new modal parameter identification approach based on mode decomposition over short windows, enabling non-linear system parameters to be tracked. It tracks



modal frequencies and mode shapes within relatively short time windows by re-evaluating the relevant mode shapes. Approximated time-varying mode shapes can also be obtained and used to decompose the modes, to separate and reconstruct individual single mode hysteresis loops for SHM using hysteresis loop analysis (HLA) [18, 147].

## 3.2 Method

### 3.2.1 Mode decoupling

Section 2.2.1 demonstrated if identification of the  $j^{th}$  mode ( $\hat{\Phi}(:, j) = \Phi(:, j)$ ) is possible and the modes  $j = 1 \dots m$  contribute to the total response with significant energy, the following partial decomposition can be achieved:

$$\bar{X}_{p,m} = \begin{bmatrix} 1 & 0 & \cdots & 0 & \cdots & \alpha_{1,n} \\ 0 & 1 & \cdots & 0 & \cdots & \alpha_{2,n} \\ \cdots & \cdots & \cdots & \cdots & \cdots & \cdots \\ 0 & 0 & \cdots & 1 & \cdots & \alpha_{m,n} \end{bmatrix} \cdot \bar{X} = \begin{bmatrix} I_{m \times m} & \bar{A} \end{bmatrix} \cdot \bar{X} = A \cdot \bar{X} \quad (3.1)$$

where  $A = \begin{bmatrix} I_{m \times m} & \bar{A} \end{bmatrix}$  is a  $m \times n$  mode scaling matrix. Thus, the  $i^{th}$  modal response will consist of the  $i^{th}$  mode itself and scaled modes ( $m < j \leq n$ ) that are omitted by a perfectly approximated ( $\hat{\Phi} = \Phi$ ) mode shape matrix ( $\hat{\Phi}$ ). The contribution of these other ( $m < j \leq n$ ) modes is thus, ideally, equal to zero or their contribution of energy to the response can be assumed negligible.

A previous chapter introduced a novel method, which performed robustly in identifying the modal parameters of a linear time-invariant systems using long duration output-only measurements. In this chapter, an innovation is introduced, which allows for identification of non-linear time-variant systems by analysing the response over relatively short time windows using the knowledge of the input excitation measurements to enable accurate identification.

### 3.2.2 Input-output identification

Assuming the absolute acceleration is measured,  $\ddot{X}^{abs} = \ddot{X} - r\ddot{X}_g$ , where  $\ddot{X}$  is the relative acceleration,  $r$  is the influence vector and  $\ddot{X}_g$  is the input excitation, the decomposed modal acceleration response of Equation (3.1),  $\bar{\ddot{X}}_{p,m}$ , can be transformed into the frequency domain and expressed as a function of the approximated mode shape matrix,  $\hat{\Phi}$ :

$$\bar{Y}^{abs}(\hat{\Phi}) = |FFT(\bar{\ddot{X}}_{p,m})| = |\bar{\ddot{X}}_{p,m} \cdot W_{FFT}| = |\hat{\Phi}^{-1} \cdot \dot{X}^{abs} \cdot W_{FFT}| \quad (3.2)$$

where  $W_{FFT}$  is the Fourier transformation matrix defined  $W_{FFT}(n, k) = W_N^{(n-1)(k-1)}$  where  $W_N = e^{(-2\pi i)/N}$ , ( $n = 1 \dots N$ ),  $N$  is the discrete length of the monitored signal  $X$ , and  $k = 1 \dots K$ , where  $K$  is the number of frequency bins in the analysis, and is a function of  $N$  and sampling rate.

Similarly, the same decomposition can be applied to the relative modal response, which can then be transformed into the frequency domain:

$$\bar{Y}^{rel}(\hat{\Phi}) = |\hat{\Phi}^{-1} \cdot \dot{X} \cdot W_{FFT}| \quad (3.3)$$

As a result  $\bar{Y}^{abs}(\hat{\Phi}) = \begin{bmatrix} \bar{y}_1^{abs} & \bar{y}_2^{abs} & \dots & \bar{y}_m^{abs} \end{bmatrix}^T$  and  $\bar{Y}^{rel}(\hat{\Phi}) = \begin{bmatrix} \bar{y}_1^{rel} & \bar{y}_2^{rel} & \dots & \bar{y}_m^{rel} \end{bmatrix}^T$  are  $m \times K$  matrices, where each row of  $\bar{Y}^{abs}(\hat{\Phi})$  and  $\bar{Y}^{rel}(\hat{\Phi})$  represents the receptance and inertance frequency response spectrum (FRS) of each mode, respectively. Notation used in the superscript, *abs* and *rel*, refer to FRS extracted from the absolute and relative response data.

Hence, in the case of a perfect identification,  $\hat{\Phi} = \Phi$ , the FRS of each mode,  $\bar{y}_i$ , will represent a Single-Degree-of-Freedom (SDOF) linear time-invariant (LTI) mechanical system, which will contain no poles/residuals from the other modes. Receptance and inertance FRS of the  $i^{th}$  mode can be analytically defined [37]:

$$\begin{aligned} \bar{y}_i^{abs}(\omega) &= \bar{F}(\omega) \cdot H_i(\omega) = \bar{F}(\omega) \cdot \frac{Q_i}{\omega_i^2 - \omega^2 + 2i\xi\omega\omega_i} \\ \bar{y}_i^{rel}(\omega) &= \bar{F}(\omega) \cdot A_i(\omega) = \bar{F}(\omega) \cdot \frac{-Q_i \cdot \omega^2}{\omega_i^2 - \omega^2 + 2i\xi\omega\omega_i} \end{aligned} \quad (3.4)$$

where  $\bar{F}(\omega)$  is the Fourier transformation of an input excitation,  $H_i(\omega)$  and  $A_i(\omega)$  are the receptance and inertance frequency response functions (FRF) for the  $i^{th}$  mode, respectively,  $\omega_i$  is the natural frequency and  $\xi_i$  is the  $i^{th}$  modal damping ratio and finally  $Q_i$  is the scaling constant.

Again, according to Equation (2.7), in the case of a perfect identification of the  $i^{th}$  mode,  $\hat{\Phi}(:, i) = \Phi(:, i)$ , the FRS of all the other modes ( $j = 1 \dots m, j \neq i$ ) will contain no residuals/poles from the  $i^{th}$  mode. The residual energy can typically be quantified by analysing the receptance FRS,  $\bar{Y}^{abs}$ , which is obtained using Equation (3.2) based on output-only measurements. However, the receptance FRS has a considerable amount of residual spectral energy in the frequency range below the natural frequency ( $\omega < \omega_i$ ), which represents a pseudo-static part of the modal response. This residual spectral energy might be relatively small for lightly damped structures subjected to broadband white-noise ground excitation, which has a constant frequency distribution in the frequency domain,  $\bar{F}(\omega) = Const.$

However, input excitations, such as earthquake, or even imperfect white noise excitation, will often contain a specific frequency spectrum with variable energy distribution across the frequency spectrum. As a result, the modes will be excited at different intensity, resulting in a unique modal receptance FRS,  $\bar{y}_i^{abs}(\omega)$ . The higher modes may thus contain considerable residual energy in the frequency range  $\omega < \omega_i$ , which can make the detection of coupling modes a challenging task using only the receptance FRS,  $\bar{Y}^{abs}$ .

Better pole detection can be achieved using the inertance FRS,  $\bar{Y}^{rel}$ , where appropriate, obtained using Equation (3.3). Spectral amplification factors below the natural frequency,  $\omega < \omega_i$ , are significantly smaller in the inertance FRF,  $A_i(\omega)$ , compared to receptance FRF,  $H_i(\omega)$ , as shown in Figure 3.1. The opposite holds above the natural frequency,  $\omega > \omega_i$ , where  $A_i(\omega) > H_i(\omega)$ .

Hence, more accurate mode shape identification can be implemented when applying these two different FRS. For example, the  $i^{th}$  mode modal identification can be carried out when using

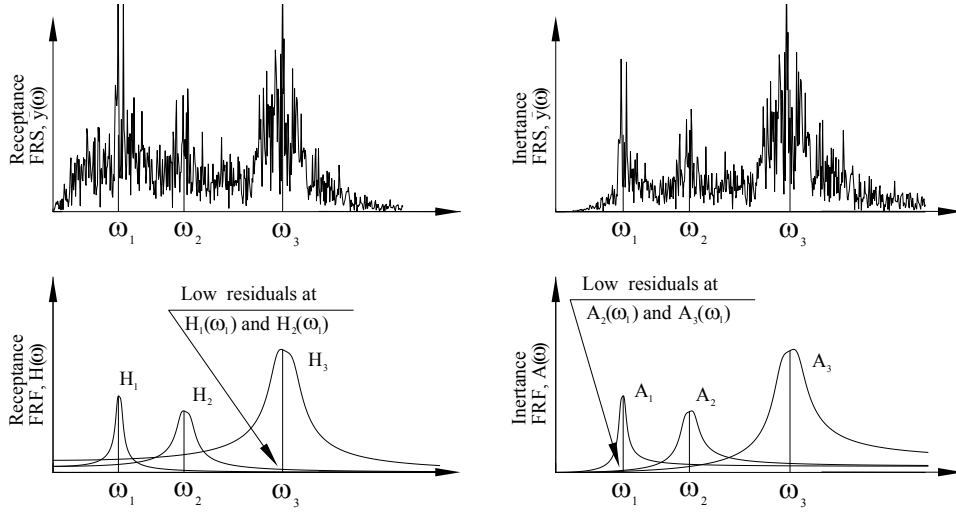


Figure 3.1: Receptance (left) and inertance (right) FRS and FRF for a 3DOF system

absolute acceleration FRS of  $j = 1 \dots i - 1$  modes and relative acceleration FRS of  $j = i + 1 \dots m$  modes. Figure 3.2 shows an example of a complete identification procedure for a 3 DOF system.

Thus, providing the  $i^{th}$  mode shape coefficients can be identified exactly,  $\hat{\Phi}(:, i) = \Phi(:, i)$ , per Equation (2.7), the FRS from the other modes will contain no pole/residuals from the  $i^{th}$  mode. Hence, the approximated mode shape coefficients for the  $i^{th}$  mode,  $\hat{\Phi}(:, i) = \begin{bmatrix} \hat{\phi}_{1,i} & \hat{\phi}_{2,i} & \dots & \hat{\phi}_{m,i} \end{bmatrix}^T$ , can be found by solving the following optimization problem:

$$(\hat{\Phi}(:, i)) = \arg \min_{\hat{\Phi}(:, i)} (Corr^{iso,i}(\hat{\Phi}(:, i))) \quad (3.5)$$

where the objective function is defined:

$$Corr^{iso,i}(\hat{\Phi}(:, i)) = \sum_{j=1}^{i-1} w_j^i \cdot corr_j^{iso,abs,i}(\hat{\Phi}) + \sum_{j=i+1}^m w_j^i \cdot corr_j^{iso,rel,i}(\hat{\Phi}) \quad (3.6)$$

where  $corr_j^{iso,abs,i}(\hat{\Phi})$  and  $corr_j^{iso,rel,i}(\hat{\Phi})$  are the cross-correlation coefficients between the  $i^{th}$  and the  $j^{th}$  mode FRS, where the terms in the subscript *abs* and *rel* refer to FRS of absolute and relative modal responses respectively, and  $w_j^i$  is the  $j^{th}$  mode scaling factor calculated using Equation (2.17) from Chapter 2. Ideally, perfect identification of  $\hat{\Phi} = \Phi$  would lead to correlations equal to zero ( $corr_j^{iso,abs,i} = corr_j^{iso,rel,i} = 0$ ), however, due to noise, mode proximity and system non-linearities the correlation coefficients will result in some small values.

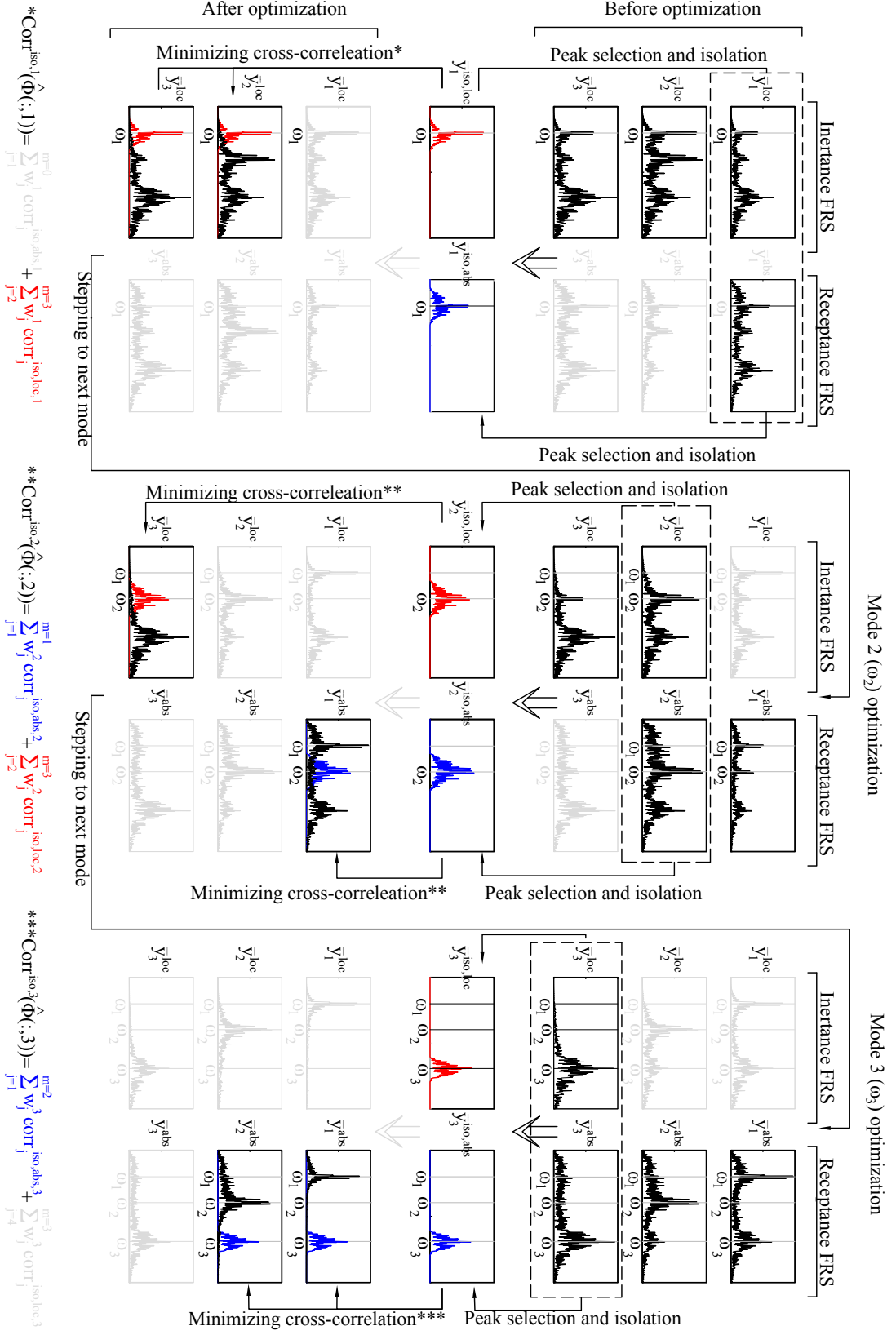


Figure 3.2: Mode-by-mode optimization example for a 3 DOF system for input excitations with non-uniform frequency content

Cross correlation vectors are calculated:

$$\begin{aligned} corr^{iso,abs,i}(\hat{\Phi}) &= \bar{y}_i^{iso,env}(\hat{\Phi}) \cdot \bar{Y}^{n,abs}(\hat{\Phi})^T \\ corr^{iso,rel,i}(\hat{\Phi}) &= \bar{y}_i^{iso,env}(\hat{\Phi}) \cdot \bar{Y}^{n,rel}(\hat{\Phi})^T \end{aligned} \quad (3.7)$$

where  $\bar{y}_i^{iso,env}$  is the lower envelope of  $i^{th}$  mode isolated inertance and receptance FRS, calculated:

$$\bar{y}_i^{iso,env}(\omega) = \min \left( \bar{y}_i^{n,iso,loc}(\omega); \quad \bar{y}_i^{n,iso,abs}(\omega) \right) \quad (3.8)$$

where  $\bar{y}_i^{n,iso,loc}$  and  $\bar{y}_i^{n,iso,abs}$  are the  $i^{th}$  mode unit normalized isolated receptance and inertance FRS calculated:

$$\begin{aligned} \bar{y}_i^{iso}(\hat{\Phi}) &= \bar{y}_i(\hat{\Phi}) \cdot \text{diag}(N_i) \\ \bar{y}_i^{n,iso}(\hat{\Phi}) &= \frac{\bar{y}_i^{iso}(\hat{\Phi})}{\max(\bar{y}_i^{iso}(\hat{\Phi}))} \end{aligned} \quad (3.9)$$

where  $N_i$  is  $K \times 1$  shape vector used to segregate a given mode's FRS to calculate its energy without other modes contributing calculated using Equation (2.21) presented in Chapter 2.

The extended objective function defined in Equation (3.6) can be adopted in situations where the input excitation,  $X_g$ , is known and can be regarded as a general equation for the objective function. If only the output measurements are available, the second term,  $corr_j^{iso,loc,i}$ , can be replaced by the first term,  $corr_j^{iso,abs,i}$ , to account for output-only measurements.

Overall, the method allows for tracking the relevant mode shapes throughout the whole excitation, thus eliminating the need of ambient vibration data, which is sometimes not available shortly after the event or is not suitably broadband white noise. In addition, identification based on ambient vibrations might not reveal the real state of the structure, as the response to ambient loads might be too low to engage the full structural response.

### 3.2.3 Initial mode identification and mode evolution

Initial modal parameter identification, when no prior knowledge about the structure is known, can be described as a step process shown in Figure 3.3. For real structures, the modal parameters can be initialized by analysing long duration ambient response data, which will provide a good approximation of the modes shapes and frequencies. The identified parameters will be a good basis/starting point for analysing the response to strong ground motion, which usually triggers a non-linear time-variant behaviour within relatively short time segment. In such cases, the modal parameters can be re-evaluated by analysing short time windows of the response. Identification of modal parameter evolution is a step process, as shown in the flowchart of Figure 3.4:

**Step 1. Data decomposition and modal parameter analysis:** Using the approximated mode shape matrix,  $\hat{\Phi}^0 = \hat{\Phi}^{init}$ , from the initial modal parameter identification, perform an approximate mode decomposition using Equation (2.3), to get  $\bar{X}_{p,m} = \begin{bmatrix} \bar{x}_{p,1} & \bar{x}_{p,2} & \cdots & \bar{x}_{p,m} \end{bmatrix}^T$ , where  $\bar{x}_{p,i}$  is the modal response of  $i^{th}$  mode. Initialize the mode number by setting  $i = 1$ .

**Step 2. Data segmentation:** Select the modal response of the  $i^{th}$  mode,  $\bar{x}_{p,i}$ , and identify the peak points and zero crossing points. Select an approximate window length based on the period of the lowest mode,  $L = c \cdot T_1$ , where  $T_1$  is the period of the lowest mode and  $c$  is the factor defining the number of cycles to be considered. Segment the response based on the identified peaks, selected window length and window overlap ratio. Modify the length of each segmented window, by finding the nearest zero crossing points, thus ensuring that a full number of cycles of the  $i^{th}$  mode are analysed. Initialize window number by setting  $k = 1$ .

**Step 3. Modal parameter updating:** Select the  $k^{th}$  time window, update the mode shape matrix  $\hat{\Phi}^k = \hat{\Phi}^{k-1}$ . Identify the modal frequency with the strongest energy from the  $i^{th}$  modes's FRS,  $\bar{y}_i^{abs}(\omega)$ , and create shape function,  $N_i$ , using Equation (2.21) for  $i^{th}$  mode, which will segregate the FRS around the selected modal frequency. Calculate the isolated FRS for mode  $i$ ,  $\bar{y}_i^{iso,env}(\hat{\Phi}^k)$ , using Equation (3.8). Use Equation (3.6) to calculate the initial correlation coeffi-

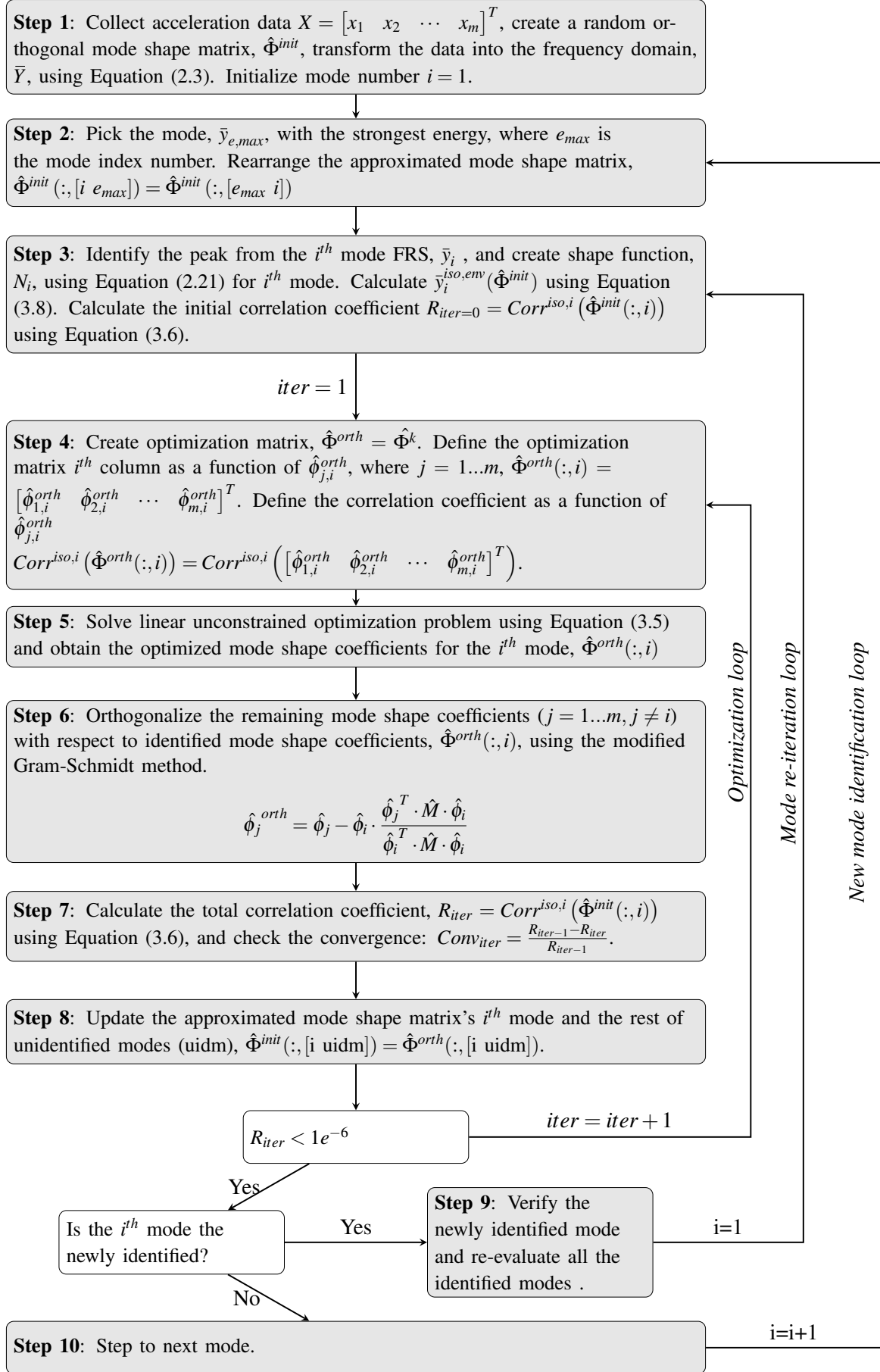


Figure 3.3: Flow chart for initial mode-by-mode optimization for any given time window



cient  $R_{iter=0} = Corr^{iso,i}(\hat{\Phi}^k(:,i))$ .

**Step 4\*. Mode shape re-evaluation:** Perform mode optimization/re-evaluation by implementing the steps **Step 4** to **Step 8** as described in Figure 3.4 for all the selected time windows.

**Step 9. Stepping to next mode:** Step to next mode,  $i = i + 1$ , and return to **Step 2**.

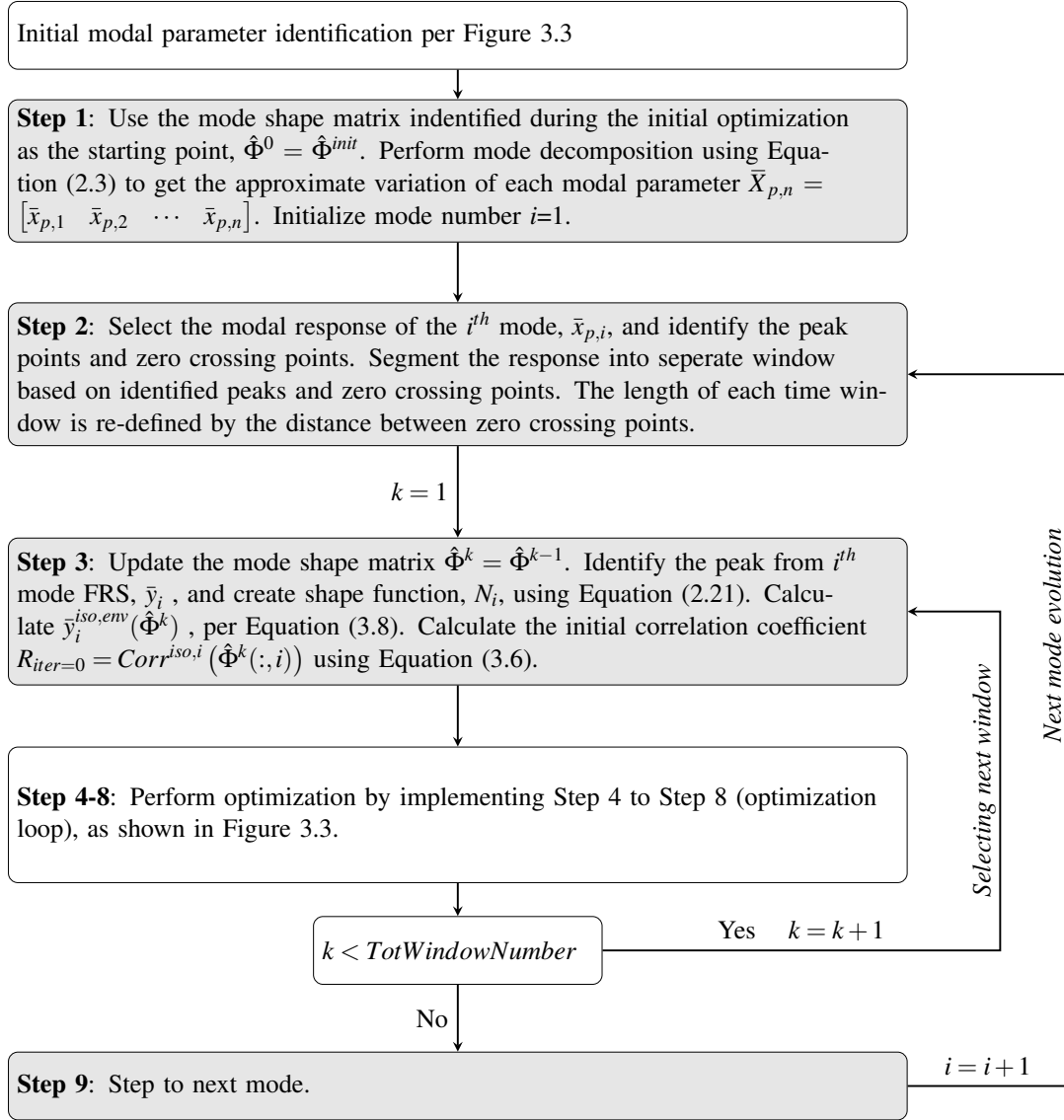


Figure 3.4: Flow chart for identification of modal parameter evolution

### 3.3 Method validation and analyses

#### 3.3.1 Test structure

The proposed method is validated analytically using a 3D FE model representing a simplified model of a bridge pier structure, as shown in Figure 2.5, which is used for method verification in Chapter 2. Thus, for brevity, structural description and model assumptions are not provided herein. Detailed description of the structure is provided in Section 2.3.1.

#### 3.3.2 Input ground motions and input parameters

Modal parameter evolution is identified for a response to an input ground motion, which consists of 120 seconds long broadband 2.5%g RMS white noise excitation with constant frequency distribution, as shown in Figure 3.5b, and a 50 seconds long earthquake excitation with peak ground acceleration (PGA) of 0.17g with frequency content, as shown in Figure 3.5c applied in  $x$  and  $y$  directions. The modal parameters are initialized by carrying out an initial modal parameter identification based on output-only identification using response measurements from the first 30 seconds (of 120) of white noise excitation.

Modal parameter identification is carried out for short time windows to track the evolution of the modal parameters. In the presence of any significant damage occurring in the structure during the ground excitation, changes in the modal parameters (frequency and mode shape coefficients) are expected to take place. To demonstrate the robustness of the method when analyzing short time windows, first, the modal parameter identification is carried out for the white noise excitation data, where a linear time-invariant system is simulated. Second, the identification is continued for the earthquake excitation induced response, where damage takes place. To simulate the damage, an abrupt decrease in stiffness around the  $y$  axis ( $I_{y,damage} = 0.3I_y$ ) is applied to the bottom 2.5m segment of the structure during the earthquake excitation, which represents the stiffness of a fully cracked section of the RC column recommended by [171]. The numerical simulation is implemented using Newmark- $\beta$  integration method with sampling

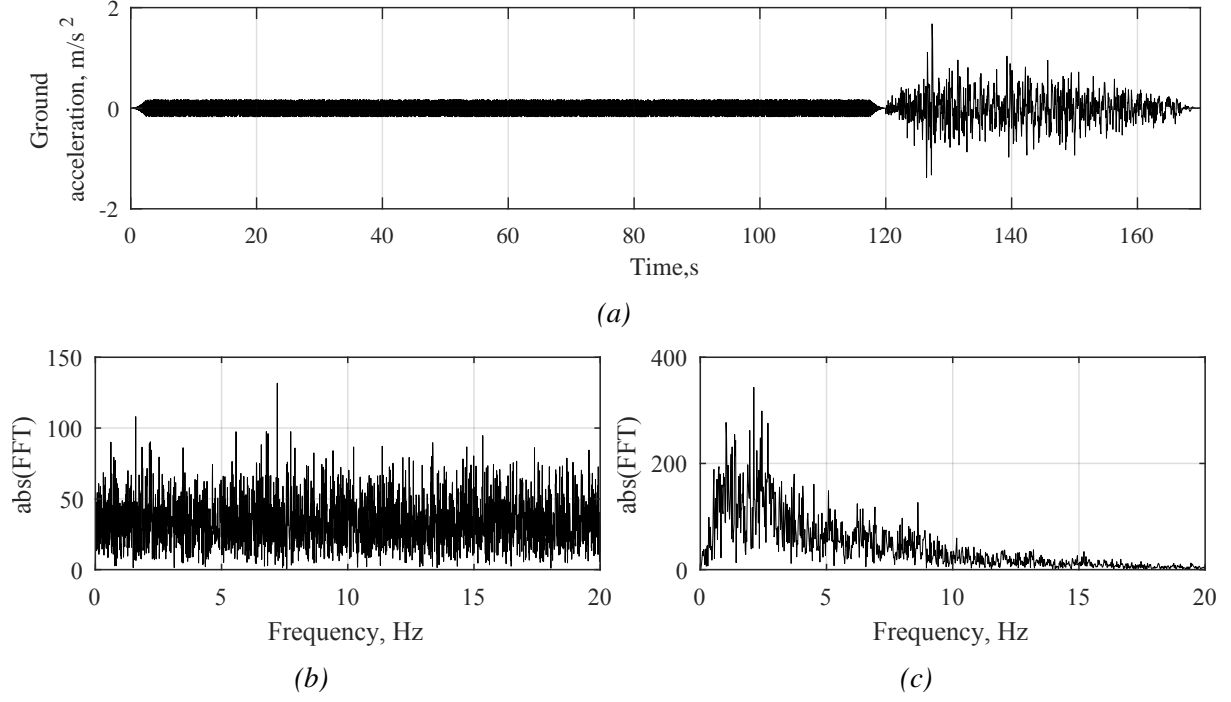


Figure 3.5: (a) Input ground motion time history in  $x$  direction and frequency spectra for (b) white noise 2.5%g RMS and (c) selected earthquake ground motions

frequency of  $f = 200\text{Hz}$ .

Modal parameter evolution is identified assuming the input ground motion is measured. For comparison, the identification is also carried out based on output-only measurements, which will demonstrate the advantages of extended objective function in Equation 3.6.

The identification is carried out using three different window lengths with 50% overlap. The selected window lengths are  $5T_1$  and  $20T_1$ , where  $T_1$  is the estimated period of the first mode, based on initial mode shape identification. To represent more realistic data acquisition situations, different levels of random RMS noise are added to the simulated response and ground motion inputs. The RMS noise is a random normal distribution of the square root of the average of the clean (no noise) simulated measurement with 99.7% of random values within the defined noise level. For brevity, the detailed identification results are presented only for the cases with added 5% and 20% RMS noise. In addition, two uncertainty levels of the assumed mass matrix,  $\hat{M}$ , are analyzed: 1) mass matrix is known exactly (0% uncertainty), and 2) the difference between assumed and exact mass matrices is 30%. It should be noted that the assumed mass

matrices affect the orthogonalization process, as described in Step 6 in the flowchart of Figure 3.3, and the calculation of the weighting factors, defined in Equation (2.17).

Finally, three different peak segregation widths ( $W = 5, 10, 20$ ), as shown in Figure 2.1 and defined in Equation (2.21), are tested to demonstrate the effect on identification accuracy. The identification accuracy is quantified by the absolute mean error (MAE). For example, MAE for the identified frequencies of the  $i^{th}$  mode is calculated:

$$MAE_{f,i} = \frac{\sum_{k=1}^K |f_i^{model}(k) - f_i^{ident}(k)|}{K} \quad (3.10)$$

where  $K$  is the total number of identified samples,  $f_i^{ident}(k)$  is the identified modal frequency of  $i^{th}$  mode at time instant  $k$  and  $f_i^{model}(k)$  is the modal frequency obtained from the simulation.

A summary of various parameters, affecting the outcome of identification, considered in this study is shown Table 3.1.

*Table 3.1: A list of parameters used for modal parameter identification*

Parameter	Units	Equation	Tested values
RMS signal noise	%	-	0/5/10/15/20/25
Window length, L	s	-	$5T_1, 10T_1, 20T_1$
Peak segregation width, W	Hz	(2.21)	$5\Delta w, 10\Delta w, 20\Delta w$
Uncertainty in mass matrix, M	%	(2.17)	0,30

## 3.4 Results

### 3.4.1 Modal parameter evolution

The simulated time history of the four monitored DOF's of the analysed structure are shown in Figure 3.6. Two excitations comprise the total input time history: 1) the time segment 0-120s corresponds to WN excitation and 2) the time segment 120-200s corresponds to earthquake excitation. The damage is introduced at  $t = 135s$ .

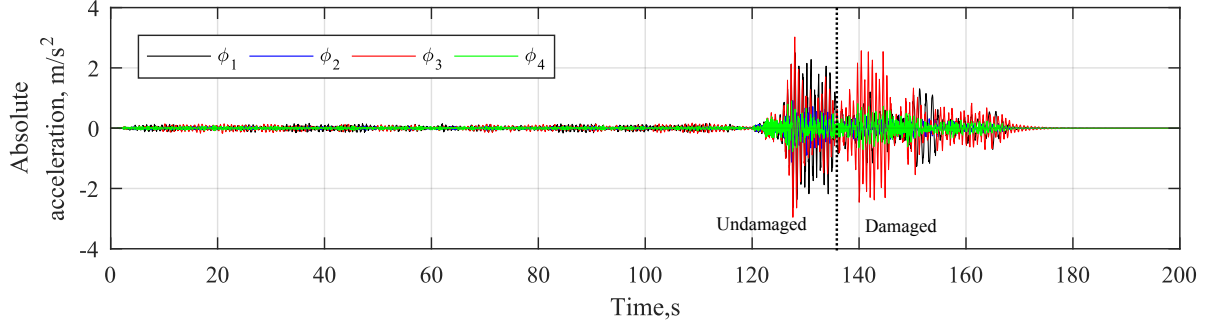


Figure 3.6: Absolute acceleration response time history of the selected DOFs ( $\phi_1$  and  $\phi_3$ ) of time-variant structure subjected to white noise (0-120s) and earthquake (120-200s) excitations, with the damage occurring at  $t = 135s$

The identified modal frequency evolution of all the modes is shown in Figure 3.7. Mode shape coefficients are unit normalized, so variation is seen only in three DOFs of four. The identification is based on measurements with 5% RMS noise level. The response data is windowed using a  $L = 5T_1$  length Hanning window. The identified modal frequencies demonstrate significant scatter, which is quantified by the mean absolute error (MAE), defined in Equation (3.10). However, the overall trend of frequency evolution is clear and the frequency shifts for Mode 1 and Mode 3 can be easily seen at the onset of the assumed damage.

Figure 3.8 shows mode shape evolution identified based on response measurements with added 5% RMS noise. The identified mode shape coefficients demonstrate relatively good consistency with the true values, especially for Modes 1 and 2. Small, arbitrary identification errors can be observed for Modes 3 and 4. However, changes in mode shape coefficients can be clearly seen at the onset of the damage. The modal parameter identification errors could be associated to the chosen relatively short windows, which typically causes poor frequency resolution when transforming the response data into the frequency domain. To reduce these errors, the identification is repeated for longer response window segments.

Figure 3.9 shows the identified frequency evolution of all the modes for response measurements with 5% RMS signal noise. The response data is windowed using a  $L = 20T_1$  length Hanning window. The identified modal frequency evolution demonstrates significantly smaller errors,  $MAE_{f,i}$ , for all the modes. Due to the longer response segment windows used, the identi-

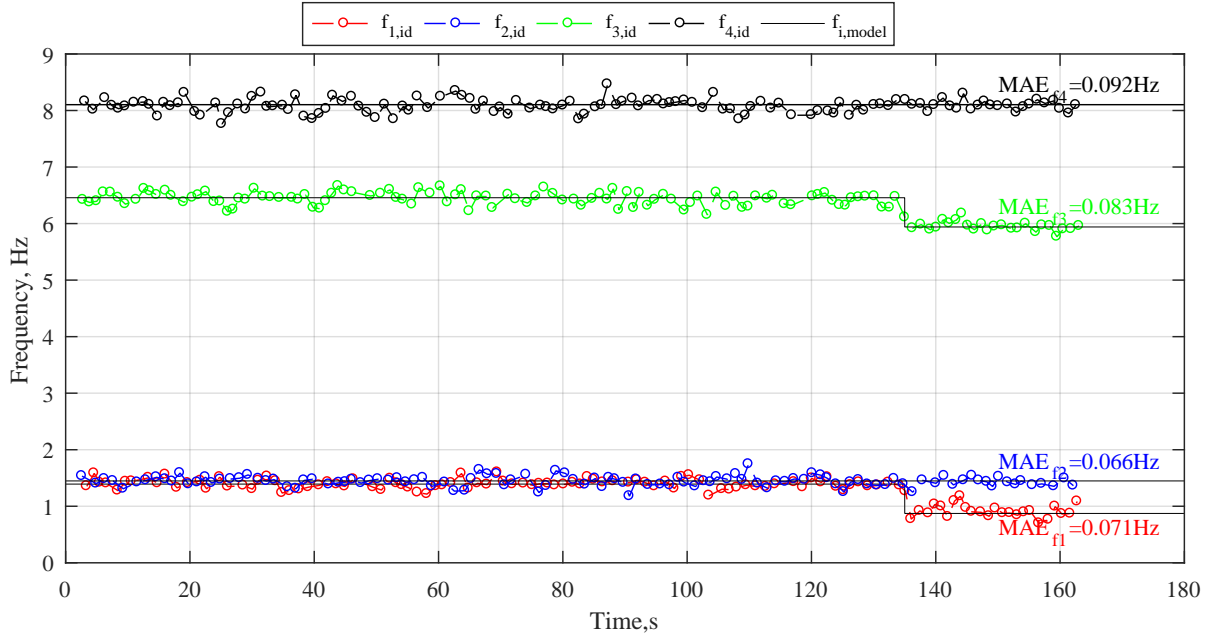


Figure 3.7: Modal frequency evolution identified based on 5% RMS signal to noise ratio using  $L = 5T_1$  window length, effective peak width  $W = 5$  and assumed mass matrix with 30% error

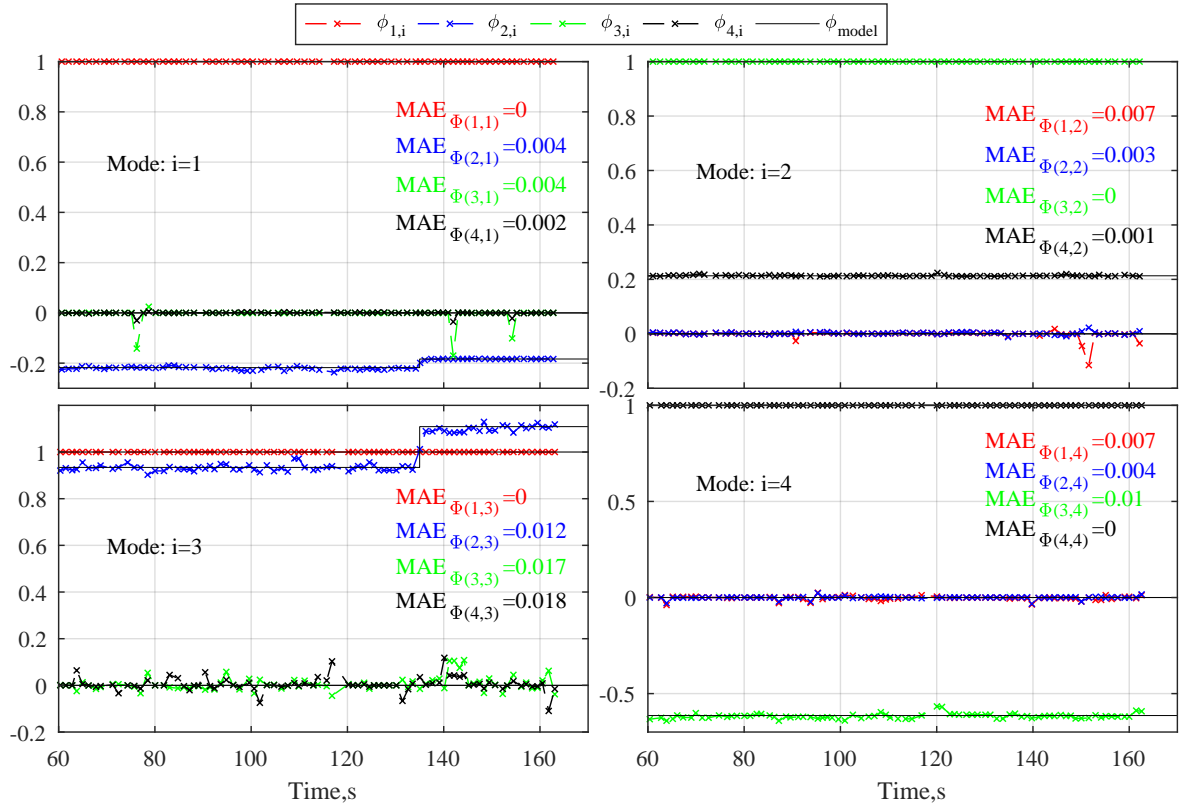


Figure 3.8: Mode shape evolution identified based on 5% RMS signal to noise ratio using  $L = 5T_1$  window length, effective peak width  $W = 5$  and assumed mass matrix with 30% error

fication takes longer to converge to the true values when damage takes place. Figure 3.10 shows the mode shape coefficients identified for the  $L = 20T_1$  long time segments. The use of longer response segments yields significantly more accurate results for Modes 3 and 4.

To demonstrate methods ability to identify modal parameters in the presence of high signal noise content, the identification is repeated for the simulated response superimposed with 20% RMS white noise. Figure 3.11 shows the identified modal frequencies and Figure 3.12 shows the identified mode shape evolution based on  $L = 20T_1$  long time segments. The identified parameters demonstrate relatively good accuracy. Larger identification errors in mode shape coefficients can be observed for Modes 3 and 4, which can most likely be associated to lower signal-to-noise (S/N) ratios. High modes inherently have lower spectral energy compared to the lower modes, leading to significantly lower S/N ratios and larger identification errors.

### 3.4.2 Output-only identification

Modal parameter identification is carried out based on response measurements only to demonstrate the advantages of introduced extended objective function defined in Equation (3.6). The identification is implemented for simulated response measurements superimposed with 5% RMS noise and segmented using  $L = 20T_1$  window length. The identified modal frequencies shown in Figure 3.13 show very good consistency. This result is expected, as the modal frequency identification is entirely based on absolute response measurements in any case. The identified mode shape coefficients shown in Figure 3.14 demonstrate larger deviations from the true values. To be more precise, the errors are larger only for the first two modes. Very poor accuracy can be seen for the identified mode shape evolution of the first mode. Meanwhile, the identification of the upper two modes yields nearly exact results as the identification based on input-output measurements. Hence, the extended objective function allows more for accurate reconstruction of the lower mode shapes for these shorter segmented responses, whereas the identification based on the objective function formulated using only the output measurements is capable of accurate reconstruction only for the higher modes, presenting potential limitation

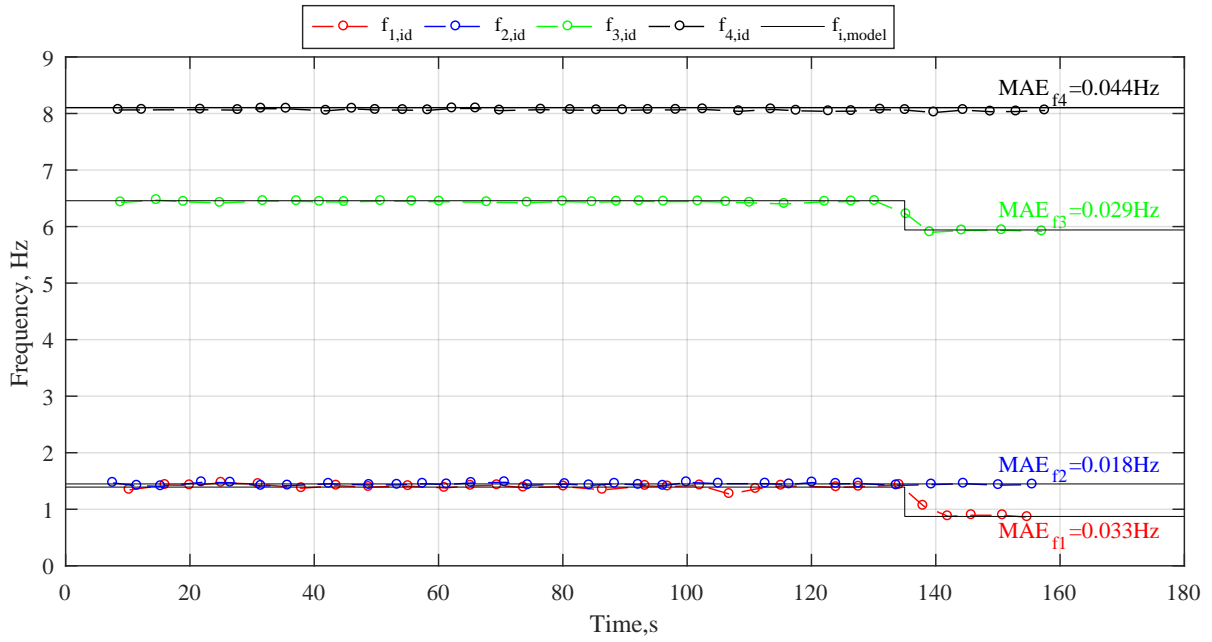


Figure 3.9: Modal frequency evolution identified based on 5% RMS signal to noise ratio using  $L = 20T_1$  window length, effective peak width  $W = 5$  and assumed mass matrix with 30% error

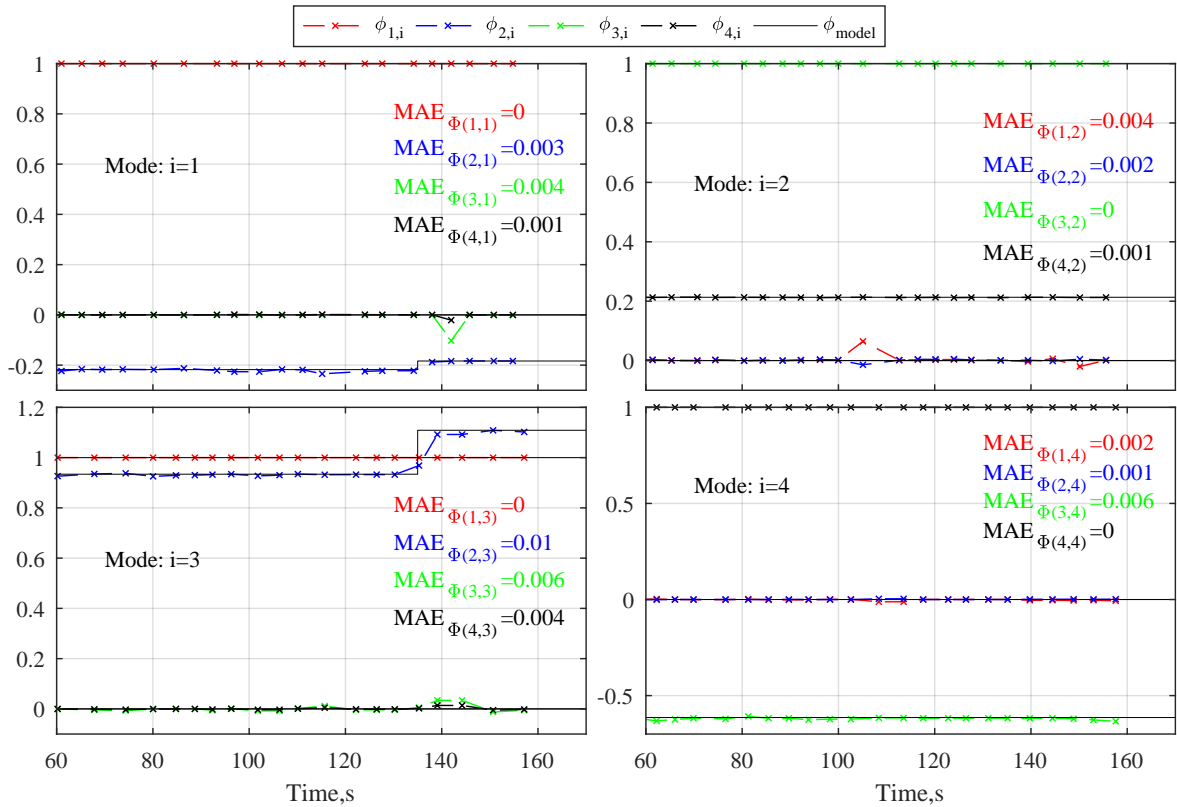


Figure 3.10: Mode shape evolution identified based on 5% RMS signal to noise ratio using  $L = 20T_1$  window length, effective peak width  $W = 5$  and assumed mass matrix with 30% error



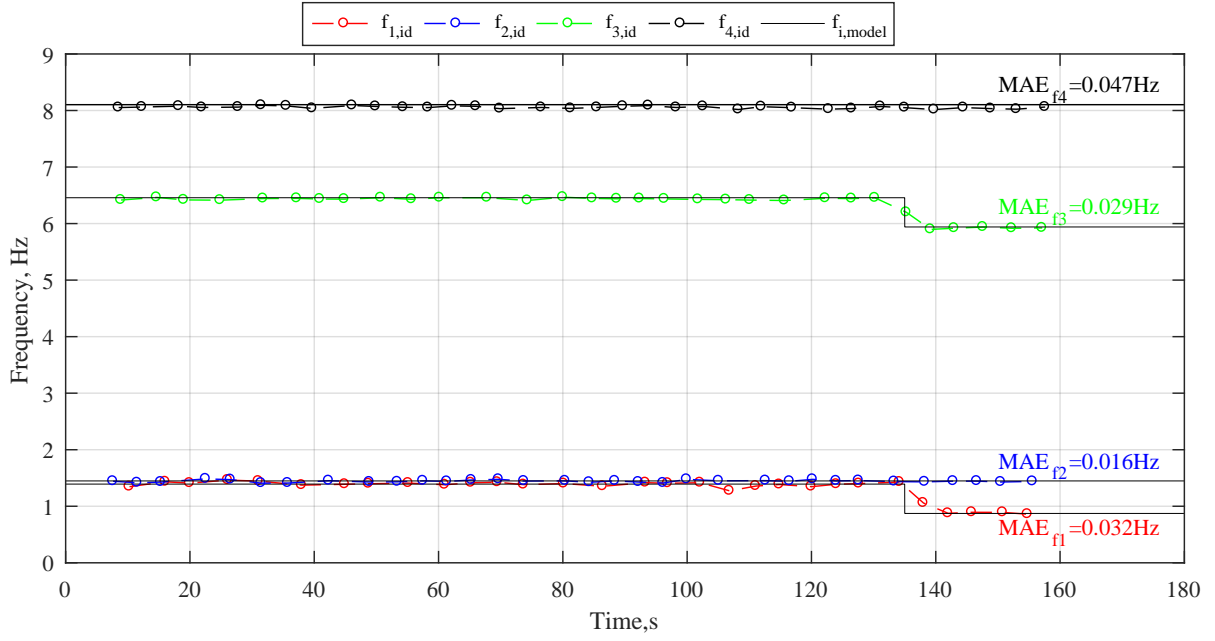


Figure 3.11: Modal frequency evolution identified based on 20% RMS signal to noise ratio using  $L = 20T_1$  window length, effective peak width  $W = 5$  and assumed mass matrix with 30% error

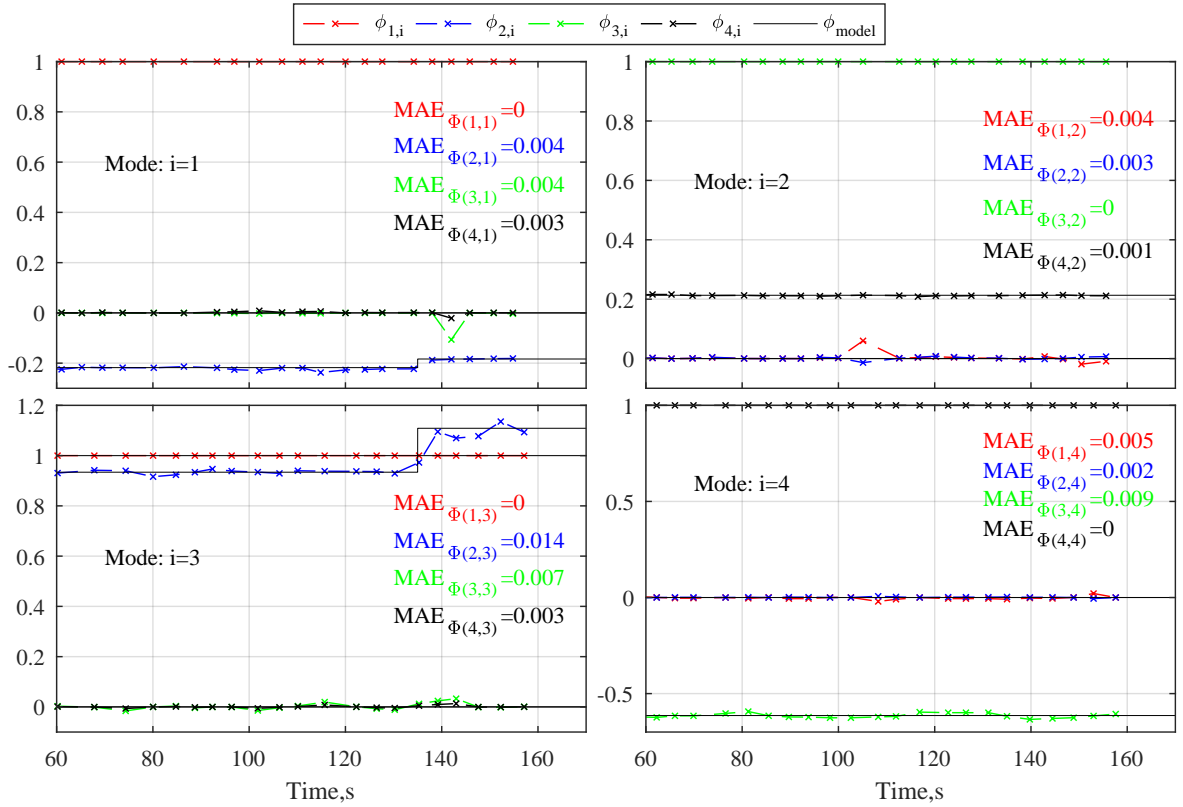


Figure 3.12: Mode shape evolution identified based on 20% RMS signal to noise ratio using  $L = 20T_1$  window length, effective peak width  $W = 5$  and assumed mass matrix with 30% error

of other ambient response, output-only methods.

### 3.4.3 Parameter sensitivity analysis

A parameter study is carried out to investigate the influence of different parameters on identification accuracy based on input-output measurements. Modal parameter evolution identification is carried out for 6 different white noise RMS levels (0%, 5%, 10%, 15%, 20% and 25%) and 3 different data segmentation lengths ( $L = 5T_1$ ,  $L = 10T_2$  and  $L = 20T_1$ ). The influence of effective peak isolation width,  $W$ , is also investigated. And finally, two different levels of mass matrix uncertainty are considered. The accuracy of identification is quantified by estimating the total mean absolute error (MAE) for the identified frequencies and mode shape coefficients:

$$\begin{aligned} MAE_f^{tot} &= \sum_{mode=1}^4 MAE_f^{mode} \\ MAE_{\Phi}^{tot} &= \sum_{mode=1}^4 \sum_{dof=1}^4 MAE_{\Phi(mode,dof)} \end{aligned} \quad (3.11)$$

where  $MAE_f^{tot}$  and  $MAE_{\Phi}^{tot}$  is the total mean absolute error of the identified frequencies and mode shape coefficients, respectively.

Figure 3.15 shows the total MAE of the identified frequencies with respect to the applied noise estimated for different sets of parameters. The identified modal frequencies show very low sensitivity to the applied noise. However, a significant reduction in the total MAE, thus increase in accuracy, is achieved by increasing the length of the time segments. In addition, the effective peak width,  $W$ , and the accuracy of the assumed mass matrix,  $\hat{M}$ , has no or very small effect on the modal frequency estimation.

Figure 3.16 shows the total MAE of the identified mode shape coefficients with respect to applied noise estimated for different sets of parameters. The identified mode shapes demonstrate larger errors with increasing levels of noise. However, the errors can significantly be reduced by analyzing the structural response in larger time segments. The selection of effective peak

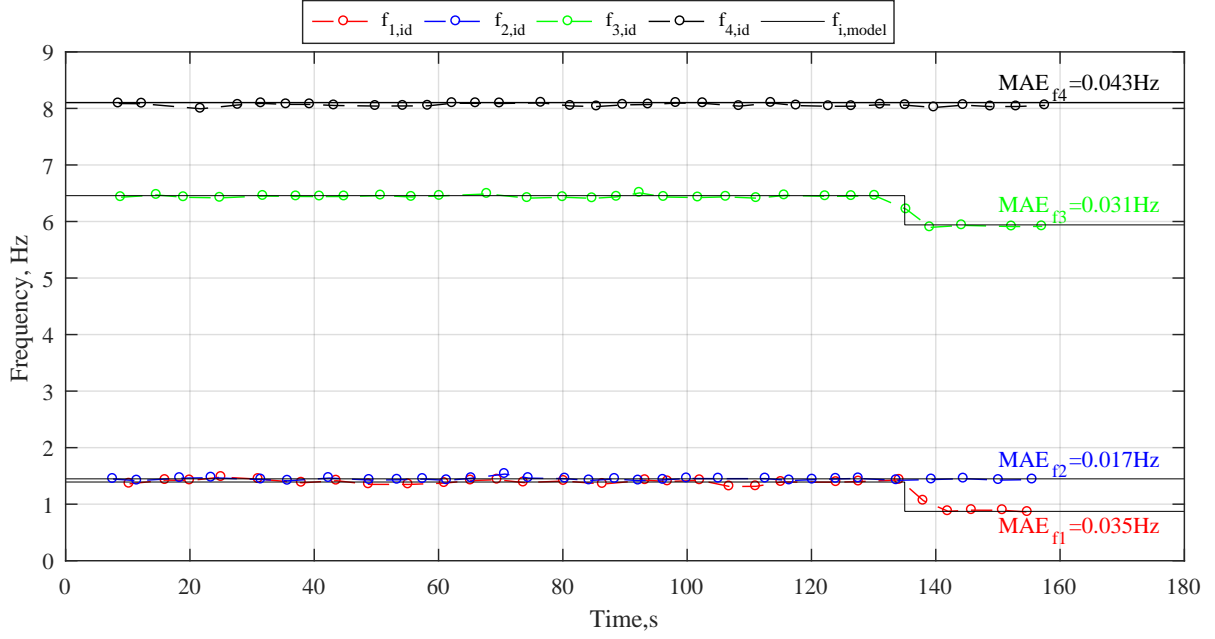


Figure 3.13: Modal frequency evolution identified based on 20% RMS signal to noise ratio using  $L = 20T_1$  window length, effective peak width  $W = 10$  and assumed mass matrix with 30% error

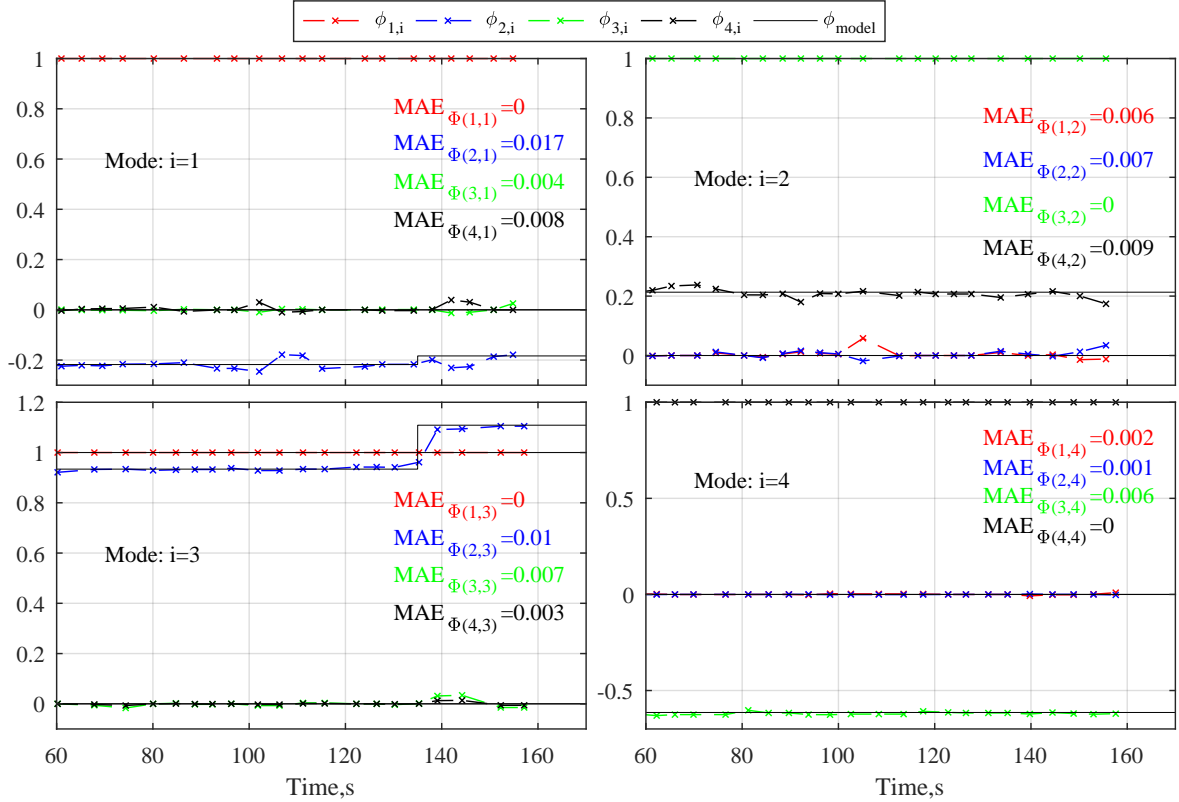


Figure 3.14: Mode shape evolution identified using output-only measurements based on 5% RMS signal to noise ratio using  $L = 20T_1$  window length, effective peak width  $W = 5$  and assumed mass matrix with 30% error

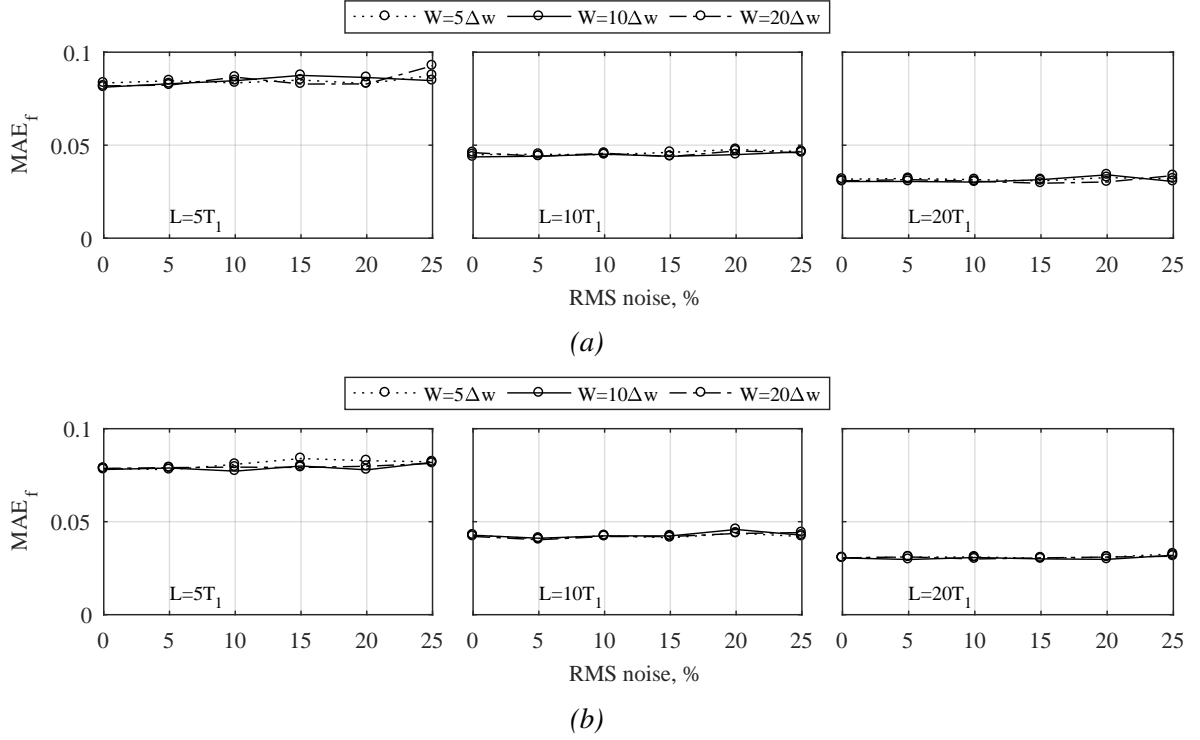


Figure 3.15: (a) Total mean absolute error (MAE) of identified frequencies estimated for different RMS noise levels, window lengths ( $L$ ) and peak widths ( $W$ ) a) assuming the mass matrix,  $M$ , is known and b) assuming 30% error in mass matrix estimation

width,  $W$ , has a very similar effect on the total error, as the application larger factors tends to reduce the errors. The parameter study also indicates that the accuracy of the assumed mass matrix,  $\hat{M}$ , has very little or no effect on the MAE of identified mode shape coefficients.

### 3.4.4 Overall discussion and limitations

Modal parameter identification for a time-variant system is presented and numerically validated by analysing short overlapping response time windows for different levels of noise. The identification results have shown the method can capture sudden changes in modal parameters if short response windows are analysed. However, the parameters identified based on short time windows demonstrate larger deviations from the simulated true values. However, further results indicate identification accuracy can be improved by increasing the length of the time windows or/and the effective peak isolation width,  $W$ .

Systems with mass disparity require reasonable estimation of the mass matrix, to ensure

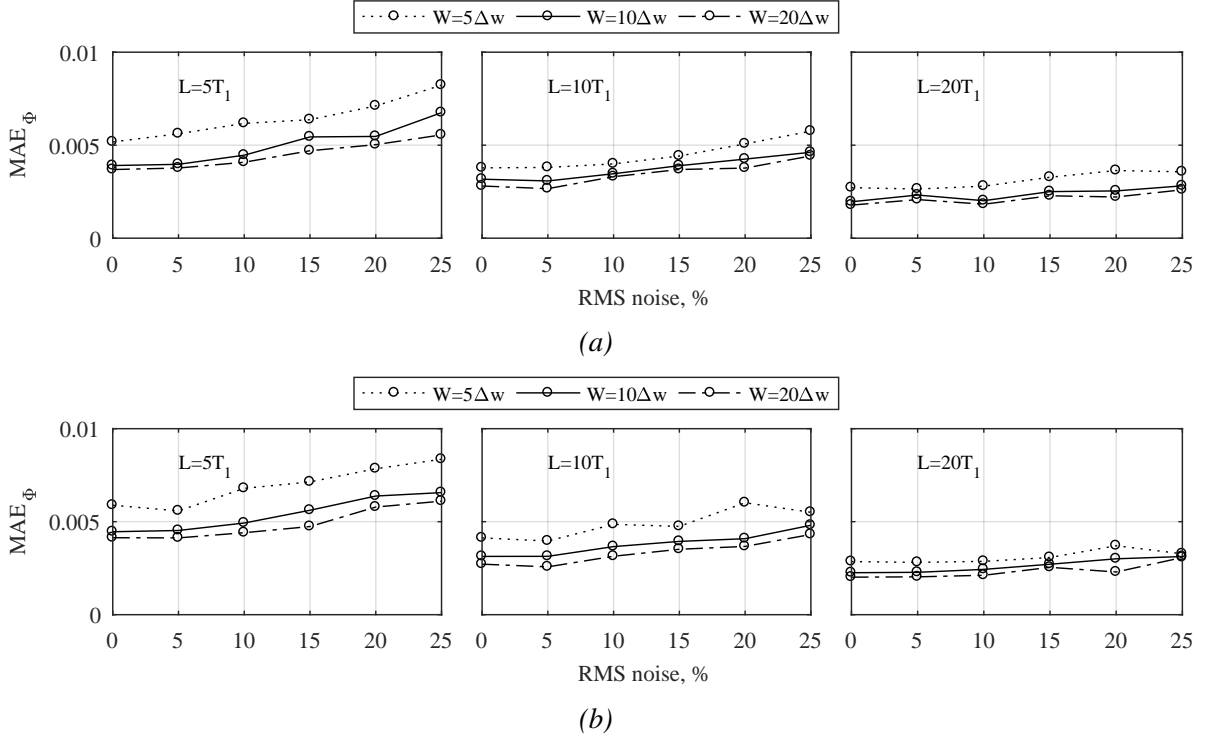


Figure 3.16: (a) Mean absolute error (MAE) estimated for different RMS noise levels, window lengths ( $L$ ) and peak widths ( $W$ ) a) assuming the mass matrix,  $M$ , is known and b) assuming 30% error in mass matrix estimation

mass scaled orthogonality, per Equation (2.17). These results indicate that even 30% error in mass matrix estimation still provides very comparable identification results, which is a very robust result. It should be noted that for systems represented by a mass matrix with small differences across different DOFs, an identity mass matrix can be adopted, as a result, avoiding complexity. Finally, all the results demonstrate relatively good accuracy for all added RMS noise levels.

It should be noted that the window length is limited not only by the period of the lowest mode,  $T_1$ , but also by the properties of FFT transformation to ensure enough frequency bins to get a good resolution FFT. Thus, the analysis of short time windows inherently provides poor frequency resolution, which in turn affects the outcome of identification. In contrast, the analysis of long time windows provides good frequency, but poor time resolution, which is a limiting factor for time-variant systems, with abrupt changes in modal parameters. Thus, for real life structures, the method can effectively be applied by employing different data segmentation strategies. For example, low intensity response data, where a linear time-invariant system

behavior is assumed, can be segmented using long time windows ( $L = 10...20T_1$ ). High intensity response time segments, where a non-linear or degrading system behavior is expected, can be segmented using short time windows.

The proposed method operates in the modal space and is based on mode decomposition, thus a linear time-invariant system (LTI) is assumed throughout the analyzed time window. Strong ground motion, however, will often trigger the inelastic system behavior, meaning that the principle of mode superposition will not be valid any more. However, most of structures exhibit a non-linear behavior only for a very short time period and the non-linear part comprises a very small part of the whole hysteresis loop. Thus, the modal parameters, identified for short response windows of a non-linear time-invariant system, will represent an average modal parameters that provide the best mode decoupling.

### 3.5 Summary

In this chapter a novel input-output modal parameter estimation technique is presented, which is extension to output-only modal identification technique introduced in Chapter 2. The method enables identification and continuous tracking of the modes participating in the response with significant energy. The method tracks the dominant modes by re-evaluating the modal frequencies and mode shape coefficients over short time windows. Hence, the approach is capable of identifying the modal parameters for linear and non-linear systems. The method can perform as output-only modal parameter identification technique using the ambient load induced vibrations and more importantly as input-output technique for earthquake generated non-linear response. Thus, the presented approach can provide a better insight into structures subjected to strong ground motion events.

The method is validated using a simulated data for a 4 DOF time-variant non-linear system representing a simplified version of a bridge pier. The results show the method enables identification and tracking of time varying modal parameters within good accuracy, which clearly

indicated the damage.

The comparison between input-output and output-only methods shows the extended method enables more accurate identification of the mode shape evolution for the lower modes. In contrast, mode shape identification of the higher modes yields the same or very marginal improvement in accuracy. In addition, the extended method provides the same identification accuracy of modal frequency evolution as the output-only method.

Overall, the input-output method performs robustly for all levels of noise added to the simulated response. The identified modal frequencies show very low sensitivity to added noise, whereas the identified mode shape coefficients demonstrate larger errors with increasing levels of added noise. These errors can be reduced by performing optimization over longer time windows or utilizing wider effective peak isolation widths. However, these parameters should be carefully chosen by the operator when identifying MDOF systems exhibiting strong nonlinearities and/or systems having closely spaced modes.

# CHAPTER 4

---

## Non-linear analysis using fiber formulation and modal parameter identification

---

### 4.1 Introduction

Modal parameter identification using one of several well-established system identification methods [99, 100, 110, 112, 121, 155] is generally limited to linear structures excited by broadband white noise loads of significant time duration. Thus, these methods are not able to estimate modal parameters when structures are subjected to unpredictable, relatively short duration earthquake loads. Particularly if they trigger non-linear response behavior.

The modal parameter identification technique presented in Chapter 3 was validated for a simple 4DOF simulated linear time-variant structure with abrupt stiffness degradation. The results show the method is able to capture changes in modal parameters with relatively good accuracy. However, structures excited by strong ground motion enter non-linear response regimes multiple times. As a result, the stiffness matrix may exhibit significant variability, which transfers to variability in mode shape coefficients and frequencies.

To explore this variability of modal parameters, a more sophisticated non-linear dynamic analysis based on fiber element formulation is carried out to simulate the structural response and provide synthetic data for subsequent identification/SHM. These models offer great accu-



racy and resolution in simulating and understanding non-linear response. Finally, time-varying modal parameters are identified using the input-output method presented in Chapter 3, and compared with simulation results from the fiber model.

## **4.2 Methodology**

### **4.2.1 FE modeling using fiber formulation**

The proposed modal parameter identification is validated for an FE model assembled using fiber elements. Fiber elements are also called distributed plasticity models, whose stiffness behaviour is purely derived from material stress-strain behaviour [172]. In contrast to concentrated plasticity elements, fiber sections can take into account the coupling behaviour between varying axial forces and bending moments [173]. The main advantage of the fiber element formulation is that it does not require determining the length of the plastic zone, as the plasticity can be formed at any element integration/control point.

However, the traditional fiber element formulation suffers from the following deficiencies [174–176]:

- Does not provide coupling between shear and flexural behavior.
- Assumes perfect bond between steel bars and surrounding concrete, which is typically partially lost at the onset of crack formation.
- Does not take into account tension stiffening.
- Does not capture strength and/or stiffness degradation associated with bond slip.
- Does not capture bar pullout (loss of stiffness) at the interface of beam-column connections and footing.

These disadvantages are solved utilizing more sophisticated fiber models [176–178]. However, the main purpose of this study is to demonstrate the sensitivity of modal parameters with respect to non-linear behavior, which can conveniently be modelled using typical fiber elements.

Non-linear numerical analysis of FE models incorporating fiber elements can be carried

out using a Newmark-Raphson iteration scheme. Fiber element state determination is implemented inside a Newton-Raphson iteration scheme as an additional loop after incremental nodal displacements are computed. More specifically, element state determination based on hybrid formulation is an iterative process determining the state of section deformations and resisting forces at selected integration points, which meet force equilibrium and displacement compatibility requirements. Thus, the whole numerical analysis consists of two loops representing the global/structure's level state determination and element level state determination. The element level state determination iteration loop is initialized after incremental nodal displacements are determined and the overall process is shown in Figure 4.1.

#### **4.2.2 Modal parameter identification**

Modal parameter identification of the non-linear time-varying system is carried out using the methodology presented in Section 3.2.2. The evolution of each mode shape can be identified by re-evaluating the mode shapes over selected relatively short time windows using Equation (3.6). This procedure can be described as a step process, as shown in Figure 4.2.

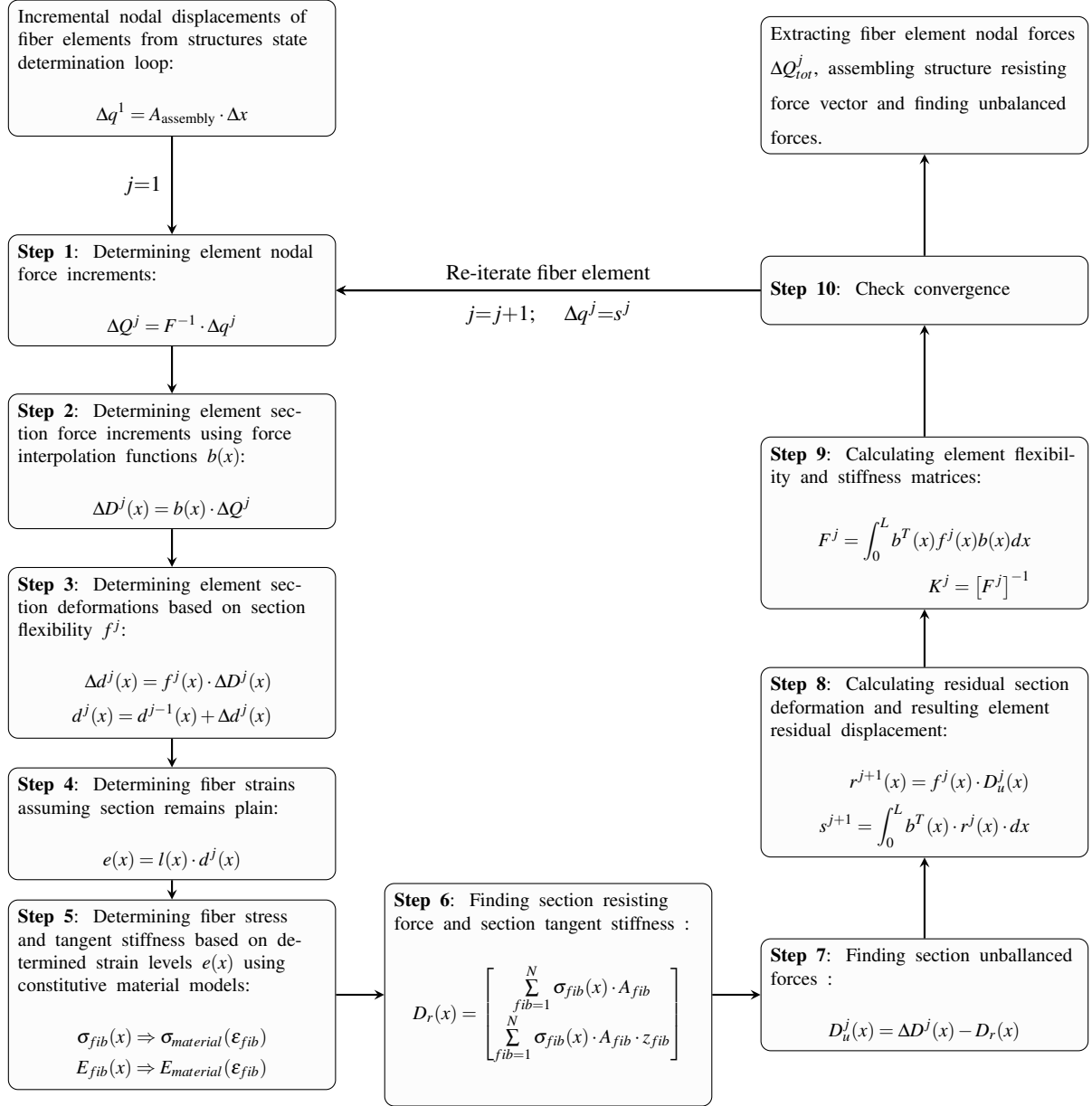


Figure 4.1: Flow chart for fiber element state determination loop implemented inside Newton-Raphson structure's integration loop [173]

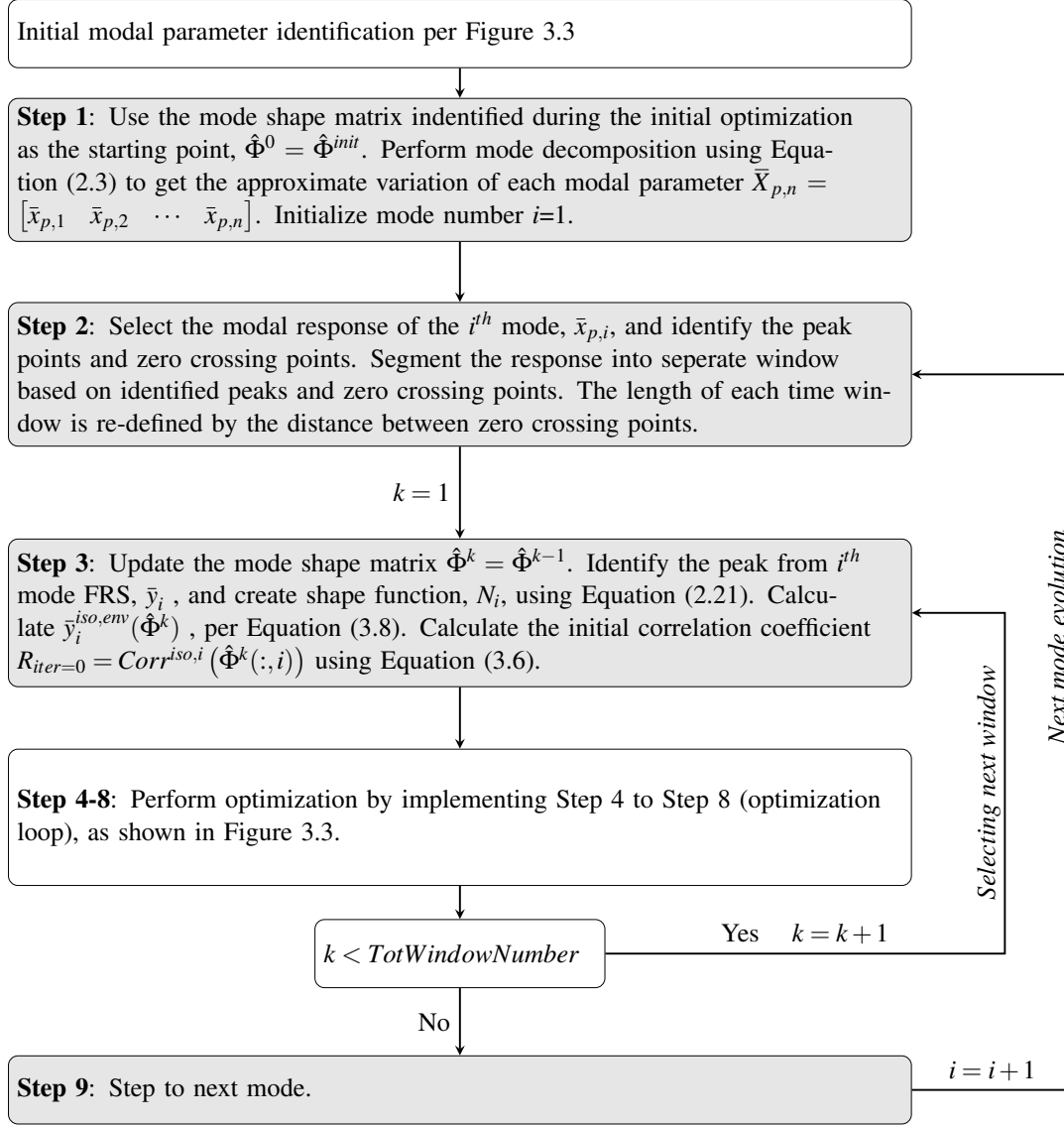


Figure 4.2: Flow chart for identification of modal parameter evolution

## 4.3 Validation study using simulated non-linear response

### 4.3.1 FE model

The proposed modal parameter identification method is validated analytically using a non-linear FE model representing the full-scale 5-story reinforced cast-in-situ concrete building, shown in Figure 4.3 [179]. The superstructure was designed to meet a performance target of 2.5% maximum inter-story drift ratio with a maximum peak floor acceleration of 0.8g.

The full-scale building has a plan dimensions of 11m by 8.1m and is 22.9m high. The mo-

ment resisting frame consists of two bays (frame and gravity) in the shaking direction and one bay in the transverse direction. The frame bay consists of moment resisting beams on each floor with equivalent moment capacities, but different detailing, where the gravity bay comprises a 200mm thick concrete slab. Lateral stiffness is ensured by two concrete transverse shear walls located on both sides of the elevator shaft. Steel bracing is added on the other side of the building between on the grid line C to prevent the structure from excessive torsional motion.

Due to the significant computational effort required to carry out a full non-linear analysis, a simplified 2D model is used. More specifically, only one of two lateral load resisting frames is modelled to simulate the response of the selected test structure. As a result, the adopted simplified 2D frame model does not account for over strength provided by two shear walls aligned in transversal direction. However, the goal here is a non-linear validation, rather than accuracy to a given experimental case that was stiff enough to provide a linear response.

In total, the FE model is assembled using 15 column fiber elements (C), 5 beam fiber elements situated in the load carrying bay and 5 elastic elements representing concrete slab situated in the gravity bay, as shown in Figure 4.3. Slab elements are assumed to be elastic to reduce computational demands as they have a negligible contribution to the lateral load carrying capacity. The effective width of the elastic slab element is assumed to be the width of column element. Column elements are assumed to be rigidly supported at the base. The test structure is designed according to the strong column-weak beam concept [179], where the main energy dissipation and lateral load capacity is provided by beam elements (B1 to B5), which have different detailing for each floor, as shown in Figure 4.3. However, for simplicity, the FE frame is modelled using only two different beam types (B1 and B5) with different flexural capacity, as shown in Figure 4.4. All the elements are connected through rigid joints, which are offset by the half height of the column element ( $L_{\text{offset}} = 0.33m$ ).

Beam (B) and column (C) elements are modelled using a hybrid formulation, which: a) ensures force equilibrium along the element; and b) satisfies displacement compatibility [173].

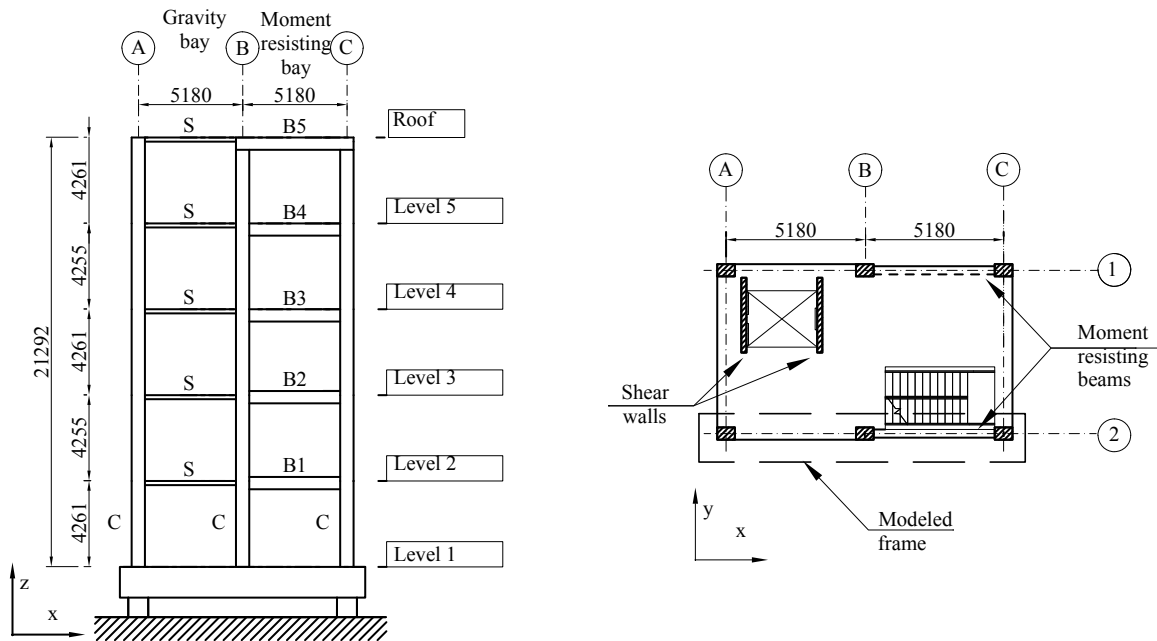


Figure 4.3: Elevation and plan views of modelled full-scale test structure [179]

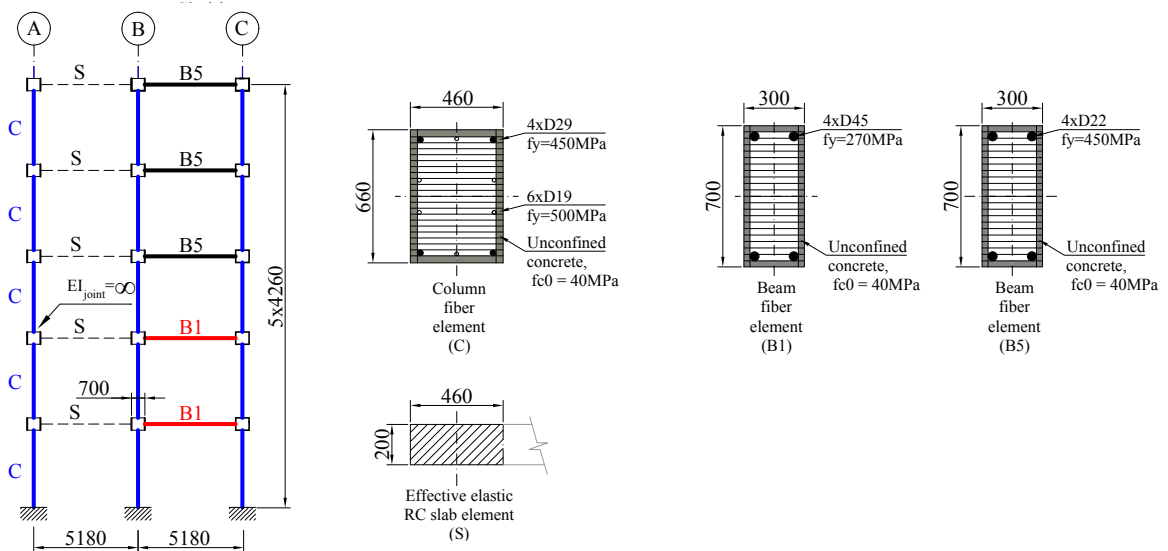


Figure 4.4: Simplified 2D fiber model constructed using beam and column fiber elements

All the fiber elements are discretized into 5 integration points. Material properties assigned to fiber elements are summarized in Table 4.1. The cyclic stress-strain behavior of the steel reinforcement material is described using Menegotto-Pinto constitutive model [180]:

$$\sigma^* = b\varepsilon^* + \frac{(1-b)\varepsilon^*}{(1+\varepsilon^{*R})^{\frac{1}{R}}} \quad (4.1)$$

$$\sigma^* = \frac{\sigma - \sigma_r}{\sigma_0 - \sigma_r} \quad \varepsilon^* = \frac{\varepsilon - \varepsilon_r}{\varepsilon_0 - \varepsilon_r}$$

where  $b$  is the strain hardening ratio,  $\varepsilon^*$  and  $\sigma^*$  are the normalized strain and stress, respectively,  $\varepsilon_r$  and  $\sigma_r$  are the stress and strain, respectively, at the last load reversal,  $R$  is the parameter controlling the transition curve and takes into account Bauschinger effect:

$$R = R_0 - \frac{a_1 \varepsilon_{pl}}{a_2 + \varepsilon_{pl}} \quad (4.2)$$

where  $\varepsilon_{pl}$  is the plastic strain,  $a_1$  and  $a_2$  are the experimentally determined parameters.

Menegotto-Pinto steel stress strain model can be successfully implemented using the following parameters [173, 181]:

$$R_0 = 20 \quad a_1 = 18.5 \quad a_2 = 0.15 \quad b = 0.05 \quad (4.3)$$

*Table 4.1: Member properties used for 2D FE model*

Member name	Dimensions, m	Cover thickness, m	Length, m	Concrete strength, $f_{c0}$ , MPa	Steel strength, $f_y$ , MPa
B1	0.70x0.30	0.05	4.48	40	480
B5	0.70x0.30	0.05	4.48	40	450
C1	0.66x0.46	0.05	3.56	40	450
S1	0.20x0.46	-	4.48	-	-

Concrete material cyclic stress-strain behavior is defined using the concrete model proposed by [182], where the loading, unloading and transition rules are adopted from [183]. A constant thickness of unconfined cover concrete is assumed for all fiber elements  $t_{unconfined} = 0.05\text{m}$ . Confined and unconfined concrete area is discretized into 20 and 10 fibers, respectively.

A diagonal mass matrix is assumed, where the floor mass is lumped uniformly at the rigid joints, with the following mass distribution starting from the ground floor:

$$M_{floor} = \begin{bmatrix} 0.37 & 0.39 & 0.50 & 0.54 & 0.35 \end{bmatrix} \cdot 1e^5 \text{kg} \quad (4.4)$$

A constant damping matrix is used, assuming Rayleigh proportional damping  $C = \alpha_0 M + \alpha_1 K_0$ , where proportionality constants  $\alpha_0$  and  $\alpha_1$  are estimated to provide  $\xi_1 = 3\%$  and  $\xi_2 = 3\%$  critical damping for the first and second modes, respectively. The initial stiffness matrix,  $K_0$ , represents the the stiffness of the undamaged structure. Calculated modal frequencies,  $f_i$ , and equivalent damping ratios,  $\xi_i$ , for all modes are shown in Table 4.2. It should be noted that estimated modal parameters are valid only for the healthy, undamaged structure. These parameters are subjected to a change once damage is induced in the structure, resulting in a changed stiffness matrix ( $K_{tan} \neq K_0$ ). Finally, non-linear dynamic analysis is carried out using Newmark- $\beta$  integration method with sampling frequency of  $f = 200\text{Hz}$ .

Table 4.2: Estimated first 5 modal parameters

Mode	1	2	3	4	5
Modal frequency, $f$ (Hz)	1.53	5.29	10.2	15.8	22.7
Modal damping, $\xi$ (%)	3.00	3.00	4.82	7.17	10.1

### 4.3.2 Non-linear simulation

The analysed FE fiber frame model is subjected to the 20 unidirectional ( $x$  dir) different intensity earthquake (EQ) inputs representing SAC records [184] shown in Table 4.3. All ground motion inputs are 100 seconds long. However, the actual effective duration of each strong ground motion is different. Hence, the remaining time duration is filled with 1%g RMS white noise (WN) excitation, which represents ambient load. A typical example of 100 seconds of excitation, consisting of EQ and WN inputs, is shown in Figure 4.5.



Table 4.3: A suite of 20 input ground motions [184]

Test	Earthquake	PGA( $m/s^2$ )
EQ1	Coyote Lake, 1979, Gilroy	5.78
EQ2	Coyote Lake, 1979, Gilroy	3.27
EQ3	Imperial Valley, El Centro	1.41
EQ4	Imperial Valley, El Centro	1.09
EQ5	Kern County , 1952	1.41
EQ6	Kern County 1952	1.56
EQ7	Landers Eqk, 1992	3.31
EQ8	Landers, 1992	3.02
EQ9	Morgan Hill, 1984, Gilroy	3.12
EQ10	Morgan Hill, 1984, Gilroy	5.36
EQ11	Parkfield, 1966	7.66
EQ12	Parkfield, 1966	6.19
EQ13	Parkfield, 1966	6.80
EQ14	Parkfield, 1966	7.75
EQ15	North Palm Springs, 1986	5.08
EQ16	North Palm Springs, 1986	3.72
EQ17	San Fernando, 1971	2.48
EQ18	San Fernando, 1971	2.27
EQ19	Whittier, 1987	7.54
EQ20	Whittier, 1987	4.69

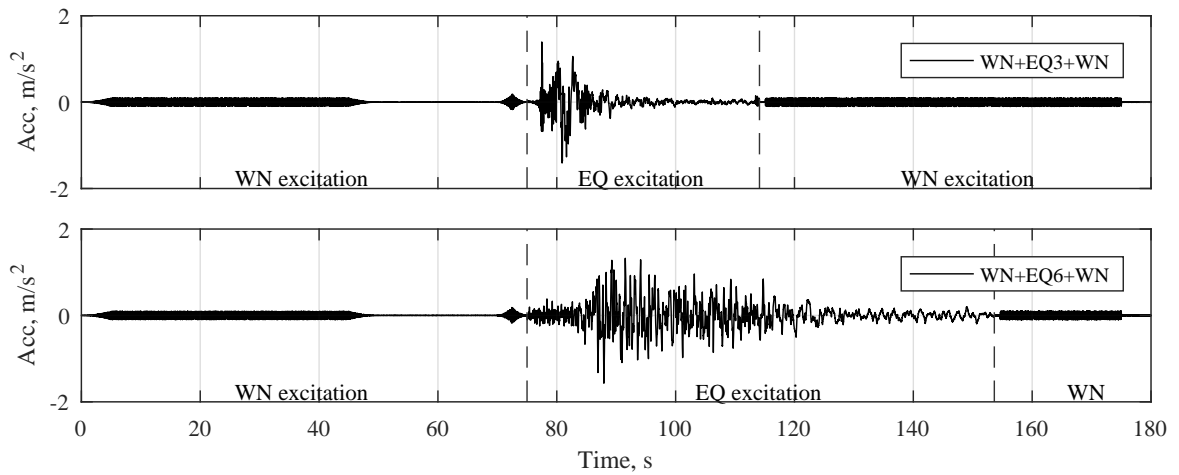


Figure 4.5: Input ground motion time histories for EQ3 and EQ6 events

### 4.3.3 Modal parameter identification

Modal parameter identification is carried out using the input-output method presented in Chapter 3. This method assumes each floor acceleration is measured. Thus, a 5DOF system is considered. Different levels of RMS white noise are added to the simulated structural response signal from the FE model to test robustness. The RMS noise is a random normal distribution of the square root of the average of the clean (no noise) simulated measurement with 99.7% of random values within the defined noise level. Identification is carried out assuming the mass matrix is estimated with 10% error. Finally, the effective peak isolation width is taken  $W = 10$ .

First, an initial modal parameter identification is carried out using 30 seconds white noise excitation response data to identify modal parameters for a healthy, undamaged structure. This step mimics a pre-event ambient modal identification, as might happen in real SHM systems. Second, white noise and earthquake response data are decomposed into separate modes, which are then analysed for peaks and zero crossing points. These points are used to characterize the start and end time of moving windows. Low intensity modal response of the  $i^{th}$  mode,  $\ddot{X}_i < 0.1m/s^2$ , is segmented into 20 second windows with 50% overlap, where high intensity modal response,  $\ddot{X}_i > 0.1m/s^2$ , is segmented into 10 second windows with 75% overlap. Third, the mode shape coefficients of each mode are re-evaluated over each moving window by solving the non-linear optimization problem introduced in Section 3.2.2 (Equation 3.6). Finally, a continuous time-varying mode shape evolution between the optimized windows is obtained by applying a piecewise  $C^1$  continuous cubic interpolation.

Identification error of mode shape coefficients is quantified by calculating the mean absolute error (MAE):

$$MAE_{\phi,i} = \frac{\sum_{j=1}^J \sum_{k=1}^K |\hat{\phi}^k(j,i) - \phi^k(j,i)|}{K \cdot J} \quad (4.5)$$

where  $\hat{\phi}^k(j,i)$  and  $\phi^k(j,i)$  are the identified and simulated  $i^{th}$  mode shape coefficient of  $j^{th}$  DOF, and  $K$  is the number of identified samples and  $J$  is the number of DOF.

## 4.4 Results and Discussion

### 4.4.1 Initial modal parameter identification

Initial modal parameters are identified using a 30s long white noise excitation. The identified modal frequencies and mode shape coefficients are shown in Figure 4.6 and Tables 4.4, 4.5 and 4.6. Initial modal parameter identification yields relatively accurate results. The maximum captured error of identified mode shape coefficients is 6.1% for noiseless signal and 5.81% for signal with 11.2% RMS noise, indicating good robustness. Good accuracy can be seen in the identified modal frequencies, where the maximum captured error is 1.7%. In contrast, modal identification for damping ratios yields poor accuracy, especially for the first mode, where the error of 21.3% is observed. However, other readily available SHM methods [43, 99, 117, 118] can be used if better modal damping identification accuracy is desired. Overall, large modal parameter identification errors are mainly seen for small values, meaning that relatively small errors result in large relative errors.

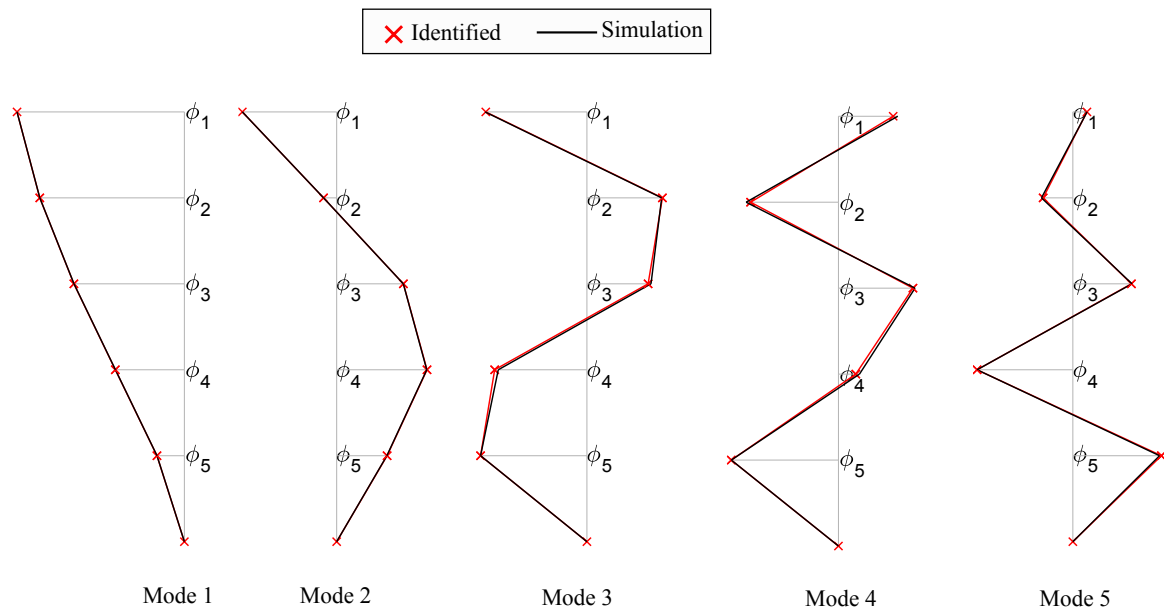


Figure 4.6: Mode shapes identified from 30 seconds white noise excitation response

Table 4.4: Comparison of simulated and identified modal parameters using 30 seconds white noise excitation response, with and without noise added to the response data before identification.

Mode		$\phi_{model}$	$\hat{\phi}_{id,0}$	$\Delta\phi, \%$	$\hat{\phi}_{id,10\%}$	$\Delta\phi, \%$
Mode 1	$\phi_{1,1}$	0.16	0.16	0.06	0.16	-0.24
	$\phi_{2,1}$	0.41	0.41	-0.05	0.41	-0.15
	$\phi_{3,1}$	0.66	0.66	-0.05	0.66	-0.20
	$\phi_{4,1}$	0.86	0.86	-0.02	0.86	-0.06
	$\phi_{5,1}$	1.00	1.00	0.00	1.00	0.00
Mode 2	$\phi_{1,2}$	-0.53	-0.53	-0.60	-0.53	0.32
	$\phi_{2,2}$	-0.96	-0.96	0.36	-0.96	0.54
	$\phi_{3,2}$	-0.71	-0.72	1.66	-0.71	0.74
	$\phi_{4,2}$	0.14	0.13	-6.48	0.14	-1.08
	$\phi_{5,2}$	1.00	1.00	0.00	1.00	0.00
Mode 3	$\phi_{1,3}$	1.00	1.00	0.00	1.00	0.00
	$\phi_{2,3}$	0.83	0.83	-0.37	0.84	0.78
	$\phi_{3,3}$	-0.60	-0.59	-1.53	-0.59	-1.99
	$\phi_{4,3}$	-0.70	-0.69	-1.75	-0.70	-0.98
	$\phi_{5,3}$	0.96	0.95	-1.02	0.95	-0.66
Mode 4	$\phi_{1,4}$	1.00	1.00	0.00	1.00	0.00
	$\phi_{2,4}$	-0.20	-0.18	-6.12	-0.17	-11.21
	$\phi_{3,4}$	-0.71	-0.68	-4.81	-0.69	-4.09
	$\phi_{4,4}$	0.86	0.83	-3.78	0.82	-4.35
	$\phi_{5,4}$	-0.55	-0.53	-4.68	-0.52	-5.83
Mode 5	$\phi_{1,5}$	-0.91	-0.89	-1.63	-0.87	-4.15
	$\phi_{2,5}$	1.00	1.00	0.00	1.00	0.00
	$\phi_{3,5}$	-0.62	-0.62	0.19	-0.62	0.24
	$\phi_{4,5}$	0.33	0.31	-4.24	0.31	-4.06
	$\phi_{5,5}$	-0.15	-0.15	-0.20	-0.15	0.87

Table 4.5: Identified modal frequencies for different signal noise levels based on white noise excitation response

Mode	$f_{model}, \text{Hz}$	$\hat{f}_{id,0}, \text{Hz}$	$\Delta f, \%$	$\hat{f}_{id,10\%}, \text{Hz}$	$\Delta f, \%$
Mode 1	1.531	1.558	1.74	1.557	1.70
Mode 2	5.312	5.320	0.14	5.322	0.19
Mode 3	10.183	10.152	-0.30	10.154	-0.28
Mode 4	15.873	15.791	-0.52	15.798	-0.47
Mode 5	22.697	22.596	-0.45	22.569	-0.56

Table 4.6: Equivalent modal damping for different signal noise levels identified from response to white noise excitation

Mode	$\xi_{model}$	$\hat{\xi}_{id,0}$	$\Delta\xi, \%$	$\hat{\xi}_{id,10\%}$	$\Delta\xi, \%$
Mode 1	0.030	0.027	-11.0	0.026	-14.67
Mode 2	0.030	0.028	-8.0	0.036	21.33
Mode 3	0.048	0.050	3.9	0.051	5.19
Mode 4	0.072	0.077	7.4	0.075	3.91
Mode 5	0.101	0.098	-3.6	0.100	-1.28

#### 4.4.2 Modal parameter identification for a suite of EQ inputs

Modal parameter evolution is obtained by carrying out an optimization problem for selected modes over relatively short overlapping response windows. Identification is carried out for two data acquisition scenarios: 1) measured response data is free of noise; and 2) the data has 10% RMS white noise added. The time history response for the 20 ground motion inputs in Table 4.3 is analysed in total. Mode shape evolution for the simulated structure is obtained by performing an eigenanalysis based on the estimated tangent stiffness matrix at any point in time:

$$[\Phi(t), \lambda(t)] = \text{eig}(K_{tan}(t), M) \quad (4.6)$$

where  $t$  is the time instant,  $\Phi(t)$  and  $\lambda(t)$  is mode shape matrix and eigen values, respectively, calculated based on tangent stiffness matrix,  $K_{tan}(t)$ .

Mode shape evolution for the first five modes identified for EQ3 and EQ6 with 10% RMS noise are shown in Figures 4.7 and 4.8. Modal parameter identification carried out for these two earthquake response time histories represent the best and poorest overall identification accuracy, respectively, estimated by mean absolute error (MAE).

The overall performance of modal parameter identification carried out for 20 different intensity and duration ground motion inputs is shown in Figure 4.9. The events are sorted in ascending identification MAE order. All mode shape coefficients are unit normalized. Thus, variations are seen in the remaining 4 DOFs. To enable a better comparison, simulated mode shape coefficients are smoothed using a 10 seconds long moving window, over which the mode shapes are identified.

The simulated mode shape coefficients demonstrate significant variability due to the non-linear behaviour of fibre elements, as expected. Hence, the identified values represent the average of time-varying mode shape coefficients over the analysed time windows. In this study, low and high intensity modal responses are segmented into 20 and 10 seconds windows, respec-

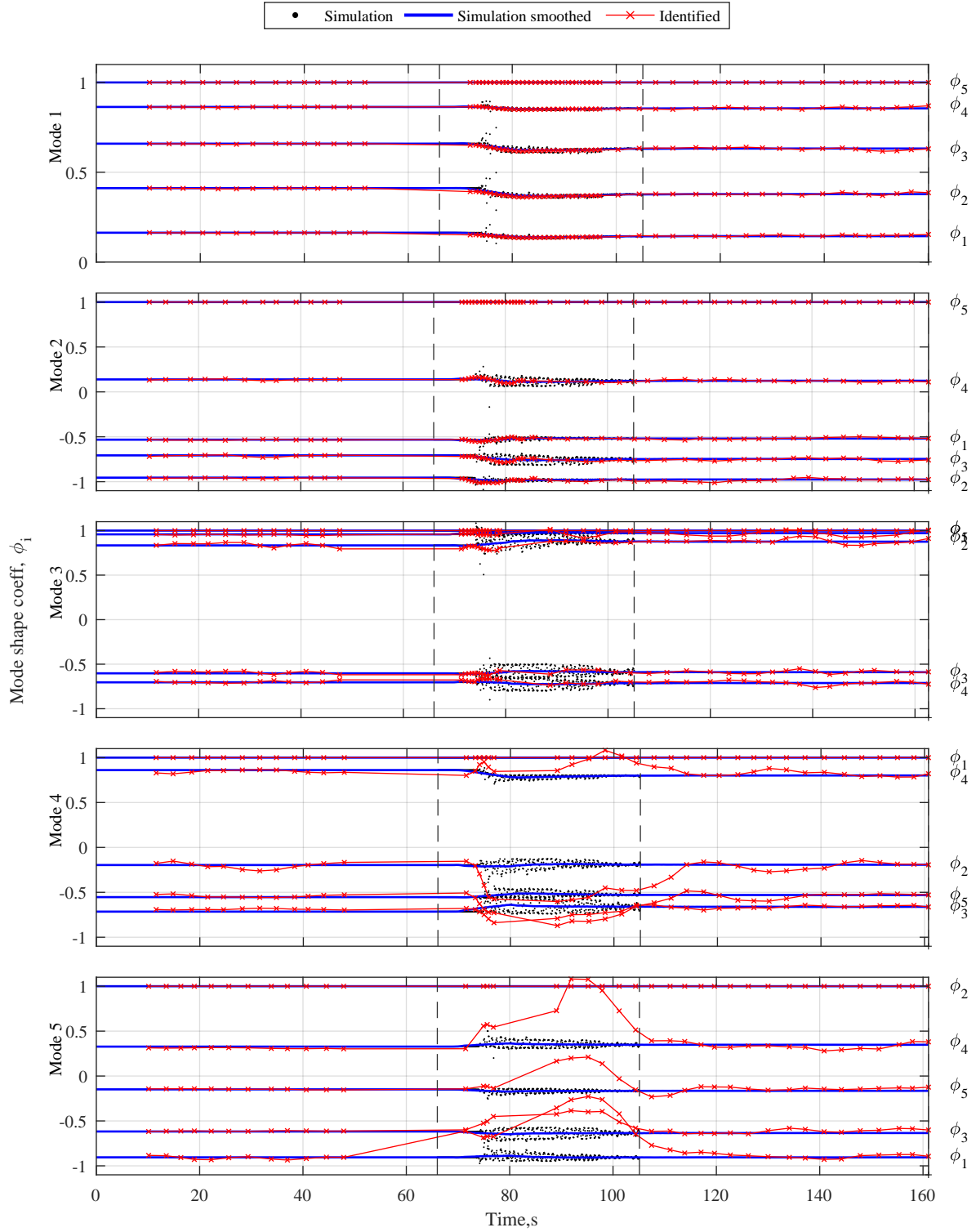


Figure 4.7: A comparison between identified and simulated mode shape evolutions of 5 modes for earthquake input EQ3. Vertical dashed line marks the effective duration of earthquake event

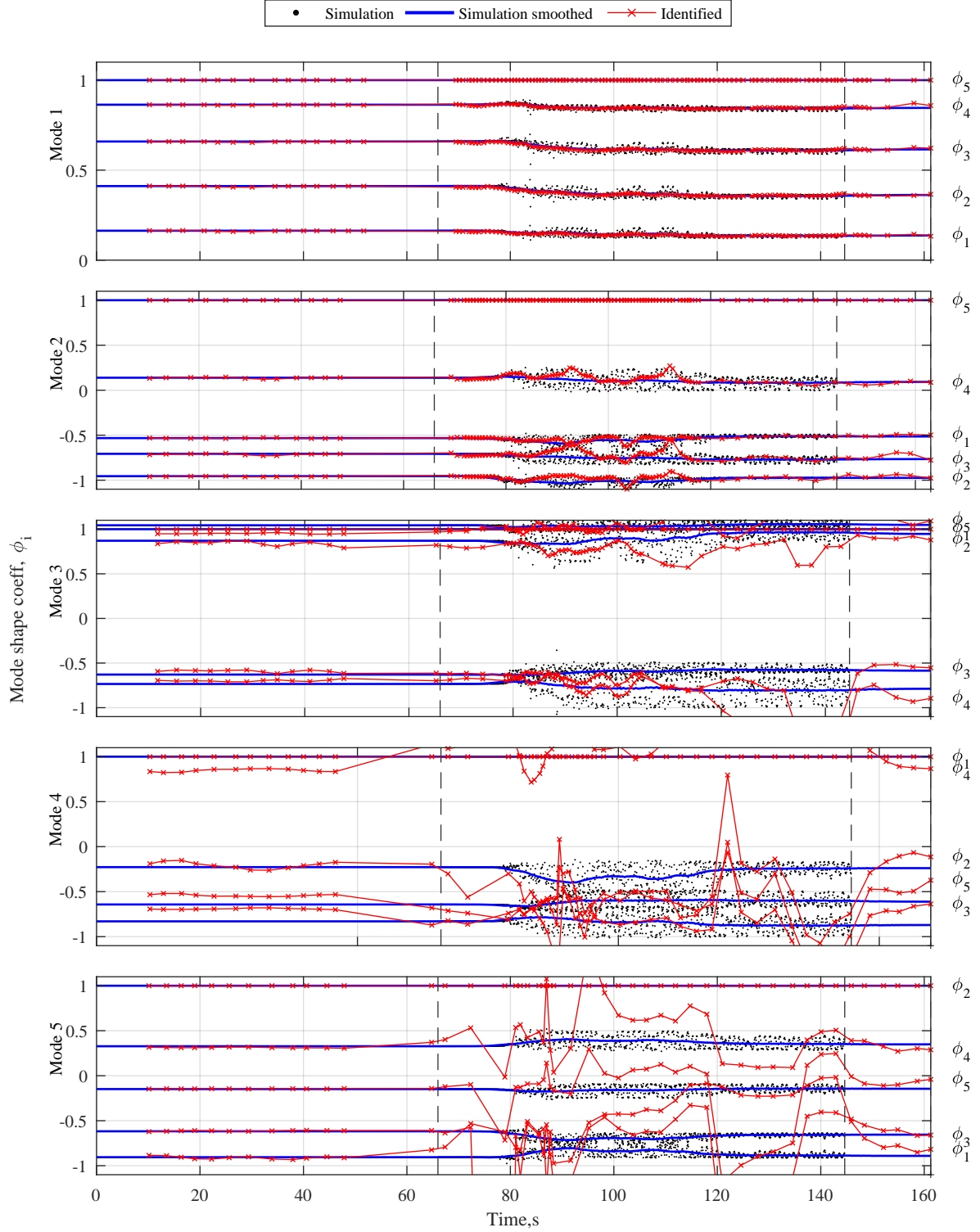


Figure 4.8: A comparison between identified and simulated mode shape evolutions of 5 modes for earthquake input EQ6. Vertical dashed line marks the effective duration of earthquake event

tively, yielding the point shown.

Comparison indicates identification of the lowest two modes yields relatively good accuracy for all analysed ground motion inputs. Mean absolute error varies in the range of  $MAE = 0.004 - 0.04$ . A clear shift and transition can be seen in mode shape evolution during strong ground motion excitation, which is caused by damage. Significantly larger MAE in identified mode shape coefficients can be seen for modes 3, 4 and 5 for different input ground motions, with  $MAE = 0.021$  to  $0.200$ .

Observed identification errors can be distinguished into 2 types:

- Errors caused by temporal high amplitude variation of mode shape coefficients, which is triggered by highly non-linear behaviour as the identified values typically represent moving averages.
- Errors caused by a constant offset as a result of poor identification accuracy.

Particularly poor identification can be seen for modes 4 and 5, where the identified mode shape coefficients are offset significantly from simulated ones during strong ground motion excitation. However, the identification converges to simulated values once white noise excitation is initiated, as might occur in weak motions at the end of the event or in weaker aftershocks. This feature is evident particularly in Figure 4.7, as the white noise excitation was sufficiently long duration to allow convergence of mode shape identification.

Large identification errors in higher modes can mainly be observed during strong ground motion excitation. This poor performance can be explained by analyzing the frequency content of selected earthquake inputs, which can be divided into two groups:

- Group 1. Earthquake inputs EQ1, EQ3 and EQ8, for which the identification yielded the best accuracy.
- Group 2. Earthquake inputs EQ6, EQ9 and EQ18, for which the identification produced the least accurate results.



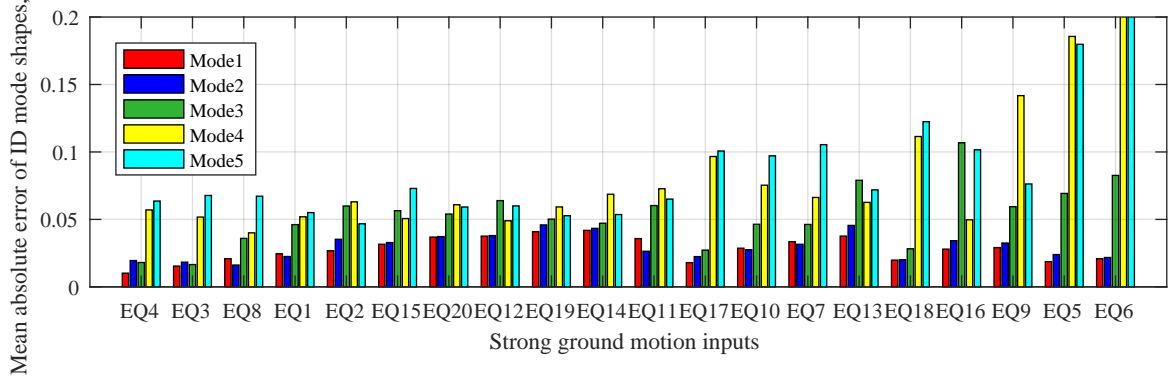
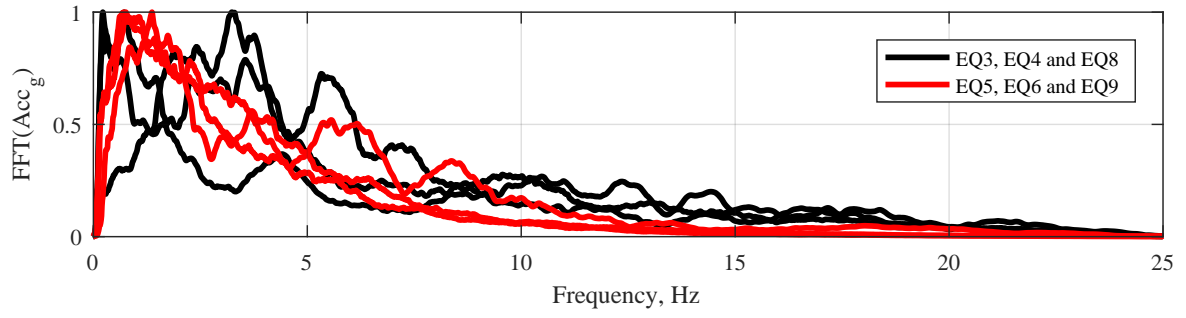


Figure 4.9: Estimated mean absolute error (MAE) of identified mode shape coefficients for different earthquake inputs using data polluted with 10% RMS noise sorted in ascending MAE order

Normalized frequency spectra for the selected input ground motions are shown in Figure 4.10. It can be clearly seen that identification yielded better results for earthquake inputs, containing less concentrated and more widely spread frequency spectrum. Hence, earthquake inputs with more uniform spectral energy distribution are exciting the higher modes with higher energy, which allows the identification to yield mode accurate results. This observation explains the relatively accurate identification using white noise excitation, which is simulated at the start and the end of each time history. In contrast, earthquake inputs with spectral energy concentrated in a narrow frequency range may excite higher modes with only limited energy, leading to poor signal/noise ratio, and consequently, inaccurate identification. It should be noted that identification error can also be significantly affected by earthquake intensity, which can trigger higher/lower non-linearities. Moreover, overall identification accuracy based on MAE can also be influenced by the effective duration of earthquake event. More specifically, as the total length of the response time history used for identification is constant for all events, large errors resulting from identification of short duration earthquake events have smaller impact on overall accuracy. The opposite holds for identification carried out based on response time histories containing long duration strong ground motion

Similar trends can be seen for the identified modal frequencies. Modal frequency evolution for a white noise excitation combined with strong ground motion events EQ3 and EQ6 is shown in Figures 4.11 and 4.12. As mentioned earlier, the method yielded the most and least accurate identification for these two events, respectively. The overall performance of frequency identification for all events is shown in Figure 4.13.



*Figure 4.10: Unit normalized smoothed frequency spectra of selected input ground motions, for which the identification produced the best and poorest accuracy of higher modes*

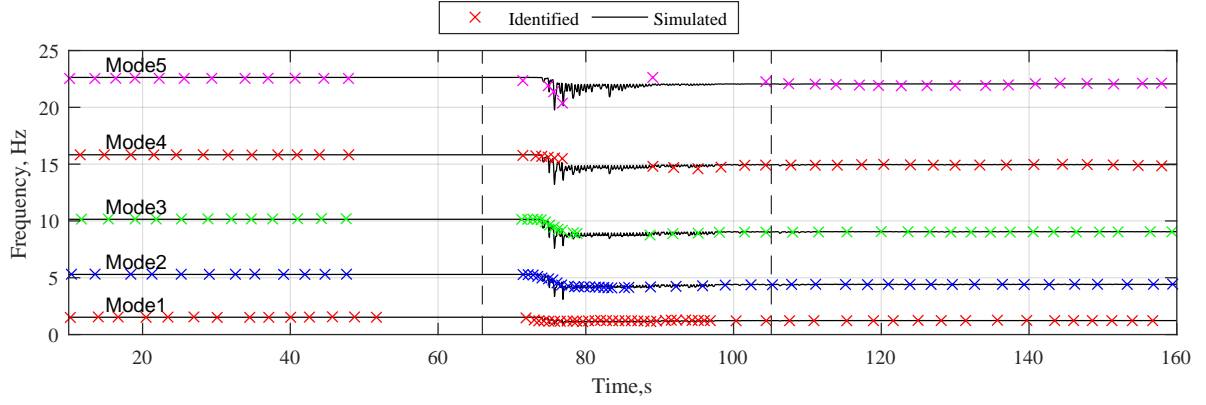


Figure 4.11: A comparison between identified and simulated modal frequency evolutions of 5 modes for earthquake input EQ3. Vertical dashed line marks the effective duration of earthquake event

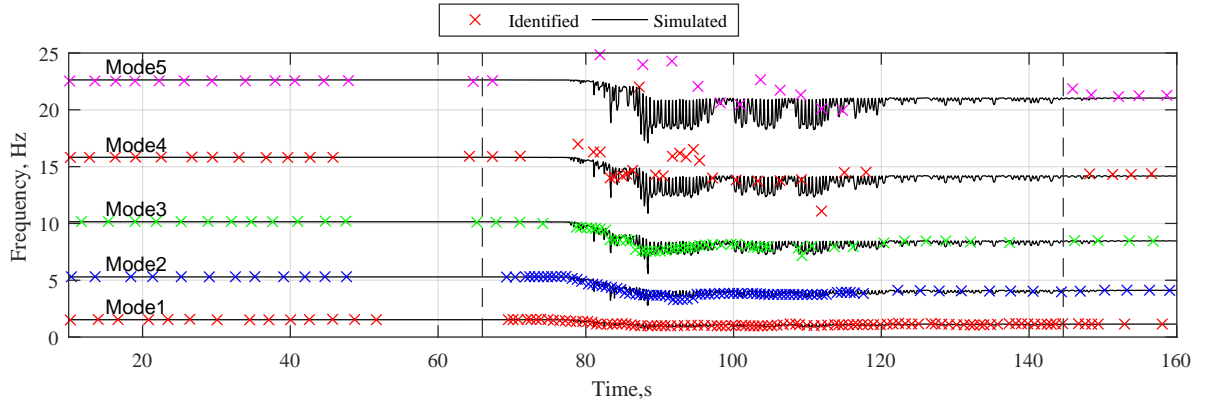


Figure 4.12: A comparison between identified and simulated modal frequency evolutions of 5 modes for earthquake input EQ6. Vertical dashed line marks the effective duration of earthquake event

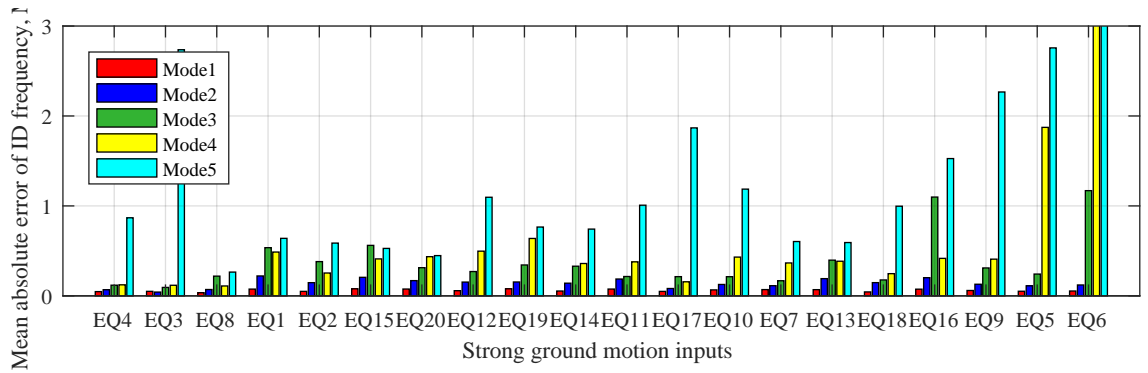


Figure 4.13: A comparison between identified and simulated modal frequency evolutions of 5 modes for earthquake input EQ6. Vertical dashed line marks the effective duration of earthquake event

The method tracks the lowest two modal frequencies with a good accuracy for majority of events, where MAE varies within the range 0.03-0.2. However, modal frequencies of Modes 3 to 5 are identified with very large errors for some tests. These errors can mainly be attributed

to poor excitation levels which lead to poor signal to added noise ratios. Large identification errors could also be related to abrupt and /or temporal variation of frequencies as the identification provides the constant/average modal parameters over monitored overlapping window, which was 20s and 10s long for white noise and strong ground motion response, respectively. However, frequency identification based on white noise excitation shows very good accuracy for all modes, as the modes are excited with sufficient energy. Overall, the method can provide a near real-time tracking of modal frequencies and capture changes which can be directly associated with damage.

## 4.5 Summary

This study investigates the application of modal parameter identification technique to non-linear structures excited by white noise and earthquake inputs. The method is validated using simulation data of non-linear 5 DOF reinforced concrete structure assembled using fiber elements. FE modeling based on fiber elements allows the simulation of more realistic behavior of RC structures exhibiting stiffness and strength degradation during strong ground motion events. Fiber element behavior is purely based on material stress-strain properties and provides a highly non-linear analytical test case with and without noise, added to the response data before identification.

The results show the modal parameter identification technique is capable of identifying mode shape coefficients with good accuracy using white noise excitation data. However, strong ground motions trigger highly non-linear behavior, resulting in some significant variation of simulated mode shape coefficients over relatively short windows. Modal parameter identification carried out over short non-linear response windows yields mode shape evolution, which represents the smoothed/average variation of simulated mode shape coefficients. Hence, the method can capture only the overall trend of mode shape variation.

Finally, the results show the method can yield inaccurate identification of higher modes for earthquake excitation data, due to mainly poor signal-to-noise ratio when these inputs do

not excite higher modes significantly. However, the method provides relatively accurate mode shape evolution for the lower modes, which can be used for mode decoupling. Mode decoupled response allows for reconstruction of single mode dominant restoring force loops, which can be readily analysed using hysteresis loop analysis.

## CHAPTER 5

---

# Damage Identification for Hysteretic Structures Using a Novel Mode Filtering Method

---

### 5.1 Introduction

A recently developed parametric identification technique based on the reconstruction of hysteresis loops, enables effective identification of both structural parameters, and the presence and level of any non-linear structural behaviour. This relatively computationally simple method relies only on measured accelerations and infrequently measured displacements, and has proven to be robust in capturing the physical parameters of a simulated SDOF pinching structure [147, 185] and non-linear experimental structures [18]. However, it has not been verified with data including measurable response contributions from higher modes. Higher modes result in irregular shape hysteresis loops, which can be hard to identify. In particular, they can lead to inaccurate identification of the structural parameters using a hysteresis loop analysis method.

Higher modes can be filtered out using a simple  $n^{th}$ -order Butterworth filter or other simple low-pass filtering. However, its performance is poor for non-linear data and it requires knowledge of the structural frequencies before and after damage occurs. As a result, an adaptive time-varying modal filtering technique is developed here to separate different vibration modes over time for linear and non-linear data to enable more precise and “smooth” reconstruction of hysteresis loops for each mode. The overall approach tracks relevant mode shapes over time by

regularly re-evaluating the mode shape matrices.

This chapter presents results of SHM carried out for a full-scale experimental bridge pier structure, which consists of two parts: a) application of modal parameter identification; and b) analysis of reconstructed single mode dominant "smooth" hysteresis loops using HLA. The core of methodology used for modal parameter identification is presented in Chapters 2 and 3. However, as the work presented in this chapter was carried out in the early stages of the whole research, minor alterations to the method exist. These existing differences represent the initial idea of modal parameter identification, which was further extended to more general methodology, presented in Chapters 2 and 3, which is applicable to any MDOF structure. However, simplifications adopted in this chapter do not affect the outcome of identification due to simplicity of analysed structure. The existing differences are:

- The effectiveness of mode shape identification (objective function) adopted in this chapter is defined using energy ratio principle, rather than cross-correlation of modal FRS, per Equations (2.14) and (3.6).
- The method proposed in this chapter uses a simplified shape function to segregate different mode FRF's, which is based on a simple windowing technique.
- The objective functions do not take into account the weighting factors, which act as a penalty coefficients for closely spaced modes with high degree of consistency.

## **5.2 Methodology**

As mentioned in introduction, the modal parameter identification adopted in this chapter resembles a simplified version of the one presented in Chapter 2 and Chapter 3. Thus, for clarity, the simplified methodology is introduced briefly herein highlighting the main differences adopted.

### **5.2.1 Reconstruction of hysteresis loops for selected modes**

The equation of motion of a linear multi-degree-of-freedom (MDOF) system is described:

$$\mathbf{M}\{\ddot{X}\} + \mathbf{C}\{\dot{X}\} + \mathbf{K}\{X\} = -\mathbf{M}r\{\ddot{X}_g\} \quad (5.1)$$

where  $\mathbf{M}$ ,  $\mathbf{C}$ ,  $\mathbf{K}$  are the mass, damping and stiffness matrices,  $r$  is the excitation influence vector,  $\{\ddot{X}\}$ ,  $\{\dot{X}\}$  and  $\{X\}$  are the acceleration, velocity and displacement vectors of MDOF system, respectively, and  $\{\ddot{X}_g\}$  is the ground motion acceleration.

The linear MDOF system response can be represented as the weighted, linear sum of individual vibration modes:

$$X(t) = \sum_{i=1}^n \phi_i \cdot \bar{X}_i(t) = \Phi \bar{X}(t) \quad (5.2)$$

where  $n$  is the number of modes,  $\bar{X}_i(t)$  is modal displacement of the  $i^{th}$  mode at time instant  $t$ , where each row of  $\bar{X}(t)$  represent each mode,  $\Phi = [\phi_1 \ \phi_2 \ \dots \ \phi_n]$  is the  $n \times n$  mode shape matrix calculated by solving an eigenvalue problem, where  $\phi_n$  is  $n \times 1$  mode shape vector of the  $n^{th}$  mode.

Assuming the mode shape matrix,  $\Phi$ , is mass orthogonal [164],  $\phi_i^T \mathbf{M} \phi_j = 0$  for  $i \neq j$ , the stiffness restoring force for the  $i^{th}$  mode can be reconstructed by rearranging Equation (5.1):

$$F_{s,i} = \mathbf{M} \cdot \phi_i \left[ \{\ddot{X}_i^{abs}\} + 2\xi_i \omega_i \{\dot{\bar{X}}_i\} \right] \quad (5.3)$$

where  $F_{s,i}$ ,  $\xi_i$ ,  $\omega_i$  are the stiffness restoring force vector, damping ratio and the natural frequency of the  $i^{th}$  mode,  $\ddot{X}_i^{abs}$  and  $\dot{\bar{X}}_i$  are the absolute modal acceleration and relative modal velocity of the  $i^{th}$  mode, respectively, calculated:

$$\begin{aligned} \ddot{X}^{abs} &= \Phi^{-1} (\ddot{X} + r \cdot \ddot{X}_g) \\ \dot{\bar{X}} &= \Phi^{-1} \dot{X} \end{aligned} \quad (5.4)$$

Equation (5.3) implies the stiffness restoring force of the structure can be constructed for each individual mode providing the mode shape matrix,  $\Phi$ , is known.



## 5.2.2 Mode shape identification

In Section 3.2.1 it has been demonstrated that mode shapes can be identified sequentially for selected time windows using optimization functions, which minimize the sum of weighted cross-correlation of modal frequency response spectra (FRS). This chapter utilizes a slightly simplified concept, which is based on minimization of energy of interfering modes. Spectral energy contribution from interfering modes is calculated using simple shape functions, which extract the spectral energy of selected mode for selected frequency range. The method is explained in detail below.

In Section 2.2.1 it was demonstrated that a sequential mode-by-mode identification is possible, which can be achieved through eliminating the modal response of the selected  $i^{th}$  mode from the modal responses of all other modes per Equation (2.7). One of the easiest ways to quantify the contribution of each mode is by calculating its energy content in the frequency domain. Ideally, other modes would have zero energy if  $\hat{\Phi}$  is perfectly identified as in Equation (2.6). Decomposed parameters can be represented in the frequency domain:

$$\bar{Y}^{abs}(\hat{\Phi}) = |FFT(\bar{\ddot{X}}_{p,m})| = |\bar{\ddot{X}}_{p,m} \cdot W_{FFT}| = |\hat{\Phi}^{-1} \cdot \ddot{X}^{abs} \cdot W_{FFT}| \quad (5.5)$$

where  $\ddot{X}^{abs}$  is the measured absolute acceleration,  $W_{FFT}$  is the Fourier transformation matrix defined  $W_{FFT}(n, k) = W_N^{(n-1)(k-1)}$  where  $W_N = e^{(-2\pi i)/N}$ , ( $n = 1 \dots N$ ),  $N$  is the discrete length of the monitored signal  $X$ , and  $k = 1 \dots K$ , where  $K$  is the number of frequency bins in the analysis, and is a function of  $N$  and sampling rate. Modulus of FFT value is defined:

$$|FFT(\bar{\ddot{X}}_{p,m})| = \sqrt{a^2 + b^2} \quad (5.6)$$

where  $a = Re(FFT(\bar{\ddot{X}}_{p,m}))$  and  $b = Im(FFT(\bar{\ddot{X}}_{p,m}))$  are the real (Re) and imaginary (Im) parts of FFT analysis.

The energy content of the  $j^{th}$  mode can be calculated:

$$E_{mode}^j(\hat{\Phi}(:,j)) = \bar{Y}(\hat{\Phi}(:,j)) \cdot N_{j,mode} = |\hat{\Phi}^{-1} \cdot X \cdot W_{FFT}| \cdot N_{j,mode} \quad (5.7)$$

where  $N_{j,mode}$  is a  $K \times 1$  shape matrix used to segregate a given mode's frequency range to calculate its energy without other modes contributing and can be formulated using any windowing function, as shown in Figure 5.1.

Similarly, the total energy of every modal parameter can be calculated:

$$E_{tot}(\hat{\Phi}(:,j)) = \bar{Y}(\hat{\Phi}(:,j)) \cdot N_{tot} = |\hat{\Phi}^{-1} \cdot X \cdot W_{FFT}| \cdot N_{tot} \quad (5.8)$$

where  $N_{tot}$  is a  $K \times 1$  shape matrix and be considered as vector of ones, selecting all frequencies and thus all modes.

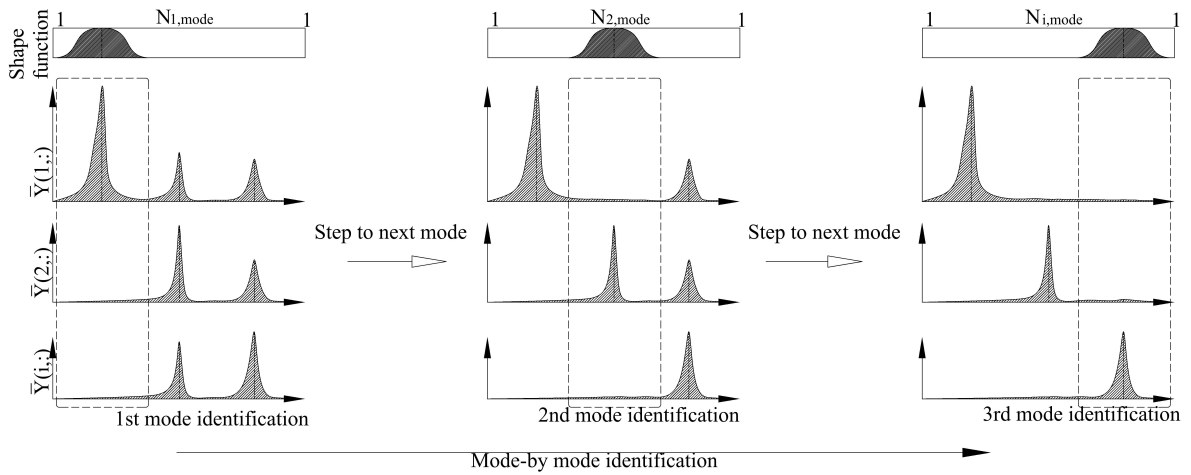


Figure 5.1: Mode-by-mode mode shape identification for a MDOF system

The efficiency of the partial decoupling for mode  $i$  can thus be estimated as the energy of

each interfering mode ( $j = 1 \dots m; i \neq j$ ) divided by the total modal energy:

$$R_j(\hat{\Phi}(:, j)) = \sum_{i=1, i \neq j}^m \left( \frac{E_{mode}^i(\hat{\Phi}(:, j))}{E_{tot}^i(\hat{\Phi}(:, j))} \right)^2 \quad (5.9)$$

This value is equal to zero if the identification of  $\hat{\Phi}$  is perfect and  $\hat{\Phi} = \Phi$ , as in Equation (2.6).

Finally, the solution to the optimal  $j^{th}$  mode shape coefficients can be written as the solution to the following optimization problem:

$$(\hat{\Phi}(:, j)) = \arg \min_{\hat{\Phi}(:, j)} (R_j(\hat{\Phi}(:, j))) \quad (5.10)$$

Once the optimal approximated mode shape coefficients  $\hat{\Phi}^k(:, j)$  for mode  $i$  are found, the optimization can proceed for the next mode, as shown in Figure 5.1. The optimization problem can be readily solved using the constrained non-linear multivariable solver available in MATLAB. A more detailed mode identification routine is shown in the flow chart in Figure 3.3.

This mode shape optimization process can be carried out for the whole record or any selected time window. In this study, an 8 second window is selected to track evolution of mode shapes throughout the response window. The mode optimization problem, as carried out for any given time segment, can be rewritten using Equation (5.10):

$$(\hat{\Phi}^k(:, j)) = \arg \min_{\hat{\Phi}^k(:, j)} (R_j(\hat{\Phi}^k(:, j))) \quad (5.11)$$

where  $\hat{\Phi}^k(:, j)$  are the approximated mode shape coefficients for mode  $j$  for the  $k^{th}$  time window. A time varying mode shape evolution,  $\hat{\Phi}^t$ , between the optimized time windows can be estimated by applying a piecewise  $C^1$  continuous cubic interpolation.

The method is based on mode decomposition, meaning a linear system behaviour is assumed for the analysed time window. Although most of concrete structures exhibit a non-linear behaviour under a strong ground motion event, the non-linear response usually comprises very

short time segment of the total response. Thus, majority of the time the structure will respond within almost linear or entirely linear range, which means that the method will be able to provide good mode shape approximations for most of the time windows. The approximated mode shapes are used to separate the modes and reconstruct single mode dominant hysteresis loops for HLA, thus any mode shape approximation errors associated to non-linear behaviour and signal noise can still be accepted, as the provided method aims to make the HLA more robust.

### **5.3 Method validation using experimental structure**

The proposed mode decomposition method is validated using experimental dynamic test data from a full scale bridge pier test available on the NEES archive [186]. The structure was subjected to the 9 strong uni-directional ground motions listed in Table 5.1, resulting in nonlinear response due to plastic hinge formation. White-noise excitations with root-mean-square acceleration of 3% g were run before each strong motion test. Stiffness and strength degradation were observed, caused by concrete spalling, concrete crushing, longitudinal bar buckling or fracturing.

The bridge pier consists of a cantilever column, footing and lumped mass, which provided a target axial load and dynamic load necessary to bring the structure into a non-linear response. The bridge pier was designed to current Caltrans design guidelines, with basic dimensions shown in Figure 5.2. Reinforced concrete column of 1.22m diameter consists of 18 equally spaced 35.8mm diameter longitudinal steel bars with a yield strength of 518.5MPa. The shear strength is provided by 16mm double hoop reinforcement with 152mm center to center spacing. The specified concrete strength is 27.6MPa. The estimated translational mass of the concrete blocks is 2.32MN and the rotational mass moment of the concrete blocks around its centre of mass is 10.7MNm<sup>2</sup>. The estimated flexural yield capacity was 5800kNm at 1.2% drift ratio, where the cracking moment is estimated to be 840kNm. The lumped mass consists of five cast-in-place concrete blocks, post-tensioned together to ensure a rigid body behaviour. The central block is mounted and anchored to top of the column ensuring a moment resisting connection.

The center of mass of all concrete blocks matches with the top of the column. The concrete column is anchored to the concrete footing through the moment-resisting connection, reinforced using 35.8mm grade 60 steel bars. Full details on the test structure can be found in [165].

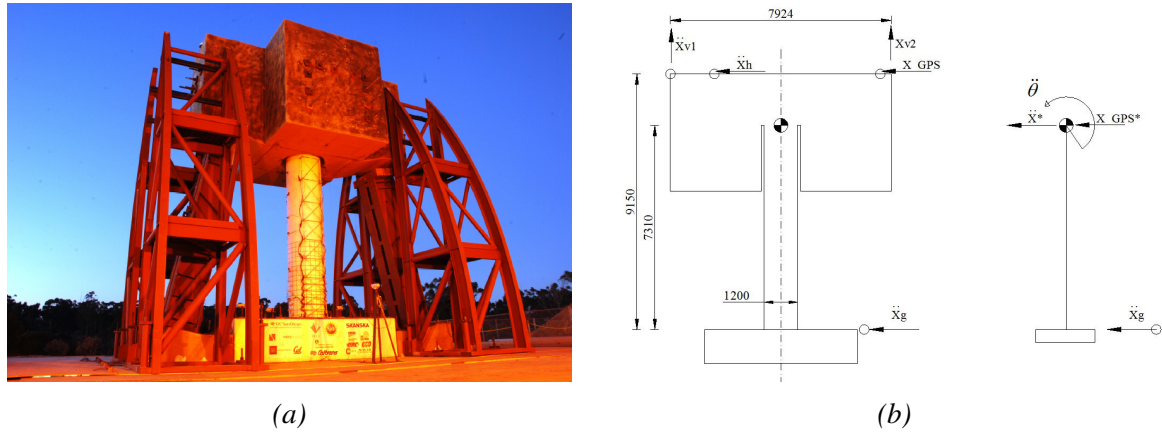


Figure 5.2: a) Bridge pier on the shake table [165]; and b) sensor location with basic dimensions

The bridge pier was instrumented with a large number of accelerometers with a sampling rate of 240Hz. However, this study relies on five sensor measurements: 1) accelerometer mounted to the foot of the bridge measuring the horizontal ground excitation; 2,3,4) three accelerometers mounted to the top edge of the superstructure measuring the horizontal and vertical response of the structure; and 5) a GPS displacement on the superstructure sampled at 50Hz. The vertical acceleration is transformed into an angular acceleration by dividing the accelerometer readings by the horizontal distance between sensors, yielding the modeled DOF in Figure 5.2.

Table 5.1: Input ground motions to test structure

Test	Earthquake	Station	Component	PGA(g)
EQ1	Loma Prieta	Agnew State Hospital	90.00	-0.20
EQ2	Loma Prieta	Corralitos	90.00	0.41
EQ3	Loma Prieta	LGPC	0.00	0.53
EQ4	Loma Prieta	Corralitos	90.00	0.45
EQ5	Kobe	Takatori	0.00	-0.53
EQ6	Loma Prieta	LGPC	0.00	-0.51
EQ7	Kobe	Takatori	0.00	0.65
EQ8	Kobe	Takatori	0.00	-0.83
EQ9	Kobe	Takatori	0.00	0.82

### 5.3.1 Analyses

Test results show the structural response is dominated by the first mode [165]. However, the presence of a very high rotational mass results in significant contribution of the second mode. As a result, the structure can be considered a 2DOF system, as in Figure 5.2. The relative horizontal acceleration is calculated as a difference between measured absolute horizontal acceleration at point X and ground excitation. The angular acceleration is calculated by dividing the vertical acceleration by the horizontal distance between sensor location and the centre of mass of the superstructure. The velocities are obtained by integrating acceleration and applying a low-pass filter to remove drift. Horizontal displacement is calculated by double integrating acceleration and fusing it with GPS data using a Kalman filtering technique [56, 147, 187, 188]. The displacement data from GPS is refined by applying cubic spline interpolation to match the sampling rate of accelerometer data. Mode shape identification is carried out only for the first two modes ( $i=1,2$ ). Mode shape evolution is carried out for each test using an 8 second Hanning window, tracking evolution in 8 second blocks. Hanning windowing technique is chosen due its performance to reduce spectral leakage associated to signal discontinuities. Mode shape evolution between the windows is obtained by applying a cubic interpolation. The identified mode shapes are used for mode separation, damping identification and reconstruction of hysteresis loops. Smoothed evolution of mode shape coefficients is obtained using a 50 sample moving window. Hysteresis loops of base moment against relative displacement are reconstructed for the first mode to demonstrate the effectiveness of the mode decomposition. To calculate the base bending moment for the  $i^{th}$  mode, Equation (5.3) is rearranged and put into incremental form to take into account the variation of the mode shape matrix,  $\hat{\Phi}^t$ :

$$M_{i,base}(t) = M_{i,base}(t-1) + \begin{bmatrix} 7.3 & 1 \end{bmatrix} \cdot M \cdot \hat{\Phi}^t(:,i) \cdot \left[ \Delta \ddot{X}_{i,abs}(t) + 2\xi_i \omega_i \cdot \Delta \dot{X}_i(t) \right] \quad (5.12)$$

$$\Delta \ddot{X}_{i,abs}(t) = (\hat{\Phi}^t)^{-1} \cdot [\Delta \ddot{X}(t) + r \cdot \Delta \ddot{X}_g(t)]$$

where the mass matrix is  $M = \begin{bmatrix} 2.36\text{kg} & 0;0 & 10.9\text{kg/m}^2 \end{bmatrix} \cdot 10^5$ , the excitation influence vector is  $r = \begin{bmatrix} 1 & 0 \end{bmatrix}^T$ . The equivalent damping ratio of the first mode,  $\xi_{i=1}$ , is determined from

the force-displacement relation. The area enclosed by this hysteresis loop is equated to the dissipated energy. As a result, the equivalent viscous damping,  $\xi_{eq}$ , can be determined [164]:

$$\xi_{eq} = \frac{1}{2\pi} \cdot \frac{E_d}{E_{s0}} \quad (5.13)$$

where  $E_{s0}$  is the maximum strain energy in each half-cycle and  $E_d$  is the energy dissipated during each half-cycle. To disregard energy dissipated by yielding and concrete cracking, only small hysteresis loops were considered in identifying damping, comprising only hysteresis loops where the maximum restoring force is less than 80% of yielding force. This choice excludes loops, where energy is dissipated by structural hysteresis/ yielding.

The average natural frequency  $\omega_{i=1}$  is selected for each test separately, since it varies as the structure degrades from test to test. Modal velocity increment,  $\Delta\dot{\bar{X}}$ , is calculated by integrating the modal acceleration increment,  $\Delta\ddot{\bar{X}}$ .

The reconstructed hysteresis loops are compared with a backbone curve, representing the stiffness of a fully cracked structure, defined for cantilever structures 8 [189]:

$$k_{cracked} = \frac{3EI_{cracked}}{L^3} \quad (5.14)$$

where  $E = 22.9\text{GPa}$  is the measured modulus of elasticity for concrete,  $I_{cracked} = \alpha I_0$  and  $I_0$  is the section modulus of undamaged cross-section, and  $\alpha = 0.3$  is the stiffness reduction coefficient for concrete columns with an axial load ratio of less than 0.1 recommended by ASCE 41. The estimated flexural stiffness of the cracked column is  $k_{cracked} = 6.6\text{MN/m}$ .

Finally, the evolution of the elastic stiffness is identified using regression analysis and the hysteresis loop analysis (HLA) method of [147]. Reconstructed single mode dominant stiffness restoring force loops represent structure's external force-deformation relationship, which varies with time due to structural degradation and and/or damage during strong motion events. In HLA method, the restoring force loops are subdivided into path dependent loading and un-

loading half-cycles, which are then assumed to be piecewise linear. F type hypothesis testing is applied to identify the number of piecewise segments that represent an approximated hysteretic model. Finally, overall least squares linear regression analysis is carried out to selected sub-half cycles to identify regression coefficients, which represent elastic stiffness, plastic stiffness and cumulative plastic deformation. In this study elastic stiffness evolution is presented as measure of damage severity. In the presence of any structural damage occurring during the monitored time period, the changes will be captured by degradation of elastic stiffness, which is presented in the form of elastic stiffness evolution. The elastic stiffness is identified for each direction (positive and negative  $x$  direction) for each half-cycle of response, since the extent of the damage on each side of the structure varies from test to test. The smoothed evolution of the average elastic stiffness presented in the results is obtained using a 10 sample moving window.

## **5.4 Results and discussion**

The following section presents validation results carried out for the presented test structure. Section 5.4.1 provides single mode dominant reconstructed hysteresis loops, which directly illustrate the effectiveness of the presented mode filtering method. Section 5.4.2 presents HLA results on reconstructed single mode dominant hysteresis loop in form of elastic stiffness evolution. Section 5.4.3 discusses mode shape identification results, which allows for mode decomposition and reconstruction of single mode dominant hysteresis loops for the analysed structure. Section 5.4.4 summarizes all the results and limitations are discussed in Section 5.4.5.

### **5.4.1 Reconstructed hysteresis loops for Tests 1 to 9**

The reconstructed hysteresis loops for white noise and earthquake excitation tests are presented in Figure 5.3. Each white noise test was done immediately prior to the corresponding number earthquake. The red line represents the theoretical backbone curve and can be used as a reference stiffness of undamaged structure. The grey solid line represents the hysteresis loops history that was obtained in the previous tests and can be used to track the test-to-test stiffness changes.



It is clear, the mode decomposition method enables reconstruction of smooth hysteresis loops for the first mode that can be readily used for primary inspection and damage identification. Analysis based on visual analysis of these hysteresis loops indicates a significant loss of elastic stiffness after Tests 1, 2 and 3. Stiffness degradation observed after Tests 1 and 2 can be related to concrete cracking and crack opening, and, from comparison with the backbone curve, it can be concluded that the structure is fully cracked. Stiffness degradation observed after Test 3 can be related to severe yielding and concrete cracking, as reported in the initial study [165].

Abrupt changes in restoring force can be observed during Tests 8 and 9. These changes can be attributed to the fracturing of longitudinal reinforcing bars. This outcome is also reported in [165].

#### 5.4.2 Hysteresis loop analysis

The HLA SHM of the hysteresis loops shown in Figure 5.5 provides an informative evolution of the elastic stiffness of the first, dominant mode. The elastic stiffness values identified at the start of the test,  $k_{start}$ , and at the end of the test,  $k_{end}$ , are presented in Table 5.2. The elastic stiffness is identified for positive,  $k_{el,pos}$  (red crosses), and negative,  $k_{el,neg}$  (blue circles),  $x$  direction, to demonstrate the level of damage in each direction. The identified positive and negative elastic stiffness values are almost identical till the onset of the Test 2 (EQ2), with the difference increasing during the test, indicating the different level of damage in each direction.

The identified average elastic stiffness,  $k_{el,avg}$ , clearly indicates a significant loss of stiffness after Tests 1, 2, 3, 5 and 8, also seen as  $k_{start}$  and  $k_{end}$  values in Table 5.2. The identified initial stiffness at the first white noise test (WN1),  $k_{start} = 12.1\text{MN/m}$  (from Table 5.2), is nearly twice as large as the estimated cracked flexural stiffness of cantilever column  $k_{cracked} = 6.6\text{MN/m}$ , shown as a red dashed line in Figure 5.4, which indicates that the structure has no or very minor cracks. Identified elastic stiffness degradation ( $\Delta k = -16.5\%$  from Table 5.2) observed during first white noise test (WN1),  $k_{end} = 10.1\text{MN/m}$ , is not surprising, since the maximum base moment reached during excitation ( $2.25\text{MNm}$ ) is well above the rated cracking moment

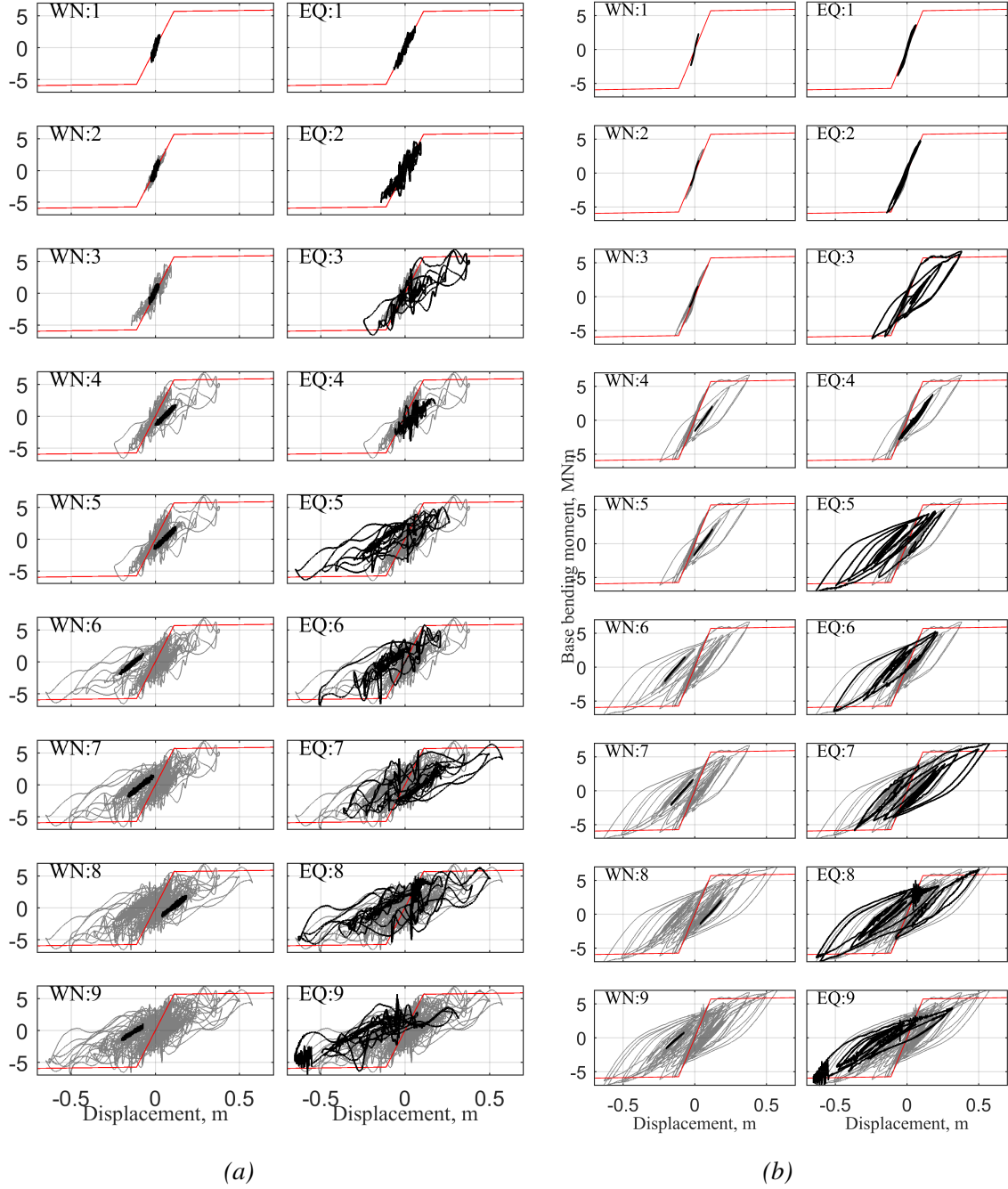


Figure 5.3: Base moment versus displacement loops reconstructed from white noise (WN) and earthquake (EQ) excitation tests 1-9 using a) raw acceleration data; and b) mode decomposed data

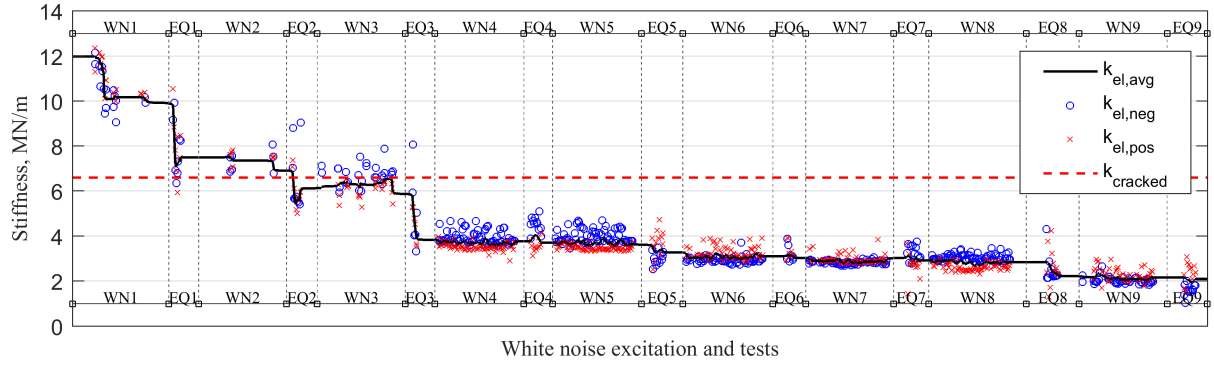


Figure 5.4: The overall evolution of the elastic stiffness from Test 1 to Test 9 (WN – white noise, EQ–earthquake excitation)

(0.84MNm). Based on visual analysis of hysteresis loops shown in Figure 5.3, loss of stiffness observed after Tests 1 and 2 ( $\Delta k = -27\%$  and  $\Delta k = -17.3\%$  respectively) can mainly be attributed to tensile concrete cracking. Stiffness degradation observed during Tests 7 and 8 ( $\Delta k = -19.2\%$  and  $\Delta k = -21.8\%$ ) can be associated to severe yielding, which resulted in concrete spalling and fracture of tensile longitudinal reinforcement, also seen as a sudden drop in restoring force during Test EQ8 in Figure 5.3. The elastic stiffness inconsistencies observed between the tests defined as the difference between the identified final stiffness,  $k_{end}$ , of one event and the identified stiffness at the start of the next event,  $k_{start}$ , are small, within 6%, and can be attributed to identification error due to noise or/and small changes.

Table 5.2: Summary of elastic stiffness evolution before and after the tests

Test	$k_{start}$	$k_{end}$	$\Delta k(\%)$	Test	$k_{start}$	$k_{end}$	$\Delta k(\%)$
WN1	12.1	10.1	-16.5	EQ1	10.4	7.6	-27.0
WN2	7.3	7.4	1.9	EQ2	7.1	5.9	-17.3
WN3	6.5	6.2	-4.8	EQ3	5.8	3.8	-33.4
WN4	3.7	3.8	0.4	EQ4	4.0	4.0	0.1
WN5	3.7	3.7	0.7	EQ5	3.6	3.4	-5.4
WN6	3.1	3.1	-0.9	EQ6	3.1	3.1	-2.3
WN7	2.9	2.8	-2.4	EQ7	3.5	2.8	-19.2
WN8	3.0	2.9	-2.9	EQ8	2.9	2.3	-21.8
WN9	2.1	2.1	2.1	EQ9	1.8	2.1	19.6

### 5.4.3 Modal parameter identification

Mode decomposition is performed using a time-varying identified, approximate mode shape matrix,  $\hat{\Phi}^k$ , as per Equation 5.11. The mode shape coefficients were identified for each 8 second time-window over each event. The mode shape coefficients are normalized, so that  $\hat{\Phi}^k(1,1) = \hat{\Phi}^k(1,2) = 1$ , and thus these two values do not change. All evolution is thus seen in the values for  $\hat{\Phi}^k(2,1)$  and  $\hat{\Phi}^k(2,2)$ . The smoothed mode shape evolution shown in Figure 5.4 indicates stiffness degradation during Tests 2, 3 5 and 9, which matches the HLA results presented in Table 5.2 and Figure 5.4. However, the stiffness degradation observed during white noise excitation before Test 1 (WN1) and during Test 1 in HLA analysis, as shown in Figure 5.3 and Table 5.2, did not affect the mode shapes. This difference can be explained by the low sensitivity of mode shape factors to the actual damage experienced [190].

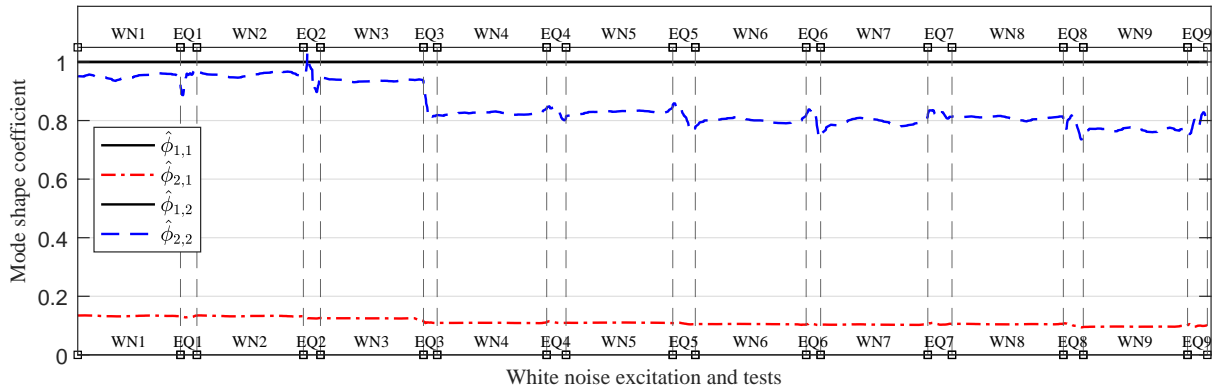


Figure 5.5: The overall mode shape evolution from Test 1 to Test 9 for  $\hat{\Phi}(2,1)$  and  $\hat{\Phi}(1,2)$ , where  $\hat{\Phi}(1,1) = \hat{\Phi}(2,2) = 1$  due to normalization

Identified modal frequencies and equivalent damping ratios for two dominant modes are shown in Figure 5.6. Modal damping ratios are identified using curve fit method per Equation (2.20), for the white noise excitation response data, segmented into 60s long windows with 75% overlap. For the earthquake response data, where frequency variation and degradation is anticipated throughout relatively short time window, the modal damping for the first mode is estimated for the whole record from force-displacement relation using Equation 5.13 and denoted as  $\xi_1(hyst)$  in Figure 5.6. Modal frequency evolution is identified using curve fit method for response data segmented into 8s windows.

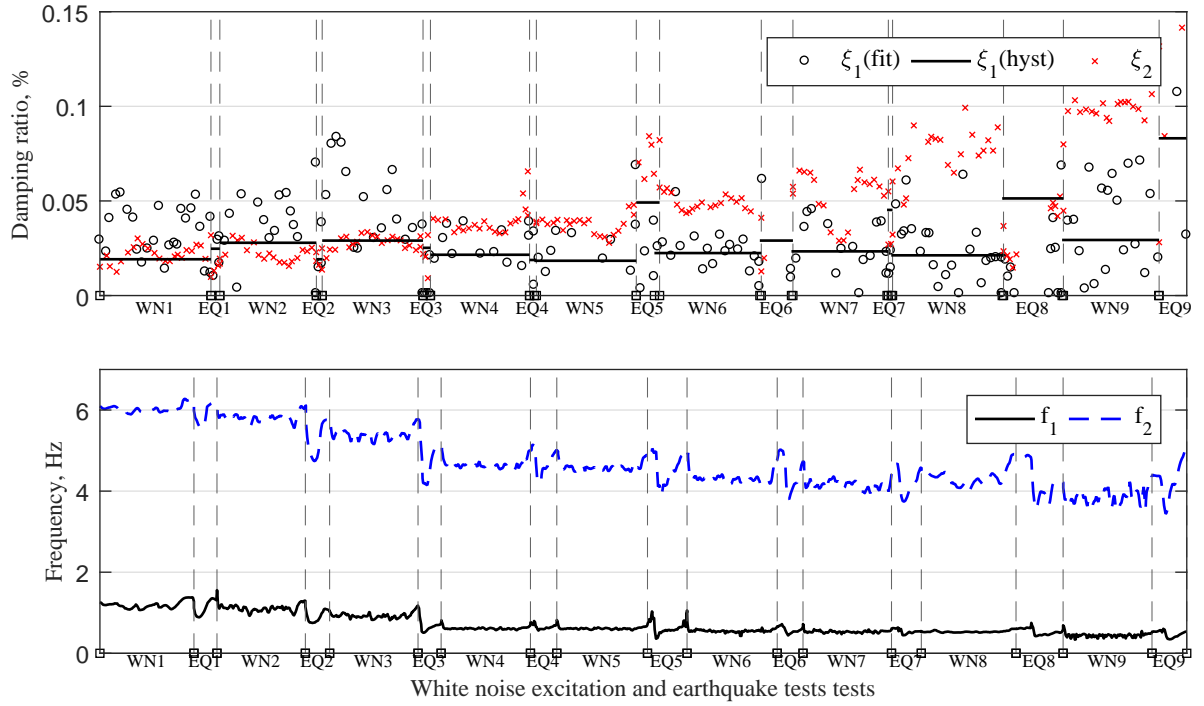


Figure 5.6: Identified modal damping ratios and frequencies for two dominant modes

The identified modal damping ratios for the first mode using curve fit method,  $\xi_1(\text{fit})$ , demonstrate a significant variability, which could be associated to varying frequency and response intensity throughout analyzed time window and/or identification error. Average damping identified for the first mode using force-displacement relation,  $\xi_1(\text{hyst})$  demonstrates relatively good consistence between the tests. Notoriously higher damping can be seen for tests EQ8 and EQ9. The identified damping ratios for the second mode,  $\xi_2(\text{fit})$ , demonstrate a lower scatter. In addition, a significant increase in damping can be observed,  $\xi_2 = 2\%$  to  $10\%$ , as the damage progresses. The identified modal frequencies demonstrate degradation with increasing damage.

#### 5.4.4 Overall damage identification

In this study, a new modal parameter identification technique is proposed. The method is initially developed for mode decomposition. This approach enables reconstruction of smooth/single mode dominant restoring force- displacement loops.

Mode shape evolution, shown in Figure 5.4, can be readily used for SHM. The evolution clearly indicates structural changes after Tests 2, 3, 5 and 9. Although the changes in mode shape evolution are clear, it does not provide the key physical parameters for estimation of damage severity, or, in some cases, the location of the damage [190]. In this study, reconstruction of the resulting mode-decomposed hysteresis loops and subsequent hysteresis loops analysis (HLA) is proposed, which, in combination, enables estimation of damage severity and location.

Hysteresis loops, as shown in Figure 5.3, reconstructed using mode decomposed data are clearly more informative in terms of damage type and severity. The damage severity is quantified by carrying out HLA for the reconstructed hysteresis loops to identify the degradation of the elastic stiffness. Elastic stiffness evolution, as shown in Figure 5.3, clearly demonstrates degradation, which is caused by the tensile concrete cracking (Tests 1 and 2) and severe inelastic behaviour (Tests 3 and 5). The elastic stiffness degradation observed during Test 8, is likely caused by the fracture of the tensile longitudinal reinforcement and, can be seen in the sudden drop in restoring force in Figure 5.3.

Overall, the mode shape evolution, shown in Figure 5.5 matches well with the elastic stiffness evolution of Figure 5.4 for all tests, except for Test 1. However, the elastic stiffness evolution obtained from HLA together with the reconstructed hysteresis loops in Figure 5.3, allows for better identification of the type of damage and its severity.

#### **5.4.5 Limitation and other aspects**

Mode shape identification, as presented in this study, is based on the principle of mode decoupling, which theoretically can only be used for linear structures. However, in this study, mode shape approximation is carried out for a structure exhibiting a significant non-linearity. For this reason the structural response and identification are analysed in relatively short overlapping time windows, in which a linear structure is assumed. Any non-linearity occurring during the

selected time window may result in large errors, as the approximated mode shapes simply represent the best mode decoupling for the analysed time window. However, in most of the cases the non-linear response will typically comprise a very short window of the total structure's response, hence for majority of the analysed time windows the structure will exhibit almost linear or entirely linear behaviour. Hence, the proposed method will be able to provide good mode shape approximations for most of the time windows, which will result in mode shape evolution.

The method has also limitations in case of high signal noise content, which results in poor signal-to-noise ratio. The method is designed to remove the energy content from the interfering modes through optimization process presented. Hence in case of high noise content, the optimization may result in a false global minima, consequently providing inaccurate mode shape coefficients. Thus, effective mode decoupling cannot be possible due to non-zero values in Equation (2.6).

Overall, poor mode decoupling causes mode interference in time domain, or spectral leakage in frequency domain due to non-zero values in Equation (2.6). Although spectral leakage of the low modes might seem to be small for acceleration data, significantly larger leakages can be observed for velocity and displacement data if single and double integrations are applied respectively to the decoupled acceleration data. This implies that in case of highly non-linear structural behaviour and/or poor mode decoupling, displacement reconstruction might result in significant errors. However, in this study the double integrated displacement is fused with GPS data using Kalman filtering technique, which allows for accurate reconstruction of displacement, which has been demonstrated by [56, 147, 187, 188].

The presented mode approximation method is limited to structures in which the principal mode frequencies do not significantly overlap. If modes are so closely spaced that frequency range segregation in Equation (5.1) becomes impossible, the method can break down. However, many structures of interest do not have such closely spaced modal frequencies.

The proposed mode approximation technique is primarily used to decouple/remove the unwanted higher modes, which allows for reconstruction of single mode dominant restoring force-displacement loops. Mode shape approximation errors associated with above mentioned non-linear behaviour, signal noise or any other method assumptions will typically result in incomplete mode decoupling, which can, based on results, still be well tolerated.

Finally, the proposed mode shape approximation method has been validated for a single test structure, which may appear rather simple. Thus, the proposed method needs to be verified for more complex MDOF structures exhibiting non-linearities and stiffness degradation, which will be the future study.

## **5.5 Summary**

This study develops an adaptive time-varying modal filtering technique to separate vibration modes for linear and non-linear data. The overall approach tracks relevant mode shapes over time by re-evaluating mode shape matrices in relatively short time windows. Identification of mode shape evolution allows for mode separation and reconstruction of “smooth” hysteresis loops for dominant modes of response. In turn, these filtered modes and resulting filtered hysteresis loops can be readily used for visual inspection and hysteresis loops analysis (HLA).

The developed method is validated using experimental dynamic test data from full scale bridge pier tests. The results show that mode decomposition allows for reconstruction of smooth hysteresis loops for the first mode that can be readily used for primary inspection and damage identification using HLA methods. The HLA method, in turn, clearly indicates the degradation of elastic stiffness, which can be used for further SHM. The identified mode shape evolution also indicates abrupt structural changes during the tests and match with most observations from HLA, however, in some cases, the mode shape evolution appeared to be less sensitive to damage compared HLA.



Finally, the overall method can be readily generalized to a range of more complex MDOF structures, as it does not depend on a specific structure and provides a method of continuous and rapid SHM.

## CHAPTER 6

---

### Modal parameter identification for a 5-story full scale test structure

---

#### 6.1 Introduction

The novel input-output modal parameter identification technique was introduced and validated using simulated response data of different complexity non-linear FE models in Chapters 3 and 4. Chapter 5 presented modal identification results of a simple full-scale bridge pier test structure exhibiting notable contribution from at least two modes. The results demonstrated the proposed method is efficient in tracking modal parameters of structures exhibiting significant non-linearities which can be used to detect damage.

In this chapter, the novel modal parameter identification technique is applied to a more complex full-scale 5-story reinforced concrete test structure, which has significant contribution from multiple higher modes. The experimental MDOF structure was tested and identified for two structural configurations: 1) base isolated (BI); and 2) fixed based (FB). The test structure was subjected to a number of different intensity white noise, pulse, and earthquake ground inputs. Time-varying mode shapes, frequencies and damping ratios are approximated using input-output modal parameter identification presented in Chapter 3. The identified modal parameter evolution can subsequently be used to detect abnormalities caused by the structural damage.

## **6.2 Method**

Modal parameter identification for experimental test structure in this chapter is implemented using the same input-output methodology as presented in Chapter 3. Hence, for references and methodology details please refer to Chapter 3.

## **6.3 Method validation and analyses**

### **6.3.1 Test structure**

The proposed modal parameter approximation is validated using experimental dynamic test data from a full-scale 5-story reinforced cast-in-situ concrete building, shown in Figure 6.1, which was constructed on the shake table at the University of California, San Diego [179]. The building was outfitted with a large range of non-structural components and systems, such as a passenger elevator, stairs, full architectural façade and interior partitions, plumbing, heating, ventilation and air-conditioning and etc. The experiments were carried out for two building configurations: 1) base isolated (BI) building equipped with four lead-rubber bearings located at each corner; and 2) fixed base (FB) building. The BI building was subjected to 7 increasing intensity uniaxial earthquake inputs listed in Table 6.1 and the FB building to 6 events listed in Table 6.2. The structure was also subjected to different intensity white-noise excitations before and after each strong motion test. The superstructure was designed to meet a performance target of 2.5% maximum inter-story drift ratio with a maximum peak floor acceleration of 0.8g.

The full-scale building has a plan dimensions of 11m by 8.1m and is 22.9m high, as shown in Figure 6.2. The moment resisting frame consists of two bays (frame and gravity) in the shaking direction and one bay in the transverse direction. The frame bay consists of moment resisting beams on each floor with equivalent moment capacities, but different detailing, where the gravity bay comprises a 200mm thick concrete slab. Lateral stiffness is ensured by two con-

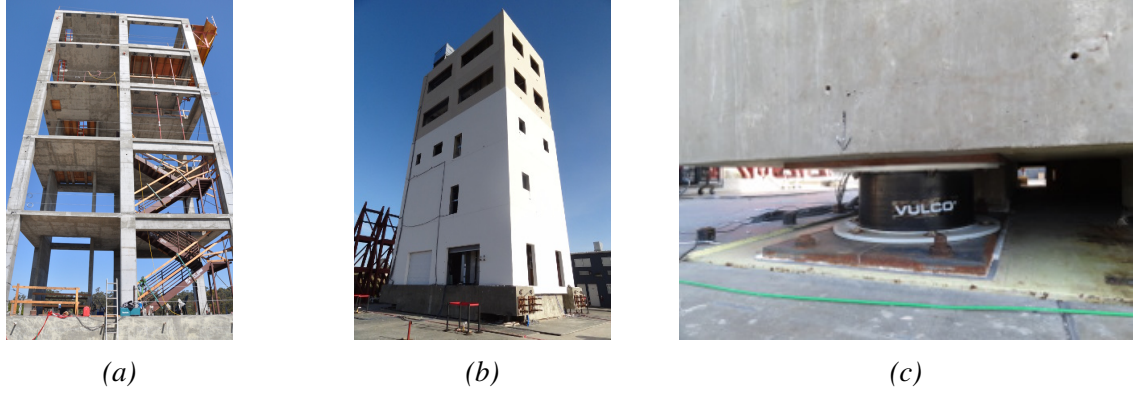


Figure 6.1: a) Bare structural frame before installation of non-structural components b) Building equipped with the facade c) Base isolator detail. Pictures taken from [191]

crete transverse shear walls located on both sides of the elevator shaft. Steel bracing is added on the other side of the building to prevent the structure from excessive torsional motion. The superstructure is erected on a stiff foundation, designed to accommodate both the BI and FB testing configurations.

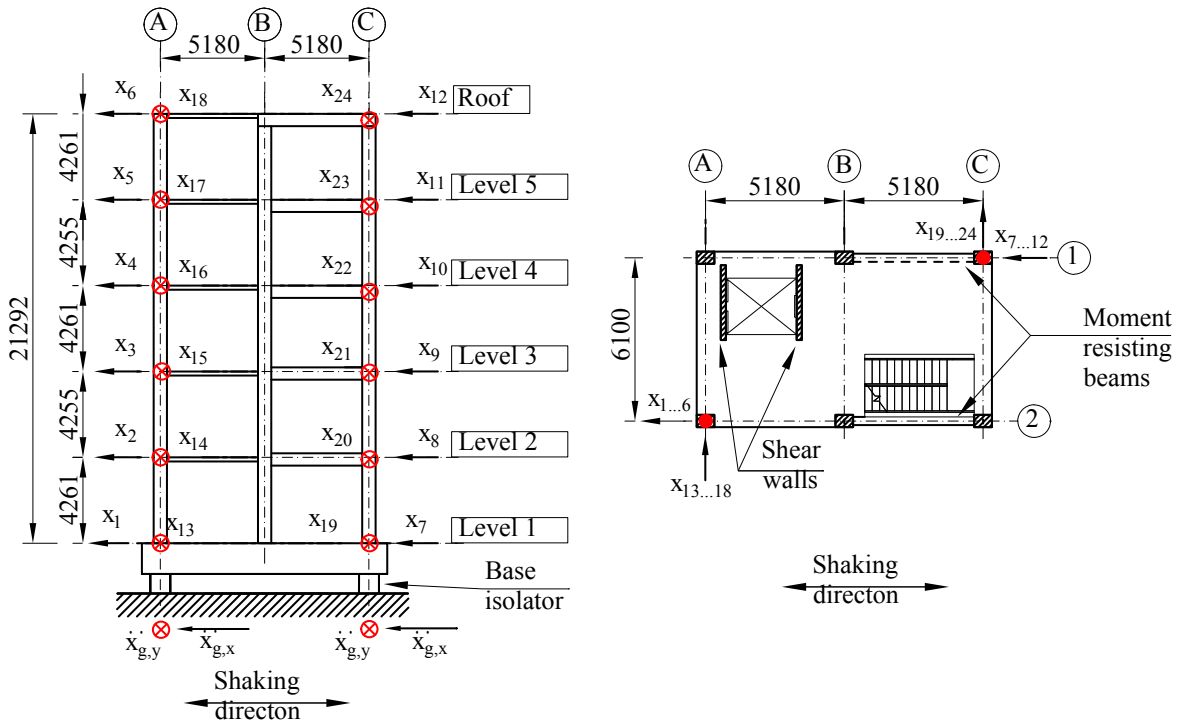


Figure 6.2: Front and plan views of the 5 storey concrete structure and accelerometer spatial arrangement

The main load carrying frame is instrumented with a large number of triaxial accelerometers placed on each corner of all the floors. The shake table is equipped to two triaxial accelerometers

placed on the opposite corners. In this study, two accelerometers placed on the opposite corners of each floor are used for identification of the modal parameters. The accelerometer data is sampled at 200Hz.

*Table 6.1: Input ground motions for the base isolated test structure*

Test	Ground motion name	PGA(g)
WN1	WN test*	-
EQ1	Northridge 1994	0.21
WN2	WN test*	-
EQ2	Northridge 1994	0.22
WN3	WN test*	-
EQ3	Northridge 1994	0.25
WN4	WN test*	-
EQ4	2010 Maule (Chile)	0.52
WN5	WN test*	-
EQ5	2007 Pisco (Peru)	0.17
WN6	WN test*	-
EQ6	2007 Pisco (Peru)	0.32
WN7	WN test*	-
EQ7	2007 Pisco (Peru)	0.50
WN8	WN test*	-

*Table 6.2: Input ground motions for the fixed base test structure*

Test	Ground motion	PGA(g)
WN1	WN test*	-
EQ1	Northridge 1994	0.21
WN2	Double pulse	-
EQ2	Northridge 1994	0.18
WN3	Double pulse	-
EQ3	2007 Pisco (Peru)	0.21
WN4	Double pulse	-
EQ4	2007 Pisco (Peru)	0.26
WN5	WN test 2**	-
EQ5	2002 Denali	0.64
WN5	WN test 2**	-
EQ6	2002 Denali	0.80

\* WN test represents the following set of increasing intensity white noise excitations: 6min WN(1.5%g RMS) + 6min WN(3.0%g RMS)+6min WN(3.5%g RMS)

\*\* WN test 2 represents the following set of increasing intensity white noise excitations: 6min WN(1.5%g RMS) + 4min WN(3.0%g RMS)

### 6.3.2 Analyses

Modal parameter identification is carried out for both (BI and FB) building configurations. First, the initial modal parameter identification is carried out using ambient and white noise excitation data collected from accelerometers. Second, the strong ground motion response data is segmented into relatively short time windows. Third, the mode re-evaluation of Equation (3.5) is carried out for each segmented time window for the selected dominant modes determined in the initial modal analysis.

Absolute floor acceleration data at two opposite corners from each floor results in a total of 24 DOFs for the BI structure, as shown in Figure 6.2. Mode shape coefficients for the other two corners are estimated assuming rigid floor motion and are used only for visual mode

shape representation. For the FB structure 4 DOF's ( $x_1, x_7, x_{13}, x_{19}$ ) located at the base of the structure (Level 1) are omitted, as shown in Figure 6.2. Input excitation data is taken from the accelerometer located in the shake table for the BI structure and from DOF's  $x_1$  and  $x_{17}$  for the FB structure. All accelerometer data is detrended, windowed to remove non-zero end values and finally filtered using high-pass 2<sup>nd</sup> order Butterworth filter with cut-off frequency of 0.1Hz.

Finally, for modal analysis, a diagonal  $24 \times 24$  lumped mass matrix is used:

$$M = \text{diag} \left( \left[ \frac{M_{floor}}{2} \quad \frac{M_{floor}}{2} \quad \frac{M_{floor}}{2} \quad \frac{M_{floor}}{2} \right] \right) \quad (6.1)$$

where  $M_{floor} = \begin{bmatrix} 0.21 & 0.74 & 0.77 & 1.00 & 1.08 & 0.71 \end{bmatrix} \text{kg} \cdot 1e^5$  is the floor mass starting from the ground floor. For the FB building configuration the floor matrix,  $M_{floor}$ , is reduced to a  $1 \times 5$  matrix by disregarding the ground floor mass.

### **Initial modal parameter identification**

Initial modal parameter identification for the BI building configuration is implemented using a 30 seconds long ambient vibration data, recorded before the start of the test protocol. Initial modal parameter identification of the FB building configuration is carried out using the first white noise excitation. This latter test comprises initial short duration very low amplitude white noise excitation, followed by two pulse excitations and three 6 minute white noise excitations of different intensity, as shown in Table 6.2. Modal parameters are identified using the first 40 seconds of low amplitude white noise excitation (0.05%g RMS), before the pulse excitation is initiated.

### **Data segmentation into time windows and identification of modal parameter evolution**

Modal parameter (mode shape, frequency and damping) evolution is obtained by carrying out an identification for all of the segmented response data. In the following, the time window is

denoted by  $t_0$  and  $t_1$ , which represents the start and the end time of the monitored response segment.

Mode shape and frequency evolution is captured using two different window lengths. Low intensity  $\ddot{X}^{abs}(t_0 : t_1) < 0.1\text{m/s}^2$  ambient vibrations and white noise excitation data is segmented using  $t_1 - t_0 = 60$  seconds windows with 50% overlap, because it is not expected to capture any abrupt changes in modal parameters for these low intensity tests. High intensity vibrations  $\ddot{X}^{abs}(t_0 : t_1) > 0.1\text{m/s}^2$  are divided into  $t_1 - t_0 = 10$  seconds windows with 75% overlap, which will capture gradual changes in modal frequency and relevant mode shapes caused by non-linear mechanical system behavior or stiffness degradation. The selected response segments are windowed using Hanning windows, to remove input non-stationarity and alleviate spectral leakage effects [192].

Mode shape evolution for the selected dominant modes is obtained by carrying out a mode-by-mode optimization using Equation (3.5) for each segmented window. To alleviate signal noise effects, the correlation factors are calculated per Equation (3.7) using unnormalized FRS,  $Y^{abs}$  and  $Y^{rel}$ , which adds more weight on strong modes. The optimized mode shape coefficients are updated for each window based on total reduction in total cross-correlation:

$$\hat{\Phi}^k(:, i) = \hat{\Phi}^{k-1}(:, i) + \left( \hat{\Phi}^{opt}(:, i) - \hat{\Phi}^{k-1}(:, i) \right) \cdot \left( \frac{\Delta Corr}{Corr^{iso, i}(\hat{\Phi}^{opt})} \right)^{0.5} \quad (6.2)$$

$$\Delta Corr = Corr^{iso, i}(\hat{\Phi}^{k-1}) - Corr^{iso, i}(\hat{\Phi}^{opt})$$

where  $k$  is the window segment number, thus  $\hat{\Phi}^{opt}(:, i)$  are the optimized  $i^{th}$  mode shape coefficients for the  $k^{th}$  time window obtained using Equation (3.5),  $Corr^{iso, i}(\hat{\Phi}^{opt}(:, i))$  is the total cross-correlation coefficient based on the optimized mode shape coefficient  $\hat{\Phi}^{opt}(:, i)$ , and finally  $Corr^{iso, i}(\hat{\Phi}^{k-1}(:, i))$  is the total cross-correlation coefficient based on the updated mode shape coefficients for the previous time window,  $k - 1$ .

Modal frequency and damping evolution is obtained by identifying the selected modes for

each segmented window using the curve fit method in Equation (2.20). Equivalent modal damping ratios are identified using only ambient vibration and white noise excitation data. Strong ground motion response data is not used due to normally highly varying modal frequency within relatively short time windows. Modal damping is estimated based on  $t_1 - t_0 = 60$  seconds long response data. Data segmentation parameters are summarized in Table 6.3.

*Table 6.3: Data segmentation summary*

	Excitation intensity	Mode shape id	Frequency id	Damping id
Window	$ \ddot{X}(t_0 : t_1)  < 0.1m/s^2$	60s/50%	60s/50%	60s/50%
length/Overlap	$ \ddot{X}(t_0 : t_1)  > 0.1m/s^2$	10s/75%	10s/75%	60s/50%
Equation No		3.5	2.20	2.20

The identified modal parameters are compared with the results from other studies [126, 127, 149], where the authors used different system identification methods (SSI-Data, NExT-ERA, EFDD, DSI and OKID-ERA) to identify the modal parameters for this same structure. However, due to method limitations, all the studies were implemented based on the ambient load and white noise excitation induced vibrations. Thus, only ambient or white noise excitation based identification results of this study are able to be compared with these other studies.

## 6.4 Results and Discussion

### 6.4.1 Base isolated structure

#### Initial modal parameter identification

Initial modal parameter identification based on 30 seconds white noise excitation data (RMS 0.05%g) resulted in 10 modes being identified. The fitted FRF for an equivalent SDOF system for each mode are shown in Figure 6.3, and the identified mode shapes are shown in Figure 6.4.

Modes 2, 5, 8 and 10 can be attributed to longitudinal (L) modes (shaking direction), modes 1, 4 are transversal (T), and modes 3, 6, 7, 9 are torsional (To). The first three modes (longitudinal translation, 1-L, transversal translation, 2-T, and torsion, 3-To) represent a typical base



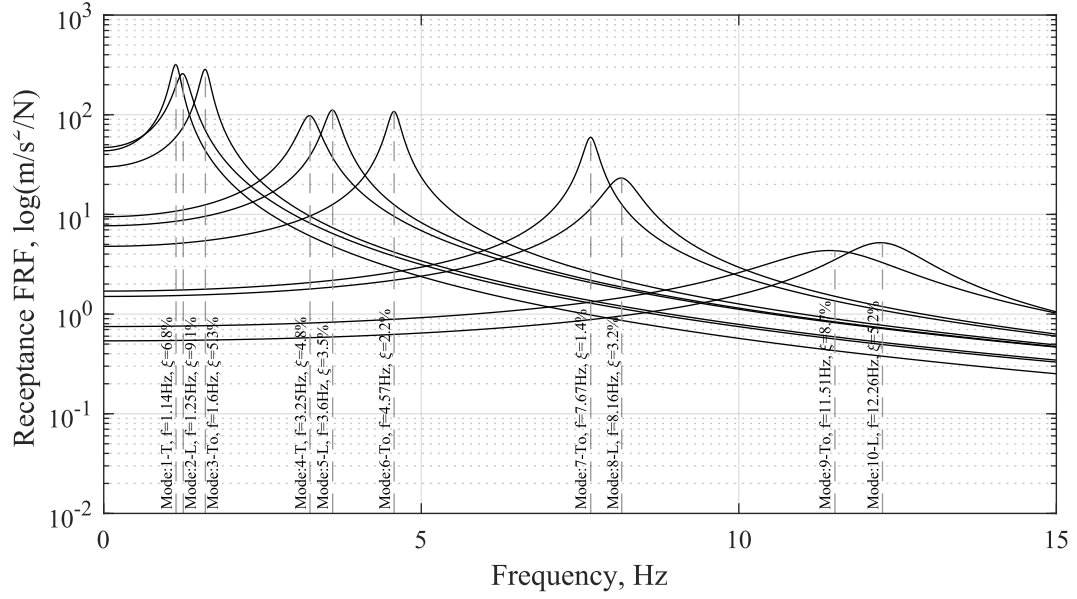


Figure 6.3: Receptance FRF of BI structure for the first lowest 10 identified modes

isolation response with a nearly rigid body superstructure response. The first two modes (1-L and 2-T) overlap due to isotropic in-plane and out-of-plane rubber bearing properties and nearly identical effective masses, which are mode shape dependent. Modes 4-T and 5-L represent typical flexural modes of a superstructure with separated modal frequencies due to different stiffness in longitudinal and transversal directions. Modes 1-T and 4-T clearly indicate that the bracing installed on the eastern transverse bay did not prevent the structure from a significant torsional motion. Although the mode has a significant spectral energy under ambient vibrations compared with other modes, its contribution to the total structural response is expected to be negligible under unidirectional test ground motions.

Overall, the identified mode shapes are comparable with those obtained by [116], where the authors applied two output-only (SSI-DATA and ERA) and one input-output (DSI) system identification methods. Based on visual inspection, the identified ten modes in this study are/appear very comparable with those obtained by the SSI-DATA method.






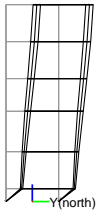
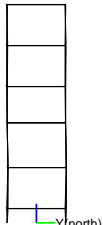
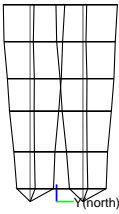
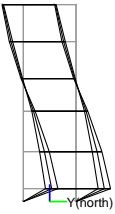
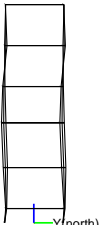
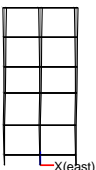
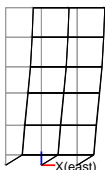
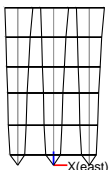
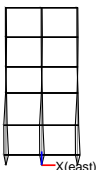
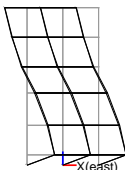


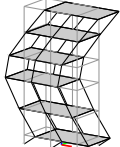

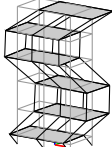
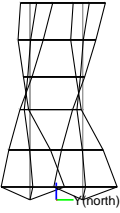
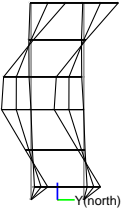
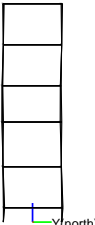
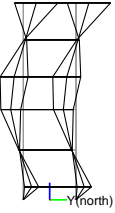


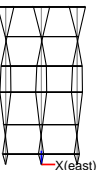
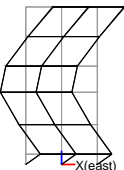
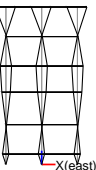
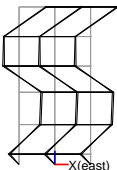
View \ Mode	1-T	2-L	3-To	4-T	5-L
3D					
North					
East					
View \ Mode	6-To	7-To	8-L	9-To	10-L
3D					
North					
East					

Figure 6.4: Identified first ten mode shapes

## Modal frequency evolution

Modal frequency evolution of the most prevailing seven modes (1-T, 2-L, 3-To, 5-L, 7-To, 8-L and 10-L) is shown in Figure 6.5. All the modal frequencies demonstrate very high variability, which can be associated with either highly non-linear behavior of the rubber bearings or poor signal-to-noise ratio .

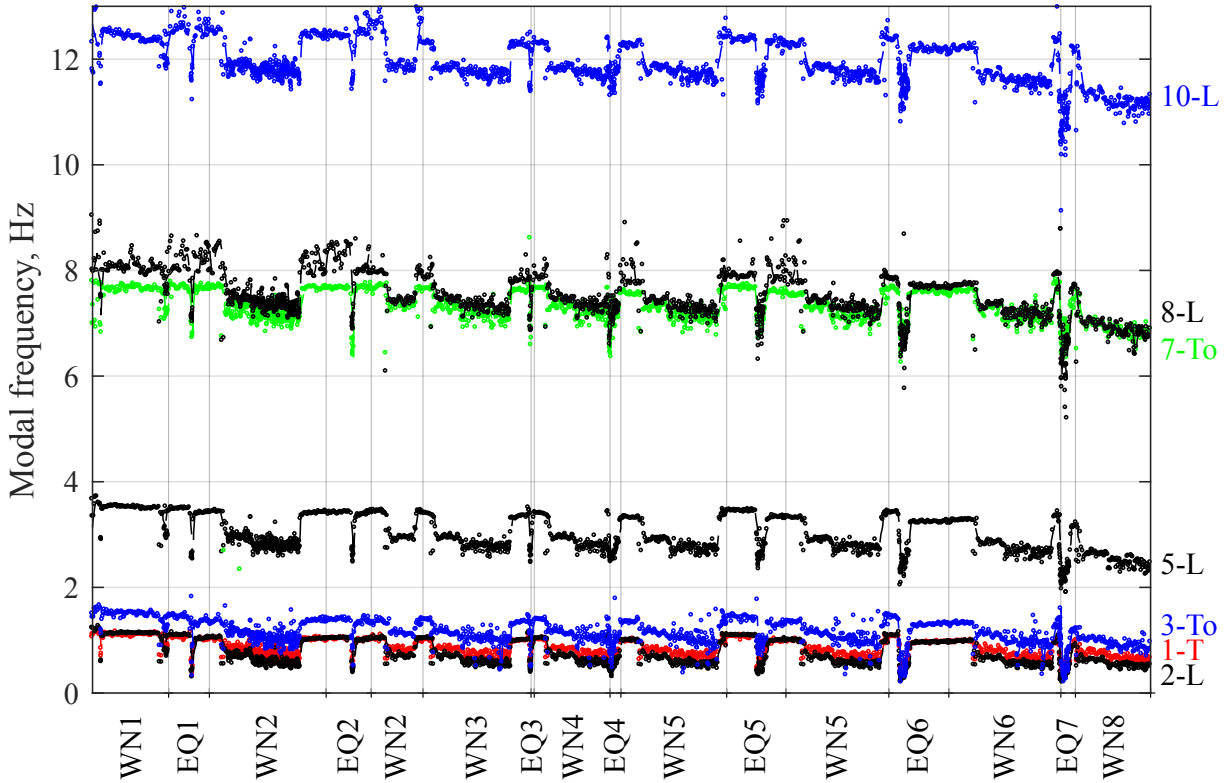


Figure 6.5: Modal frequency evolution

In addition, the modal frequencies experience a sudden drop once a certain ground excitation intensity is reached even for the white noise excitations. This can be explained by the well known Payne effect [193, 194], where the added carbon black changes the stiffness properties of the rubber compound, which becomes highly non-linear for small and large amplitude strains, where the maximum damping is reached at intermediate strain amplitudes [195]. Rubber insulator non-linear restoring force behaviour can be approximated using various existing complex mathematical models [196, 197]. However, it can also be considered as a simple bi-linear hysteretic system [198]. At small amplitude ambient or ground excitation induced vibrations, the base isolator's effective shear stiffness is equal to the initial slope ( $k_{eff} = k_1$ ),

whereas for large amplitude vibrations the effective shear stiffness will be displacement dependent ( $k_2 < k_{eff} < k_1$ ). For this reason, it is more relevant to compare the identified modal frequencies with respect to base excitation intensity.

Figure 6.6 shows modal frequency relation to the root-mean-square (RMS) input acceleration for the analysed time window for selected test groups. The selected tests were divided into two groups. The first group consists of the tests carried out at the start of the testing protocol (WN1, EQ1, WN2, EQ2 and WN3) as shown in Table 6.1. The second group includes the tests carried out at the end of the test protocol (EQ7 and WN7). The presented modal frequencies of the strongest modes (Modes 2-L, 5-L and 8-L) demonstrate a consistent decrease with increasing input ground motion.

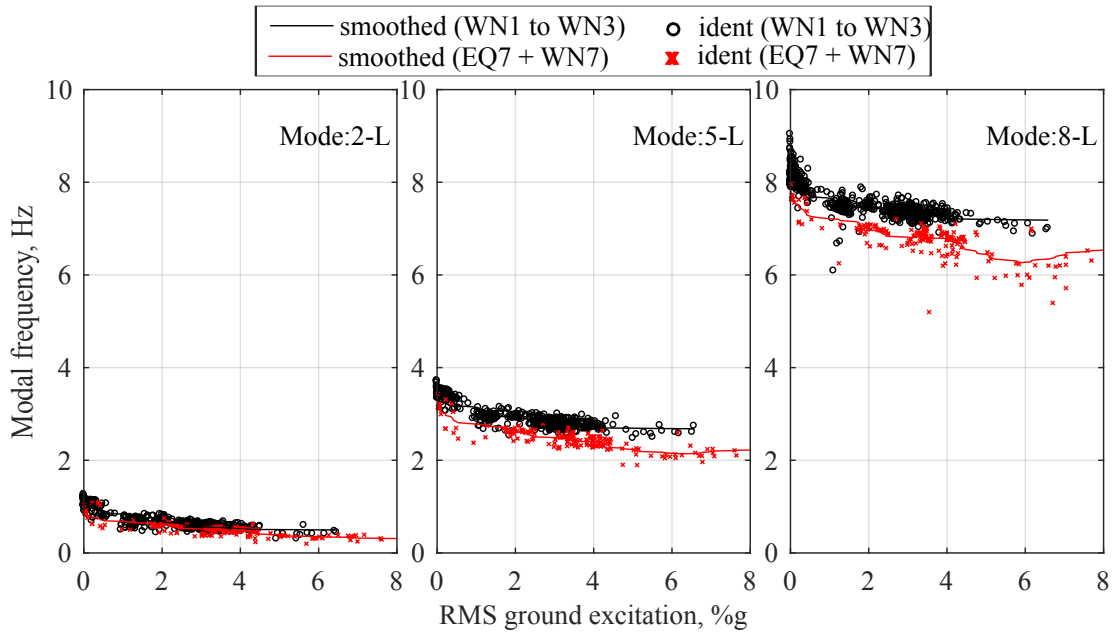


Figure 6.6: Modal frequency versus RMS ground excitation estimated for two selected test groups

In addition, overall frequency reduction can be seen in Figure 6.6, where the solid black line represents the averaged modal frequency distribution with respect to RMS ground excitation for tests WN1, EQ1, WN2, EQ2 and WN3, whereas the solid red line represents the averaged frequency distribution for tests EQ7 and WN7. Very small reductions in modal frequency can be seen for mode 2-L, where significantly larger reductions in modal frequency are observed for

modes 5-L and 8-L across the whole input excitation intensity range. The observed modal frequency reduction could be related to concrete cracking in the superstructure or rubber bearing Muller/scragging effect. The Muller effect is defined as the change in strength and stiffness of the rubber bearing from first half-cycle of loading of a virgin bearing (unscragged properties) to subsequent cycles of loading of scragged bearing (scragged properties) [199]. This reduction is well-known to be temporary and the rubber compound recovers its virgin properties, as seen in the modal frequency evolution in Figure 6.5. However, the length of this recovery process varies [193]. Although the time difference between the start and the end of the test protocol is 11 days, the time difference between the last 3 strongest ground motions is only one day, which could have resulted in incomplete recovery of the mechanical properties of the rubber bearings.

Similar findings can be seen in Astroza et al. [116] study shown in Figure 6.7, where the SSI-DATA system identification method for ambient vibrations only, resulted in temporal evolution of the natural frequencies. However, the evolution of Astroza et al. study cannot be directly compared with Figure 6.5, since, in this study, the system identification is carried out for both, low amplitude white noise, ranging 0.05-2.5%g RMS, and strong ground motion inputs. Nevertheless, both evolutions demonstrate a similar overall trend.

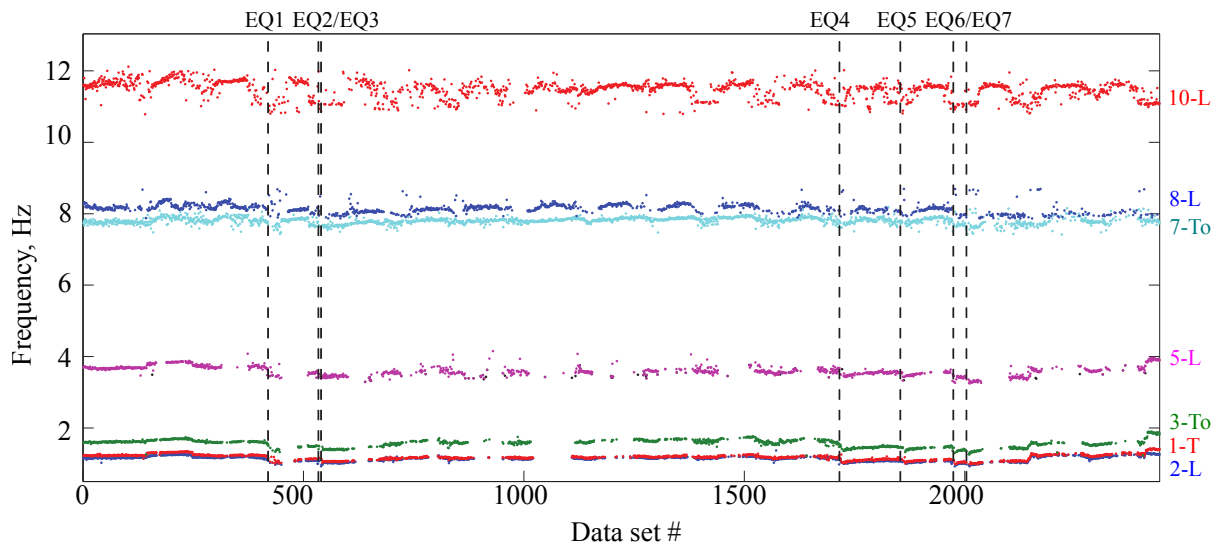


Figure 6.7: Modal frequency evolution identified in Astroza et al. [116] study using only ambient vibration data. Figure modified from [116]

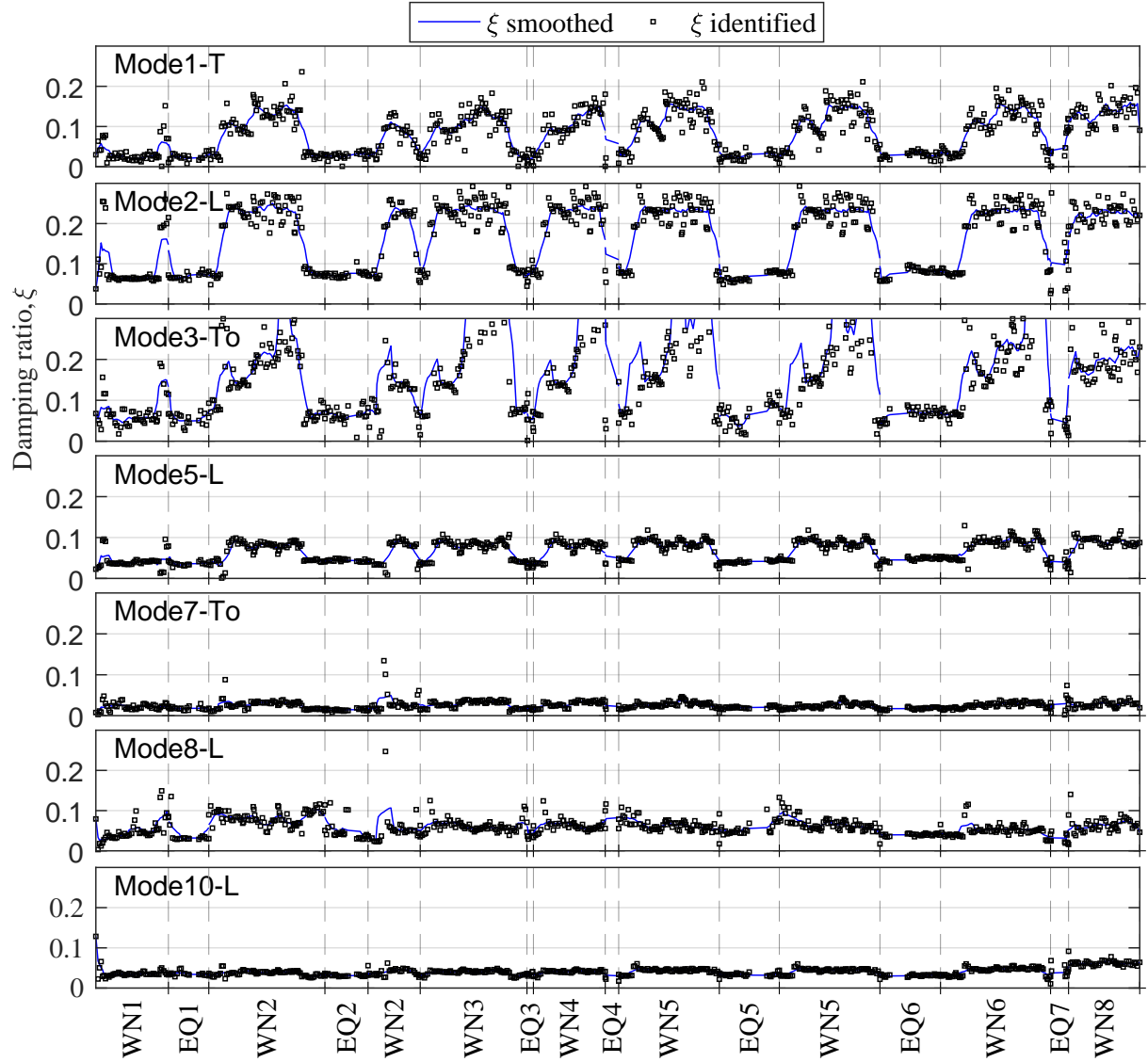


Figure 6.8: Equivalent modal damping ratio evolution for the selected modes identified from the ambient vibrations and white noise excitation

### Modal damping evolution

The equivalent modal damping ratio evolution for each mode is shown in Figure 6.8. Modal damping evolution for each mode is calculated using windowed 1 minute long response data with 50% overlap obtained from the white noise excitation or ambient vibration events. Modal damping evolution does not include the actual earthquake excitation, due to highly varying modal frequency within relatively short time windows, leading to inaccurate estimation of the damping ratio,  $\zeta$ .

Again, as for the identified modal frequencies, the identified modal damping coefficients demonstrate very high variability, which is excitation intensity dependent. Modal damping ratios for the lowest three modes vary between 5% and 25%, due to energy dissipative properties of the rubber bearings. In addition, the damping ratio of the transversal and torsional modes (1-T, 3-To) appears more variable, which can be attributed to low signal-to-noise ratio. It must be noted that maximum manufacturer's rated damping is approximately 18.5% [179], which corresponds to a 50mm shear deformation, and is the lowest deformation tested by the manufacturer. The difference between identified and rated rubber bearing damping can thus be attributed to dynamic effects, as it is known that the effective damping increases with strain rate [200, 201], and/or low shear deformations, that vary from 10-30mm for the white noise base excitations. The higher modes (5-L, 7-L, 8-L and 10-L) also show a certain degree of variability, particularly mode 5-L, but it can be related to non-linear mechanical properties of the superstructure. Modal damping relation to RMS value of the ground excitation is shown in Figure 6.9. As can be seen, the lowest three modes (1-L, 2-T and 3-To) are excitation intensity dependent, whereas the remaining identified higher modes show lower sensitivity with respect to ground excitation intensity. No changes in critical damping ratio are observed throughout all the tests.

The identified modal damping values for the first three modes (1-T, 2-L and 3-To) are higher than those identified in [116]. The other modes (5-L, 7-To, 8-L and 10-L) show smaller differences in comparison to this study.

### **Mode shape evolution**

Mode shape evolution of the strongest two modes (2-L and 5-L) is shown in Figure 6.10. All mode shapes for all tests are unit normalized. Thus, one of the mode shape coefficients for each mode does not vary. The mode shape evolutions presented demonstrate high variability, which is excitation intensity dependent. Mode shape evolution for Mode 2-L directly illustrates the efficiency of the rubber bearings, which are typically designed to isolate the superstructure from strong ground motion. As seen in Figure 6.10a, under high intensity ground motion, the total deformation of the superstructure, defined as the difference between the top and ground floor

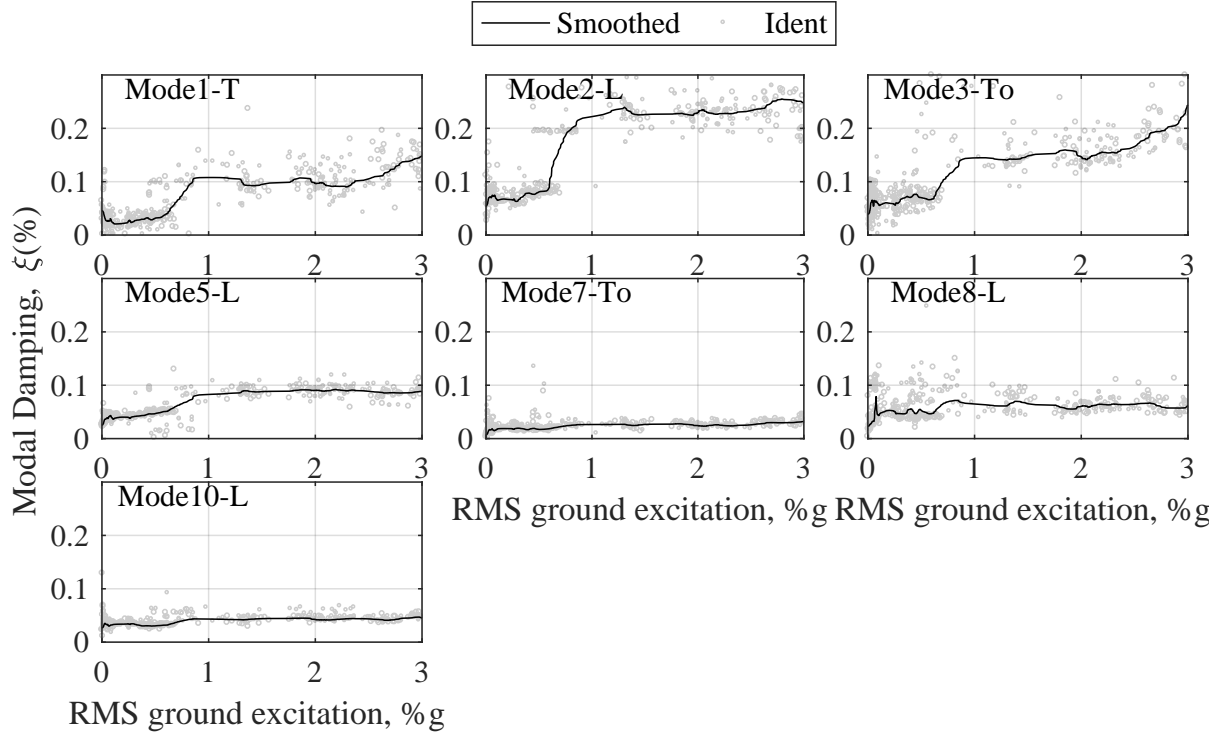


Figure 6.9: Modal damping versus RMS ground excitation identified from the ambient and white noise ground excitation

displacement, decreases as a result of lower base isolator effective stiffness, as expected. Large mode shape variations of Mode 5-L seen in Figure 6.10b can be attributed to low signal-to-noise ratios, as well as strong non-linear behaviour of rubber isolators.

Due to the uni-directional ground motion, the lateral and torsional modes are being excited at significantly lower intensity compared to longitudinal modes. Hence, the modes have significantly lower signal-to noise-ratio, which leads to larger mode shape identification errors.

Overall, due to the high and temporary variability of the mode shapes it is difficult to observe any permanent mode shape changes, which are caused by the structural damage. As a result, no attempt has been made to use statistical analysis based on changes in the mode shape coefficients to capture the damage. However, the identified mode shapes can be utilized to decompose the modes and reconstruct single mode dominant hysteresis loops, which can be analysed using HLA [18, 147]. The HLA method should provide a better and more intuitive insight on systems structural behavior and its evolution of structural stiffness than a modal method.



## **6.4.2 Fixed base structure**

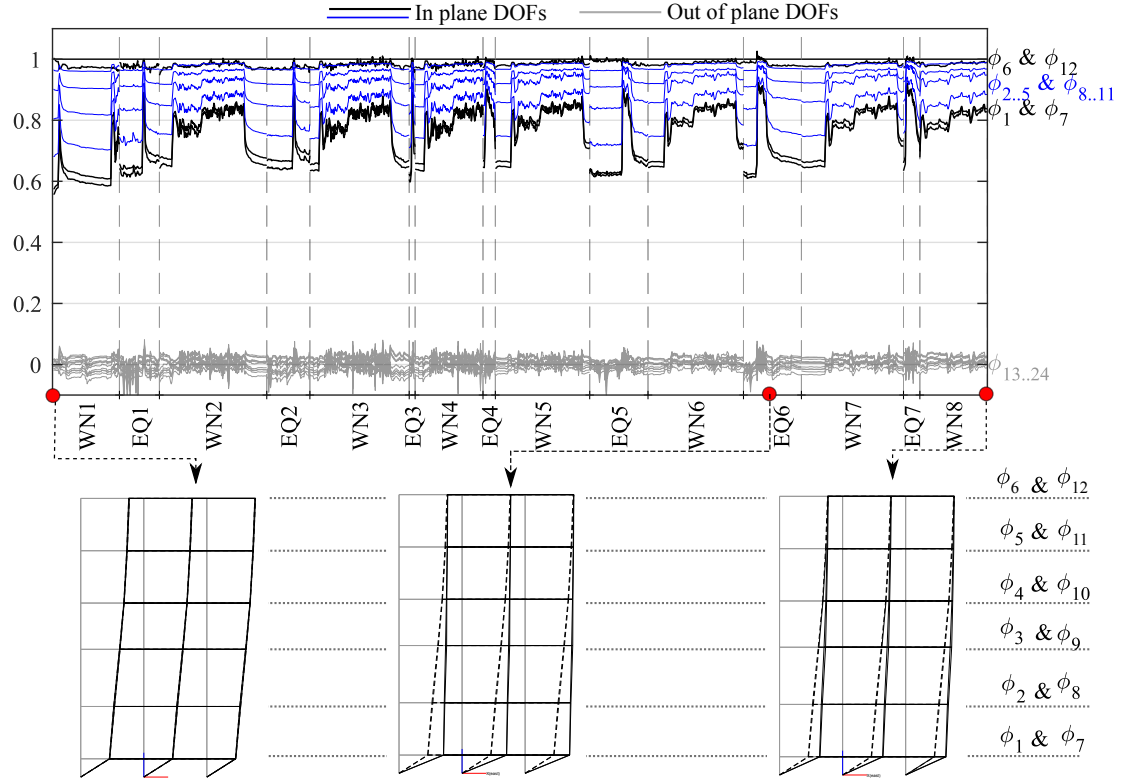
### **Initial modal parameter identification**

Initial modal parameter identification for the FB building configuration is carried out using 40 seconds long ambient vibration data, which resulted in 10 modes being identified. Figure 6.11 shows the fitted FRFs of the first ten identified modes and Figure 6.12 shows the identified mode shapes. The first two modes, the longitudinal 1-L and transversal 2-T flexural modes, are at almost identical frequencies, resulting in overlapping FRFs. Mode 2-L involves a small torsional deformation caused by the asymmetric transversal stiffness of two bays, due to the presence of the transversal shear walls in one of the bays. The identified modal frequencies for the FB structure are significantly different from the identified superstructure flexural mode frequencies of BI structure, shown in Figure 6.3, due to different support conditions. No structural changes have been implemented in the superstructure, which would affect the structural stiffness or building mass.

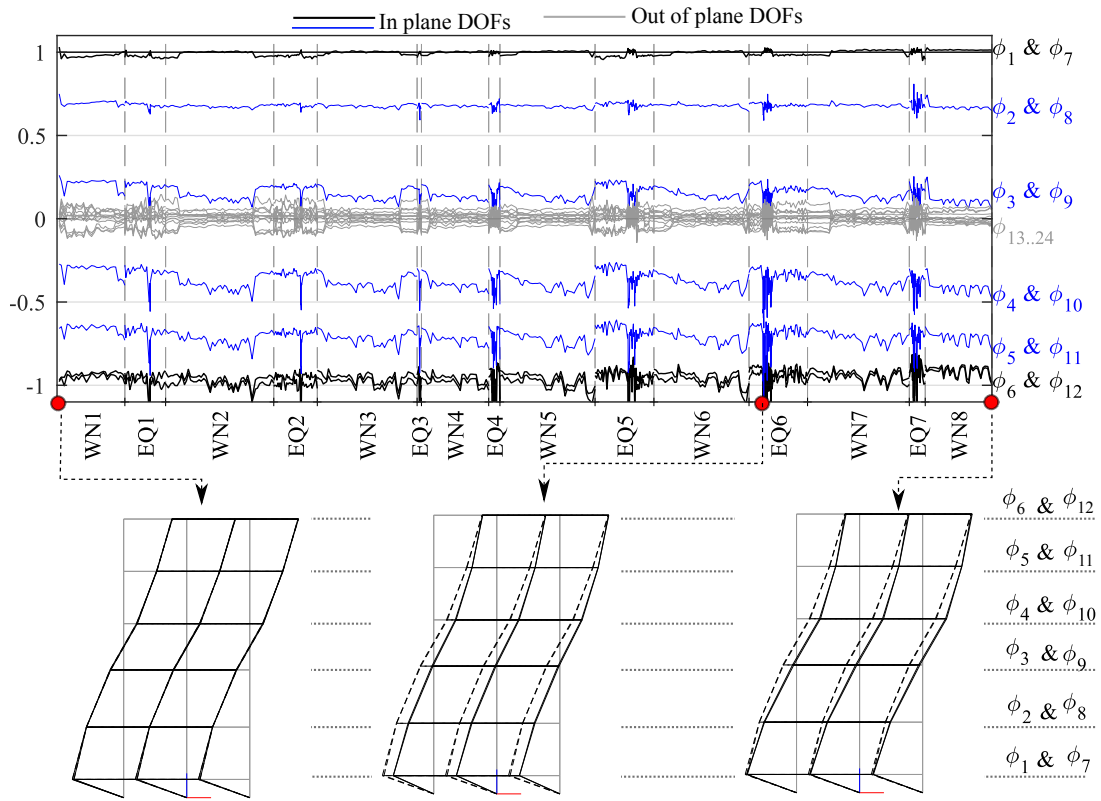
### **Modal frequency evolution**

Modal frequency evolution of the selected first seven modes (1-L, 2-T, 3-To, 4-To, 5-L, 6-To and 7-L) is shown in Figure 6.13. Modal frequency evolution of the other three modes (8-L, 9-To and 10-L) is not presented, due to poor consistency of the results, which can be attributed to either relatively high damping or/and poor signal-to-noise ratio.

The identified modal frequencies demonstrate very high variability, which can be distinguished into short-term variability and permanent overall degradation. Short-term variability, seen as gentle variation in WN tests and a sudden, but recovering, variation in EQ tests, can most likely be related to either pinching effect of concrete elements [18, 202] or contribution from non-structural building components (NSC), which can have a significant contribution to the total structural stiffness and strength [203, 204]. Short-term variability is excitation intensity dependent. Thus, some of the modal frequency evolution discontinuities seen between the tests



(a) Mode 2-L



(b) Mode 5-L

Figure 6.10: Mode shape  $\Phi(:,i) = [\phi_1 \dots \phi_{24}]$ , evolution for white noise (WN) and earthquake (EQ) excitations

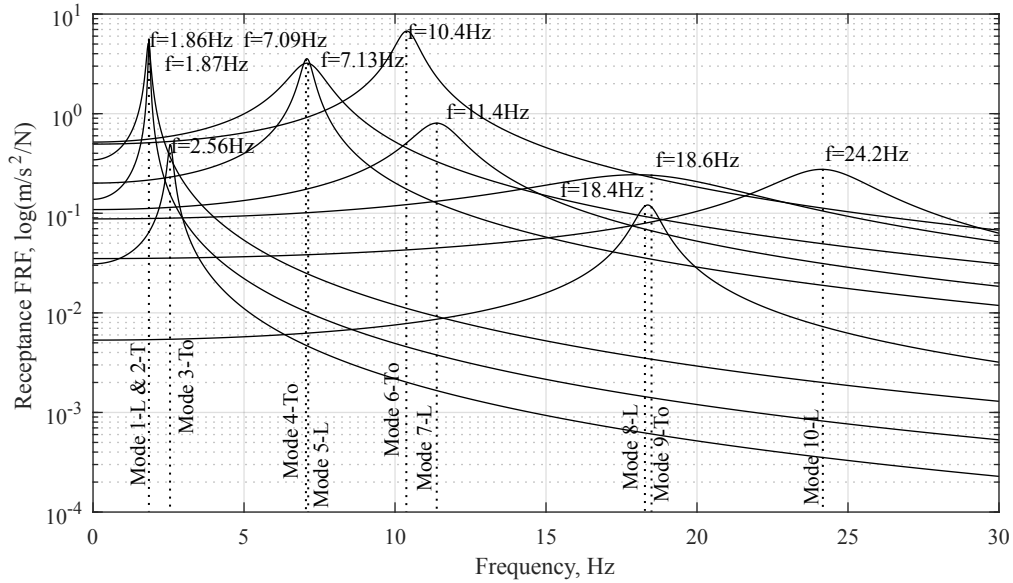


Figure 6.11: FRFs for the first ten identified modes

(WN1 and EQ1) is the result of different ground motion intensity. Permanent overall frequency degradation can also be observed throughout the series of tests, as expected for the FB case, which is more pronounced for longitudinal modes (1-L, 5-L and 7-L) and can be associated with the structural damage in the longitudinal bays. In addition, during the initial modal parameter identification two mode couples (1-L & 2-T and 4-To & 5-L) were identified with overlapping FRF's, as shown in Figure 6.11. However, at the end of the testing protocol, as seen in Figure 6.13, the gap between the modes increases. This result, again, confirms the fact that most of the structural damage took place in longitudinal bays, as expected in the direction of shaking.

Figure 6.14 shows the modal frequency relative to RMS input acceleration for the three strongest modes (1-L, 5-L and 7-L) for each EQ event combined with the low amplitude WN excitation carried out after each EQ event (EQ+WN). The solid lines represent the averaged frequency-RMS ground excitation relation, which indicates that the modal frequency evolution is non-linear, excitation intensity dependent. With increasing ground motion intensity all the modal frequencies drop at different rate, which can again be attributed to crack opening or closing in concrete members and/or stiffness contribution from NSC, which decreases with increasing inter-story deformations. In addition, as structural damage progresses, the modal frequencies tend to drop at a higher rate with increasing ground motion intensity. At small am-







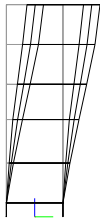
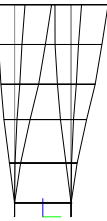
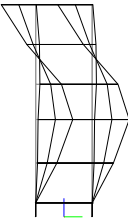

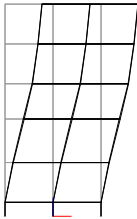

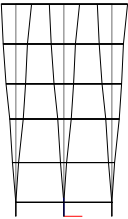
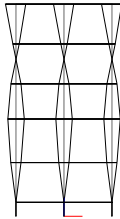
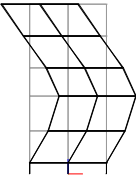


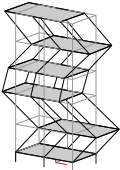

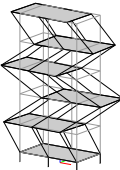
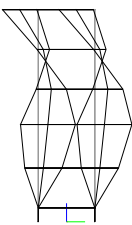


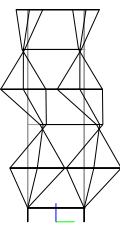

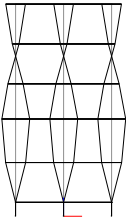
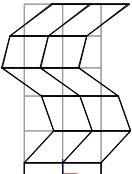
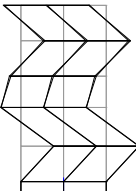
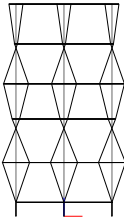
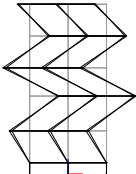
View \ Mode	1-L	2-T	3-To	4-To	5-L
3D					
North					
East					
View \ Mode	6-To	7-L	8-L	9-To	10-L
3D					
North					
East					

Figure 6.12: Identified first ten mode shapes for the FB building

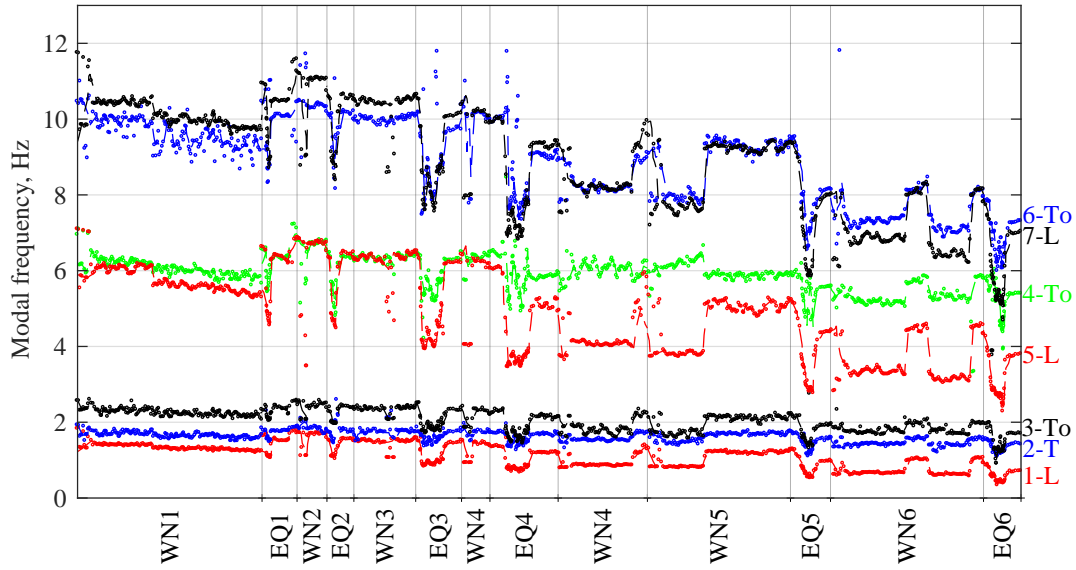


Figure 6.13: Modal frequency evolution of the first seven modes for white noise (WN) and earthquake (EQ) excitations

plitude vibrations the cracks remain partially closed, which results in higher member stiffness, and thus a higher observed modal frequency. As damage progresses, more and more cracks develop resulting in significantly lower effective stiffness and modal frequencies at high amplitude vibrations. Hence, temporarily varying identified modal frequencies with an increasing disparity between small and large amplitude vibrations can reveal the extent of member cracking. Permanent modal frequency changes are also obvious, which can be associated with permanent stiffness degradation due to concrete cracking.

### Modal damping evolution

Figure 6.15 shows the modal damping,  $\xi_i$ , evolution of the first seven selected modes (1-L, 2-T, 3-To, 4-To, 5-L, 6-To and 7-L). Again, as observed for the modal frequency evolution, modal damping demonstrates significant excitation dependent variability.

The three strongest principal longitudinal modes (1-L, 5-L and 7-L) exhibit relatively high damping, which is in the range of 5%-to 10% of the critical damping ratio. Increase in the modal damping ratio from 5% to 10% for Modes 4-T and 7-L can be observed after test EQ4 for higher WN excitation intensities, where the damping of the lower modes remains in the same range (4% to 6%). Overall, damping ratios of the transversal modes (2-T, 3-To and 6-To) have a higher variance due to low excitation levels in transversal direction, which results in

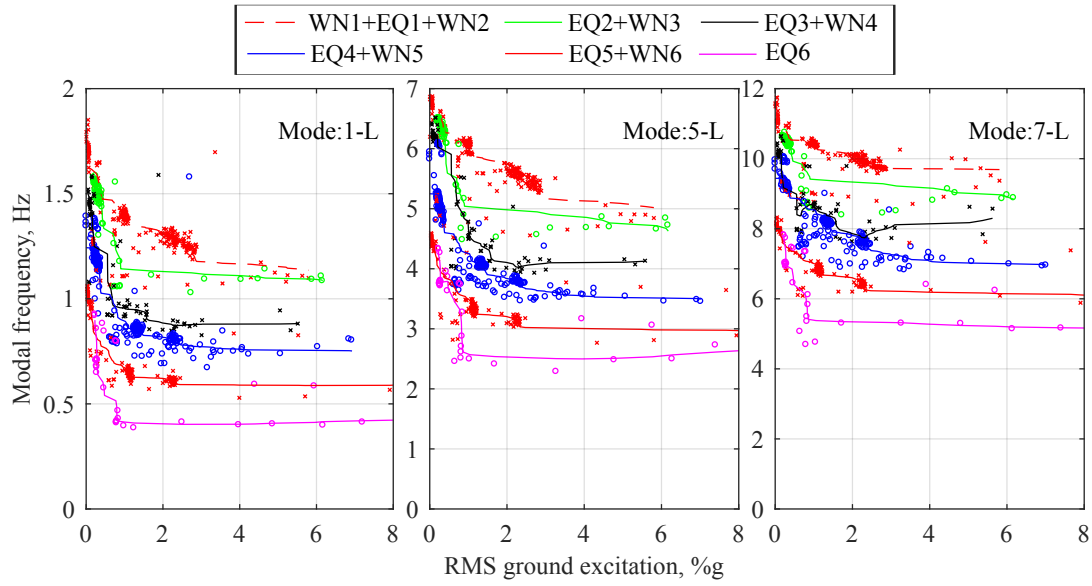


Figure 6.14: Modal frequency relation to RMS ground excitation at different stages of the test protocol for modes 1-L, 5-L and 7-L

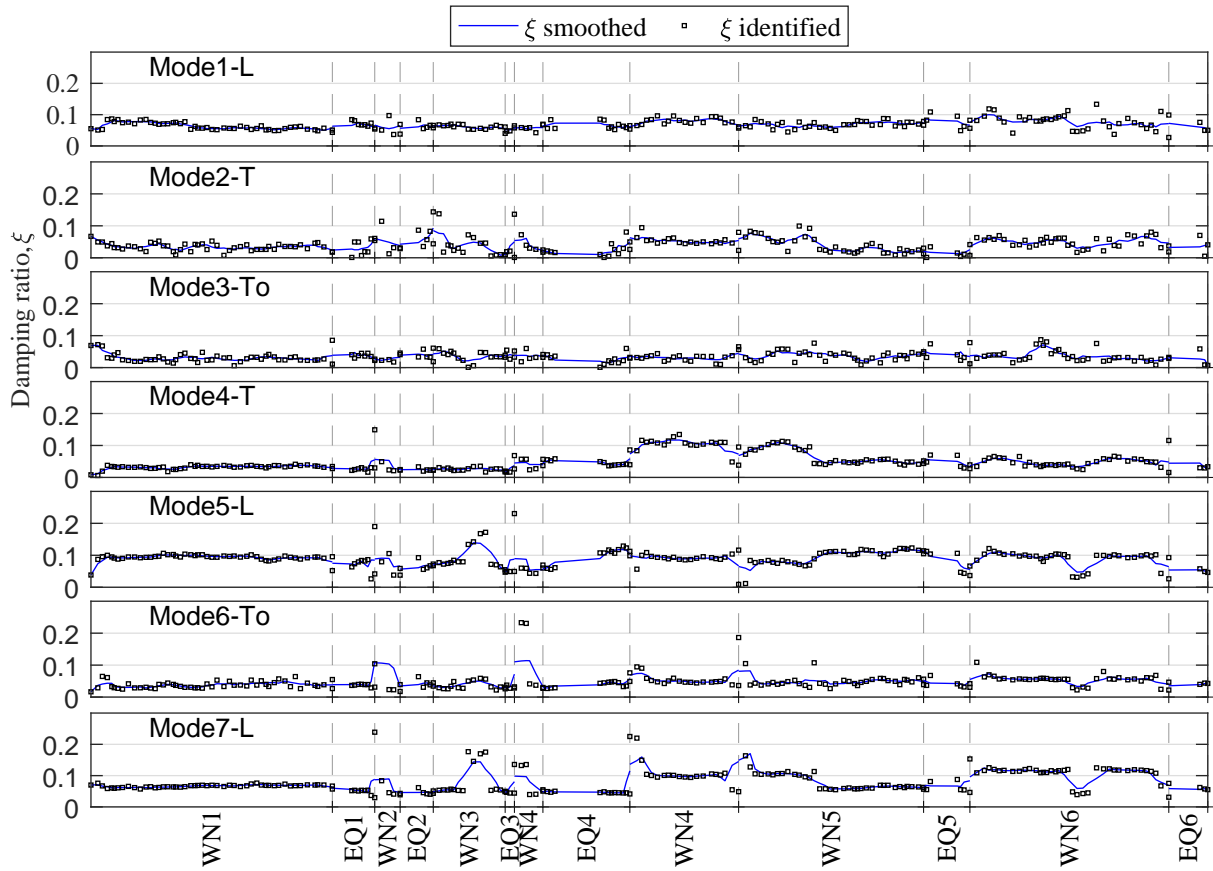


Figure 6.15: Modal damping,  $\xi$ , evolution of the first seven modes for white noise (WN) and earthquake (EQ) excitations

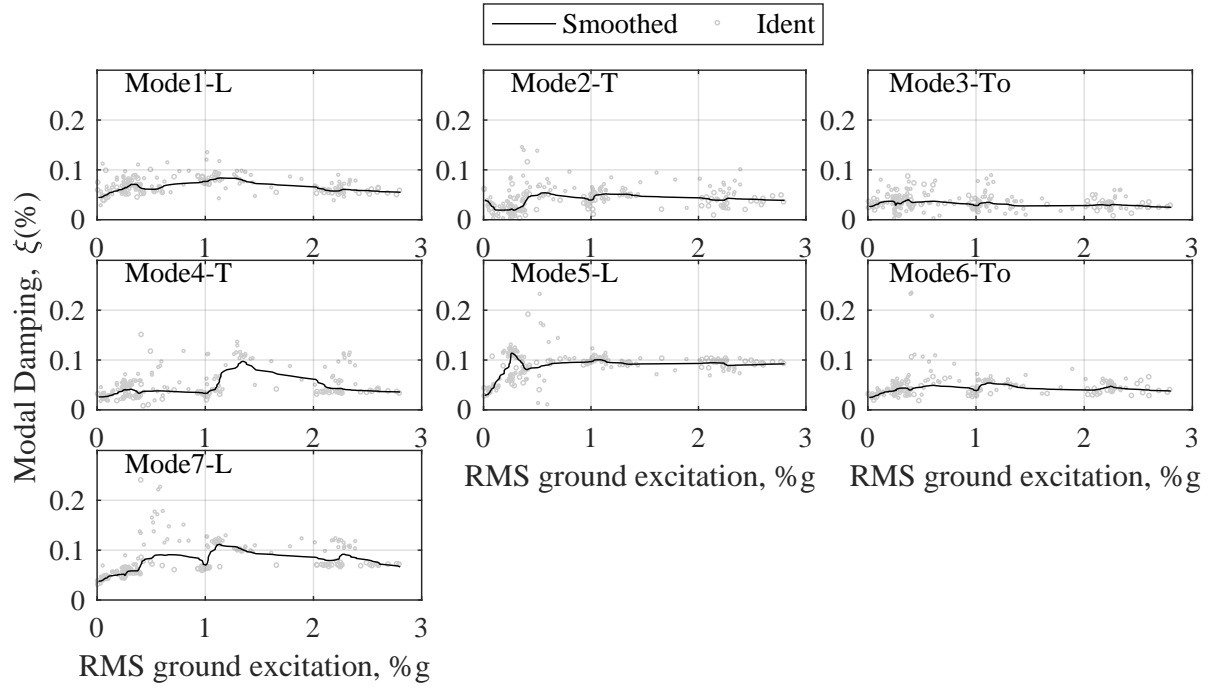


Figure 6.16: Modal damping,  $\xi$ , of the first seven modes identified for different RMS input ground excitation levels

poor signal-to-noise ratio and consequently larger errors in modal damping identification. In general, modal damping evolution does not demonstrate a clear increasing or decreasing trend with increasing damage.

Figure 6.16 shows modal damping versus RMS ground excitation for all the tests. It is clear modal damping is excitation intensity dependent, which is especially more pronounced for longitudinal modes (1-L, 5-L and 7-L) in the direction of shaking, as might be expected. The transversal and torsional modes show lower dependence to excitation intensity, because the modes are not excited at a high intensity.

### Mode shape evolution

Mode shape evolution for the three selected strongest modes (1-L, 5-L and 7-L) is shown in Figures 6.17-6.19. Since these modes are in the longitudinal shaking direction, the evolution of longitudinal DOF's,  $\phi_{2...12}$ , is represented in solid black lines, where evolution of the transversal DOFs is shown in grey solid lines.

Evolution of mode 1-L in Figure 6.17 shows small variations through EQ1, WN2 and EQ2. At the end of these tests, the difference between DOFs  $\phi_3$  and  $\phi_8$  increases, which can be attributed to unsymmetrical structural damage, since these DOFs are located on the same level, but different corners. This difference between two modal coefficients reduces after the test EQ4, which implies the damage occurring during test EQ4 re-balances the structural stiffness of the two longitudinal bays. Notable permanent changes in all DOF's can be observed after EQ5 and EQ6, which can be attributed to a significant structural damage.

Overall mode shape evolution of 5-L and 7-L in Figures 6.18 and 6.19 exhibit higher variability compared to mode 1-L. This result is mainly due to greater sensitivity to structural changes and signal noise.

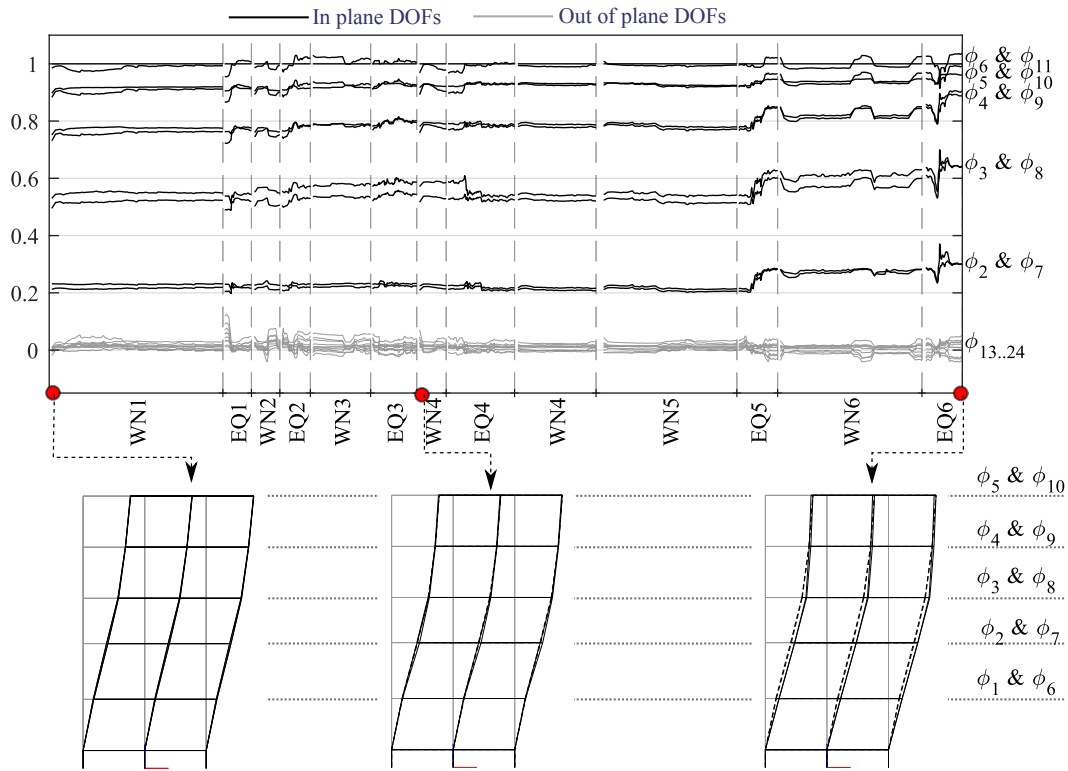


Figure 6.17: Mode shape 1-L,  $\Phi(:, i) = [\phi_1 \dots \phi_{24}]^T$ , evolution for white noise (WN) and earthquake (EQ) excitations.



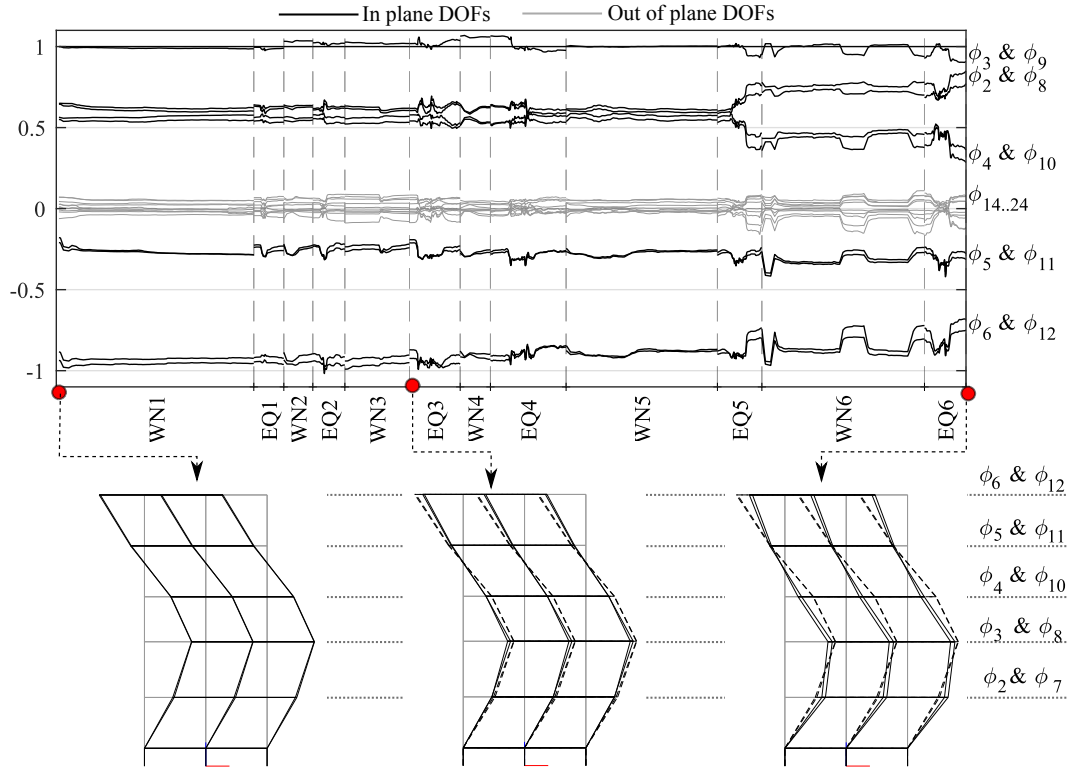


Figure 6.18: Mode shape 5-L,  $\Phi(:, i) = [\phi_1 \dots \phi_{24}]^T$ , evolution for white noise (WN) and earthquake (EQ) excitations.

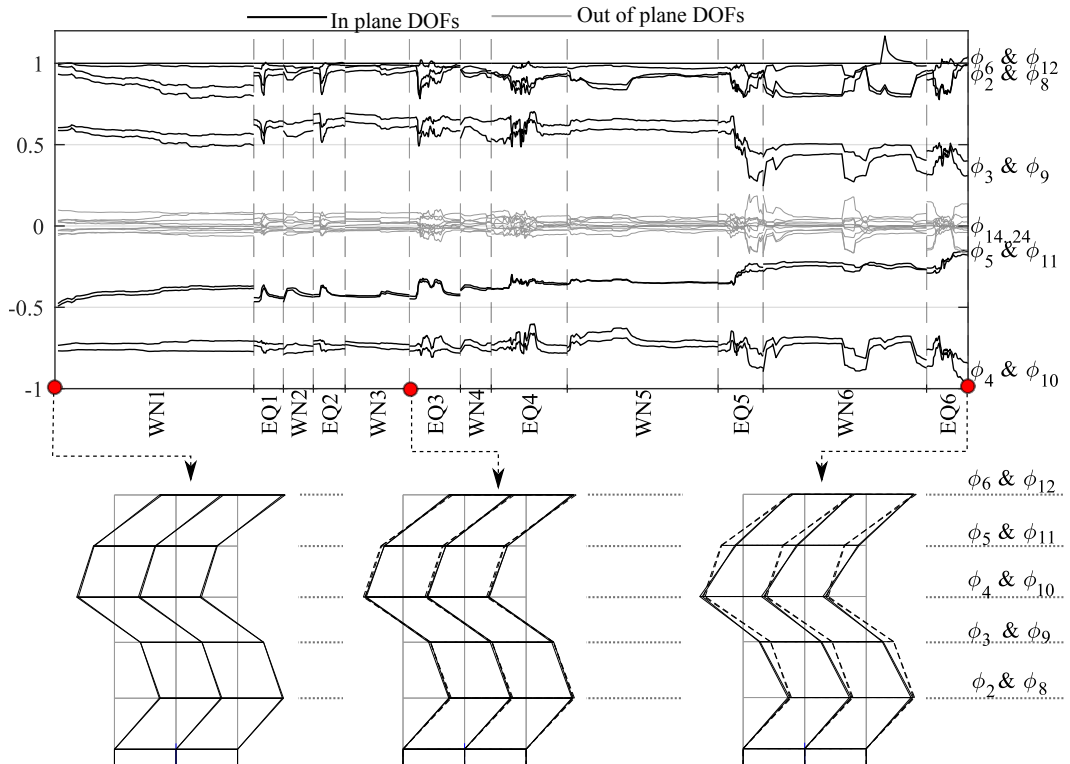


Figure 6.19: Mode shape 7-L,  $\Phi(:, i) = [\phi_1 \dots \phi_{24}]^T$ , evolution for white noise (WN) and earthquake (EQ) excitations.

## 6.5 Summary

This study presents a novel modal parameter estimation technique, which is capable of identification and continuous tracking of the modes participating in the response. The method is based on tracking the dominant modes of response by re-evaluating the modal frequencies and mode shape coefficients over short, overlapping time windows. Hence, the approach is capable of identifying the modal parameters for linear and non-linear systems. The method can perform as an input-output technique for earthquake generated non-linear responses. Thus, the approach presented can provide a better insight into structures subjected to strong ground motion events.

The method is applied to identify the modal parameters of a 5-story full-scale reinforced concrete test structure, which was tested for two structural configurations: base isolated and fixed base. The results demonstrate the method is capable of tracking the relevant modal parameters for all types of input excitation. The identified mode shape evolution for the BI structure indicates that the structure exhibits highly non-linear behavior, which is excitation intensity dependent and is consistent with expectations for a BI structure and other studies. Modal frequency degradation is observed at the end of the test protocol, which can be associated with concrete cracking of the superstructure or incomplete recovery of the rubber bearings. The identified modal parameters for the FB structure identify the expected progressive structural damage induced by increasing intensity earthquake inputs. The observed changes in modal parameters can be distinguished into temporary and permanent changes. Temporary variation in modal parameters can be attributed to non-linear behavior of superstructure, caused by concrete crack opening/closing and contribution from non-structural components, and is excitation intensity dependent. Permanent changes in modal parameters are related to stiffness degradation of the superstructure due to concrete cracking/spalling and yielding of steel reinforcement.

Overall, the method performs robustly and can be used for identification of any MDOF structure subjected to long duration earthquake excitations. The method requires input force measurements and a relatively rich spatial arrangement of monitored DOFs to fully delineate

the response of closely spaced modes. The identified mode shape evolution can be used to decompose the modes and reconstruct single mode dominant hysteresis loops, which can be analysed using HLA [18, 147].

# CHAPTER 7

---

## Application of mode decomposition and HLA

---

### 7.1 Introduction

SHM based on hysteresis loop analysis (HLA) [147] offers a simple, effective and intuitive SHM tool for damage identification in structures that have undergone non-linear response. The method performs well when the structural response is single mode dominant, thus producing regular shape hysteresis loops. However, strong ground motion can trigger higher modes, which have a significant contribution to the total response. The presence of higher modes typically results in irregular hysteresis loops, which are hard to identify as accurately using HLA. Single mode dominant hysteresis loops can be obtained by segregating the modes using mode decomposition, which relies on the identified approximate mode shape coefficients. The previous study (Section 6.4.1 and Section 6.4.2), demonstrated that mode shape coefficients can successfully be tracked over relatively short time windows using a novel method.

Thus, this chapter presents the second part of the SHM implementation process, which consists of mode decomposition, reconstruction of single mode dominant hysteresis loops, and the resultant application of HLA. This overall proposed SHM strategy is applied to an experimental full-scale 5-story reinforced concrete building, which was tested for two structural configurations: 1) base isolated (BI); and 2) fixed base (FB). The test structure was subjected to number of different type ground motions. The results show that mode segregation allows the extraction of regular shape hysteresis loops, which can readily be used for visual inspection and HLA.

The identified stiffness evolution profiles from HLA clearly indicate the loss of stiffness during strong ground motion events, which can be attributed to extensive concrete cracking and yielding of steel reinforcement. Thus, the presented SHM implementation strategy can successfully be used to perform a continuous tracking of hysteretic structures.

## 7.2 Method

### 7.2.1 Modal parameter identification and mode decoupling

Modal parameter identification can be successfully implemented using input-output method presented in Chapter 3. The identified modal parameter evolution is used to decouple the structural response into separate modes and reconstruct single mode dominant hysteresis loops, as demonstrated in Section 5.2.1 per Equation (5.3):

$$F_{s,i} = \mathbf{M} \cdot \hat{\phi}_i \left[ \{\ddot{\bar{X}}_i^{abs}\} + 2\xi_i \omega_i \{\dot{\bar{X}}_i\} \right] \quad (7.1)$$

where  $\mathbf{M}$  is the mass matrix,  $\hat{\Phi} = [\hat{\phi}_1 \quad \hat{\phi}_2 \quad \dots \quad \hat{\phi}_i]$  is the identified mode shape matrix, where  $\hat{\phi}_n$  is the identified mode shape vector of the  $n^{th}$  mode.  $F_{s,i}$ ,  $\xi_i$ ,  $\omega_i$  are the stiffness restoring force vector, damping ratio and the natural frequency of the  $i^{th}$  mode, respectively,  $\ddot{\bar{X}}_i^{abs}$  and  $\dot{\bar{X}}_i$  are the absolute modal acceleration and relative modal velocity of the  $i^{th}$  mode, respectively, calculated:

$$\begin{aligned} \ddot{\bar{X}}^{abs} &= \hat{\Phi}^{-1} (\ddot{X} + r \cdot \ddot{X}_g) \\ \dot{\bar{X}} &= \hat{\Phi}^{-1} \dot{X} \end{aligned} \quad (7.2)$$

where  $\ddot{X}$ ,  $\dot{X}$  are the relative acceleration and velocity, respectively,  $\ddot{X}_g$  is the input ground acceleration and  $r$  is the influence vector.

### 7.2.2 Hysteresis loop analysis (HLA)

Stiffness restoring force,  $F_{s,i}$ , versus displacement hysteresis loops can be reconstructed for the dominant  $i^{th}$  mode to represent the structure's external force-deformation relationship, which varies with time due to structural degradation and/or damage during strong ground motion events. In the HLA method, the reconstructed path dependent hysteresis loops are subdivided into different loading and unloading sub-half cycles, which can be approximated by a series of piecewise linear segments. F-type hypothesis testing is applied to identify the number of piecewise segments that represent an approximated hysteretic model. Finally, overall least squares linear regression analysis is carried out to selected sub-half cycles which allows the identification of the elastic stiffness, plastic stiffness and cumulative plastic deformation. Full details of the HLA method and its application to test structures can be found in [18] and [147].

The original HLA method has been modified to increase the number of successfully identified half-cycles by introducing parametric constraints. A general  $r$ -phase piecewise linear approximated hysteretic model can be expressed [147] :

$$\begin{aligned}
 G(x) &= g_1(x) = a_1x + b_1 & X_1 \leq x \leq X_{t1} \\
 &= g_2(x) = a_2x + b_2 & X_{t1} \leq x \leq X_{t2} \\
 &= \dots \\
 &= g_r(x) = a_rx + b_r & X_{t_{r-1}} \leq x \leq X_n
 \end{aligned} \tag{7.3}$$

where  $X_{t1} \dots X_{t_{r-1}}$  are the breakpoints in sub-half cycles,  $X_1, X_n$  are the start and end hysteretic displacements of the analyzed sub-half cycle and  $Y_1, Y_n$  are the corresponding restoring force components, as shown in Figure 7.1. The reconstructed hysteresis loop points,  $(X_i, Y_i)$ , can be approximated by a piecewise linear model:

$$Y_i = G(X_i) + e_i \quad i = 1 \dots n \tag{7.4}$$

where  $e_i$  is the measurement noise and/or modeling error. The overall residual sum squared

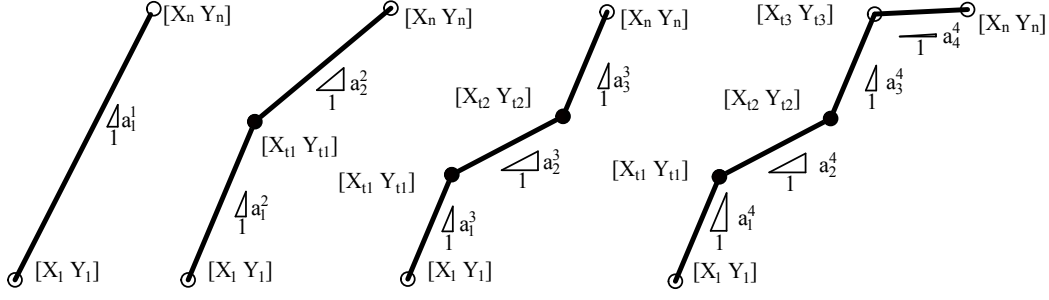


Figure 7.1: Piecewise linear hysteretic models ( $r = 1, 2, 3, 4$ ) for an arbitrary sub-half cycle

error for  $r$ -phase linear model can be expressed:

$$R_r(\hat{X}_{t_1}, \dots, \hat{X}_{t_{r-1}}, a_1, b_1, \dots, a_r, b_r) = \sum_{i=1}^{t_1} [Y_i - g_1(X_i)]^2 + \sum_{i=t_1+1}^{t_2} [Y_i - g_2(X_i)]^2 + \dots \quad (7.5)$$

$$\dots + \sum_{i=t_{r-1}+1}^n [Y_i - g_r(X_i)]^2$$

As a result, a solution to the most optimal parameters,  $(\hat{X}_{t_1}, \dots, \hat{X}_{t_{r-1}}, a_1, b_1, \dots, a_r, b_r)$ , producing the lowest residual sum of squares,  $R_r$ , for this  $r$ -phase linear model can be written as an optimization problem:

$$(\hat{X}_{t_1}, \dots, \hat{X}_{t_{r-1}}, a_1, b_1, \dots, a_r, b_r) = \arg \min_{(\hat{X}_{t_1}, \dots, \hat{X}_{t_{r-1}}, a_1, b_1, \dots, a_r, b_r)} (R_r(\hat{X}_{t_1}, \dots, \hat{X}_{t_{r-1}}, a_1, b_1, \dots, a_r, b_r)) \quad (7.6)$$

where the optimization problem can be solved by dividing the sub-half cycle hysteresis segment into a number of possible  $r$  piecewise segments and solving the optimization problem for each potential segment configuration.

Solution to Equation (7.6) yields the overall minimum of all possible piecewise segment configurations. The values  $(\hat{X}_{t_1}, \dots, \hat{X}_{t_{r-1}})$  are the breakpoints. The values  $(a_1, b_1, \dots, a_r, b_r)$  are the regression coefficients representing each segment of an approximated  $r$ -segment ( $r = 1, 2, 3, 4$ ) piecewise hysteretic model, as shown in Figure 7.1.

Due to the presence of sensor noise, higher mode effects and limitations in objective function (under-constrained parameters), the optimization problem may yield an unrealistic piecewise  $r$ -segment hysteretic model that has less or limited physical meaning. Thus, inaccurate regression

coefficients will be obtained. More realistic piecewise approximations of the hysteretic model can be achieved by adding constraints to the least squares objective function in Equation (7.6):

$$(X_{t_1}, \dots, X_{t_{r-1}}, a_1, b_1, \dots, a_r, b_r) = \arg \min_{Constr} (R_r(X_{t_1}, \dots, X_{t_{r-1}}, a_1, b_1, \dots, a_r, b_r)) \quad (7.7)$$

where *Constr* indicates the imposed constraints for different  $r$ -segment hysteretic models and can be divided into three groups:

1. **Model continuity** constraints are applied to multi-segment ( $r = 2, 3, 4$ ) hysteretic models to impose regression function continuity at the estimated break points ( $\hat{X}_{t_1}, \dots, \hat{X}_{t_{r-1}}$ ):

$$\begin{aligned} g_i(\hat{X}_{t_i}) &= g_{i+1}(\hat{X}_{t_i}) \\ a_i \cdot \hat{X}_{t_i} + b_i &= a_{i+1} \cdot \hat{X}_{t_i} + b_{i+1} \end{aligned} \quad (7.8)$$

2. **Minimum segment length** constraints are applied to each segment of the approximated hysteric sub-half cycle to ensure that only significant hysteretic features are captured during the optimization process:

$$|\hat{X}_{t_{i+1}} - \hat{X}_{t_i}| = \Delta_{r,i} \quad (7.9)$$

3. **Regression coefficient** constraints are applied to  $r = 2, 3, 4$  segment piecewise hysteretic models to ensure that only specific sub-half cycles are captured. For example,  $r = 3$  segment piecewise models are used to identify sub-half cycles exhibiting significant pinching, which typically can be described:

$$a_1^r > a_2^r \quad a_3^r > a_2^r \quad a_1^r \approx a_3^r \quad (7.10)$$

Similarly, regression coefficients for a typical  $r = 4$  segment piecewise hysteretic model can be described:

$$a_1^r > a_2^r \quad a_3^r > a_2^r \quad a_1^r \approx a_3^r \quad a_4^r < a_3^r \quad (7.11)$$

A full list of such constraints imposed on  $r$ -segment piecewise hysteretic models is shown



in Table 7.1. Hence, the constrained least sum of squares optimization function in Equation (7.7) allows for approximation of more realistic sub-half cycles, despite issues with noise and higher modes, and which comply with the imposed physical boundaries. This approach makes the hypothesis testing more robust.

Table 7.1: Constrains imposed on HLA

Constrain type	$r$ segment model			
	$r = 1$	$r = 2$	$r = 3$	$r = 4$
Model continuity	-	$g_1(\hat{X}_{t_1}) = g_2(\hat{X}_{t_1})$		
	-	-	$g_2(\hat{X}_{t_2}) = g_3(\hat{X}_{t_2})$	
	-	-	-	$g_3(\hat{X}_{t_3}) = g_4(\hat{X}_{t_3})$
Minimum length	$ X_n - X_1  = \Delta_{r,1}$	$ \hat{X}_{t_1} - \hat{X}_1  = \Delta_{r,1}$	$ \hat{X}_{t_1} - \hat{X}_1  = \Delta_{r,1}$	$ \hat{X}_{t_1} - X_1  = \Delta_{r,1}$
	-	$ X_n - \hat{X}_{t_1}  = \Delta_{r,2}$	$ \hat{X}_{t_2} - \hat{X}_{t_1}  = \Delta_{r,2}$	$ \hat{X}_{t_2} - \hat{X}_{t_1}  = \Delta_{r,2}$
	-	-	$ X_n - \hat{X}_{t_2}  = \Delta_{r,3}$	$ \hat{X}_{t_3} - \hat{X}_{t_2}  = \Delta_{r,3}$
	-	-	-	$ X_n - \hat{X}_{t_3}  = \Delta_{r,4}$
Regression coefficient	-	$a_2^r < a_1^r$	$a_2^r < a_1^r$	$a_2^r < a_1^r$
	-	-	$a_3^r \approx a_1^r$	$a_3^r \approx a_1^r$
	-	-	-	$a_4^r < a_3^r$

More specifically, F-type hypothesis testing is used to identify the optimal number of segments, which approximate the hysteretic model. First, a constrained optimization problem is solved (Equation (7.7)) to identify each  $r$ -phase ( $r = 1, 2, 3, 4$ ) piecewise linear hysteretic model over the specific half-cycle. Each identified  $r$ -phase linear model is defined by regression coefficients  $a_1, b_1 \dots a_r, b_r$  and corresponding breakpoints  $\hat{X}_{t_1}, \dots, \hat{X}_{t_{r-1}}$ . The optimal number of segments,  $r$ , is determined by assuming an  $r = 4$  phase linear model, which is characterised by three break points  $\hat{X}_{t_1}, \hat{X}_{t_2}$  and  $\hat{X}_{t_3}$ . Next, it assumed that  $r = 4$  phase linear model can be approximated by  $r - 1 = 3$  segments. Thus, one of the breakpoints  $\hat{X}_{t_i}$  is removed by considering two segments connected through this breakpoint as a single segment. Then the residual sum of squares is calculated assuming the other break points are kept fixed,  $\hat{X}_{t_j}$ , ( $j = 1 \dots r - 1, j \neq i$ ). The overall residual sum of squares of the assumed  $r - 1$  phase model is calculated:

$$R'_{r-1} = \min_{j=1 \dots r-1} \min_{i=1 \dots r-1} R_{r-1}(\hat{X}_{t_1}, \dots, \hat{X}_{t_{j-i}}, \hat{X}_{t_{j+i}}, \dots, \hat{X}_{t_{r-1}}) \quad (7.12)$$

The hypothesis test is carried out between the null hypothesis  $H_0$  and the alternative hypothesis  $H_1$ . The null hypothesis assumes the hysteresis model can be approximated using  $r$  segments. The alternative hypothesis states the approximated model can be simplified to  $r - 1$  number of segments. The F-type testing is defined [205]:

$$F(r-1|r) = \frac{N(R'_{r-1} - R_r)}{R'_{r-1}} \quad (7.13)$$

where  $N$  is the number of points  $(X_i, Y_i)$  representing the hysteresis loop. Equation (7.13) calculates the relative improvement in overall minimum value of squared residuals (cumulative error) between the approximated  $r$  segment model and assumed  $r - 1$  segment model.

Thus, rejection in favour of a model with  $r$  segments is allowed if the estimated cumulative error of model with  $r$  segments,  $R_r$ , is sufficiently smaller than the estimated cumulative error,  $R'_{r-1}$ , of a model simplified to  $r - 1$  segments. The critical values,  $S_{\theta}^r$ , defining the significance levels of the hypothesis testing are provided by [205]. In this study, the significance level  $\theta$  is set to 0.01, resulting in the following critical values for  $q = 2$  degrees of freedom regression model:

$$S_{0.01}^1 = 16.64 \quad S_{0.01}^2 = 17.98 \quad S_{0.01}^3 = 18.66 \quad (7.14)$$

If rejection in favor of alternative hypothesis is concluded, an  $r - 1$  segment model is assumed to represent the hysteretic model, which has been approximated using the constrained optimization problem in Equation (7.7). Model simplification, by removing one of the breakpoints  $X_{t_i}$  is repeated again and checked for significance test using Equation (7.13) until the alternative hypothesis is rejected. Thus, the best model for  $r = 1, 2, 3, 4$  segments can be found.

Finally, once the optimal number of segments/breakpoints is identified, the regression coefficients  $(a_1, b_1, \dots, a_r, b_r)$  are obtained from constrained optimization analysis as per Equation (7.7).

It must be noted that the proposed number of segments (breakpoints) identification proce-

dure presented here differs slightly from that presented in [147] and [205]. The latter methods initially assume an  $r$  segment model, and then perform F-type hypothesis testing to check the presence of additional breakpoints/segments. In this study, the reverse process is proposed.

Specifically, first, a constrained  $r$  segment piecewise hysteretic model is assumed and then the hypothesis test is carried out to check whether the model can be simplified to a  $r - 1$  piecewise linear model. In addition, the imposed constraints allow identification of realistic hysteretic models, that exhibit expected features, such as elastic loading/unloading, pinching and yielding. Hence, when F-type hypothesis testing is carried out to determine the number of segments, only realistic hysteretic models are compared.

Typically, unconstrained hysteretic models with  $r + 1$  segments will always result in lower or the same residual sum of squares than  $r$  segment model. In some cases, the improvement might be significant enough to assume the presence of  $r + 1$  segments using hypothesis testing, even though the assumed additional segment/breakpoint cannot be associated with any of specific, known hysteresis phases. These spurious segments simply capture higher modes, noise, or data processing error. Therefore, application of the constraints in the optimization function in Equation (7.7) makes the HLA less sensitive to these aforementioned errors, and thus more robust. This overall process is shown as a flowchart in Figure 7.2.

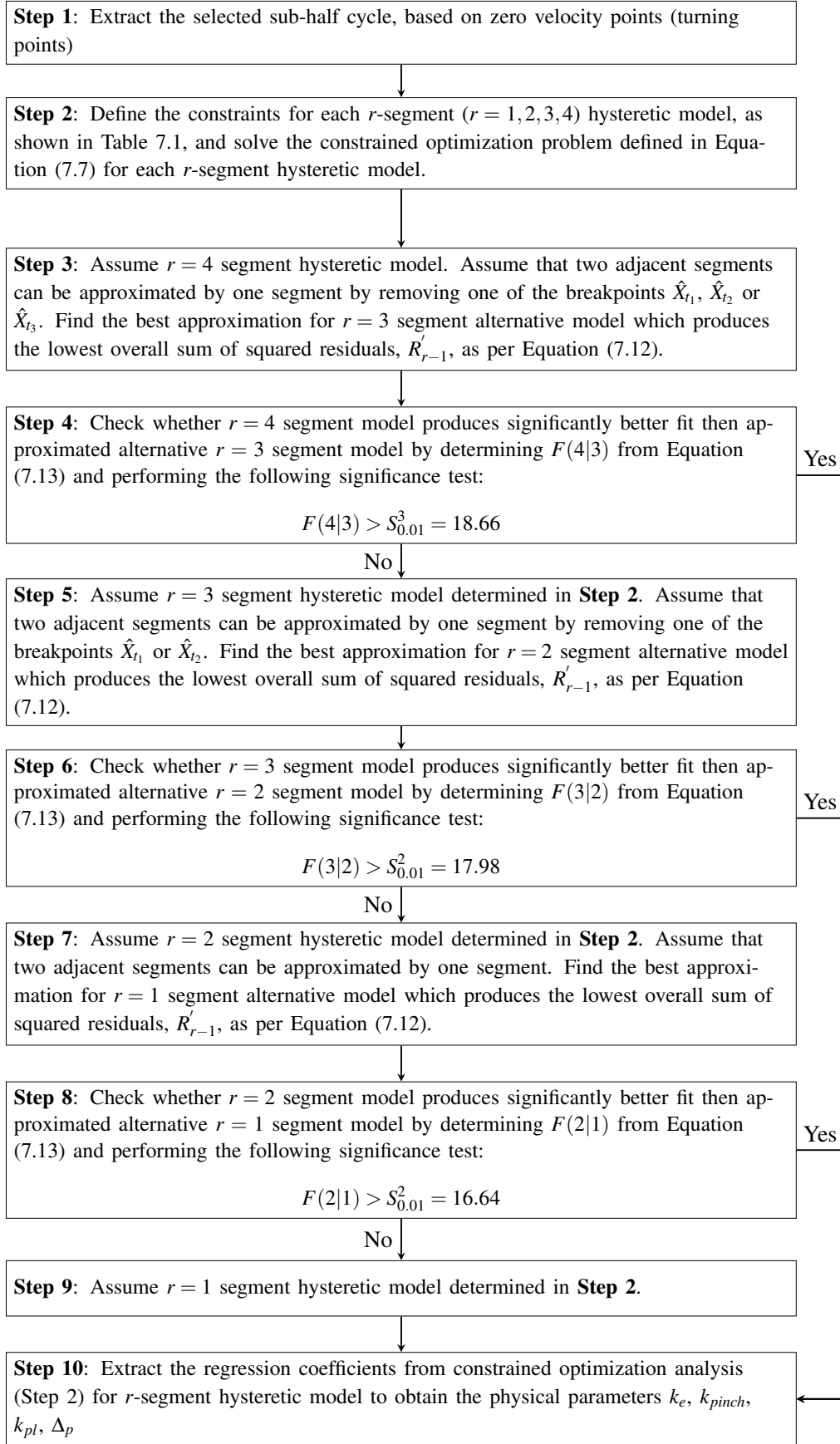


Figure 7.2: Flow chart for optimal number of segments identification for selected sub-half cycle

## 7.3 Method validation

### 7.3.1 Test structure

This section presents the second part of the SHM implementation process. Mode segregation, reconstruction of single mode dominant hysteresis loops and application of HLA are implemented to the full-scale 5-story reinforced concrete structure, which was introduced in Chapter 6. Hence, for brevity, the description of the test structure used to validate aforementioned SHM steps is omitted herein.

### 7.3.2 Analyses

#### Mode decomposition and reconstruction of hysteresis loops for the dominant modes

To take into account the time-varying mode shape coefficients,  $\hat{\Phi}^t$ , Equation (2.2) is re-arranged and expressed in the incremental form:

$$\Delta \bar{X}^{abs}(t) = (\hat{\Phi}^t)^{-1} \cdot \Delta X^{abs}(t) \quad (7.15)$$

Thus, the inter-story stiffness restoring shear force increment vector of the  $i^{th}$  mode can be calculated by substituting Equation (7.15) into Equation (7.1) and re-arranging:

$$\begin{aligned} \Delta V^i(:, t) &= B_{xdir} \cdot M \cdot S_i(t) \cdot (\hat{\Phi}^t)^{-1} \cdot \left[ \Delta \ddot{X}^{abs}(:, t) + 2\xi_i \omega_i \Delta \dot{X}(:, t) \right] \\ &= T_i \left[ \Delta \ddot{X}^{abs}(:, t) + 2\xi_i(t) \omega_i(t) \Delta \dot{X}(:, t) \right] \end{aligned} \quad (7.16)$$

where the term  $T_i = B_{xdir} \cdot M \cdot S_i \cdot (\hat{\Phi}^t)^{-1}$  can be considered as the  $C \times m$  decomposition matrix for the  $i^{th}$  mode and is used to calculate the story shear force increment,  $\Delta V$ , generated by the  $i^{th}$  mode,  $B_{xdir}$  is a  $C \times m$  summation matrix, which adds all the floor inertia forces acting in  $x$  direction (direction of shaking),  $C$  is the number of floors,  $\xi_i(t)$  is the average critical damping ratio estimated from the white noise excitation,  $\omega_i(t)$  is the average identified angular frequency for the  $i^{th}$  mode,  $\hat{\Phi}^t$  is the identified mode shape matrix, and  $S_i$  is the “isolated”  $i^{th}$  mode shape

matrix defined:

$$S_i(t) = \begin{bmatrix} \{0\}_{m \times i-1} & \hat{\Phi}^t(:, i) & \{0\}_{m \times m-i+1} \end{bmatrix} \quad (7.17)$$

The diagonal mass matrix,  $M$ , is defined:

$$M = \text{diag} \left( \left[ \frac{M_{floor}}{2} \quad \frac{M_{floor}}{2} \quad \frac{M_{floor}}{2} \quad \frac{M_{floor}}{2} \right] \right) \quad (7.18)$$

where  $M_{floor} = \begin{bmatrix} m_1 & m_2 & m_3 & m_4 & m_5 & m_6 \end{bmatrix} = \begin{bmatrix} 0.21 & 0.74 & 0.77 & 1.00 & 1.08 & 0.71 \end{bmatrix} kg \cdot 1e^5$  is the floor mass starting from the ground floor. For the FB building configuration the floor matrix,  $M_{floor}$ , is reduced to  $1 \times 5$  matrix by disregarding the ground floor mass.

The relative velocity increment,  $\Delta\dot{X}$ , is obtained by integrating the relative acceleration increment,  $\Delta\ddot{X}$ , and the relative displacement increment,  $\Delta X$ , is obtained by double integration of the relative acceleration increment. Total relative displacement of each floor,  $X_i$ , is filtered using  $2^{nd}$  order high-pass Butterworth filter with cut-off frequency of 0.1Hz to remove only the drift, due to double integration.

Hence, the total inter-story shear force time history can be obtained:

$$V^i(:, t) = V^i(:, t-1) + \Delta V^i(:, t) \quad (7.19)$$

For the BI structure the hysteresis loops for the dominant mode are reconstructed for two independent mechanical hysteretic systems: 1) SDOF system consisting of a soft rubber bearing-rigid superstructure; and 2) SDOF system representing the superstructure's flexural deformation. Total base shear force for the dominant mode is calculated using Equation (7.19) based on the computational model shown in Figure 7.3b. Base isolation deformation is calculated as the average difference between the 1<sup>st</sup> floor and ground displacements. Total superstructure deformation is calculated as the average difference between the roof and the first floor displacements.

For the FB building configuration the hysteresis loops are reconstructed for each inter-story,

as shown in Figure 7.3c.

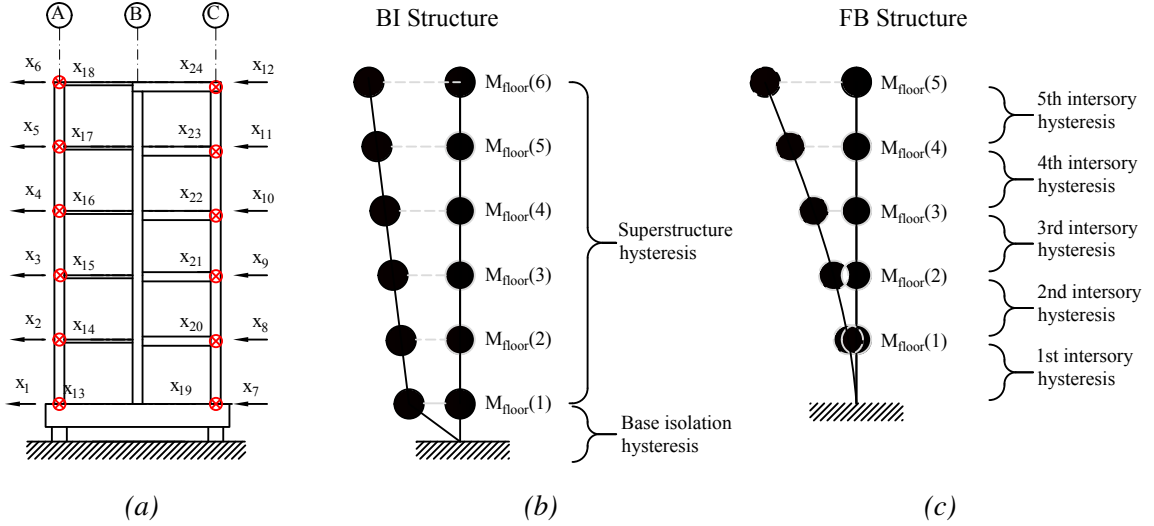


Figure 7.3: a) Structure with monitored 24 DOFs b) Assumed hysteretic model for the BI structure c) Assumed hysteretic model for the FB structure

## Hysteresis loop analysis

The HLA method is applied to single-mode dominant restoring force-displacement sub-half cycles to identify the stiffness components. For the BI structure a typical rubber bearing hysteretic behavior can be characterized using a bi-linear approximation [198], which makes HLA a convenient tool for stiffness identification using one-segment ( $r = 1$ ) and two-segment ( $r = 2$ ) piecewise linear models. The estimated slopes of the identified segments represent the elastic,  $k_{\text{elastic}}$ , and post-elastic,  $k_{\text{post-elastic}}$ , stiffness components of bi-linear model, as shown in Figure 7.4a. The HLA is carried out by imposing the constraints presented in Table 7.1. The minimum length of each segment is set to  $\Delta_{r,i} = 0.002m$  to capture only the significant hysteretic features.

For the FB structure HLA is applied to identify elastic and pinching stiffness components, as shown in Figure 7.4b. The minimum length of each segment is set to  $\Delta_{r,i} = 0.002m$ . In the presence of any structural damage occurring during the monitored time period, the changes are

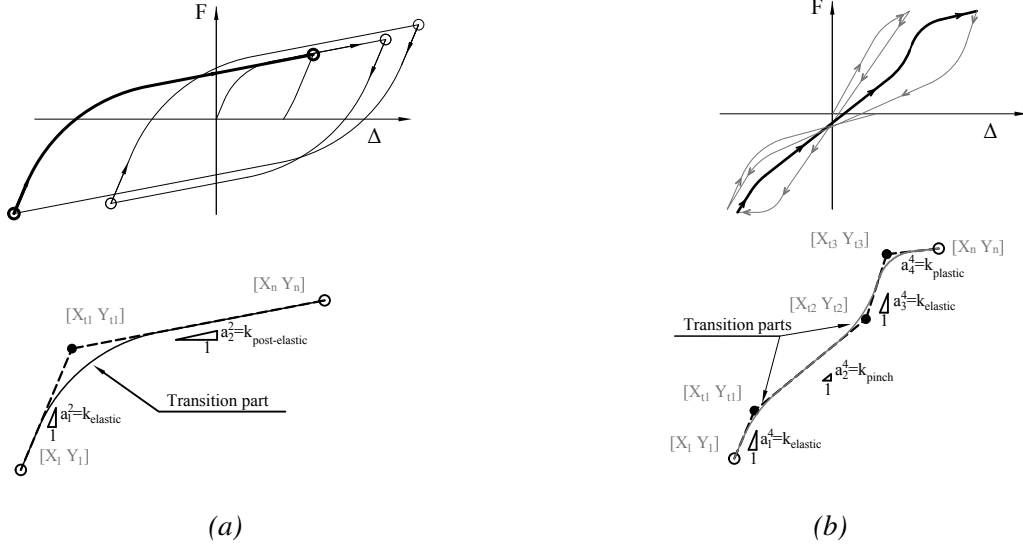


Figure 7.4: a) Typical hysteretic behavior of base isolators and HLA approximation and b) typical hysteretic pinching behavior of RC structure and HLA approximation using  $r = 4$  segment model

captured by degradation of elastic stiffness, which is presented in the form of stiffness evolution plots over time.

## 7.4 Results and Discussion

### 7.4.1 Base isolated structure

#### Hysteresis loop reconstruction

Single mode dominant base isolator and the total superstructure hysteresis loops are reconstructed for HLA implementation. HLA enables physical parameter identification that is easy to interpret and more intuitive, especially for non-linear cases, which is the case for the BI structure. In this study, the hysteresis loops are reconstructed for mode 2-L using the modal filtering process described in Section 6.4.1, which is, by far, the most dominant mode in the structural response. To demonstrate rubber bearing energy dissipative properties, the damping force component from Equation (7.16) is not taken into account,  $\xi_2 = 0\%$ . Thus only the dynamic component is considered.

Base isolator and superstructure hysteresis loops reconstructed from the white noise and



earthquake excitations are shown in Figures 7.5 and 7.6, respectively. Overall, based on visual analysis, hysteresis loops reconstructed for the rubber bearings do not show any obvious signs of strength and stiffness degradation. Muller or scragging effects, defined as a reduction in peak strength and effective stiffness after the first half-cycle [193, 199], can be clearly seen in tests EQ1, EQ2, EQ3 and EQ4.

## Hysteresis loop analysis

### *Base isolator HLA*

HLA is carried out for the stiffness restoring force loops reconstructed for the rubber bearings, shown in Figure 7.5. The identified post elastic stiffness,  $k_{post-elastic}$ , evolution profiles for the base isolator are shown in Figure 7.7. Circles represent the actual identified post elastic stiffness,  $k_{post-elastic}$ , where the solid black line represents the moving average, based on robust locally weighted least squares regression (RLOWESS), which assigns lower weights to outliers in the regression analysis [206]. The identified post-elastic stiffness is compared to the manufacturer's rated stiffness approximated based on pseudo-static tests using a bi-linear model [179].

Figure 7.7 clearly shows the identified post-elastic stiffness,  $k_{post-elastic}$ , is highly variable and excitation dependent. At small amplitude shear displacements, the rubber isolators exhibit relatively stiff behavior,  $k_{p-e,id} \approx 5MN/m$ , compared to the approximated manufacturer's rated post-elastic stiffness,  $k_{p-e,est} \approx 2.5MN/m$ , which results in higher load demands on the super-structure. Notoriously stiff behavior can be observed in the test WN1, which could be related to Muller's effect. However, for the actual design events, the rubber bearings demonstrate significantly softer behavior,  $k_{p-e,id} \approx 2 - 3MN/m$ , which indicates the effectiveness of the base isolation, as designed.

In addition, white noise tests carried out after each EQ event also indicate that the rubber bearings fully recover their mechanical properties. Post-elastic stiffness discontinuities between the tests, as shown in Table 7.2, can be attributed to highly varying hysteretic displacements. During the WN tests the base isolators do not develop the post-elastic regime fully. Thus, the

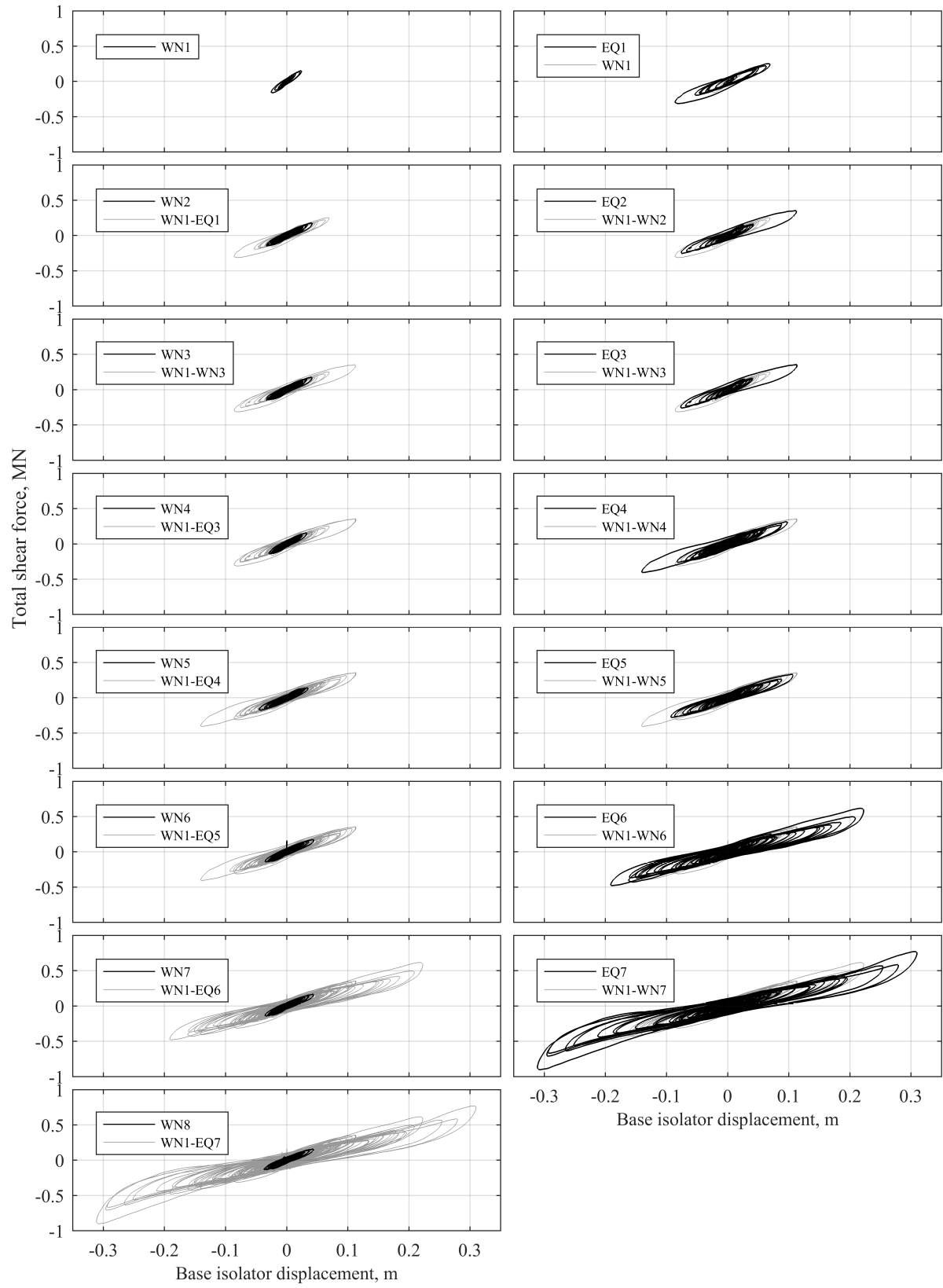


Figure 7.5: Base isolator hysteresis loops reconstructed for white noise(WN) and earthquake excitations (EQ). The grey lines represent restoring force history from the previous cycles

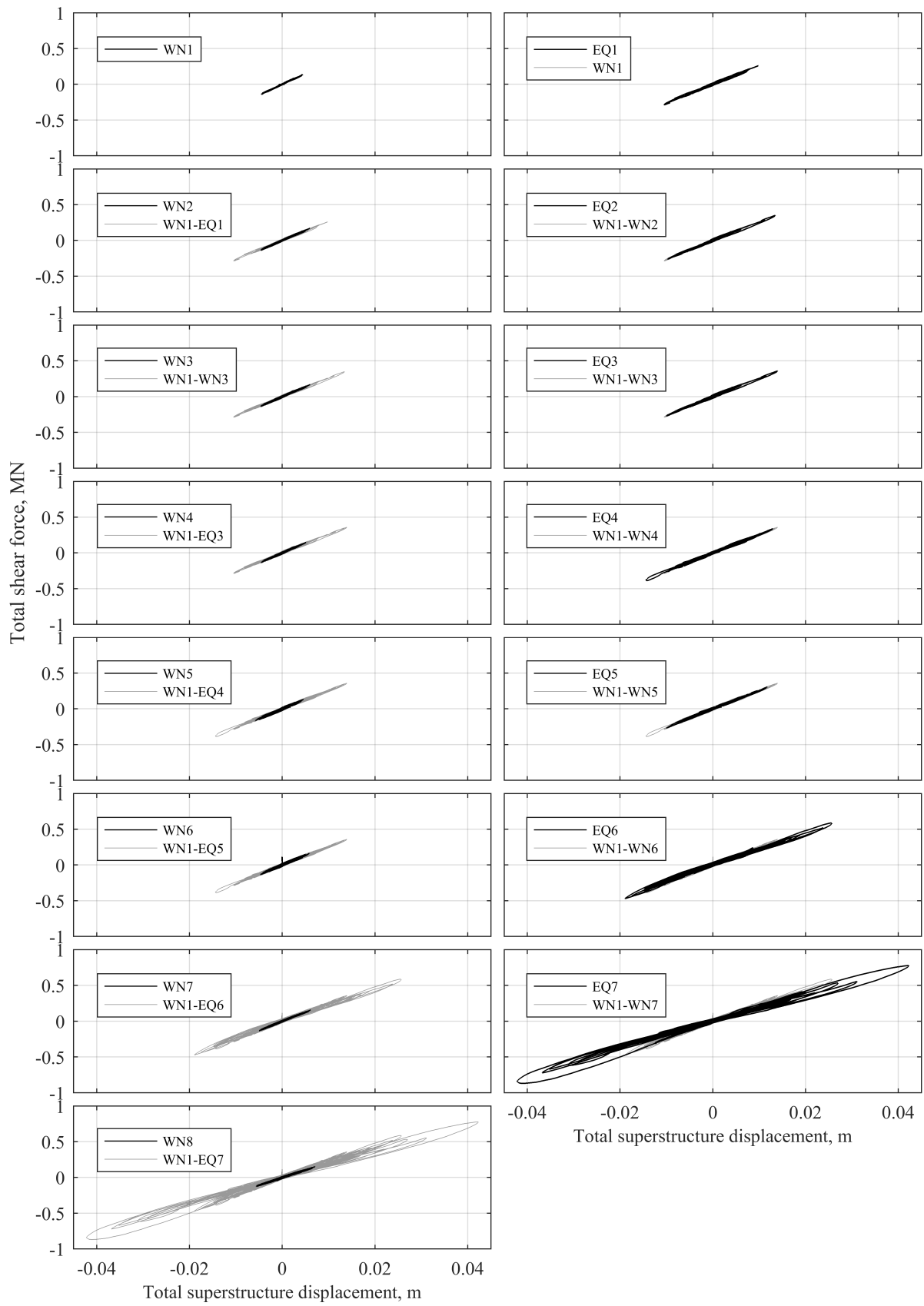


Figure 7.6: Base isolator hysteresis loops reconstructed for white noise (WN) and earthquake excitations (EQ). The grey lines represent restoring force history from the previous cycles

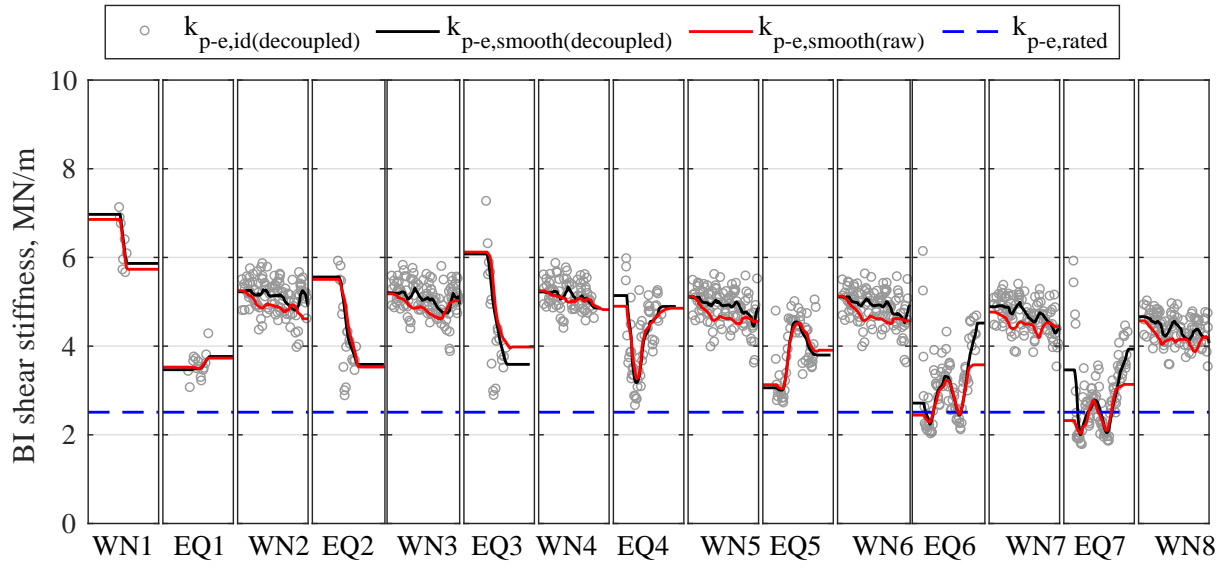


Figure 7.7: Post-elastic stiffness evolution of rubber bearings for earthquake (EQ) and white noise (WN) tests

identified post-elastic stiffness captures the transition part, as shown in Figure 7.4a. In contrast, during the EQ tests the isolators are excited well beyond the elastic regime. For example, in tests EQ5 and EQ6, the base excitation starts abruptly, which results in large hysteretic displacements at the start of the test and consequently lower post-elastic stiffness.

### Superstructure HLA

HLA on the reconstructed hysteresis loops is carried out using one segment fit, which represents an effective shear stiffness of the whole superstructure. The identified elastic shear stiffness evolution is shown in Figure 7.8. Circles represent the actual identified elastic shear stiffness, where the solid black line represents a 10 sample moving average, which is based on robust locally weighted least squares regression (RLOWESS) [206].

The superstructure exhibits relatively stiff,  $k_{eff,id} \approx 32MN/m$ , behavior during the first white noise test (WN1) compared to subsequent tests. Slightly lower effective shear stiffness,  $k_{eff,id} \approx 25MN/m$ , of superstructure can be observed for all strong ground motion test (EQ), which can be attributed to pinching behavior or identification error, since the stiffness is recovered during much lower amplitude response white noise events (WN). Permanent reductions in effective shear stiffness are captured after tests EQ6 and EQ7, which, in total, resulted in an overall 25% reduction to  $k_{eff,id} \approx 21.4MN/m$ . The observed stiffness degradation can

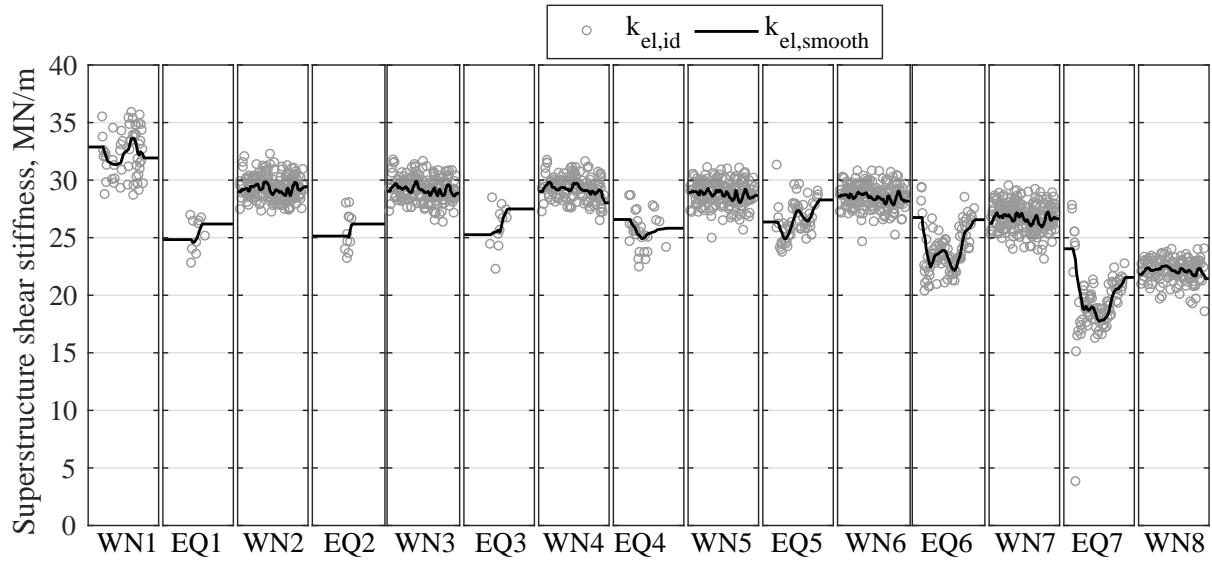


Figure 7.8: Elastic stiffness evolution of the superstructure for earthquake (EQ) tests for the BI structure

most likely be associated to minor concrete cracking, which has been reported in the technical report [179] based on visual inspection carried out after the testing. Overall, as show in Table 7.2, superstructure shear stiffness evolution demonstrates relatively good consistency between the tests, which indicates that HLA method performs robustly, as it was demonstrated in other studies [18, 147, 185].

Table 7.2: Identified total shear stiffness of the superstructure at the start and the end of the earthquake (EQ) and white noise (WN) tests

Test	Base isolator shear stiffness			Total superstructure shear stiffness		
	$k_{start}$ MN/m	$k_{end}$ MN/m	$\Delta k$ %	$k_{start}$ MN/m	$k_{end}$ MN/m	$\Delta k$ %
WN1	7	5.9	-15.9	32.9	31.9	-2.9
EQ1	3.5	3.8	8.6	24.8	26.2	5.5
WN2	5.2	4.8	-8.5	29	29.4	1.5
EQ2	5.6	3.6	-35.4	25.1	26.2	4.2
WN3	5.2	4.8	-7.3	29	28.9	-0.6
EQ3	6.1	3.6	-41	25.3	27.5	8.9
WN4	5.2	4.9	-6.9	29	28	-3.4
EQ4	5.1	4.9	-4.8	26.6	25.8	-2.9
EQ5	5.1	3.8	47.1	28.9	28.3	8.7
WN6	5.1	4.5	-11.1	28.6	28.2	-1.5
EQ6	2.7	4.5	66.5	26.8	26.6	-0.7
WN7	4.9	4.5	-8.8	26.3	26.6	1.5
EQ7	3.5	3.9	13.6	24	21.5	-10.4
WN8	4.7	4.6	-1.3	21.8	21.4	-1.7

### **Unconstrained HLA using raw data**

Base isolator hysteresis loops are also reconstructed using raw acceleration data to show the effect of mode decoupling. Figure 7.9 shows restoring force loops reconstructed for tests EQ3, EQ4 and EQ5. During these tests the higher modes are excited at significantly higher energy, which are successfully segregated using mode decomposition. It is clear that the hysteresis loops reconstructed using mode decomposed data are easier to interpret than raw hysteresis loops, due to the absence of higher mode effects.

Unconstrained HLA [18, 147, 185] is applied to raw base isolator hysteresis loops to demonstrate the effect of mode decoupling. HLA results are shown in Figure 7.7 in the solid red line, representing a 10 sample moving average based on RLOWESS. Although the applied mode segregation method creates "smoother", easy to read hysteresis loops, the resulting HLA provides slightly different results than HLA applied to raw hysteresis loops. Hence, in the situations where a simple bi-linear hysteretic behavior is expected, which can be identified using  $r = 2$  segment piecewise models, hysteretic parameters can effectively be tracked using unconstrained HLA applied to raw hysteresis loops.

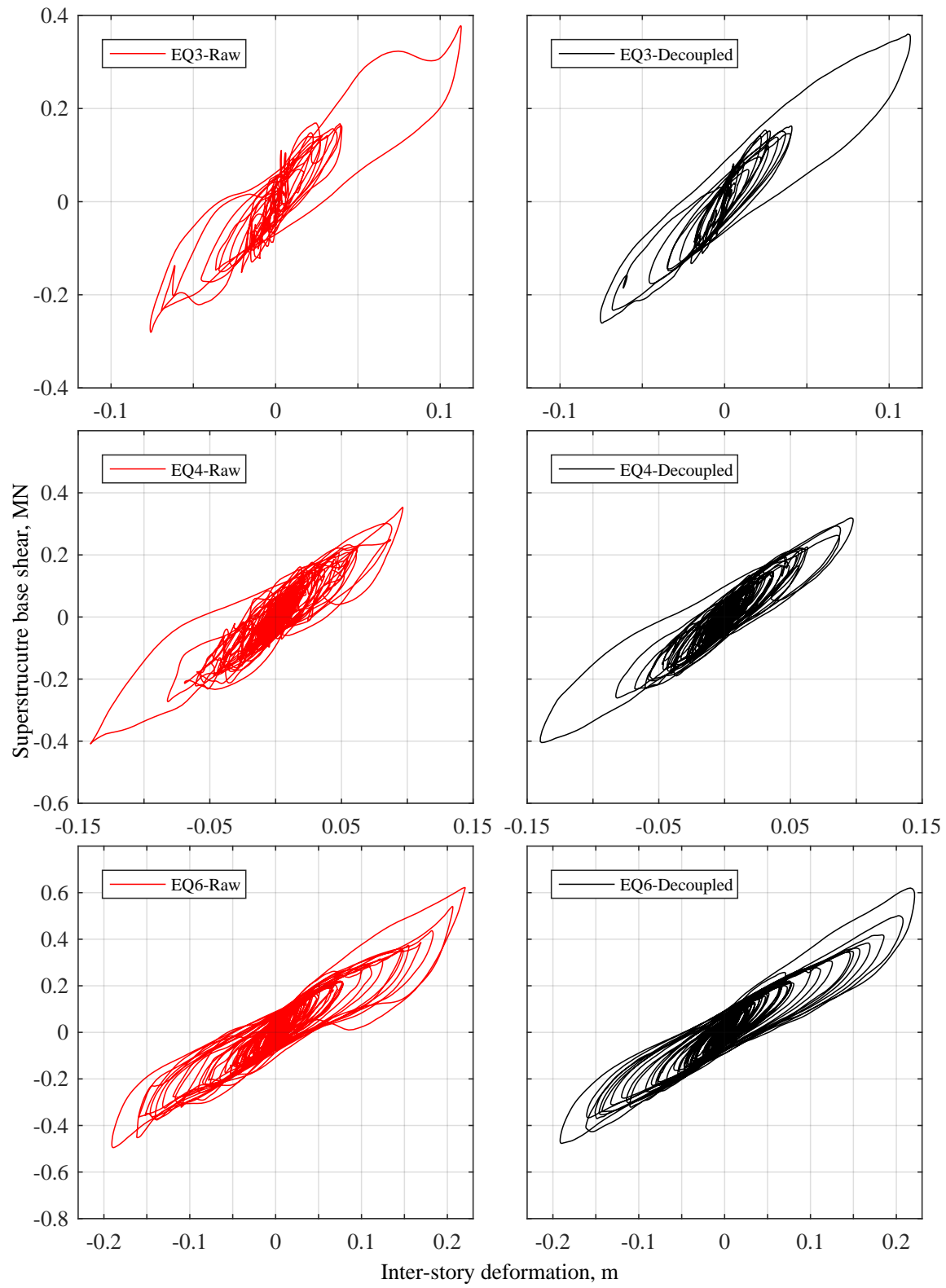


Figure 7.9: A comparison of hysteresis loops reconstructed for tests EQ3, EQ4 and EQ6 using raw (left) and decoupled (red) acceleration data

## 7.4.2 Fixed base structure

### Hysteresis loops reconstruction

The identified evolution of mode shape coefficients presented in Section 6.4.2) enables segregation of the modes and analysis of the response of each mode individually. For SHM implementation of the FB structure, single mode dominant stiffness restoring force hysteresis loops are reconstructed using the segregated response of mode 1-L, which is the most dominant mode in the structural response. Inter-story shear force triggered by mode 1-L is calculated using Equation (7.19). Inter-story shear force versus deformation loops for each inter-story are shown in Figures 7.10 to 7.12. It must be noted that the inter-story restoring force loops are reconstructed using unfiltered raw data and it can be clearly seen that the loops are relatively smooth and almost free of the higher modes for most of the tests, which allows for a direct visual analysis that can be readily applied for HLA. Higher mode contribution seen in hysteresis loops during event EQ6 is most likely caused by the rupture of steel reinforcement, leading to a sudden load redistribution and subsequent acceleration spikes across the floors. Notable stiffness degradation can be clearly seen in tests EQ3 and EQ4 caused by concrete cracking and yielding of the reinforcement. Severe yielding can be observed in tests EQ5 and EQ6. Significant strength degradation can also be seen in test EQ6.

### Hysteresis loop analysis

HLA is implemented for the single mode dominant restoring shear force-inter-story deformation loops in Figures 7.10 to 7.12, reconstructed for the most dominant mode 1-L. Elastic,  $k_{el,id}$ , and pinching,  $k_{p,id}$ , stiffness components are identified for each inter-story, as shown in Figures 7.4b. HLA results are shown in Figure 7.13, where the solid black line represents smoothed pinching stiffness evolution,  $k_{p,smooth}$ , and the dashed line represents smoothed elastic stiffness evolution,  $k_{el,smooth}$ , using a 10 sample moving average based on RLOWESS. To demonstrate and compare the overall load carrying performance of the superstructure between the FB and BI building configurations, HLA is also applied to single mode dominant hysteresis loops recon-



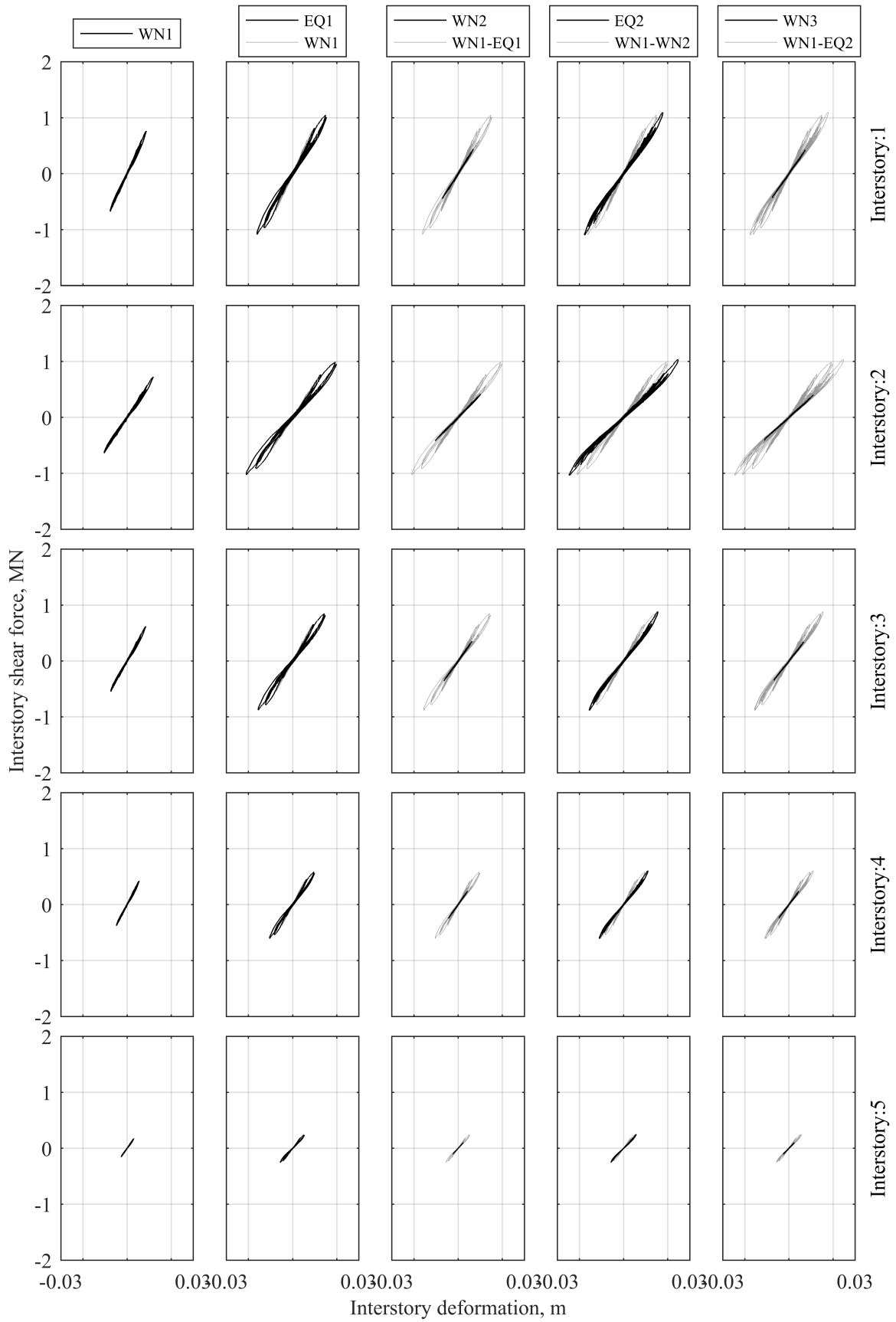


Figure 7.10: Hysteresis loops reconstructed for each inter-story of FB building for tests WN1 to WN3

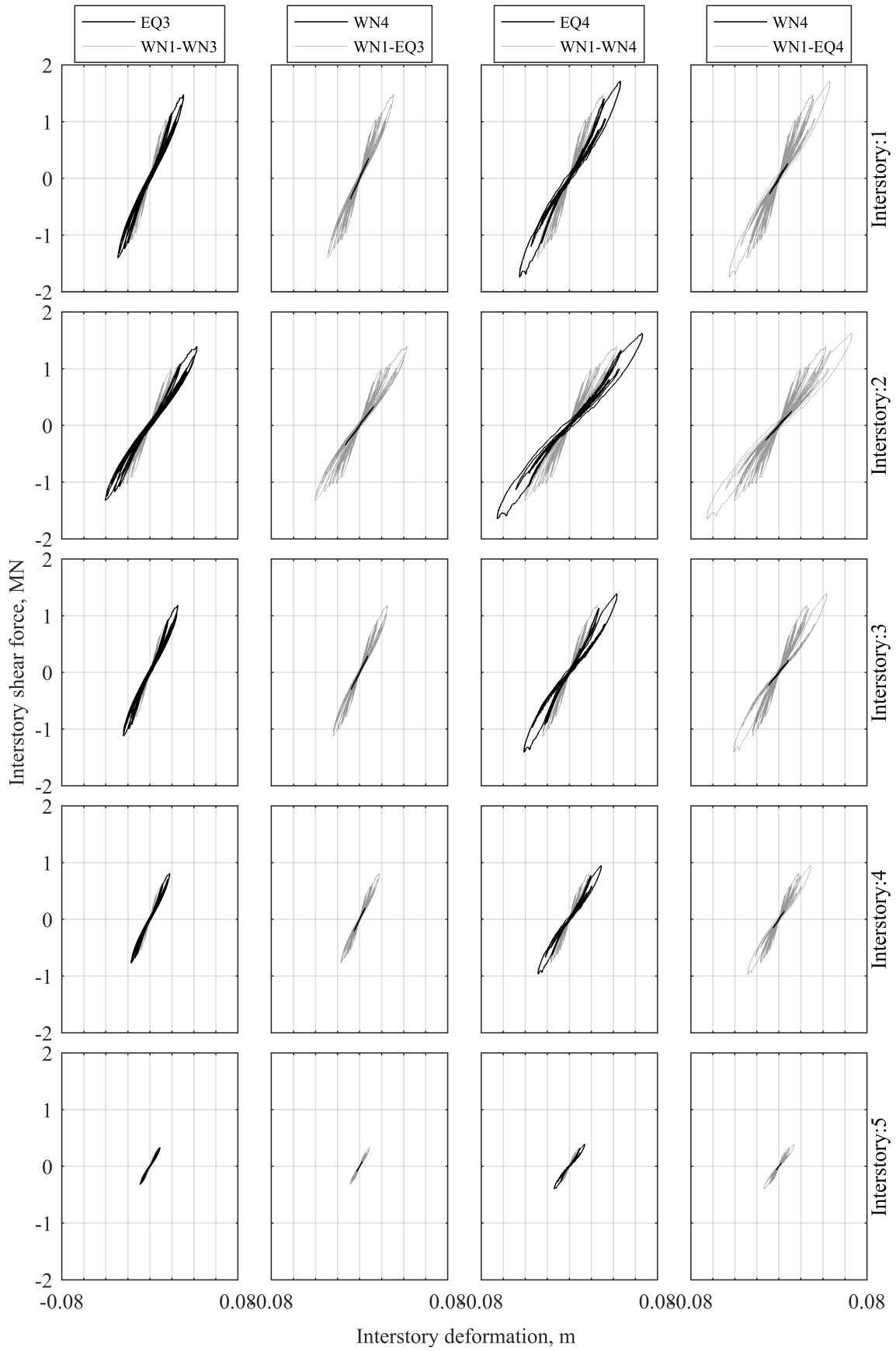


Figure 7.11: Hysteresis loops reconstructed for each inter-story of FB building for tests EQ3 to WN4

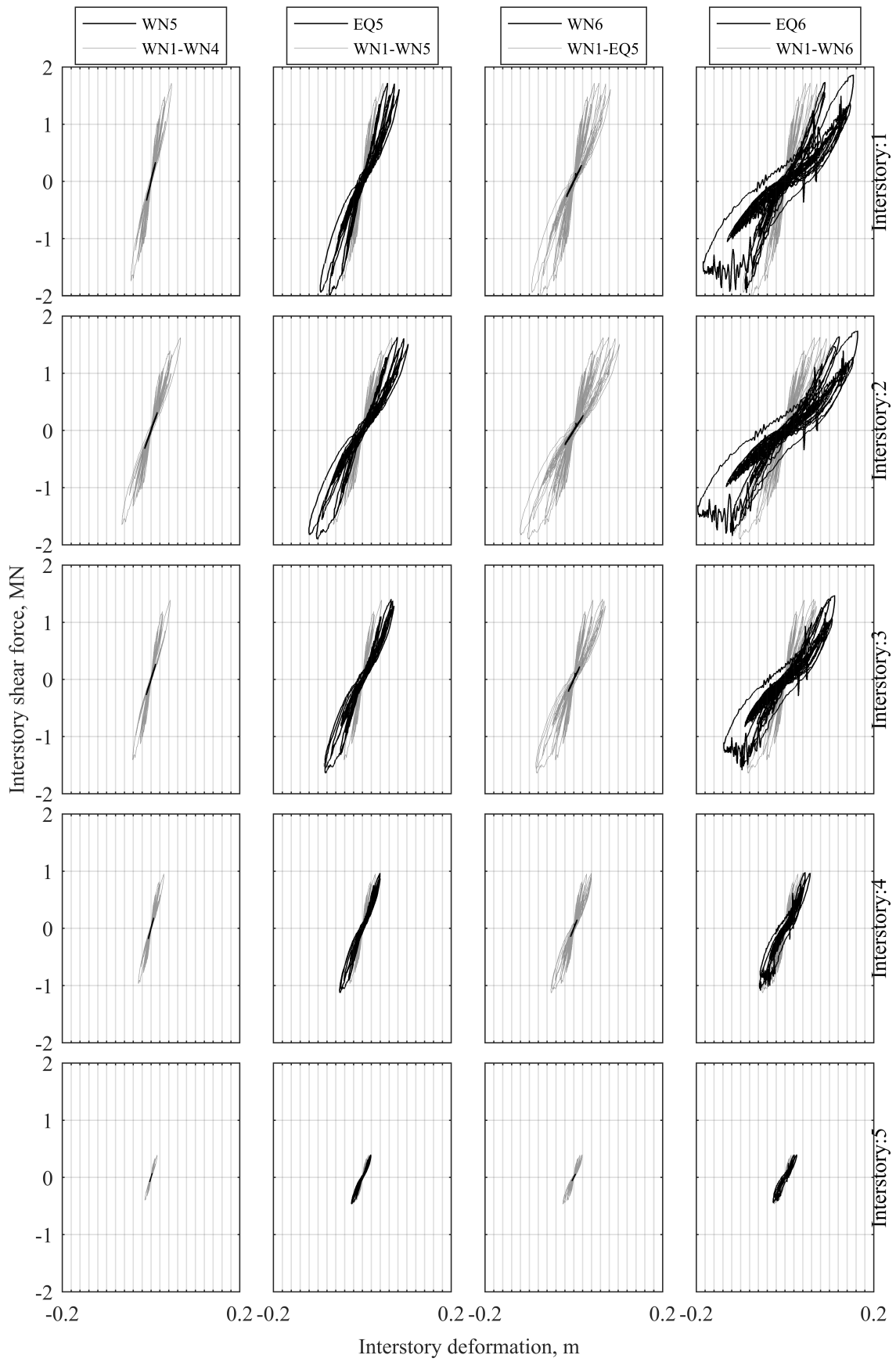


Figure 7.12: Hysteresis loops reconstructed for each inter-story of FB building for tests WN5 to EQ6

structed for the superstructure as a whole. Superstructure HLA results are shown in Figure 7.14.

The elastic stiffness,  $k_{el,id}$ , is captured only at large amplitude vibrations, which are typically triggered by the strong ground motion data. Hence, the elastic stiffness evolution is shown only for the earthquake events. The identified elastic stiffness,  $k_{el,smooth}$ , and pinching stiffness,  $k_{p,smooth}$ , evolution follows very similar trend as the damage progresses. In addition, elastic stiffness evolution,  $k_{el,smooth}$ , demonstrates a lot higher variability, which can be associated with relatively small hysteretic displacements.

The transition part between pinching and elastic regimes is relatively long, meaning if restoring force reversal occurs in the transition regime or shortly after the end of the transition regime, the identified elastic stiffness will be greatly affected by the transition part. Since both identified stiffness components demonstrate a similar trend, it can be concluded that SHM can successfully be implemented based on pinching stiffness evolution alone. Hence, all further HLA discussion will be based on identified pinching stiffness evolution,  $k_{p,smooth}$ . Tables 7.3 and 7.4 provide the identified pinching stiffness values at the start and the end of the test event.

Inter-story shear stiffness degradation (7-20%) can be observed for all the inter-stories for the initial white noise test (WN1), which is most likely attributable to minor concrete member cracking, as the hysteresis loops shown in Figure 7.10 do not indicate any obvious signs of steel reinforcement yielding. A significant loss of stiffness can be seen during the first two strong ground motion tests, EQ1 and EQ2, where the damage has resulted in a 6-30% reduction in shear stiffness for different inter-stories during each test, which can be associated to extensive concrete cracking accompanied by localized yielding. The visual inspection carried out after test EQ2 indicated most of the damage occurred on level 2, where small cracks (0.1mm) were observed in the slab around the north and south central columns, with a minor concrete crushing at the base of NW column. Equally, only very minor cracks were found in the upper floors, further supporting this study.

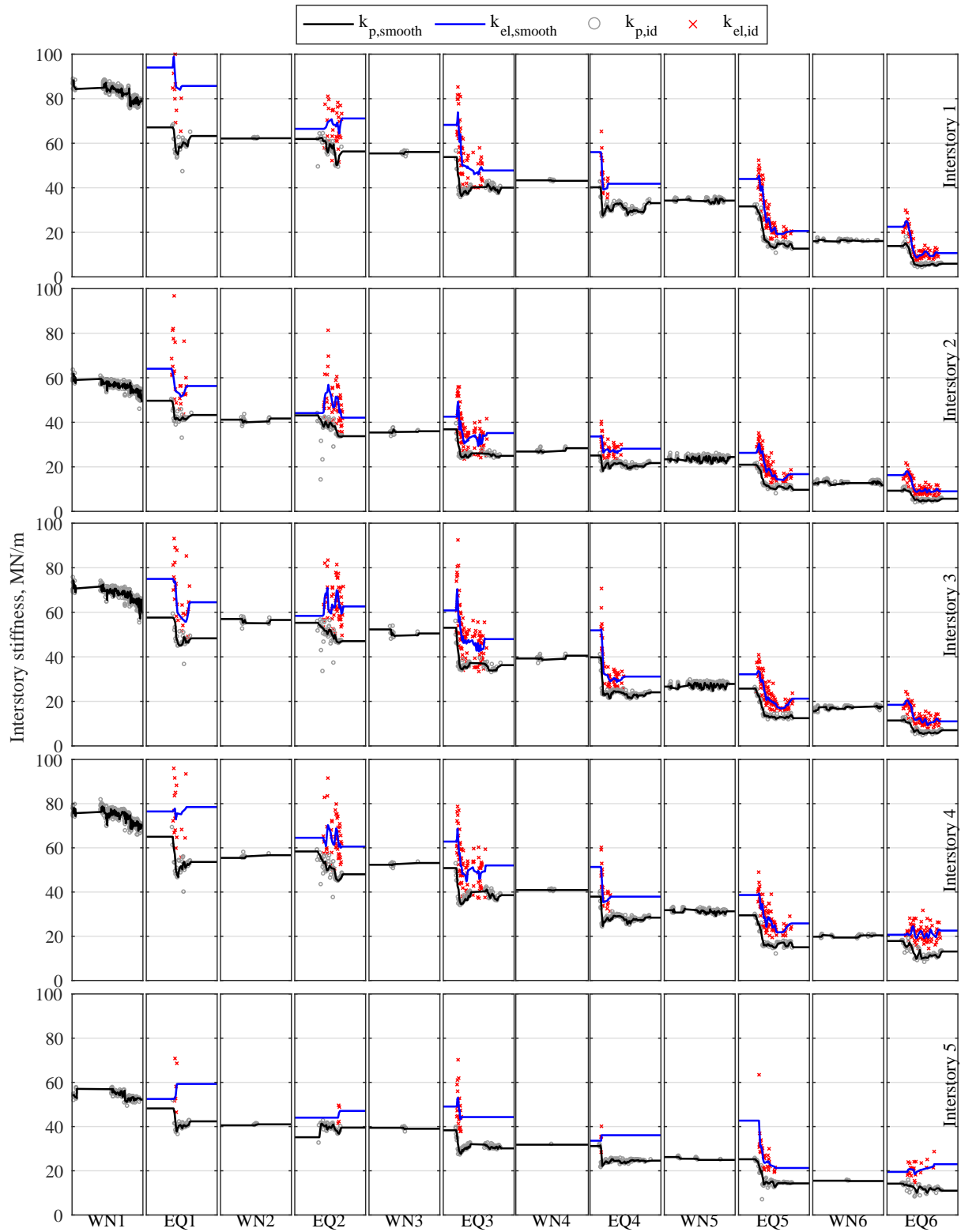


Figure 7.13: Interstory stiffness evolution for white noise (WN) and earthquake (EQ) excitations

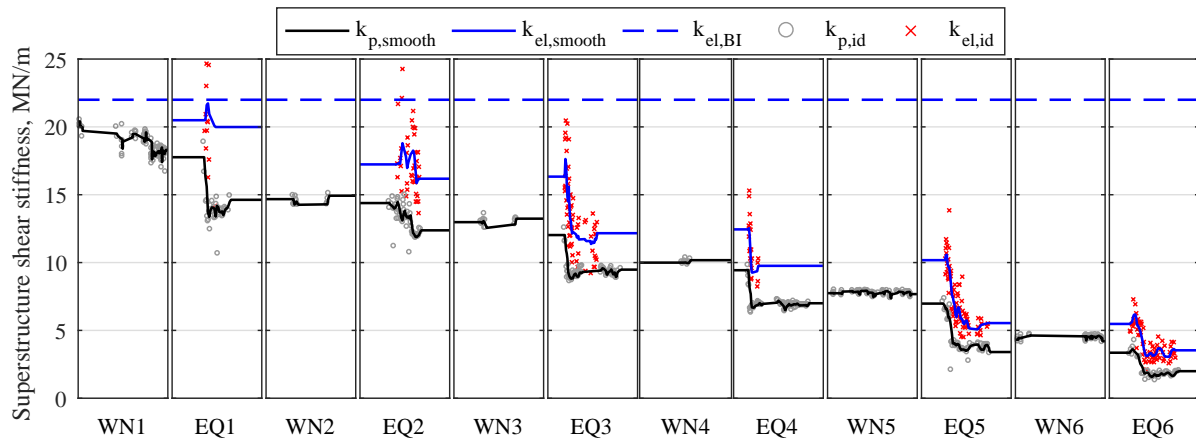


Figure 7.14: Overall superstructure shear stiffness evolution for white noise (WN) and earthquake tests (EQ), where the dashed blue line represents the shear stiffness identified at the end of BI testing, as shown in Figure 7.8

Significant progression in damage is seen for tests EQ3 and EQ4 for all inter-stories as the structure experiences yielding and concrete cracking, resulting in approximately 20-40% shear stiffness reduction after each event. Concrete cracking at the base of the first floor columns, mainly concentrated at the north frame, was observed during the visual inspection. Significant cracking was also reported in the concrete slab and beam elements in different places of level 2. In contrast, significantly less damage was observed for level 3. No additional cracking was observed in level 4 or the roof.

During test EQ5, the structure reached nearly 2.5% inter-story drift, which is the design performance target. Yielding was observed for all inter-stories, which consequently resulted in a 40-60% reduction in inter-story shear stiffness across different inter-stories. According to the visual inspection report, the damage was mainly concentrated at the first three floors, where significant crack propagation and concrete spalling occurred at the base of the first floor columns.

During the last earthquake test, EQ6, the structure experienced significant damage, which led to loss of stiffness from 22% to 57% for different inter-stories. Based on HLA it can be concluded that the damage has concentrated in the first three levels, where 38-57% reduction in stiffness is observed after the test, where the top two levels had a 21-26% loss in stiffness, all of which is supported by the visual inspection observations. Significant concrete spalling was

reported around the base of the first floor columns. Severe damage was observed in different members of second and third levels. In contrast, negligible damage was reported in the 5th and roof levels.

Tables 7.3 and 7.4 summarize the identified shear stiffness values before and after each test. The identified stiffness changes observed during white noise (WN) tests can be attributed to identification error due to relatively small hysteretic displacements. Stiffness inconsistencies between tests are relatively small, within 10%, except for a few tests. For example, the difference between the end of test WN1 and beginning of EQ1 for inter-story 1 was large. In this case, stiffness inconsistencies arise mainly from smoothing effect, as very few significant half-cycles are being identified before the onset of stiffness degradation.

*Table 7.3: Identified inter-story shear stiffness at the start and the end of the earthquake (EQ) and white noise (WN) tests for the FB configuration*

Test	1 <sup>st</sup> interstory			2 <sup>nd</sup> interstory			3 <sup>rd</sup> interstory		
	$k_{start}$ MN/m	$k_{end}$ MN/m	$\Delta k$ %	$k_{start}$ MN/m	$k_{end}$ MN/m	$\Delta k$ %	$k_{start}$ MN/m	$k_{end}$ MN/m	$\Delta k$ %
WN1	88.2	79	-10.4	61.7	49.5	-19.8	74.2	60	-19.3
EQ1	67.1	63.2	-5.8	49.7	43.3	-12.9	57.6	48.3	-16.2
WN2	62.1	62.2	0.2	41.2	41.7	1.3	57	56.5	-0.8
EQ2	61.9	56.3	-9.1	43.1	33.8	-21.7	55.3	47	-14.9
WN3	55.4	56.1	1.2	35.4	36	1.6	52.3	50.5	-3.5
EQ3	53.8	40.1	-25.5	36.9	24.9	-32.3	53.1	36.3	-31.6
WN4	43.4	43.1	-0.5	26.9	28.4	5.6	39.3	40.5	3.2
EQ4	40.2	33.1	-17.7	25.1	21.7	-13.5	39.8	24.1	-39.5
WN5	34.3	34.2	0	23.4	24.4	4.3	26.6	27.8	4.5
EQ5	31.6	12.7	-59.9	21	9.7	-53.7	25.7	12.5	-51.6
WN6	16	16.1	0.6	12.4	11.7	-5.5	15.5	17.6	13.1
EQ6	13.8	5.9	-57.3	9.3	5.7	-38.8	11.4	7.1	-38.3

Overall shear stiffness of the superstructure is calculated in a similar manner as for the BI structure and can be described as the total base shear force versus total roof drift. Identified elastic and pinching shear stiffness evolution of the superstructure is shown in Figure 7.14. The blue dashed line represents the identified shear stiffness of the superstructure at the end of BI structure testing, as shown in Figure 7.8. The identified pinching shear stiffness at the start of the testing protocol (EQ1),  $k_{p,smooth} = 20MN/m$ , is slightly lower than the identified stiffness at the end of BI structure testing protocol,  $k_{el} \approx 22MN/m$ , and can be attributed to higher amplitude

Table 7.4: Identified inter-story shear stiffness at the start and the end of the earthquake (EQ) and white noise (WN) tests for the FB configuration

Test	4 <sup>th</sup> interstory			5 <sup>th</sup> interstory			Total		
	$k_{start}$ MN/m	$k_{end}$ MN/m	$\Delta k$ %	$k_{start}$ MN/m	$k_{end}$ MN/m	$\Delta k$ %	$k_{start}$ MN/m	$k_{end}$ MN/m	$\Delta k$ %
WN1	76.6	70.1	−8.5	54.3	52.2	−3.8	20.4	18.3	−10.3
EQ1	65	53.6	−17.5	48.2	42.4	−12.1	17.8	14.6	−17.7
WN2	55.5	56.7	2.2	40.6	41	1.1	14.7	14.9	1.7
EQ2	58.4	48	−17.7	35.2	39.5	12.4	14.4	12.4	−14
WN3	52.3	53.1	1.5	39.5	39	−1.1	13	13.2	2
EQ3	50.8	38.6	−24.1	38.3	30.1	−21.3	12	9.5	−21.2
WN4	40.9	40.9	0	31.8	31.8	0	10	10.2	1.8
EQ4	37.9	28.4	−25.1	31.2	24.6	−21.2	9.4	7	−25.8
WN5	31.8	31.3	−1.6	26.2	24.9	−5	7.7	7.7	−0.9
EQ5	29.5	15	−49	25.2	14.3	−43.3	7	3.4	−51.2
WN6	19.8	20.4	3.1	15.5	15.4	−0.9	4.3	4.2	−2.5
EQ6	17.9	13.1	−26.7	14.2	11	−22.5	3.4	2	−40.6

vibrations, since the effective stiffness is excitation dependent.

### Unconstrained HLA using raw data

A comparative study is carried to demonstrate the effect of mode decoupling and application of constrained HLA. Inter-story shear force versus deformation loops are reconstructed using raw acceleration data and then subsequently analysed using unconstrained HLA method [18, 147, 185]. For brevity, raw hysteresis loops are presented herein only for tests EQ4 and EQ5, as shown in Figure 7.15 and Figure 7.16. These tests demonstrate a prominent contribution from the higher modes, thus can best illustrate the effect of mode decoupling. It is obvious that hysteresis loops reconstructed only for mode 1-L are significantly smoother, especially for the higher inter-stories.

Unconstrained HLA is carried out for raw inter-story shear force-deformation loops and compared with the HLA results presented in Figure 7.13. The comparison is shown in Figure 7.17, where only pinching stiffness evolution profiles are compared for each test. Comparison study suggests that application of mode decoupling in conjunction with constrained HLA provides marginally more accurate evolution of stiffness. Better agreement can be seen between the identified stiffness at the end of test and the start stiffness of the successive test. In addi-



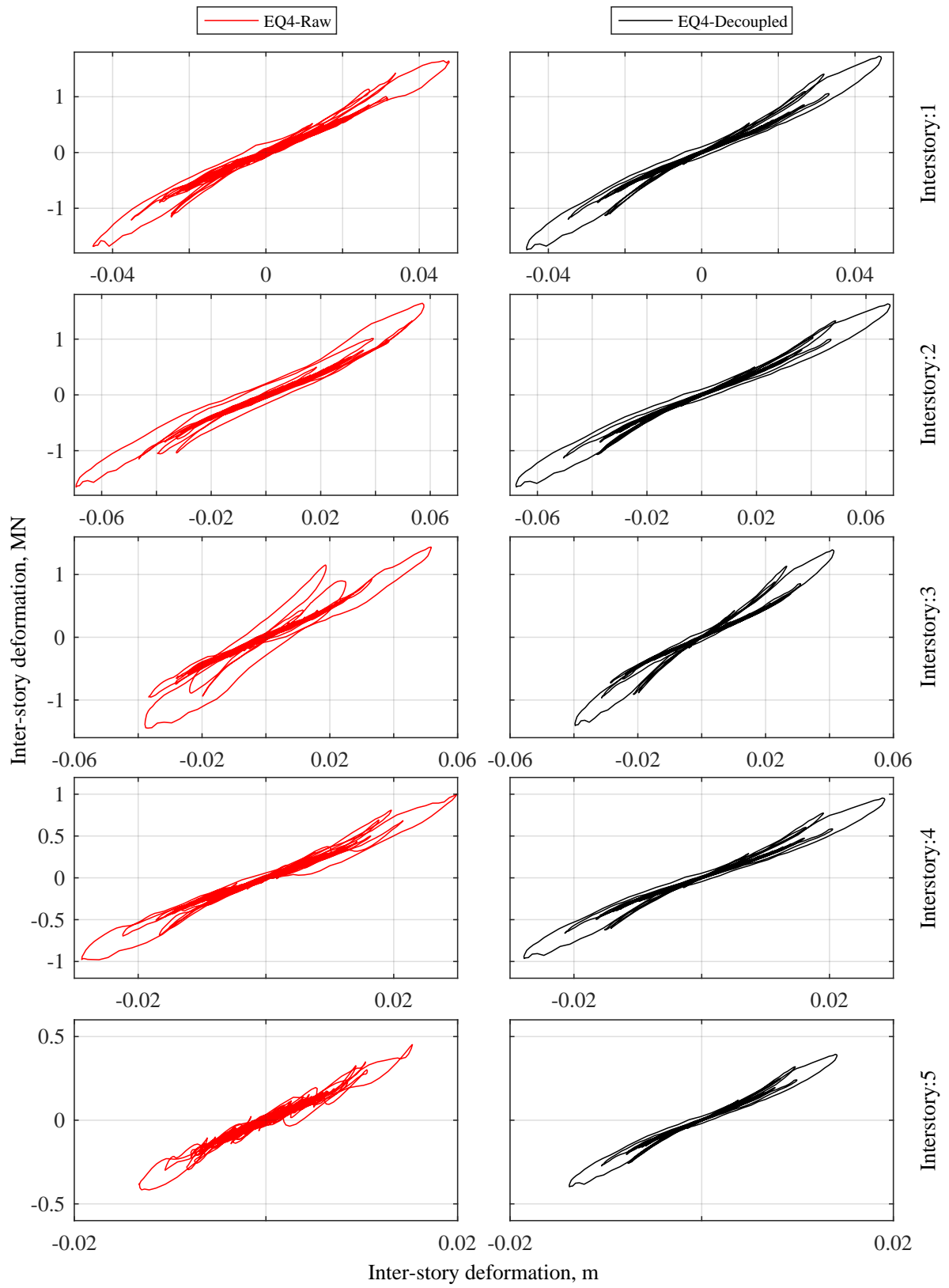


Figure 7.15: Comparison of inter-story shear force versus displacement loops reconstructed for test EQ4 using raw (left) and decoupled (right) acceleration data

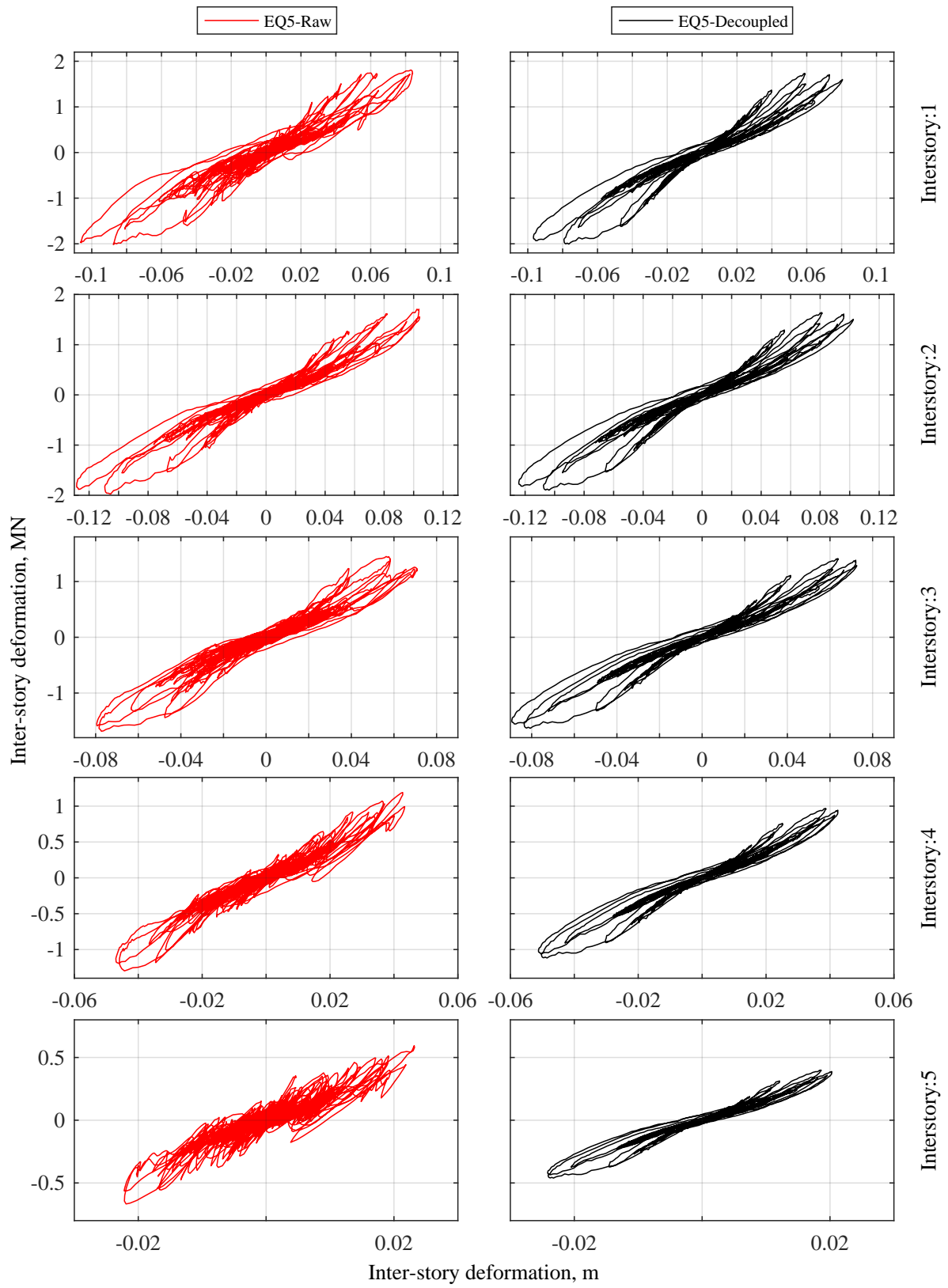


Figure 7.16: Comparison of inter-story shear force versus displacement loops reconstructed for test EQ5 using raw (left) and decoupled (right) acceleration data

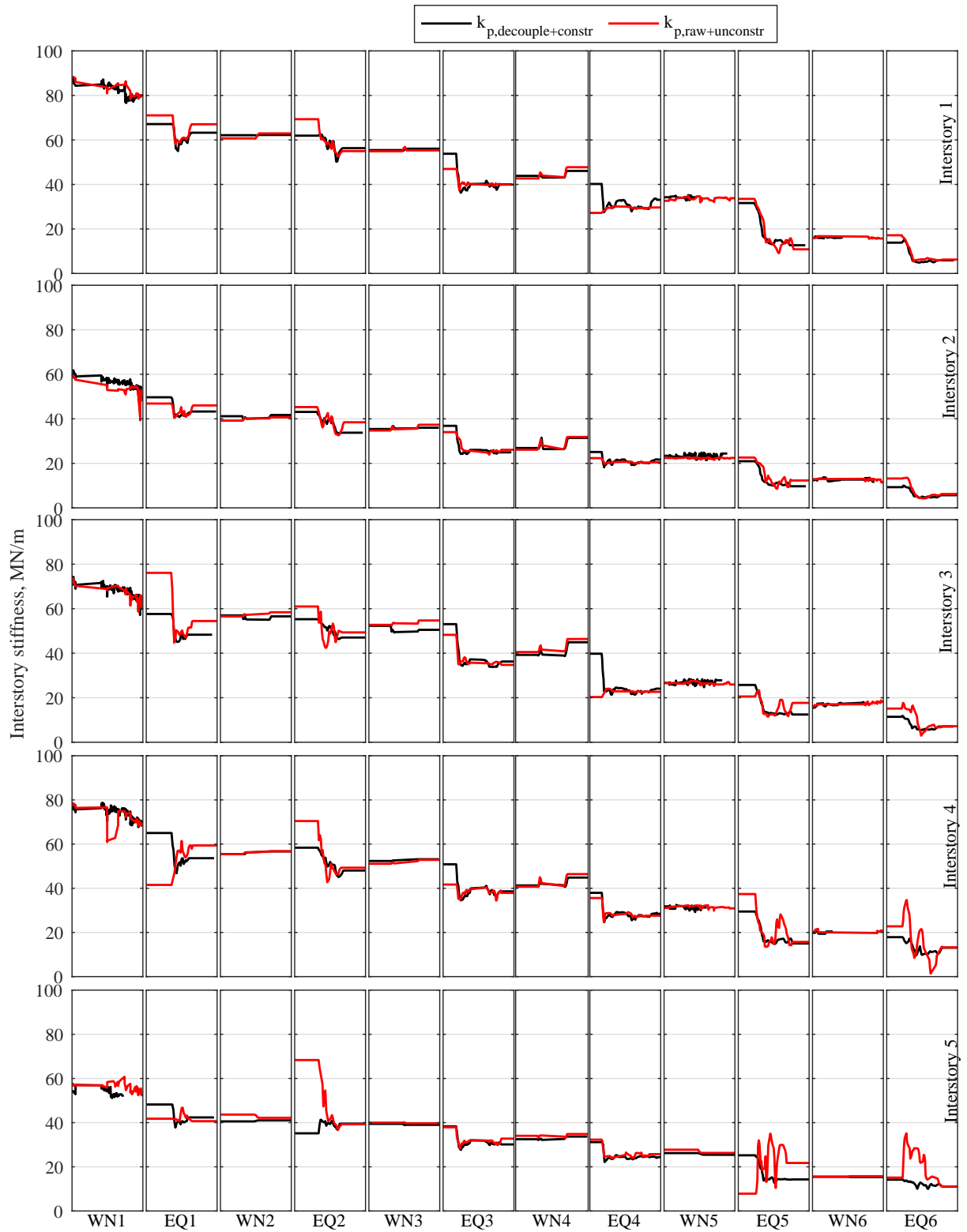


Figure 7.17: A comparison of inter-story pinching stiffness evolution profiles obtained using decoupled (black) and raw (red) hysteresis loops for white noise (WN) and earthquake (EQ) excitations

tion, more regular evolution of stiffness profiles can be seen during strong ground motion tests, especially for the higher inter-stories.

## 7.5 Summary

This chapter presents the second part of a novel SHM technique, which is capable of tracking stiffness components of non-linear hysteretic structures. The method is based on modified hysteresis loop analysis (HLA), which is applied to reconstructed single mode dominant hysteresis loops. Path dependent restoring force-deformation loops are reconstructed using mode decomposed data, which is approximated using the identified time-varying modal parameters (frequency, damping ratio and mode shapes).

The presented SHM technique is applied to a full-scale five-story test structure, which was tested for two structural configurations: 1) base isolated (BI) and 2) fixed based (FB). Hysteresis loop reconstruction and HLA are applied to both building configurations. For the BI structure, the hysteresis loops are reconstructed for two independent hysteretic systems: base isolator and superstructure. The results show that the base isolators exhibit highly non-linear behaviour, which demonstrates expected stiffness softening and isolation with increasing ground motion intensity. No significant changes in stiffness are observed after strong ground motion events, which could be related to damage. In contrast, HLA on the reconstructed hysteresis loops of the superstructure indicate the presence of structural damage after the first and last two earthquake events. Based on the visual analysis of the reconstructed hysteresis loops, it can be concluded that the experienced damage is minor and can be most likely related to concrete cracking.

For the FB building configuration the hysteresis loops are reconstructed for each inter-story. The identified stiffness components clearly indicate a progressive damage through stiffness degradation, which is induced by increasing intensity ground motion input. However, as the building is designed according to strong beam-weak column concept, with expected energy dissipation through formation of plastic hinges in the beam elements in multiple floors, it is difficult to estimate damage location accurately.

Reconstruction of overall superstructure hysteresis loops and HLA may be especially appealing to structural engineers when estimating the damage due to its intuitive meaning. A typical structural design or assessment process often involves the pushover analysis, which characterizes the expected backbone path of an overall restoring force under different imposed displacements. Hence, the reconstructed hysteresis loops obtained can be directly overlapped and compared with the estimated backbone curve to estimate the performance and infer the remaining capacity of the structure.

Overall, the results show that the proposed SHM implementation strategy consisting of modal parameter identification and constrained HLA is robust and effective in tracking the performance of non-linear structures. Although the analyzed full-scale test structure did not exhibit very large contribution from the higher modes for all tests, few tests demonstrated potential advantages of proposed SHM strategy consisting of mode decomposition and constrained HLA. Based on findings of this study, it should be noted, that the robustness of HLA can be improved by decomposing the response and/or applying constraints to HLA itself. Finally, the proposed technique can be implemented as a nearly real-time system and directly used to estimate the structural damage effectively immediately after an event.

## CHAPTER 8

---

### Conclusions

---

This thesis proposed a two step SHM implementation strategy consisting of: 1) damage identification, and 2) damage quantification. For damage identification, a novel modal parameter identification method is developed in this work. For damage quantification, the application of a recently developed hysteresis loop analysis (HLA) is explored, particularly for cases where higher modes interfere with response and make HLA methods less accurate and effective.

The developed modal parameter identification technique addresses some of the limitations of existing methods currently used for system identification. More specifically, the introduced method allows near real-time modal parameter identification and can be used to track the performance of non-linear structures subjected to earthquake excitation. The identified modal parameters and detected changes can indicate the presence of damage, but typically provide limited information about damage location, severity and type directly. Thus, a method based on mode decomposition and reconstruction of single mode dominant hysteresis loops is explored. The revised, filtered hysteresis loops produced can be subsequently assessed using HLA to precisely quantify the damage and location. In turn, the HLA method provides operators with easy to interpret information, which can be conveniently used by professional practitioners of engineering for immediate and long term decision making.

The development and validation of a novel modal parameter identification method was presented in Chapters 2, 3, 4 and 6 of this thesis. The subsequent application of HLA for damage

identification was explored in Chapters 5 and 7. These validation studies include numerical, known cases, and independent experimental cases.

Chapter 2 presented the methodology for a novel output-only modal parameter identification technique. The method is limited to linear structures and can perform identification using long duration recorded response. The technique is based on iterative mode-by-mode optimization, which minimizes cross-correlation of frequency response spectra of interfering modes. The method relies on mode superposition and can perform system identification using both white noise and earthquake input excitations as demonstrated on the simulated response of a 4 DOF time-invariant linear structure. It performs equally robustly to both input excitation types and demonstrated good accuracy for high levels of noise added to response and excitation data.

Chapter 3 presented an extension to the output-only modal parameter identification. The method takes advantage of measured input excitation, thus considered an input-output identification technique. The technique is based on the same principle as the output-only identification the decoupling frequency response spectra of interfering modes through iterative optimization. However, using the measured input excitation enables formulation of an objective function utilizing two different frequency response spectra, namely, the receptance and inertance spectra. This innovation allows for more accurate system identification, which can be carried out over relatively short response windows enabling near real-time tracking of the active modes of the system response exhibiting non-linearities.

The presented input-output modal parameter identification technique is subsequently validated for the simulated non-linear response of a 4 DOF non-linear structure subjected to different types of bi-directional input excitation. A sensitivity study quantified the influence of different parameters on the identification accuracy. Although the technique requires estimation of the mass matrix, the analysis shows even 30% error in mass matrix estimation has a relatively small effect on mean absolute error. The results demonstrated the method is robust and effective in identifying time-varying modal parameters even for high levels of added noise (20% RMS).

Chapter 4 presented the validation results of the input-output identification technique developed in Chapter 3. Validation was carried out using non-linear simulation results of a more complex FE model. A fiber element formulation was utilized to simulate the non-linear response of a 2D FE model representing a simplified version of an experimental 5 story RC structure. This type of FE allows analysis of realistic effects of non-linear behavior resulting in a varying stiffness matrix transferring into varying mode shape coefficients.

The method's results showed the simulated mode shape coefficients may exhibit significant variations and the degree of variability increases with increasing non-linearity and increasing mode order, while accurately capturing modeled non-linear behaviour. In particular, the mode shape identification algorithm successfully captures the average variation of simulated mode shapes for the lower, dominant modes. In contrast, identification of the higher modes yielded relatively poor results for some earthquake inputs, mainly attributed to low signal-to-noise ratios, as some earthquakes contained spectral energy concentrated in a narrow frequency range, leading to poor excitation of some modes. Overall, this study demonstrated the applicability of the novel input-output identification technique to structures exhibiting strong non-linearities, validated against known structure properties.

In Chapter 5, the proposed modal parameter identification technique and its application with HLA is validated for a full-scale experimental reinforced concrete bridge pier. The analyzed test structure was subjected to 9 increasing intensity earthquake excitations and had a notable contribution from at least two modes. The results show the method is robust in tracking time-varying modal parameters. However, the identified mode shapes demonstrated relatively low sensitivity to light levels of damage such as concrete cracking. The identified modal frequencies indicated a clear degradation suggesting the loss of stiffness caused by damage. In contrast, the identified equivalent damping of the second mode increased consistently with increasing levels of damage. Hysteresis loops reconstructed using the decomposed response demonstrated excellent regularity, and could be readily used for primary visual inspection and HLA. The HLA method



applied to single mode dominant hysteresis loops clearly quantified and localized the degradation of elastic stiffness. Overall, the proposed SHM strategy demonstrated a good potential in identifying and tracking the performance of non-linear hysteretic structures.

A similar validation study for the proposed SHM implementation strategy was carried using test results of a more complex full-scale 5-story reinforced concrete structure in Chapters 6 and 7. In Chapter 6, the experimental structure was tested for base isolated and fixed base structural configurations. The results demonstrate the identification technique is robust in tracking the modal parameters of base isolated and fixed based structures exhibiting highly non-linear behavior. The identified changes in modal parameters indicated the presence of damage, which was then refined using HLA in Chapter 7.

Chapter 7 presented the validation results of the recently developed HLA applied to single mode dominant hysteresis loops reconstructed using a modal decoupling technique. It shows the modal parameter segregation method enables extraction of regular shaped, "smooth" hysteresis loops that are easy to interpret. The HLA was modified by adding constraints to extract more realistic hysteric models. The subsequent application of the modified HLA quantified the damage for both structural configurations in terms of stiffness evolution. The original HLA method was also applied to raw hysteresis loops, reconstructed using unprocessed accelerations to quantify the improvements. A comparison study showed the proposed two step technique had marginal advantages over HLA applied to raw hysteresis for this analyzed test structure due to limited participation of the higher modes in this specific test case.

Overall, this thesis presented a 2 step SHM process consisting of a novel modal parameter identification and its subsequent application to recently developed HLA. The proposed modal identification extends the limitations of modal SHM to non-linear cases and earthquake inputs. The technique performs without any operator input and can be easily automated to track the modal parameters and detect damage. Validation studies carried out to simulated and test structures demonstrated the proposed strategy is robust and efficient in tracking non-linear behavior

of systems subjected to various types of input excitation. The presented method is novel, computationally efficient, and demonstrates great potential to be used for near real-time SHM, stand alone and/or in combination with other SHM methods to quantify damage. However, its full limitations and wider applications need to be investigated further.

## CHAPTER 9

---

### Future research

---

#### 9.1 Improving time resolution and accuracy of modal parameter tracking

The proposed modal parameter identification operates in modal space and is based on decoupling frequency response spectra (FRS) of modal responses contributing to the total response with significant energy. FRS of modal response is computed using Fast Fourier Transformation (FFT) over selected relatively short time segments. In this thesis, validation studies were carried out for simulated and experimental response data segmented into moving  $L = 8$  to 10 seconds windows. However, the validation study carried out for the simulated highly non-linear structure in Chapter 5 demonstrated that the simulated mode shape coefficients might exhibit a very high temporal variation. However, the proposed modal identification method identifies only the average variation of mode shape coefficients for selected response window.

Hence, to improve the time resolution and accuracy the mode shape identification, future work could analyse the following extensions/variations to the method:

- The use of shorter time windows could provide more accurate variation. However, the minimum window length is often limited by the properties of FFT, which provides poor frequency resolution for short time windows resulting in inaccurate identification. Wavelet transformation is known to be superior to windowed Fourier transformation, when bet-

ter frequency resolution is desired. Thus, future work could investigate the application of wavelets to enable the analysis of shorter time windows and increase the time resolution of varying modal parameters.

- In addition to the application of wavelets, future work could analyse the application of mode shape coefficient shape functions, which would mimic/approximate the temporal variation of simulated/true mode shape coefficients.

## **9.2 Identification using limited number of DOFs**

The majority of the validation studies carried out in this thesis used a complete or nearly complete set of response measurements to identify modal parameters. Future work should analyse the robustness of method for cases where a limited amount of sensors is available. More specifically, the proposed modal identification technique should be validated for cases where the number of relatively active modes is higher than number of measured DOFs, which is very common for bridge SHM situations, and in buildings with sparse instrumentation.

## **9.3 Formulation of objective functions using raw FRS**

For the proposed novel modal identification method, mode shape coefficients are identified through an iterative optimization process. The objective function is formulated by estimating the weighted sum of cross-correlations of normalized modal response FRS, per Equations (2.14) and (3.6). Some validation studies demonstrated that the use of raw FRS may yield more robust modal parameter tracking, especially for the cases with low signal-to-noise ratios, as it adds some extra weighting to modal FRS. Hence, the use of raw FRS should be subjected to further investigation in the future studies.

## 9.4 Identification of non-classically damped systems

The proposed modal identification technique is based on mode decomposition. It assumes the modes can be fully segregated and the modes are classically damped. However, for non-classically damped systems the modes cannot be fully delineated due to mode coupling. Hence, future studies should assess the performance of the method for these cases or investigate modifications to the method to accommodate the identification of non-classically damped systems.

## 9.5 Incorporation of EMD

Method validation results presented in Section ?? demonstrated that the novel input-output modal parameter identification technique may result in relatively large modal damping estimation errors, especially for the lower modes. In addition, the same study in Section ?? demonstrated that large mode shape coefficient identification errors are possible for signals with poor signal-to-noise ratios. A number of studies [70, 117, 118] demonstrated the potential of empirical mode decomposition (EMD) in alleviating signal noise effects, enabling an increase in the robustness of system identification methods. Thus, future work could attempt to increase the robustness of the proposed input-output modal identification method by incorporating EMD to develop a hybrid identification method.

## 9.6 Comparison to other identification methods

The proposed modal parameter identification extends the application of modal SHM to non-linear cases and enables identification using the response of relatively short earthquake events. The majority of well established existing modal SHM methods are generally capable of identifying linear structures subjected to white noise excitations. Hence, the performance of proposed modal identification technique should be thoroughly compared with other SID methods for linear structures excited by white noise loads.

## 9.7 Further validation with HLA

Chapter 5 and 7 demonstrated the effect of modal filtering on the reconstruction of single mode dominant hysteresis loops. The validation studies demonstrated the hysteresis loops reconstructed using mode decomposed data are easier to interpret visually than raw hysteresis loops, which have a significant contribution from the higher modes. However, a comparison study in Chapter 7 has shown that subsequent application of HLA on mode decoupled hysteresis loops had a marginal improvement on identification accuracy compared to HLA applied to raw hysteresis loops for the analysed test case. Hence, the application of modal identification in conjunction to HLA should be further validated for the test cases, which have a significant contribution from the higher modes.

---

## Bibliography

---

- [1] Miles Parker and Daan Steenkamp. Reserve Bank of New Zealand Bulletin. *Reserve Bank of New Zealand Bulletin*, 75(3):1–79, 2012.
- [2] James E Daniell, Friedemann Wenzel, and Bijan Khazai. The cost of historic earthquakes today – economic analysis since 1900 through the use of CATDAT. *Australian Earthquake Engineering Society Conference*, (May 2014), 2010.
- [3] Hemchandra Chaulagain, Hugo Rodrigues, Vitor Silva, Enrico Spacone, and Humberto Varum. Seismic risk assessment and hazard mapping in Nepal. *Natural Hazards*, 78(1):583–602, 2015.
- [4] Dan M. Frangopol and Mohamed Soliman. Life-cycle of structural systems: recent achievements and future directions. *Structure and Infrastructure Engineering*, 12(1):1–20, 2016.
- [5] Stephanie E Chang, Timothy L McDaniels, Joey Mikawoz, and Krista Peterson. Infrastructure failure interdependencies in extreme events: power outage consequences in the 1998 Ice Storm. *Natural Hazards*, 41(2):337–358, 2007.
- [6] Alberto Decò and Dan M Frangopol. Risk assessment of highway bridges under multiple hazards. *Journal of Risk Research*, 14(9):1057–1089, 2011.
- [7] J B Mander, F D Panthaki, and A Kasalanati. Low-Cycle Fatigue Behavior of Reinforcing Steel. *Journal of Materials in Civil Engineering*, 6(4):453–468, 1994.
- [8] J B Mander and G W Rodgers. Analysis of low cycle fatigue effects on structures due to the 2010-2011 Canterbury earthquake sequence. In *Proceedings of the Tenth Pacific Conference on Earthquake Engineering*. Sydney, 2015.

- [9] Dan M. Frangopol and Min Liu. Maintenance and management of civil infrastructure based on condition, safety, optimization, and life-cycle cost. *Structure and Infrastructure Engineering*, 3(1):29–41, 2007.
- [10] K Smarsly, KH Law, and D Hartmann. Towards life-cycle management of wind turbines based on structural health monitoring. *Proceedings of the First International Conference on Performance-based Life-cycle Structural Engineering*, (Lcm), 2012.
- [11] K. Smarsly, D. Hartmann, and K. H. Law. A computational framework for life-cycle management of wind turbines incorporating structural health monitoring. *Structural Health Monitoring*, 12(4):359–376, 2013.
- [12] André D. Orcesi, Dan M. Frangopol, and Sunyong Kim. Optimization of bridge maintenance strategies based on multiple limit states and monitoring. *Engineering Structures*, 32(3):627–640, 2010.
- [13] A Titi and F Biondini. Resilience of concrete frame structures under corrosion. *Ellingwood & Frangopol*, pages 978–1, 2013.
- [14] Fabio Biondini, Elena Camnasio, and Andrea Titi. Seismic resilience of concrete structures under corrosion. *Earthquake Engineering & Structural Dynamics*, 44(14):2445–2466, nov 2015.
- [15] Nader M Okasha, Dan M Frangopol, and Alberto Decò. Integration of structural health monitoring in life-cycle performance assessment of ship structures under uncertainty. *Marine Structures*, 23(3):303–321, 2010.
- [16] Tolga Kurtoglu, Stephen B Johnson, Eric Barszcz, Jeremy R Johnson, and Peter I Robinson. Integrating system health management into the early design of aerospace systems using functional fault analysis. In *Prognostics and Health Management, 2008. PHM 2008. International Conference on*, pages 1–11. IEEE, 2008.
- [17] James Anderson and Ahmed Mantawy. Earthquake Damage Potential Due to Low-Cycle Fatigue in R.C. Moment Frame Buildings. *10th U.S. National Conference on Earthquake Engineering*, 2014.



- [18] Cong Zhou, J Geoffrey Chase, Geoffrey W Rodgers, and Chao Xu. Comparing model-based adaptive LMS filters and a model-free hysteresis loop analysis method for structural health monitoring. *Mechanical Systems and Signal Processing*, 84:384–398, 2017.
- [19] Cong Zhou, J. Geoffrey Chase, Geoffrey W. Rodgers, and Chikara Iihoshi. Damage assessment by stiffness identification for a full-scale three-story steel moment resisting frame building subjected to a sequence of earthquake excitations. *Bulletin of Earthquake Engineering*, 15(12):1–20, 2017.
- [20] Cong Zhou, J. Geoffrey Chase, and Geoffrey W. Rodgers. Efficient hysteresis loop analysis-based damage identification of a reinforced concrete frame structure over multiple events. *Journal of Civil Structural Health Monitoring*, 7(4):541–556, 2017.
- [21] Anders Rytter. Vibrational Based Inspection of Civil Engineering Structures. *Fracture and Dynamics*, 1993.
- [22] I. Amenabar, A. Mendikute, A. López-Arraiza, M. Lizaranzu, and J. Aurrekoetxea. Comparison and analysis of non-destructive testing techniques suitable for delamination inspection in wind turbine blades. *Composites Part B: Engineering*, 42(5):1298–1305, 2011.
- [23] Fei Yan, Roger L Royer Jr, and Joseph L Rose. Ultrasonic guided wave imaging techniques in structural health monitoring. *Journal of intelligent material Systems and Structures*, 21(3):377–384, 2010.
- [24] Seth S Kessler, S Mark Spearing, and Constantinos Soutis. Damage detection in composite materials using Lamb wave methods. *Smart materials and structures*, 11(2):269, 2002.
- [25] S Mahadev Prasad, Krishnan Balasubramaniam, and C V Krishnamurthy. Structural health monitoring of composite structures using Lamb wave tomography. *Smart materials and structures*, 13(5):N73, 2004.
- [26] Philip J Withers and Michael Preuss. Fatigue and damage in structural materials studied by X-ray tomography. *annual review of materials research*, 42:81–103, 2012.

- [27] L Babout, W Ludwig, E Maire, and J Y Buffiere. Damage assessment in metallic structural materials using high resolution synchrotron X-ray tomography. *Nuclear Instruments and Methods in Physics Research Section B: Beam Interactions with Materials and Atoms*, 200:303–307, 2003.
- [28] Christian U Grosse and Masayasu Ohtsu. *Acoustic emission testing*. Springer Science & Business Media, 2008.
- [29] Seok Been Im and Stefan Hurlebaus. Non-destructive testing methods to identify voids in external post-tensioned tendons. *KSCE Journal of Civil Engineering*, 16(3):388–397, 2012.
- [30] Jack Blitz. *Electrical and magnetic methods of non-destructive testing*, volume 3. Springer Science & Business Media, 2012.
- [31] Charles J Hellier. *Handbook of Nondestructive Evaluation*, volume 69. 2012.
- [32] Liang Cheng and Gui Yun Tian. Comparison of nondestructive testing methods on detection of delaminations in composites. *Journal of sensors*, 2012, 2012.
- [33] Claus-peter Fritzen. Vibration-Based Methods for SHM. pages 1–24, 2013.
- [34] J.E. Mottershead and M.I. Friswell. Model Updating In Structural Dynamics: A Survey, 1993.
- [35] S.W. Doebling, C.R. Farrar, M.B. Prime, and D.W. Shevitz. Damage identification and health monitoring of structural and mechanical systems from changes in their vibration characteristics: A literature review. *The Shock and Vibration Digest*, LA–13070-(August 2016):127, 1996.
- [36] John E. Mottershead, Michael Link, and Michael I. Friswell. The sensitivity method in finite element model updating: A tutorial. *Mechanical Systems and Signal Processing*, 25(7):2275–2296, 2011.
- [37] D. J. Ewins. *Modal testing : theory, practice, and application*. Research Studies Press, 2000.

- [38] M. I. Friswell. Damage identification using inverse methods. *Philosophical Transactions of the Royal Society A: Mathematical, Physical and Engineering Sciences*, 365(1851):393–410, 2007.
- [39] M Imregun, W J Visser, and D J Ewins. Finite element model updating using frequency response function data: I. Theory and initial investigation. *Mechanical Systems and Signal Processing*, 9(2):187–202, 1995.
- [40] Anne Teughels, Johan Maeck, and Guido De Roeck. Damage assessment by FE model updating using damage functions. *Computers and Structures*, 80(25):1869–1879, 2002.
- [41] Anne Teughels and Guido Roeck. Damage detection and parameter identification by finite element model updating. *Archives of Computational Methods in Engineering*, 12(2):123–164, 2005.
- [42] Byung Kwan Oh, Min Sun Kim, Yousok Kim, Tongjun Cho, and Hyo Seon Park. Model Updating Technique Based on Modal Participation Factors for Beam Structures. *Computer-Aided Civil and Infrastructure Engineering*, 30(9):733–747, 2015.
- [43] B Moaveni, X He, JP Conte, and RA de Callafon. Damage identification of a composite beam using finite element model updating. *Computer-Aided Civil and Infrastructure Engineering*, 23(5):339 – 359, 2008.
- [44] Babak Moaveni, Andreas Stavridis, Geert Lombaert, and Joel P Conte. Finite-Element Model Updating for Assessment of Progressive Damage in a 3-Story Infilled RC Frame. *Journal of Structural Engineering*, 139(10), 2013.
- [45] J. Geoffrey Chase, K. Leo Hwang, L. R. Barroso, and J. B. Mander. A simple LMS-based approach to the structural health monitoring benchmark problem. *Earthquake Engineering & Structural Dynamics*, 34(December 2004):575–594, 2005.
- [46] J. Geoffrey Chase, Hannes A. Spieth, C. Francois Blome, and J .B. Mander. LMS-based structural health monitoring of a non-linear rocking structure. *Earthquake Engineering and Structural Dynamics*, 34(8):909–930, 2005.

- [47] Mostafa Nayyerloo. *Real-time Structural Health Monitoring of Nonlinear Hysteretic Structures*. PhD thesis, (Doctoral Dissertation). University of Canterbury, 2011.
- [48] Shih-Yu Chu and Shih-Chieh Lo. Application of the on-line recursive least-squares method to perform structural damage assessment. *Structural Control and Health Monitoring*, 18(3):241–264, apr 2011.
- [49] J. Geoffrey Chase, Vincent Begoc, and Luciana R. Barroso. Efficient structural health monitoring for a benchmark structure using adaptive RLS filters. *Computers and Structures*, 83(8-9):639–647, 2005.
- [50] Jann N. Yang and Silian Lin. On-line identification of non-linear hysteretic structures using an adaptive tracking technique. *International Journal of Non-Linear Mechanics*, 39:1481–1491, 2004.
- [51] Jann N. Yang and Hongwei Huang. Sequential non-linear least-square estimation for damage identification of structures with unknown inputs and unknown outputs. *International Journal of Non-Linear Mechanics*, 42:789–801, 2007.
- [52] Jann N. Yang and Hongwei Huang. Sequential non-linear least-square estimation for damage identification of structures with unknown inputs and unknown outputs. *International Journal of Non-Linear Mechanics*, 42:789–801, 2007.
- [53] Jann N. Yang, Hongwei Huang, and Shuwen Pan. Adaptive Quadratic Sum-Squares Error for Structural Damage Identification. *Journal of Engineering Mechanics*, 135(2):67–77, 2009.
- [54] Tengfei Mu, Li Zhou, and Jann Yang. Comparison of adaptive structural damage identification techniques in nonlinear hysteretic vibration isolation systems. *Earthquake Engineering & Engineering Vibration*, 12(4):659–667, 2013.
- [55] Jann N Yang, Ye Xia, and Chin-hsiung Loh. Damage Detection of Hysteretic Structures with a Pinching Effect. *Journal of Engineering Mechanics*, 140(March):462–472, 2014.

- [56] Re E Kalman. A New Approach to Linear Filtering and Prediction Problems. *Transactions of the ASME-Journal of Basic Engineering*, 82(Series D):35–45, 1960.
- [57] Masaru Hoshiya and Etsuro Saito. Structural identification by extended Kalman filter. *Journal of Engineering Mechanics*, 110(12):1757–1770, 1985.
- [58] R. Y Tan and C. C Chen. Structural identification of a nonlinear MDOF system by extended Kalman Filter. In *Proceedings, Ninth World Conference on Earthquake Engineering*, 1989.
- [59] Chan Ghee Koh, Lin Ming See, and Thambirajah Balendra. Estimation of structural parameters in time domain. A substructure approach. *Earthquake Engineering & Structural Dynamics*, 20(September 1990):787–801, 1991.
- [60] C.G Koh and L.M See. Identification and Uncertainty Estimation of Structural Parameters. *Journal of Engineering Mechanics*, 120(6):1219 – 1236, 1994.
- [61] R. Ghanem and G. Ferro. Health monitoring for strongly non-linear systems using the Ensemble Kalman Filter. *Structural Control and Health Monitoring*, 13(December 2005):245–259, 2006.
- [62] Meiliang Wu and Andrew Smyth. Real-time parameter estimation for degrading and pinching hysteretic models. *International Journal of Non-Linear Mechanics*, 43:822–833, 2008.
- [63] Jann N. Yang, Silian Lin, Hongwei Huang, and Li Zhou. An adaptive extended Kalman filter for structural damage identification. *Structural Control and Health Monitoring*, 13(4):849–867, jul 2006.
- [64] J. N. Yang, S. Pan, and H. Huang. An adaptive extended Kalman filter for structural damage identifications II: unknown inputs. *Structural Control and Health Monitoring*, 14(3):497–521, apr 2007.

- [65] Li Zhou, Shinya Wu, and Jann N. Yang. Experimental Study of an Adaptive Extended Kalman Filter for Structural Damage Identification. *Journal of Infrastructure Systems*, 14(1):42–51, mar 2008.
- [66] Y Lei, H Zhou, and Z.-L. Lai. A Computationally Efficient Algorithm for Real-Time Tracking the Abrupt Stiffness Degradations of Structural Elements. *Computer-Aided Civil and Infrastructure Engineering*, 31(6):465–480, 2016.
- [67] R. Omrani, R. E. Hudson, and E. Taciroglu. Parametric Identification of Nondegrading Hysteresis in a Laterally and Torsionally Coupled Building Using an Unscented Kalman Filter. *Journal of Engineering Mechanics*, 139(4):452–468, apr 2013.
- [68] NE Huang, Z Shen, SR Long, MC Wu, HH Shih, Q Zheng, NC Yen, CC Tung, and HH Liu. The empirical mode decomposition and the Hilbert spectrum for nonlinear and non-stationary time series analysis. *Proceedings of the Royal Society A: Mathematical, Physical and Engineering Sciences*, 454(1971):995, 903, 1998.
- [69] Darryll Pines and Liming Salvino. Structural health monitoring using empirical mode decomposition and the Hilbert phase. *Journal of Sound and Vibration*, 294(1-2):97–124, 2006.
- [70] Dan Jiang Yu and Wei Xin Ren. EMD-based stochastic subspace identification of structures from operational vibration measurements. *Engineering Structures*, 27(12 SPEC. ISS.):1741–1751, 2005.
- [71] Davood Rezaei and Farid Taheri. Experimental validation of a novel structural damage detection method based on empirical mode decomposition. *Smart Materials and Structures*, 18(4):045004, 2009.
- [72] Davood Rezaei and Farid Taheri. Health monitoring of pipeline girth weld using empirical mode decomposition. *Smart Materials and Structures*, 19(5):055016, 2010.
- [73] N. Roveri and A. Carcaterra. Damage detection in structures under traveling loads by Hilbert-Huang transform. *Mechanical Systems and Signal Processing*, 28:128–144, 2012.

- [74] Y L Xu and J Chen. Structural Damage Detection Using Empirical Mode Decomposition: Experimental Investigation. *Journal of engineering mechanics*, 130(11):1279–1289, 2005.
- [75] Silian Lin, Jann N Yang, and Li Zhou. Damage identification of a benchmark building for structural health monitoring. *Smart Materials and Structures*, 14:S162–S169, 2005.
- [76] Jean-Claude Junqua and Jean-Paul Haton. *Robustness in automatic speech recognition: fundamentals and applications*, volume 341. Springer Science & Business Media, 2012.
- [77] Turgay Partal and Özgür Kişi. Wavelet and neuro-fuzzy conjunction model for precipitation forecasting. *Journal of Hydrology*, 342(1):199–212, 2007.
- [78] Michael Unser and Akram Aldroubi. A review of wavelets in biomedical applications. *Proceedings of the IEEE*, 84(4):626–638, 1996.
- [79] K-M. Lau and Hengyi Weng. Climate Signal Detection Using Wavelet Transform: How to Make a Time Series Sing. *Bulletin of the American Meteorological Society*, 76(12):2391–2402, dec 1995.
- [80] C Torrence and G.P. Compo. A practical guide to wavelet analysis. *Bull. Amer. Meteor. Soc.*, 79:61–78, 1998.
- [81] Z. Sun and C. C. Chang. Structural Damage Assessment Based on Wavelet Packet Transform. *Journal of Structural Engineering*, 128:1354–1361, 2002.
- [82] Z. Hou, M. Noori, and R. St. Amand. Wavelet-Based Approach for Structural Damage Detection. *Journal of Engineering Mechanics*, 126(7):677–683, jul 2000.
- [83] Xiaomo Jiang, Sankaran Mahadevan, and Hojjat Adeli. Bayesian wavelet packet denoising for structural system identification. *Structural Control and Health Monitoring*, 14(2):333–356, mar 2007.
- [84] Hongjin Kim and Hojjat Adeli. Hybrid Control of Smart Structures Using a Novel Wavelet-Based Algorithm. *Computer-Aided Civil and Infrastructure Engineering*, 20(1):7–22, 2005.

- [85] Zhijun Li, Hyo Seon Park, and Hojjat Adeli. New method for modal identification of super high-rise building structures using discretized synchrosqueezed wavelet and Hilbert transforms. *Structural Design of Tall and Special Buildings*, 26(3):1–16, 2017.
- [86] Z Sun and C C Chang. Statistical wavelet-based method for structural health monitoring. *Journal of Structural Engineering-Asce*, 130(7):1055–1062, jul 2004.
- [87] Juan P Amezcuita-Sanchez and Hojjat Adeli. Synchrosqueezed wavelet transform-fractality model for locating, detecting, and quantifying damage in smart highrise building structures. *Smart Materials and Structures*, 24(6):065034, 2015.
- [88] R. O. Curadelli, J. D. Riera, D. Ambrosini, and M. G. Amani. Damage detection by means of structural damping identification. *Engineering Structures*, 30(12):3497–3504, 2008.
- [89] Chris M. Bishop. Neural networks and their applications. *Review of Scientific Instruments*, 65(6):1803–1831, 1994.
- [90] Lalu Mangal, V.G. Idichandy, and C. Ganapathy. ART-based multiple neural networks for monitoring offshore platforms. *Applied Ocean Research*, 18(2-3):137–143, apr 1996.
- [91] S. F Masri, A. W Smyth, A. G Chassiakos, T. K. Caughey, and N. F Hunter. Application of neural networks for detection of changes in nonlinear systems. *Journal of Engineering Mechanics*, 126(7):666–676, 2000.
- [92] C. Gonzalez-Perez and J. Valdes-Gonzalez. Identification of Structural Damage in a Vehicular Bridge using Artificial Neural Networks. *Structural Health Monitoring*, 10(1):33–48, 2011.
- [93] Roque A. Osornio-Rios, Juan Pablo Amezcuita-Sanchez, Rene J. Romero-Troncoso, and Arturo Garcia-Perez. MUSIC-ANN Analysis for Locating Structural Damages in a Truss-Type Structure by Means of Vibrations. *Computer-Aided Civil and Infrastructure Engineering*, 27(9):687–698, 2012.



- [94] E. Peter Carden and Paul Fanning. Vibration Based Condition Monitoring: A Review. *Structural Health Monitoring*, 3:355–377, 2004.
- [95] G. F. Sirca and H. Adeli. System identification in structural engineering. *Scientia Iranica*, 19(6):1355–1364, 2012.
- [96] J. T. Kim and N. Stubbs. Crack detection in beam-type structures using frequency data. *Journal of Sound and Vibration*, 259(1):145–160, 2003.
- [97] S Park, N Stubbs, and R W Bolton. Damage detection on a steel frame using simulated modal data. *Proceedings of the International Modal Analysis Conference - IMAC*, 1(3):616–622, 1998.
- [98] Norris Stubbs, Jeong-tae Kim, and Charles R Farrar. Field Verification of a Nondestructive Damage Localization and Severity Estimation Algorithm. 182.
- [99] Jer-Nan Juang and Richard S Pappa. Eigensystem realization algorithm for modal parameter identification and model reduction. *Journal of Guidance, Control, and Dynamics*, 8(5):620 – 627, 1985.
- [100] Richard S Pappa, George H James, and David C Zimmerman. Autonomous Modal Identification of the Space Shuttle Tail Rudder. *Journal of Spacecraft and Rockets*, 35(2):163–169, 1998.
- [101] Hever Moncayo, Johannio Marulanda, and Peter Thomson. Identification and Monitoring of Modal Parameters in Aircraft Structures Using the Natural Excitation Technique (NExT) Combined with the Eigensystem Realization Algorithm (ERA). *Journal of Aerospace Engineering*, 23(2):99–104, apr 2010.
- [102] Juan Martin Caicedo, Shirley J. Dyke, and Erik A. Johnson. Natural Excitation Technique and Eigensystem Realization Algorithm for Phase I of the IASC-ASCE Benchmark Problem: Simulated Data. *Journal of Engineering Mechanics*, 130(1):49–60, jan 2004.

- [103] G. Fraraccio, A. Brügger, and R. Betti. Identification and Damage Detection in Structures Subjected to Base Excitation. *Experimental Mechanics*, 48(4):521–528, feb 2008.
- [104] Hilmi Luş, Raimondo Betti, Jun Yu, and Maurizio De Angelis. Investigation of a System Identification Methodology in the Context of the ASCE Benchmark Problem. *Journal of Engineering Mechanics*, 130(January):71–84, 2004.
- [105] Babak Moaveni, Xianfei He, Joel P. Conte, and Jose I. Restrepo. Damage identification study of a seven-story full-scale building slice tested on the UCSD-NEES shake table. *Structural Safety*, 32(5):347–356, 2010.
- [106] Ah Lum Hong, Raimondo Betti, and Ching-Chang Lin. Identification of dynamic models of a building structure using multiple earthquake records. *Structural Control and Health Monitoring*, 16(2):178–199, 2009.
- [107] Hilmi Luş, Raimondo Betti, and Richard W. Longman. Obtaining refined first-order predictive models of linear structural systems. *Earthquake Engineering and Structural Dynamics*, 31(7):1413–1440, 2002.
- [108] D Benedetti and C Gentile. Identification of modal quantities from two earthquake responses. *Earthquake engineering & structural dynamics*, 23(4):447–462, 1994.
- [109] Dionysius M Siringoringo and Yozo Fujino. Seismic response analyses of an asymmetric base-isolated building during the 2011 Great East Japan (Tohoku) Earthquake. *Structural Control and Health Monitoring*, 22(1):71–90, 2015.
- [110] Peter Van Overschee and B L De Moor. *Subspace identification for linear systems: Theory—Implementation—Applications*. Springer Science & Business Media, 2012.
- [111] Bart Peeters and Guido De Roeck. Stochastic System Identification for Operational Modal Analysis: A Review. *Journal of Dynamic Systems, Measurement, and Control*, 123(4):659, 2001.

- [112] Bart Peeters and Guido De Roeck. Reference-Based Stochastic Subspace Identification for Output-Only Modal Analysis. *Mechanical Systems and Signal Processing*, 13(6):855–878, 1999.
- [113] Edwin Reynders and Guido De Roeck. Reference-based combined deterministic-stochastic subspace identification for experimental and operational modal analysis. *Mechanical Systems and Signal Processing*, 22(3):617–637, 2008.
- [114] Bart Peeters, Herman Van der Auweraer, Frederik Vanhollenbeke, and Patrick Guillaume. Operational Modal Analysis for Estimating the Dynamic Properties of a Stadium Structure during a Football Game. *Shock and Vibration*, 14(4):283–303, 2007.
- [115] L Mevel, M Basseville, and M Goursat. Stochastic subspace-based structural identification and damage detection- application to the steel-quake benchmark. *Mechanical Systems and Signal Processing*, 17(1):91–101, 2003.
- [116] Rodrigo Astroza, Hamed Ebrahimian, Joel P. Conte, José I. Restrepo, and Tara C. Hutchinson. System identification of a full-scale five-story reinforced concrete building tested on the NEES-UCSD shake table. *Structural Control and Health Monitoring*, 23(3):535–559, 2016.
- [117] Wen-Hwa Wu, Sheng-Wei Wang, Chien-Chou Chen, and Gwolong Lai. Application of stochastic subspace identification for stay cables with an alternative stabilization diagram and hierarchical sifting process. *Structural Control and Health Monitoring*, 23(9):1194–1213, 2016.
- [118] Wen-Hwa Wu, Chien-Chou Chen, Shen-Wei Wang, and Gwolong Lai. Modal parameter determination of stay cable with an improved algorithm based on stochastic subspace identification. In *EWSHM-7th European Workshop on Structural Health Monitoring*, 2014.
- [119] Jian Huang Weng, Chin Hsiung Loh, Jerome P. Lynch, Kung Chun Lu, Pei Yang Lin, and Yang Wang. Output-only modal identification of a cable-stayed bridge using wireless monitoring systems. *Engineering Structures*, 30(7):1820–1830, 2008.

- [120] J. M.W. Brownjohn, Filipe Magalhaes, Elsa Caetano, and Alvaro Cunha. Ambient vibration re-testing and operational modal analysis of the Humber Bridge. *Engineering Structures*, 32(8):2003–2018, 2010.
- [121] Rune Brincker, Lingmi Zhang, and Palle Andersen. Modal identification from ambient responses using frequency domain decomposition, 2000.
- [122] Rune Brincker, Lingmi Zhang, and Palle Andersen. Modal identification of output-only systems using frequency domain decomposition. *Smart Materials and Structures*, 10(3):441–445, 2001.
- [123] Rune Brincker, C Ventura, and Palle Andersen. Damping estimation by frequency domain decomposition. In *19th International Modal Analysis Conference*, pages 698–703, 2001.
- [124] Svend Gade, Nis B Møller, Henrik Herlufsen, and Hans Konstantin-Hansen. Frequency Domain Techniques for Operational Modal Analysis. *First International Operational Modal Analysis Conference*, (Type 7760):261–271, 2005.
- [125] Rune Brincker. Automated Frequency Domain Decomposition for Operational Modal Analysis. *Conference: 2007 IMAC-XXV: Conference & Exposition on Structural Dynamics*, pages 1–7, 2007.
- [126] Rodrigo Astroza, Hamed Ebrahimian, Joel P. Conte, José I. Restrepo, and Tara C. Hutchinson. Influence of the construction process and nonstructural components on the modal properties of a five-story building. *Earthquake Engineering & Structural Dynamics*, 45(7):1063–1084, jun 2016.
- [127] Rodrigo Astroza, Hamed Ebrahimian, Joel P. Conte, José I. Restrepo, and Tara C. Hutchinson. System identification of a full-scale five-story reinforced concrete building tested on the NEES-UCSD shake table. *Structural Control and Health Monitoring*, 23(3):535–559, 2016.

- [128] Zhaohui Yang, Utpal Dutta, Feng Xiong, Niren Biswas, and Harley Benz. Seasonal frost effects on the dynamic behavior of a twenty-story office building. *Cold Regions Science and Technology*, 51(1):76–84, 2008.
- [129] Zhaohui Joey Yang, Utpal Dutta, Deju Zhu, Elmer Marx, and Niren Biswas. Seasonal Frost Effects on the Soil–Foundation–Structure Interaction System. *Journal of Cold Regions Engineering*, 21(4):108–120, dec 2007.
- [130] Samuel da Silva, Milton Dias Júnior, Vicente Lopes Junior, and Michael J. Brennan. Structural damage detection by fuzzy clustering. *Mechanical Systems and Signal Processing*, 22(7):1636–1649, 2008.
- [131] Chin Hsiung Loh and Horng Mo LIN. Application of Off-Line and on-Line Identification Techniques To Building Seismic Response Data. *Earthquake engineering & structural dynamics*, 25(June 1995):269–290, 1996.
- [132] Sherif Beskhyroun, Leon D Wegner, and Bruce F Sparling. New methodology for the application of vibration-based damage detection techniques. *Structural Control and Health Monitoring*, 19(1):88–106, 2011.
- [133] Mustafa Gul and F. Necati Catbas. Structural health monitoring and damage assessment using a novel time series analysis methodology with sensor clustering. *Journal of Sound and Vibration*, 330(6):1196–1210, 2011.
- [134] K. Krishnan Nair, Anne S. Kiremidjian, and Kincho H. Law. Time series-based damage detection and localization algorithm with application to the ASCE benchmark structure. *Journal of Sound and Vibration*, 291(1-2):349–368, 2006.
- [135] Ruigen Yao and Shamim N. Pakzad. Autoregressive statistical pattern recognition algorithms for damage detection in civil structures. *Mechanical Systems and Signal Processing*, 31:355–368, 2012.
- [136] Bart Peeters, Herman Van der Auweraer, Patrick Guillaume, and Jan Leuridan. The PolyMAX Frequency-Domain Method: A New Standard for Modal Parameter Estimation? *Shock and Vibration*, 11(3-4):395–409, 2004.

- [137] Bart Peeters, Guillaume Patrick, Van Der Auweraer Herman, Cauberghe Bart, Verboven Peter, and Leuridan Jan. Automotive and aerospace applications of the PolyMAX modal parameter estimation method. *Proceedings of IMAC*, 22(1), 2004.
- [138] Bart Peeters and Herman Van Der Auweraer. Polymax: a Revolution in Operational Modal Analysis. *Proceedings of the 1st International Operational Modal Analysis Conference.*, (January), 2005.
- [139] Edwin Reynders, Jeroen Houbrechts, and Guido De Roeck. Fully automated (operational) modal analysis. *Mechanical Systems and Signal Processing*, 29:228–250, 2012.
- [140] F. Magalhães, E Reynders, A Cunha, and G De Roeck. Online automatic identification of modal parameters of a bridge using the p-LSCF method. *International Operational Modal Analysis Conference*, pages –, 2009.
- [141] Wei-hua Hu, Samir Said, Areva Multibrid, and North Sea. Resonance phenomenon in a wind turbine system under operational conditions 1,2,3,4. *9Th International Conference on Structural Dynamics*, 5000(July):3619–3626, 2014.
- [142] Byeong Hwa Kim, Norris Stubbs, and Taehyo Park. A new method to extract modal parameters using output-only responses. *Journal of Sound and Vibration*, 282(1-2):215–230, 2005.
- [143] Jeong Tae Kim and Norris Stubbs. Damage detection in offshore jacket structures from limited modal information. *International Journal of Offshore and Polar Engineering*, 5(1):58–66, 1995.
- [144] Edwin Reynders. System Identification Methods for (Operational) Modal Analysis: Review and Comparison. *Archives of Computational Methods in Engineering*, 19(1):51–124, 2012.
- [145] Wilfred D Iwan. R-SHAPE: a real-time structural health and performance evaluation system. In *Proceedings of the US-Europe Workshop on Sensors and Smart Structures Technology*, pages 33–38. Wiley, 2003.

- [146] C. Xu, J.G. Chase, and G.W. Rodgers. Nonlinear regression based health monitoring of hysteretic structures under seismic excitation. *Shock and Vibration*, 2015, 2015.
- [147] Cong Zhou, J. Geoffrey Chase, Geoffrey W. Rodgers, Hamish Tomlinson, and Chao Xu. Physical parameter identification of structural systems with hysteretic pinching. *Computer-Aided Civil and Infrastructure Engineering*, 30(4):247–262, apr 2015.
- [148] Ka Veng Yuen and He Qing Mu. Real-Time System Identification: An Algorithm for Simultaneous Model Class Selection and Parametric Identification. *Computer-Aided Civil and Infrastructure Engineering*, 30(10):785–801, 2015.
- [149] R Astroza, H. Ebrahimian, J.P. Conte, J.I. Restrepo, and T.C. Hutchinson. Statistical analysis of the identified modal properties of a 5-story RC seismically damaged building specimen. In *Safety, Reliability, Risk and Life-Cycle Performance of Structures and Infrastructures - Proceedings of the 11th International Conference on Structural Safety and Reliability, ICOSSAR 2013*, number ii, pages 4593–4600, 2013.
- [150] S. Nagarajaiah and B. Basu. Output only modal identification and structural damage detection using time frequency & wavelet techniques. *Earthquake Engineering and Engineering Vibration*, 8(4):583–605, 2009.
- [151] Tarek Edrees Saaed and George Nikolakopoulos. Identification of building damage using ARMAX model: a parametric study. *Diagnostyka*, 17, 2016.
- [152] Ajay Singhal and Anne S Kiremidjian. Method for probabilistic evaluation of seismic structural damage. *Journal of Structural Engineering*, 122(12):1459–1467, 1996.
- [153] Wei-Xin Ren and Guido De Roeck. Structural damage identification using modal data. II: Test verification. *Journal of Structural Engineering*, 128(1):96–104, 2002.
- [154] J. M. Caicedo. Practical guidelines for the natural excitation technique (NExT) and the eigensystem realization algorithm (ERA) for modal identification using ambient vibration. *Experimental Techniques*, 35(August):52–58, 2011.

- [155] Jer-Nan Juang, Minh Phan, Lucas G Horta, and Richard W Longman. Identification of observer/Kalman filter Markov parameters: theory and experiments. *Journal of Guidance, Control, and Dynamics*, 16(2):320–329, 1993.
- [156] Francesco Vicario, Minh Q Phan, Raimondo Betti, and Richard W Longman. Output-only observer/Kalman filter identification (O3KID). *Structural Control and Health Monitoring*, 22(5):847–872, 2015.
- [157] E. Peter Carden and James M W Brownjohn. ARMA modelled time-series classification for structural health monitoring of civil infrastructure. *Mechanical Systems and Signal Processing*, 22(2):295–314, 2008.
- [158] J B Bodeux and J C Golinval. Application of ARMAV models to the identification and damage detection of mechanical and civil engineering structures. *Smart Materials and Structures*, 10(3):479–489, 2001.
- [159] Hoon Sohn and Charles R Farrar. Damage diagnosis using time series analysis of vibration signals. *Engineering Analysis*, 10(3):446–451, 2001.
- [160] Niels-Jørgen Jacobsen, Palle Andersen, and Rune Brincker. Applications of frequency domain curve-fitting in the EFDD technique. In *Proceedings IMAC XXVI Conference*, 2008.
- [161] Charles R Farrar, Scott W Doebling, Phillip J Cornwell, and Erik G Straser. Variability of modal parameters measured on the Alamosa Canyon Bridge. Technical report, Los Alamos National Lab., NM (United States), 1996.
- [162] CEN. Eurocode 8: Design of structures for earthquake resistance. 120:1–229, 2004.
- [163] Randall J Allemang. The Modal Assurance Criterion –Twenty Years of Use and Abuse. *SOUND AND VIBRATION*, 1(August):14–21, 2003.
- [164] Anil K. Chopra. *Dynamics of structures : theory and applications to earthquake engineering*. Prentice Hall, 1995.



- [165] Matthew J Schoettler, Jose Restrepo, Gabriele Guerrini, David E Duck, and Francesco Carrea. A Full-Scale, Single-Column Bridge Bent Tested by Shake-Table Excitation. Technical Report August, PEER Report No. 2015/02, Department of Civil Engineering, University of Nevada, PEER Report No. 2015/02, Department of Civil Engineering, University of Nevada, Reno, 2012.
- [166] Reza D Nayeri. A novel approach for the structural identification and monitoring of a full-scale 17-story building based on ambient vibration measurements. *Smart materials and structures*, 17(2):25006, 2008.
- [167] J W Lin and R Betti. On-line identification and damage detection in non-linear structural systems using a variable forgetting factor approach. *Earthquake Engineering & Structural Dynamics*, 33(4):419–444, 2004.
- [168] H Lus, R Betti, and R W Longman. Identification Of Linear Structural Systems Using Earthquake-Induced Vibration Data. *Earthquake Engineering and Structural Dynamics*, 28(11):1449–1467, 1999.
- [169] Fabio Pioldi, Rosalba Ferrari, and Egidio Rizzi. Seismic FDD modal identification and monitoring of building properties from real strong-motion structural response signals. *Structural Control and Health Monitoring*, (November 2016):1–20, 2017.
- [170] Izuru Takewaki and Mitsuru Nakamura. Temporal variation in modal properties of a base-isolated building during an earthquake. *Journal of Zhejiang University SCIENCE A*, 11(1):1–8, 2009.
- [171] American Society of Civil Engineers. Seismic Evaluation and Retrofit of Existing Buildings: ASCE Standard ASCE/SEI 41-13. American Society of Civil Engineers, 2014.
- [172] J O Malley, G Dierlein, H Krawinkler, J R Maffei, M Pourzanjani, J Wallace, and J A Heintz. Modeling and Acceptance Criteria for Seismic Design and Analysis of Tall Buildings. *Applied Technology Council*, 2010.
- [173] Fabio Taucer, Enrico Spacone, and Filip C Filippou. *A fiber beam-column element for seismic response analysis of reinforced concrete structures*, volume 91. Earthquake En-

- gineering Research Center, College of Engineering, University of California Berkeley, California, 1991.
- [174] Marco Petrangeli, Paolo Emilio Pinto, and Vincenzo Ciampi. Fiber element for cyclic bending and shear of RC structures. I: Theory. *Journal of Engineering Mechanics*, 125(9):994–1001, 1999.
  - [175] Filip C. Filippou and Ahmad Issa. Nonlinear Analysis of Reinforced Concrete Frames Under Cyclic Load Reversals. *Computers*, 13(1-3):111, 1988.
  - [176] Giorgio Monti and Enrico Spacone. Reinforced concrete fiber beam element with bond-slip. *Journal of Structural Engineering*, 126(6):654–661, 2000.
  - [177] Marco Petrangeli. Fiber element for cyclic bending and shear of RC structures. II: Verification. *Journal of engineering mechanics*, 125(9):1002–1009, 1999.
  - [178] J Murcia-Delso, Andreas Stavridis, and Benson Shing. Modeling the Bond-Slip Behaviour of Confined Large-Diameter Reinforcing Bars. *ECCOMAS Thematic Conference on Computational Methods in Structural Dynamics and Earthquake Engineering*, (May), 2011.
  - [179] Michelle Chen, Elide Pantoli, Xiang Wang, Rodrigo Astroza, Hamed Ebrahimian, Steven Mintz, Tara Hutchinson, Joel Conte, and José Restrepo. BNCS Report #1: Full-scale structural and nonstructural building system performance during earthquakes and post-earthquake fire – specimen design, construction, and test protocol. Technical Report December 2013, 2013.
  - [180] Marco Menegotto. Method of analysis for cyclically loaded RC plane frames including changes in geometry and non-elastic behavior of elements under combined normal force and bending. In *Proc. IABSE symposium on resistance and ultimate deformability of structures acted on by well defined repeated loads*, pages 15–22, 1973.
  - [181] Wei Yu. Inelastic Modeling of Reinforcing Bars and Blind Analysis of the Benchmarks Tests on Beam-Column Joints under Cyclic Loading. Technical report, Rose

- School–European School for Advanced Studies in Reduction of Seismic Risk, Pavia, 2006.
- [182] J. Enrique Martínez-Rueda and A. S. Elnashai. Confined concrete model under cyclic load. *Materials and Structures*, 30(3):139–147, apr 1997.
  - [183] G A Chang and John B Mander. Seismic energy based fatigue damage analysis of bridge columns: part 1-evaluation of seismic capacity. 1994.
  - [184] Paul G Somerville, N Smith, S Punyamurthula, and J Sun. *Development of ground motion time histories for phase 2 of the FEMA/SAC steel project*. SAC Joint Venture, 1997.
  - [185] Cong Zhou, J. Geoffrey Chase, Geoffrey W. Rodgers, Chao Xu, and Hamish Tomlinson. Overall damage identification of flag-shaped hysteresis systems under seismic excitation. *Smart Structures and Systems*, 16(1):163–181, 2015.
  - [186] Jose Restrepo. Large-Scale Validation of Seismic Performance of Bridge Columns, 2007.
  - [187] Yehuda Bock, Diego Melgar, and Brendan W. Crowell. Real-time strong-motion broadband displacements from collocated GPS and accelerometers. *Bulletin of the Seismological Society of America*, 101(6):2904–2925, 2011.
  - [188] Andrew Smyth, Meiliang Wu, and . Multi-rate Kalman filtering for the data fusion of displacement and acceleration response measurements in dynamic system monitoring. *Mechanical Systems and Signal Processing*, 21:706–723, 2007.
  - [189] Cao Thanh, Ngoc Tran, and Bing Li. Initial Stiffness of Reinforced Concrete Columns with Moderate Aspect Ratios. *Advances in Structural Engineering*, 15(2):265–277, 2012.
  - [190] Jean-Jacques Sinou. A review of damage detection and health monitoring of mechanical systems from changes in the measurement of linear and non-linear vibrations. *Mechanical Vibrations: Measurement, Effects and Control*, pages 643–702, 2009.
  - [191] Joel Conte, Jose Restrepo, and Tara Hutchinson. NEESR-CR: Full-Scale Structural and Nonstructural Building System Performance during Earthquakes.

- [192] Kui Fu Chen, Jing Tao Jiang, and Stephen Crowsen. Against the long-range spectral leakage of the cosine window family. *Computer Physics Communications*, 180(6):904–911, 2009.
- [193] Mattias Sjöberg and Leif Kari. Testing of nonlinear interaction effects of sinusoidal and noise excitation on rubber isolator stiffness. *Polymer testing*, 22(3):343–351, 2003.
- [194] A R Payne and R E Whittaker. Low strain dynamic properties of filled rubbers. *Rubber chemistry and technology*, 44(2):440–478, 1971.
- [195] Mattias Sjöberg. On dynamic properties of rubber isolators, 2002.
- [196] Masato Abe, Junji Yoshida, and Yozo Fujino. Multiaxial Behaviors of Laminated Rubber Bearings and Their Modeling. II: Modeling. *Journal of Structural Engineering*, 130(8):1133–1144, 2004.
- [197] Yong Yuan, Wei Wei, Ping Tan, Akira Igarashi, Hongping Zhu, Hirokazu Iemura, and Tetsuhiko Aoki. A rate-dependent constitutive model of high damping rubber bearings: modeling and experimental verification. *Earthquake Engineering & Structural Dynamics*, 45(11):1875–1892, 2016.
- [198] Athanasios A. Markou and George D. Manolis. Mechanical formulations for bilinear and trilinear hysteretic models used in base isolators. *Bulletin of Earthquake Engineering*, 14(12):3591–3611, 2016.
- [199] Muna H. Gheryani, Hashim Abdul Razak, and Mohammed Jameel. Dynamic Response Changes of Seismic Isolated Building Due to Material Degradation of HDRB. *Arabian Journal for Science and Engineering*, 40(12):3429–3442, 2015.
- [200] A. Dall’Asta and L. Ragni. Experimental tests and analytical model of high damping rubber dissipating devices. *Engineering Structures*, 28(13):1874–1884, 2006.
- [201] A. R. Bhuiyan, Y. Okui, H. Mitamura, and T. Imai. A rheology model of high damping rubber bearings for seismic analysis: Identification of nonlinear viscosity. *International Journal of Solids and Structures*, 46(7-8):1778–1792, 2009.

- [202] G. C. Foliente, M. P. Singh, and M. N. Noori. Equivalent Linearization of Generally Pinching Hysteretic, Degrading Systems. *Earthquake Engineering & Structural Dynamics*, 25(6):611–629, 1996.
- [203] Bing Li, Graham L. Hutchinson, and Colin F. Duffield. The influence of non-structural components on tall building stiffness. *Structural Design of Tall and Special Buildings*, 20(7):853–870, nov 2011.
- [204] R. K L Su, A. M. Chandler, M. N. Sheikh, and N. T K Lam. Influence of non-structural components on lateral stiffness of tall buildings. *Structural Design of Tall and Special Buildings*, 14(2):143–164, 2005.
- [205] Jushan Bai and Pierre Perron. Estimating and testing linear models with multiple structural changes. *Econometrica*, pages 47–78, 1998.
- [206] William S Cleveland. Robust locally weighted regression and smoothing scatterplots. *Journal of the American statistical association*, 74(368):829–836, 1979.